Velocity Distribution Prediction in Rectangular and Compound Channels under Smooth and Rough Flow Conditions

Wisam Abd Ali Khalaf Alawadi

School of Computing, Science and Engineering

University of Salford, Salford, UK

Submitted in Partial Fulfilment of the Requirements of the Degree of Doctor of Philosophy in Civil Engineering

2019

Table of Contents

List of Tables

List of Figures

List of symbols

A	Cross-sectional area of channel, (m^2).
Ar	Aspect ratio (the ratio of channel width to flow depth).
$A1, A2$	Integration constants in the analytical solution of SKM model.
B	Channel width, (m).
b	Width of the main channel in compound channels, (m).
C_f	Dimensionless friction coefficient.
Dr	Relative depth (the ratio of the flow depth in the floodplain to that of the main channel).
D_{50}	Median size diameter of particles fixed on the bed of the channel, (m).
D_{84}	Representative particle size where 84% of the particles in the total grain-size distribution are smaller than this size, (m).
f	Darcy–Weisbach friction factor.
g	Gravitational acceleration, (m/s^2).
H	Flow depth as a function of lateral distance y, (m).
h	Flow depth in rectangular channels or bank-full depth in compound channels, (m).
Δh	Differential head measured using the pressure transducer, (m).
K	Roughness height, (m).
Ks	Nikuradse’s equivalent roughness or equivalent sand roughness height, (m).
ℓ_t	Turbulence length scale, (m).
n	Manning’s resistance coefficient, ($s/m^{1/3}$).
n_{comp}	Composite or global value of Manning coefficient, ($s/m^{1/3}$).
Q	Total cross-section discharge, (m^3/s).
q	Lateral inflow, (m^2/s).
p	Pressure, ($Pa = N/m^2$).
P_s	Static pressure, (Pa).

P_v	Dynamic pressure, (Pa).
Δp	Pressure difference between the static and dynamic pressures, (Pa).
P	Wetted perimeter of the channel, (m).
R	Hydraulic radius (=A/P), (m).
Re	Reynolds number.
$Re*$	Roughness Reynolds number.
RANS	Reynolds-averaged Navier-Stokes (RANS) modelling.
S_o	Bed slope of the channel, (m/m).
S_f	Friction slope or energy slope, (m/m).
SKM	Shiono and Knight method.
t	Time, (s).
u, v, w	Instantaneous velocity in the x, y and z directions, (m/s).
U, V, W	Time-averaged velocities in the x, y, z directions, (m/s).
u', v', w'	Turbulent fluctuations with respect to the mean velocities, (m/s).
$\overline{u_i' u_j'}$	Reynolds stresses tenser, (m^2/s^2).
u_t	Turbulence velocity scale, (m/s).
u_*	Local shear velocity, (m/s).
U_d	Depth-averaged longitudinal velocity (i.e. in x direction), (m/s).
$U*$	Average shear velocity, (m/s).
U_{max}	Maximum longitudinal velocity (i.e. in x direction), (m/s).
U_{sec}	Secondary flow velocity ($= \sqrt{V^2 + W^2}$), (m/s).
V	Time-averaged velocity in the y-direction, (m/s).
V_d	Depth-averaged crosswise velocity (y-direction), (m/s).
W	Time-averaged velocity in the z-direction, (m/s).
x	Horizontal, streamwise or longitudinal direction, (m).
y	Lateral or cross-stream direction, (m/s).

z	Vertical direction or distance from the wall, (m/s).
z_o	The zero-velocity level, (m/s).
z^+	non-dimensional vertical distance which is a function of distance from the wall, the flow velocity and viscosity.
α	Coriolis or kinetic energy correction coefficient.
β	Boussinesq or momentum correction coefficient.
Γ	Secondary flow term in SKM model.
ΔB	The shift in the velocity profile due to the roughness effect.
δ	Thickness of the boundary layer, (m).
ε	Rate of viscous dissipation in the k-ε turbulence model.
ξ	Normalized z-coordinate.
κ	von Karman’s constant.
λ	Dimensionless depth-averaged eddy viscosity.
μ	Dip correction factor.
ν	Kinematic viscosity of the fluid, (m^2/s).
ν_t	Turbulent eddy viscosity, (m^2/s).
Π	Wake strength parameter after Coles (1956).
ρ	Fluid density, (Kg/m^3).
σ_g	Geometric standard deviation for particles.
τ_b	Boundary shear stress, (N/m^2).
τ_w	Wall shear stress, (N/m^2).
τ_{yx}	Reynolds stresses on vertical plane, normal to y-axis in x direction, (N/m^2).
τ_{zx}	Reynolds stresses on horizontal plane, normal to z-axis in x direction, (N/m^2).
ω	Specific dissipation rate in the k-ω turbulence model.

Acknowledgement

I would like to give my heart-felt thanks first to my supervisor, Dr. Prasad Tumula, who helped me from the first day to the eventual completion of this research. His invaluable guidance and continuous support have made this research easier. I know very well that I would struggle to finish this study in limited time scale, without his enthusiastic supervision and his encouragement of me. I also would like to thank my Co-Supervisor, Dr. Tahsin Toma Sabbagh, for his help and support.

I would like to thank the Iraqi Ministry of Higher Education and Scientific Research and their reprehensive Iraqi Cultural Attaché for all support they provided to me during the time of the study. Likewise, I thank the University of Basrah for awarding me this scholarship to do the PhD degree and develop my academic skills.

I would like to give my special thanks to all technicians at the Hydraulic Lab in University of Salford for their kind help and creative suggestions in installing and using the experimental facilities.

Last but not least, I thank my family deeply, especially my mother and my wife, for their patience, understanding and support during this research.

Declaration

This thesis is submitted to the University of Salford rules and regulations for the award of a PhD degree by research. While the research was in progress, some research findings were published in refereed journals papers prior to this submission.
The researcher declares that no portion of the work referred to in this thesis has been submitted in support of an application for another degree of qualification of this, or any other university or institution of learning.

Signature of candidate: Wisam Abd Ali Alawadi

Affirmation

Journal papers

1. Wisam Alawadi & Tumula, P. D. (2018). Depth-averaged simulation of flows in asymmetric compound channels with smooth and rough narrow floodplains. *Australasian Journal of Water Resources*, *22*(2), 137-148.
2. Wisam Alawdi & Prasad, T. D. (2018). Comparison of Performance of Simplified RANS Formulations for Velocity Distributions against Full 3D RANS Model. *International Journal of Hydraulic Engineering*, *7*(2), 33-42.
3. Wisam Alawadi & Prasad, T. D. (2018). Assessing the Impact of Velocity Dip and Wake Coefficients on Velocity Prediction for Open Channel Flows. *Research Journal of Applied Sciences, Engineering and Technology*, *16*(1):9-14.

Conference papers

1. Wisam Alawdi, Prasad, T. D. and Osamah Al-salih. (2018). Application of the Shiono and Knight Model in Asymmetric Compound Channels with Smooth and Rough Narrow Floodplains. 2^{ed} International Conference on Structural and Civil Engineering (ICSCE), University of Lisbon, Portugal, September 26-28, 2018.

Papers under consideration

1. Wisam Alawdi1, Prasad, T. D. (Computational Study of Non-Uniformity of Primary Velocity Distribution in Rectangular Channels). *Journal of Applied Water Engineering and Research*.

Abstract

Many practical problems in river engineering require predictions of velocity distributions in single and compound open channels. In this study, velocity distributions in rectangular and compound open channels under different flow regimes, in terms of roughness and turbulence conditions, were investigated experimentally and numerically. The detailed results from the experiments and numerical simulations were then used to assess and improve two velocity distribution models, which are widely used for rectangular and compound channel flows. The focus was mainly on the flow in narrow open channels.

Two sets of experiments were conducted on rectangular and compound channels that had different hydraulic and roughness characteristics. In these experiments, three flow regimes in terms of the roughness (smooth, transitional and rough regimes) were established by changing roughness of the bed. Detailed measurements of velocity distributions were carried out to study the effect of roughness on the non-uniformity of velocity distributions in such channels. The channel flows tested in the experiments were also simulated using Computational Fluid Dynamic (CFD) models. The CFD models were developed and run using CFX package (v.15).

The effect of the roughness on the velocity distributions in outer region was found to be significant. The non-uniformity of the velocity distribution, which can be described by the energy coefficient (α) and momentum coefficient (β), was considerably high in fully rough flow regime than in smooth and transitionally rough flows. The values of α are ranging from 1.07 to 1.16 in fully rough regimes while α values are varying from 1.05 to 1.13 in the corresponding smooth flow cases. The similar trend can be seen for β values, where β lies within a range of (1.013 – 1.032) in smooth flows and (1.022 - 1.045) in rough flows. It was also found that the velocity distribution coefficients (α and β) can be related to roughness Reynolds number (Re^*) and aspect ratio (Ar) in rectangular channels and to the relative depth (Dr) in compound channels. The relationships for the velocity distribution coefficients (α or β) proposed in the present study can be used to describe the non-uniformity of the velocity distributions and solve engineering flow problems that depend on the velocity distribution such as sediments and pollution transports.

The detailed CFD results were also used as part of an investigation in the significance of secondary flows and turbulent eddy viscosity in the calculations of primary velocity distributions. Two analytical models for velocity distribution were used in this study. For

rectangular channel flows, the dip-modified log wake law (DMLW-law) was used. The DMLW-law accounts for the effects of the secondary flow and turbulence by two representative parameters. These two parameters are the dip correction factor (μ) and the wake strength parameter (Π). The analytical model developed by Shiono and Knight (1988, 1991), which called SKM model, was applied for depth-averaged velocity calculations in compound channels. The SKM model relies on three parameters, namely friction factor (*f*), dimensionless eddy viscosity (λ), and secondary flow term (Γ).

For velocity prediction in rectangular channels, expressions for estimating the values of μ and Π has been proposed in this study. Comparison with the experimental results indicated that the proposed expressions to calibrate the parameters (Π and μ) can provide efficiency to the application of the analytical model (DMLW-law) for rectangular channel flows under different flow regimes. For compound channel flows, it was found that the application of analytical SKM model with the existing expressions for the three parameters (f, λ, Γ) does not fit to the compound channel with narrow floodplains such as the one used in the present study. Therefore, the detailed Computational Fluid Dynamics (CFD) results were used to modify the traditional expressions. The modified expressions for λ and Γ parameters proposed in the present study were proved to give better predictions for the narrow compound channel flows than the traditional calibration expressions.

Chapter 1

Introduction

1.1 Research Motivation

The velocity distribution of open channel flows has constantly interested river engineers and researchers for its practical implications on many engineering applications. Accurate prediction of velocity distribution is necessary, for example, to study river water sediment transport, pollutant dispersion, channel scouring, and bank protection works.

In order to predict the velocity distribution in rivers and open channels, measurements of local velocity and some hydraulic properties (e.g. depth and discharge) are often required. However, taking the measurements in open channels and rivers is not always convenient and may be impossible in some cases (e.g. during flood events). This has prompted a need to develop accurate and reliable models for predicting the velocity distribution and, at the same time, these models should be simple to be implemented by hydraulic engineers. Thus, several analytical models based on a simplified form of the Reynolds-averaged Navier–Stokes equations (RANS) has been developed for predicting the vertical and lateral distributions of velocity in rectangular and compound channels. In these models, all the physical effects on the velocity distribution are often represented by a so called (calibration parameters). As suggested from the name, calibration parameters require a specific calibration process to produce accurate results. Therefore, the central concern of this research is to study the velocity distributions in open channel flows under different conditions in terms of roughness, focusing on the calibration process of most common models used for velocity prediction in open channels. A brief background of the most relevant issues to consider in the velocity distribution prediction are given in the following section.

1.2 Research Background

1.2.1 Primary and secondary flows

In case of a three-dimensional turbulent flow, the flow is often regarded as comprising of two flow components, namely primary flow and secondary flow. Primary flow is parallel to the direction of fluid motion, whereas secondary flow is transverse to the primary flow direction. In most flow cases, the secondary flow is a relatively minor component compared to the primary flow and is commonly termed secondary currents.

The velocity of primary flow in open channels is not uniformly distributed over the cross-section. This non-uniformity is caused by the presence of free surface and frictional resistance along the channel perimeter, (Singh, 2012). The turbulent flow field in open channel can be divided into three flow layers (Nezu and Nakagawa, 1993). These layers are defined as; wall shear layer ($z < 0.2h$), intermediate layer ($0.2h \leq z \leq 0.6h$) and free surface layer ($0.6h < z \leq h$), where z is the distance from the solid boundary and h is the flow depth. The wall shear layer is often called inner layer, while the intermediate layer and free surface layer together compose what is called the outer layer.

The boundary roughness plays an important role in defining the velocity distribution in both the inner and the outer layer (Hinze, 1975 and Schlichting, 1979). Based on the experimental findings on roughness, the flow regimes are classified as hydraulically smooth, rough, and transitional flows (Figure 1.1) (Schlichting, 1979). The roughness Reynolds number $R*$ is used as a decisive parameter to define the flow regimes. The roughness Reynolds number can be expressed as ($R^* = u_* K_S/v$), where u_* is the shear velocity, K_S is called equivalent sand roughness which represents the boundary roughness height and v is the fluid viscosity.

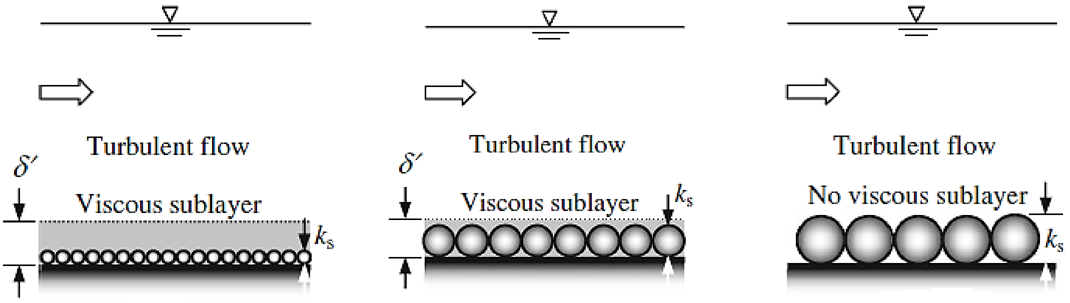

(a) smooth (b) transition (c) rough

Figure 1.1 Classification of flow regimes.

In hydraulically smooth flow, for which $R^* \leq 5$, the boundary roughness height K_S is much smaller than the viscous sublayer thickness (δ'). Thus, the roughness elements are submerged by the viscous sublayer. In hydraulically rough flow, where $R^* \geq 70$, the boundary roughness height is much larger than the viscous sublayer thickness. The roughness elements are therefore exposed to the main flow region and would affect significantly the velocity distribution in the outer region.

In addition to the effects of the boundary roughness on the primary flow velocity, the secondary flow and the momentum transfer due the turbulence may also have significant effects on the velocity distribution. In straight open channels, secondary flows may generate because of turbulence anisotropy of normal Reynolds stresses (Tominaga et al., 1989). This type of secondary flows is often defined as turbulence-driven secondary currents and no channel curvature is required to generate them. Turbulence-driven secondary currents were experimentally observed in simple open channels with rectangular or trapezoidal cross-section (Gessner, 1973; Müller & Studerus, 1979; Nezu & Nakagawa, 1984; Nezu and Rodi, 1985; Tominaga et al., 1989; Wang & Cheng, 2006). Figure 1.2 schematically shows the secondary currents in wide and narrow rectangular channels. The wide and narrow channels are defined based on the ratio of channel width (*B*) to flow depth (*h*), termed aspect ratio ($Ar = B/h$). For narrow channels, *Ar* is less 5, while for wide channels *Ar* is larger than 5, (Nezu and Rodi, 1985).

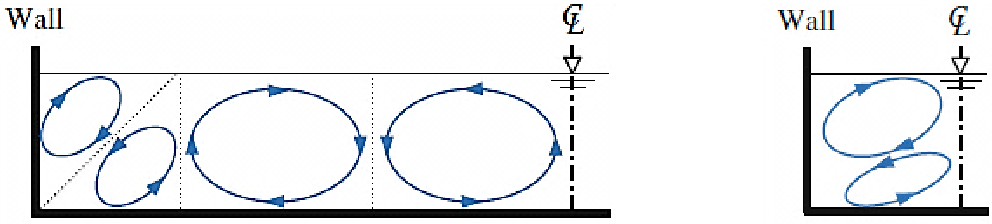

(a) wide channel (b) narrow channel

Figure 1.2 Schematic rectangular open channel with secondary currents.

As a result of the generation of secondary currents, the maximum velocity appears below the free surface, which is called the dip phenomenon (Tominaga et al., 1989). This indicates that the secondary currents in simple open channels may introduce significant changes in the turbulence structure and then the primary flow. Therefore, the effects of the secondary flow on the primary flow, particularly in narrow open channels, should not be neglected.

In compound open channels, the flow field becomes more complex due to the strong interaction developing between the flows in the main channel and on the floodplains (Shiono & Knight, 1991). In such a flow, a lateral interfacial shear is created due to the steep velocity gradients at the main channel floodplain interface, leading to generation of large-scale horizonal vortices, which also called planform vortices. In addition to these vortices, streamwise secondary currents can often be observed in compound channels, especially near the junction between the main channel (MC) and floodplain (FP), as shown in Figure 1.3 (Shiono & Knight, 1991; Nezu and Nakagawa, 1993). The existence of planform vortices and secondary currents play an important role in momentum exchange between the main channel and floodplain, affecting the distribution of the primary flow velocity.

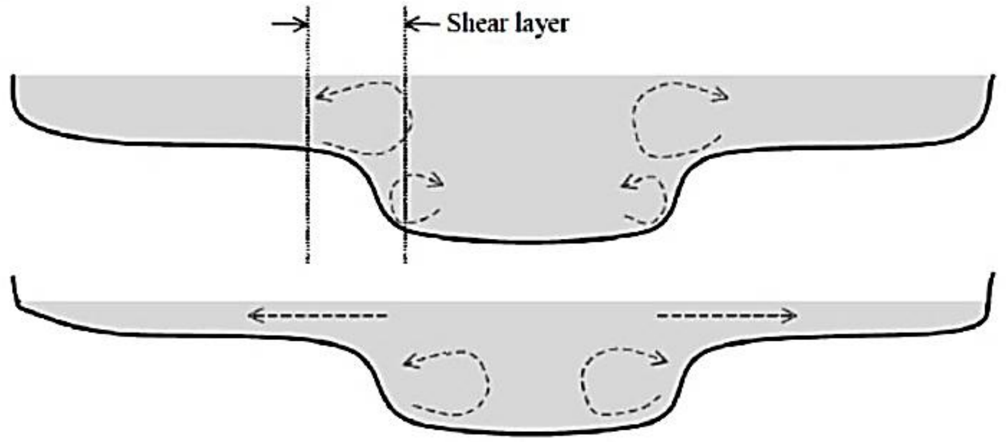

Figure 1.3 Typical sketch for overbank flow in compound channels.

1.2.2 Predicting velocity distribution in open channels

The traditional laws, such as the law of the wall, may fail to express the velocity distribution in the outer region because they cannot capture the effects of the secondary flows (Guo & Julien, 2003; Yang et al. 2004). Therefore, several analytical models are developed to account for the effects of the secondary flows and turbulence on the primary flow calculations. Almost all the analytical models are based on analytical solutions of the Reynolds-averaged Navier-Stokes (RANS) equations by applying specific assumptions for the secondary currents and turbulence effects. These analytical solutions produce laws for velocity distribution that depends on parameters for secondary currents, turbulence and boundary roughness. For uniform flows in narrow rectangular channels, Yang et al. (2004) derived an analytical model called dip-modified logarithmic law (DML-law), including the dip phenomenon caused by the secondary flows. To simplify RANS equations, Yang et al. (2004) assume an empirical model for secondary flow term and use a parabolic distribution for eddy viscosity. Although this law can adequately simulate smooth flows, it fails to predict the velocity well in the rough channels (Guo & Julien, 2008; Bonakdari et al., 2008; Absi, 2011 and Lassabatere et al., 2012). The dip-modified log-wake law (DMLW-law) was also developed to predict the velocity distribution in open channels under secondary currents effects (Absi, 2011). In this model, instead of a parabolic distribution used in DML-law, the eddy viscosity (ν_t) was approximated in accordance with the log-wake law given by Nezu and Rodi (1986). In addition to the above two models, there are other analytical models for predicting the velocity distributions (e.g., Guo & Julien, 2008; Bonakdari et al., 2008, Absi, 2011 and Lassabatere et al. 2012). However, it was found that the DMLW-law is the most practical model for both smooth and rough flows (Absi, 2011; Lassabatere et al. 2012). Therefore, only this law is considered in this study. The focus was on the calibration of the model parameters that represents the effects of the secondary flow and turbulence on the primary flow velocity.

For compound channel flows, the Shiono & Knight model (SKM) is widely used to predict the lateral distribution of depth-averaged velocity and boundary shear stress (Shiono & Knight, 1991; Abril and Knight, 2004; Liao and Knight, 2007; Tang & Knight, 2008; and Devi & Khatua, 2016). The application of SKM model needs to divide the cross-section of the channel into a number of sub-areas and properly estimate the friction factor (f), the dimensionless eddy viscosity parameter (λ) and the secondary flow parameter (Γ) for each sub-area. The accuracy of the SKM results was found to depend substantially on these three calibration coefficients (i.e. f, λ and Γ) (Abril and Knight, 2004). Different methods have been suggested to calibrate each one of these three coefficients in the compound channel with wide floodplains, i.e. the floodplain width is equal to or larger than the main channel width (Shiono & Knight, 1991; Abril and Knight, 2004; Devi & Khatua, 2016). However, using the expressions suggested for a compound channel with wide floodplains to calculate the SKM parameters are not tested for a compound channel with narrow floodplains. Therefore, in the present study, the focus was on the application of SKM model to the narrow floodplain channels.

Although the uniform flow is an important type of flow, which often occurs in long open channels with unvarying cross-section and bottom slope, natural river flows are frequently affected by upstream or downstream controls. This makes the flow non-uniform and even possibly unsteady. Under these circumstances, the flow velocity can be computed from the one-dimensional (1-D) momentum or energy equations. The major issue to appreciate when applying the 1-D flow models is how the three-dimensional velocity field can be included in a 1-D formulation of energy or momentum equations (Knight et al., 2010). This is usually achieved by use of the kinetic energy and momentum correction coefficients (α, β). These two coefficients, which are also referred to as velocity distribution coefficients, are applied in momentum and energy equations to account for the non-uniformity of the velocity distribution by correcting the errors resulted from averaging the velocity over the cross-section. In some engineering applications, the effect of nonuniform velocity distribution is assumed to be small. Thus, the energy and momentum correct coefficients are assumed to be unity. However, several previous studies have indicated that the velocity distribution coefficients (α, β) have a significant effect on the accuracy of the 1D flow solution (Xia and Yen, 1994; Fenton, 2005 and Costabile & Macchione, 2010). Therefore, there is a growing need to gain a better understanding of how various hydraulic conditions in the open channel, or river, may influence the velocity distribution coefficients.

1.2.3 Computation Fluid Dynamics (CFD)

Growing in computing power encourages on using Computational Fluid Dynamics (CFD) modelling to perform extensive studies on the turbulent flows in open channels. The 3D numerical simulations by the CFD may provide clearer explanations of the interactions of the key hydraulic components than do the traditional laboratory measurements (Bates et al., 2005). Many validation studies indicated that the CFD models can predict the most important characteristics of different pattern flows with an acceptable level of accuracy (e.g. Jing et al., 2009; Sharifipour et al., 2015; Asnaashari et al. 2016, Wu et al., 2018).

The CFD framework used in the present study are theoretically based on solving the Reynolds-Averaged Navier-Stokes (RANS) equations. In RANS approach, a turbulence model is usually developed to compute Reynolds stress tensor and close RANS equations (Bates et al., 2005). The Reynolds Stress Models (RSM), which solve directly an equation for the transport of Reynolds stresses, was used to close the RANS equations. It is known that the RSM models are more sophisticated than the two-equation (eddy-viscosity) turbulence models (Cokljat & Younis, 1995a). However, they are still the most practical turbulence models in use for the environmental applications because they can produce reasonably accurate solutions with the available computer power (Andersson et al., 2011). Furthermore, RSM models can predict secondary currents generated by the anisotropy in the normal Reynolds stresses because they can model the individual stresses (Cokljat & Younis, 1995a; Kang & Choi, 2006a). Therefore, the Reynolds Stress Model was used as a turbulence model in the present work.

1.3 Research hypotheses

The 1-D numerical are often used for non-uniform flow problems because these models approximate the complicated 3-D flow equations and make their solution more handy and feasible. However, the non-uniformity distribution of velocity field has certain implications with respect to energy, momentum flux. Therefore, the energy and momentum coefficients (α and β), which also called velocity distribution coefficients are introduced into the 1-D energy and momentum equations. Based on the previous studies reviewed in this research, it can be noted that the velocity distribution coefficients (α and β) should properly be considered in 1D flow formulations for obtaining accurate flow calculations. Furthermore, most previous studies focused on the flows in simple or compound open channels with smooth beds only, expressing the velocity distribution coefficients as a function of some flow parameters. It is hypothesized that the velocity distribution coefficients (α and β) can possibly be expressed as a function of the whole flow regime in terms of the boundary roughness rather than some flow parameters.

The analytical models based on the simplified RANS equations are commonly used for predicting the primary velocity distribution in uniform flow problems. The dip-modified log-wake law (DMLW-law) is the most feasible model for obtaining the vertical distribution of flow velocity in simple open channels. This analytical model requires two parameters to be carefully estimated, namely the wake strength parameter (Π) and the dip-correction parameter (μ). These two parameters represent the effects of the turbulence and the secondary flow on the primary flow. Previous studies have suggested typical values and expressions for estimating these two parameters but are only applicable for smooth channels. Hence, it is hypothesised that the expressions of calculating the parameters (Π, μ) should be modified to be usable for both smooth and rough channels.

On the other hand, the Shiono and Knight model (SKM) is widely used to analytically obtain depth-averaged velocity distributions. The solution of this analytical model relies on the calibration of three parameters that represent the boundary roughness, secondary currents and lateral shear stress. Previous studies on the SKM model have nearly always been made in wide compound channels, where the floodplain width is larger than the main channel width. Therefore, in the present study, it is suggested modifying the conventional methods for calibrating the key coefficients in SKM model to improve the accuracy of the model for narrow floodplain channels.

1.4 Research aim and objectives

In this study, turbulent flow over a smooth and rough open-channel flows are examined to establish two aims. The first aim is to investigate the primary flow velocity in rectangular and compound open channels under different flow regimes in terms of roughness conditions. The second aim is to use detailed Computational Fluid Dynamics (CFD) results as part of an investigation in the significance of assumptions about secondary flows and turbulent eddy viscosity in calculations of velocity distributions.

The overall objectives of this research are:

1. To carry out the velocity measurements in the rectangular and compound channels to study the relationship between the velocity distribution coefficients (α and β) and flow regime from the point of roughness conditions.
2. To construct 3D models by means of the CFD modelling for studying the effects of the secondary flow and turbulence on the primary flow in narrow rectangular and compound channels.
3. To assess and improve the capability of the analytical model that derived from the simplified RANS equation to predict the velocity distributions in narrow rectangular and compound channels.
4. To suggest new methods for evaluating the non-uniformity of velocity distributions for different flow regimes with respect to roughness conditions.
5. To give references for treating and calibrating the secondary flows and eddy viscosity in the SKM model for compound channels with a narrow floodplain.
6. To make further assessment of applying RSM models to turbulent flow cases in which the anisotropic Reynolds stress has a large effect on the fluid flow structures.

This thesis consists of eight chapters. Chapter 1 gives the motivation, background and objectives of this research. Chapter 2 provides a broad review of the literature on open channel hydraulics and velocity distribution prediction to identify the research gap in this study. The experimental investigation is described in detail in chapter 3. Chapter 4 illustrates the numerical methodologies of CFD and all numerical requirements (e.g., domain geometry, mesh size and boundary conditions) to define the simulations of the rectangular and compound channel flows. Chapter 5 concentrates on the prediction of the velocity distribution for the rectangular and compound channel by the analytical models. Chapters 6 and 7 provide an analysis of the experimental and numerical results for the flow cases considered in this research and present proposed equations that addresses the effects of the roughness, secondary flow and turbulence on the velocity distributions. Chapter 8 summarises the important findings from the research and makes recommendations for future research.

Chapter 2

Literature Review

2.1 Introduction

Corresponding to the main objectives of the present study listed in the previous chapter, the literature review is mainly focused on the primary velocity distribution, secondary currents, flow resistance and momentum transfer mechanisms for two patterns of open channel flow. The first type of flows is the inbank flow in simple open channels, and the second is the overbank flow which occurs in compound open channels. the detailed and intensive literature review carried out here covers various aspects concerning the flow structure for inbank and overbank flows in engineered and natural open channels. Initially, the most important issues regarding the primary flow and main factors that could affect the velocity distributions in a simple open channel is presented. Thereafter, flow resistance and momentum transfer mechanisms with their impacts on the velocity distribution for compound channel flows are reviewed. Finally, a review is provided for numerical and analytical modelling approaches that can be employed to simulate open channel flows.

2.2 Inbank flow in straight simple open channels

2.2.1 Primary flow and stramwise velocity distribution

In one-dimensional analysis of fluid flow, understanding the mean primary velocity distribution in the plane perpendicular of the solid boundary is of great interest to both researchers and engineers. It is known that most of flows in practical open channel problems are turbulent boundary-layer flows. Therefore, it is natural to start with review of the boundary layers before exploring the most common expressions or laws that are developed to describe the distributions of primary velocity over a cross section.

In general, two different but overlapping regions of the flow can be recognized, namely inner and outer regions, as shown in Figure 2.1, (Rouse, 1959; Hinze, 1975; Schlichting, 1979). The inner region occupies only a small percentage of the flow depth, no more than 10–20%, (Grass, 1971). In terms of the relative importance of viscous shear stress and turbulent shear stress, there is a subtle difference between the smooth and rough flows at the inner region. In rough flow, the entire depth of the flow is dominated by turbulence, and there may be no viscosity-dominated layer, but there are still inner and outer regions. In smooth flow, three integrating but well-defined layers (the viscous sublayer, the buffer layer, and the fully turbulent layer) can be recognised as shown in Figure 2.2.

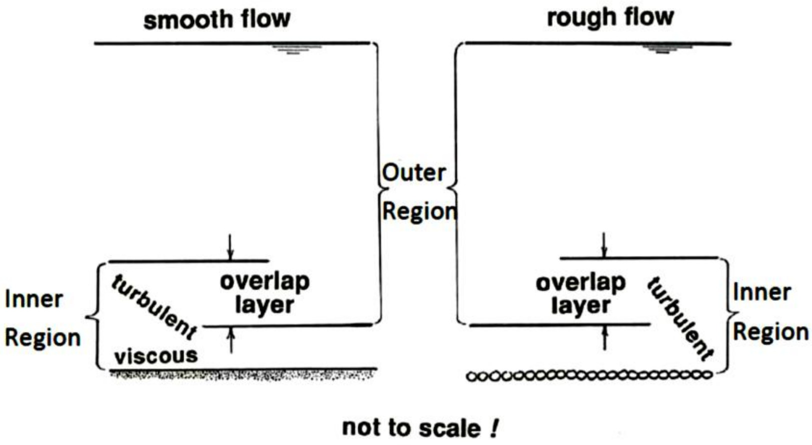

Figure 2.1 Inner and Outer regions in turbulent open-channel flow

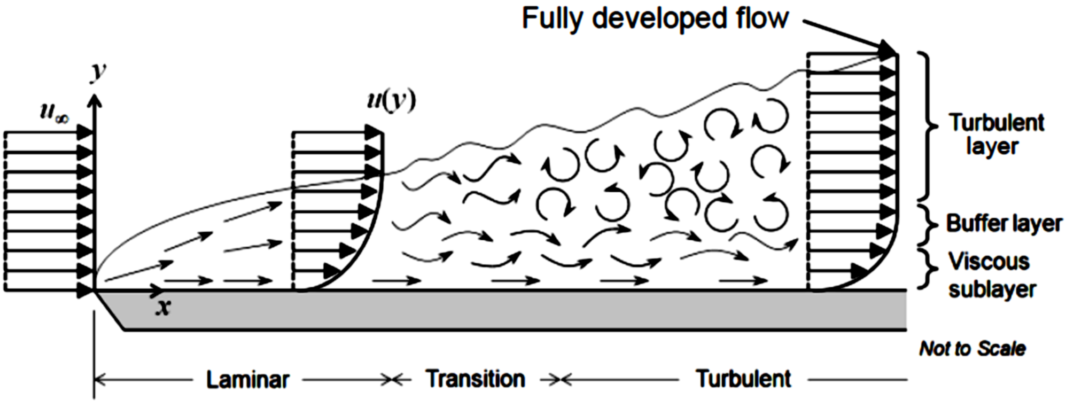

Figure 2.2 Division of turbulent open-channel flow into layers based on turbulence structure.

Various semi-empirical models have been developed to obtain the velocity profiles of fully developed turbulent flow in both inner and outer regions. Some of the widely used expressions for this purpose are given in the following subsections.

2.2.1.1 Inner region velocity profile

In the viscous sublayer of the boundary layer for flow over a smooth surface, the mean velocity is generally controlled by the wall shear stress (τ_w), wall roughness (K), distance from the wall (*z*), density (ρ) and the viscosity of the fluid (υ), (Cebeci & Smith, 1974). Experiments by Klebanoff (1955) showed that the total shear stress at some small distance from the wall is constant and equals the wall shear stress (τ_w). Therefore, the integration of Newton law of viscosity gives the velocity distribution in the viscous sublayer as:

$$\frac{u}{u_*} = \frac{u_*\, z}{\upsilon} \tag{2.1}$$

or

$$u^+ = z^+ \quad when\ (z^+ < 5) \tag{2.2}$$

where u_*= ($\sqrt{\tau_o/\rho}$) = the shear velocity; ρ = the density; υ = the kinematic viscosity of the fluid; *z* = the distance from the solid boundary. Thus, the velocity distribution in the viscous sublayer of the inner region can be considered linear.

In the fully turbulent layer of the inner region, the logarithmic velocity distribution of von Kanman and prandtl, known as law of the wall or the inner law, is the universally accepted formula,

$$\frac{u}{u_*} = A \ln(\frac{u_*\, z}{\upsilon}) + B \tag{2.3}$$

or

$$u^+ = \frac{1}{k}\ ln(z^+) + B \quad when\ (0.2\delta > z^+ > 30) \tag{2.4}$$

where δ is the thickness of the boundary layer, *A & B* are constants and *k* =von Karman's constant. Although $k \approx 0.4$ and *B* = 5.5 were given for pipe flows by Nikuradse, (Schlichting, 1979), the values of *k* = 0.412 and *B* = 5.29 were obtained by Nezu & Rodi, (1986) for smooth open channel flows.

For flow over rough surfaces, the velocity distribution is affected by the grading, shape, and spacing of the surface's roughness elements. The most common practice to represent the velocity distribution in rough flows is to use Nikuradse expression for fully rough turbulent flow in pipes, (Schilchting, 1979):

$$u^+ = 2.5\ ln(\frac{z}{K_s}) + 8.5 \tag{2.5}$$

in which *Ks* is Nikuradse's original uniform sand grain roughness, which represents the equivalent sand roughness for any type of rough surface, and *z* is the distance from the bottom of the roughness elements. Nezu & Nakagawa (1993a) suggested a general form of the log-law to describe the velocity distribution within the fully turbulent layer (log-law layer) on both smooth and rough surfaces, which can be written as:

$$u^+ = \frac{1}{k} l n\, z^+ + B - \Delta u^+ \tag{2.6}$$

where $k \approx 0.4$ is the von-Karman constant and the additive constant B = 5.0 for a smooth surface and Δu^+ is the roughness shift for flow over a rough surface.

2.2.1.2 Outer region velocity profile

In the outer region of turbulent flow, the primary velocity is mainly controlled by the turbulent shearing and the velocity distribution can be described by the velocity-defect law:

$$\frac{u_m - u}{u_*} = -\frac{1}{k} l n \frac{z}{\delta} \tag{2.7}$$

in which u_m = the maximum velocity in the distribution; δ = the thickness of the boundary layer; and k ≈ 0.4. It is supposed that Eq. (2.7) can be applied to both smooth and rough walls, (Hinze J. O., 1975).

Typical dimensionless velocity profile for turbulent boundary-layer flows are shown in Figure 2.3, summarizing the laws that govern the velocity distribution in the inner and outer regions. The regions of inner and outer laws are not full separated regions. There is an overlapping region between the lower limit of the outer law (z_1) and the upper limit of the inner law (z_2) as shown in Figure 2.3. In this overlapping region, the equations of the inner law (2.4) and outer law (2.7) both can be applied.

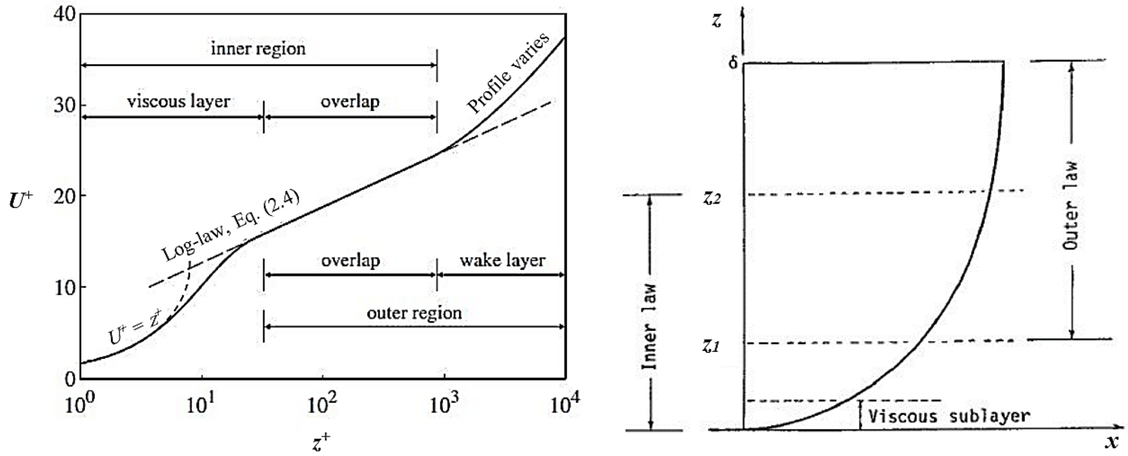

Figure 2.3 Representative velocity distribution in turbulent flows

The law of wall is commonly believed to be insufficient to represent the outer region of the velocity profile. Therefore, Coles (1956) improved the law of wall by proposing the law of wake which can be used to predict the velocity profile in the fully turbulent part of inner region as well as in outer region. The law of wake can be given as follows:

$$\frac{u}{u_*} = \frac{1}{k} l\,n(\frac{u_* z}{\nu}) + B + \frac{\Pi}{k} w(\frac{z}{\delta}) \qquad (2.8)$$

where Π is the wake strength parameter (which ranges from 0 to 0.55), and $w(\frac{z}{\delta})$ is called the function of the wake. For zero pressure gradient $w(\frac{z}{\delta})$ can be given by $[2\sin^2(\pi z/2\delta)]$, so Eq. (2.8) can be rewritten to take the following form:

$$\frac{u}{u_*} = \frac{1}{k} l\,n(\frac{u_* z}{\nu}) + B + \frac{2\Pi}{k} sin^2\left(\frac{\pi z}{2\delta}\right) \qquad (2.9)$$

The log-wake law was found to be more accepted than the conventional log law for describing the velocity profile in outer region, provided that the wake strength parameter to be set to an empirically determined value, (Cardoso et al., 1989; Nezu and Rodi, 1986). However, in case of narrow open channel flows, the log-wake law was found to deviate from the experimental data near the free surface (Imamoto and Ishigaki, 1988; Wang and Cheng, 2005). This is because such a law cannot be able to capture the velocity dip phenomenon, which causes the maximum velocity to occur below the water surface. The velocity dip phenomenon occurs due to strong secondary currents generated in three-dimensional open channel flow (Nezu and Nakagawa 1993). Therefore, several analytical models have recently been proposed, trying to predict the velocity dip phenomenon in open channels by accounting for the effect of the secondary currents (Yang et al., 2004; Yang et al., 2006; Guo and Julien, 2008; Bonakdari et al., 2008; Absi, 2011; Lassabatere et al., 2013; Pu J. H., 2013). These analytical models are discussed in detail in subsequent sections.

2.2.2 Roughness and resistance

Channel roughness provides the primary resistance to the force driving the flow and this affects the fluid flow. The sum of all the forces on individual roughness elements on the boundary (or, in the case of a physically smooth boundary, the sum of the viscous shear stresses at all points of the boundary) constitutes the overall drag on the boundary, or conversely the overall resistance to the flow. When expressed as force per unit area, this boundary resistance is called the boundary shear stress and is denoted by (τ_b). Understanding the nature of this resistive force or boundary shear stress is therefore essential in determining the water level, since a greater resistance will result in a slower flow and higher water level. Due to the turbulent flow being the situation in most flows that are of practical interest, therefore this section provides a review to the principles of flow resistance along with the mutual processes between a turbulent flow and its solid boundary.

In the past years considerable research has been undertaken into the resistance to flow. Early methods for describing flow resistance are based on semi-empirical formulae, e.g. Chezy and Manning equations, which are not based on strict physics and include roughness coefficients that are increased to account for channel losses due to shape effects, (Chow, 1959). In the 19th century, Darcy and Weisbach produced an equation for pipes flowing full which was similar to Chezy's equation taking the form:

$$U = \left(\frac{8g}{f}\right)^{1/2} R^{1/2} S_f^{1/2} \tag{2.10}$$

where f is friction factor, R is the hydraulic radius (= area/wetted perimeter), and S_f is the slope of the energy grade line.

In river engineering, Manning's equation is usually used to represent channel resistance and is given by the relationship:

$$n = \frac{R^{1/2} S_f^{1/2}}{U} \tag{2.11}$$

where n is Manning's roughness parameter, R is hydraulic radius, S_f is energy slope and U is mean flow velocity. Equating the Darcy and Manning equations leads to:

$$n = R^{1/6} \left(\frac{f}{8g}\right)^{1/2} \tag{2.12}$$

The main difficulty in using Manning's equation is estimating accurately a value of the roughness parameter n. Each channel exhibits its own characteristics and the roughness parameter is dependent on the size and shape of channel, the bed materials, the depth of water and other different features within the channel e.g. vegetation and boulders, (Knight et al., 2009). Field observations have shown that, at a given cross-section, the Manning's n varies with depth. Therefore, the Darcy friction factor (f) may be preferred to Manning coefficient (n) in defining the roughness of channel surfaces.

Colebrook & White (1937) clarified how f varies in smooth and rough pipes, conduits running part full and open channels. The variation of f is usually expressed in terms of two parameters, the relative roughness (K_s/d) and the Reynolds Number, Re $(= 4UR/\nu)$. Two forms of the Colebrook-White equation are usually given, one for pipes and another for channels, but these are essentially the same, since the pipe diameter $D = 4R$:

$$\frac{1}{\sqrt{f}} = -2.0 log\left[\frac{K_s}{3.71d} + \frac{2.51}{\left(\frac{ud}{\nu}\right)\sqrt{f}}\right] \quad \text{(pipes \& culverts running full)} \qquad (2.13)$$

$$\frac{1}{\sqrt{f}} = -2.0 log\left[\frac{K_s}{14.8R} + \frac{2.51}{\left(\frac{4UR}{\nu}\right)\sqrt{f}}\right] \quad \text{(open channels and pipes part full)} \qquad (2.14)$$

The Colebrook-White equation (Eq. 2.14) is physically well established, since it tends towards two theoretically limiting cases, described by Schlichting (1979). For very smooth surfaces, as $K_s \rightarrow 0$, Eq. (2.14) becomes the Prandtl (smooth law), in which f depends solely on Reynolds Number (Re) giving:

$$\frac{1}{\sqrt{f}} = -2.0 log\left(Re\sqrt{f}\right) - 0.80 \qquad (2.15)$$

On the other hand, as $Re \rightarrow \infty$, Eq. (2.14) becomes the fully (rough law), in which f is independent of Re and depends solely on the ratio of surface roughness (K_s) to hydraulic radius (R), giving:

$$\frac{1}{\sqrt{f}} = -2.0 log\left[\frac{K_s}{14.8R}\right] \qquad (2.16)$$

Based on Eq. (2.14), the roughness of any surface can be characterized by K_s, the so-called Nikuradse equivalent sand roughness size, which is defined as a measure of the size of roughness on a flat surface that would yield the same resistance as that in a circular pipe roughened with uniform grains of sand. Technically flow regime can be defined by the Roughness Reynolds Number, $Re^*(=U_*Ks/\nu)$, as: Hydraulically smooth ($Re^* < 5$), transitional flow ($5 < Re^* < 70$), or hydraulically rough ($Re^* > 70$). Where U_* is known as the shear velocity $(= \sqrt{\tau_o/\rho})$.

In recent years, much research and data has provided the basis for a comprehensive understanding of river roughness and boundary shear stress. Experimental measurements of boundary shear stress have been taken for inbank flow in uniform and non-uniform open channel by a number of researchers, (e.g., Knight, Demetriou& Hamed, 1984; Wasantha, 1995; Ramesh et al., 2000; Morvan et al., 2008). Valuable data obtained from these experimental measurements have greatly enhanced the understanding of how the boundary shear stress distribution and the wall roughness can affect the vertical and lateral distribution of the primary velocity. This helped in developing more accurate formulae for the calculation of the primary velocity in open channels.

The energy losses in open channels, particularly in natural channels, could not only arise from the friction or the resistance caused by surface roughness, but they may arise from development of vortex structures on a variety of length scales, (Ikeda & McEwan 2009). Once vorticity is created, the streamwise translational kinetic energy is thus transferred in part to rotational kinetic energy, which no longer contributes to the primary flow. The resulting vorticity motion is referred to as the secondary flow which is closely related to the nature of the channel geometry i.e. a simple or compound, straight or meandering. Some general review for the occurrence and development of secondary flows in simple straight channels are disused in the next section.

2.2.3 Secondary flow and vorticity

As indicated previously, secondary flows which is also termed as secondary currents may be created and lead to energy losses in straight channels with inbank flow conditions. Prandtl (1952) divided the secondary currents into two categories. The first kind of secondary currents are generated as a consequence of the mean primary flow skewing due to curvilinearity in the streamwise direction and are called the secondary currents of Prandtl’s first kind. Secondary currents of this kind are also called pressure- or geometry-driven secondary currents. The other kind of secondary currents are generated by the anisotropy of turbulence and are called secondary currents of Prandtl's second kind. These secondary currents are also called turbulence-driven secondary currents. The second category is the main focus here because it is induced by the turbulence and may be existing in straight uniform open-channel flows.

Many researchers have investigated the mechanisms by which the secondary currents are generated in straight open channels. Einstein & Li (1958) first attributed the origin of secondary currents in straight channel flows to the gradient of Reynolds stresses based on the vorticity equation for fully developed turbulent flow. This suggestion was also supported by Gessner (1973). However, Nezu & Nakagawa (1984) verified experimentally and Demuren & Rodi (1984) verified numerically the dominant effects of the cross-stream gradients of turbulent normal stresses on the generation of the secondary currents. Nezu & Nakagawa (1993) further concluded that anisotropy between lateral fluctuation (v') and vertical fluctuation (w') of turbulent flow velocities plays the main role in generating the secondary currents. They also indicated that this anisotropy of turbulence is caused by the boundary conditions at the solid walls and at the free surface.

Secondary currents (Prandtl's second kind) have been observed by experimental measurements using different measurement techniques. Müller & Studerus (1979) first measured the secondary current in an open channel by making use of a low-power Laser Doppler Anemometer (LDA). Nezu & Nakagawa (1984) firstly measured cellular secondary currents in straight open channel flow by making use of the X-type hot-films. They indicated that although the maximum magnitude of the secondary currents is within only 5% of the maximum streamwise velocity (U_{max}), the experimental values of secondary current velocity show comparatively large scatters. Nezu and Rodi (1985) also measured secondary currents in rectangular open channel flows with a two-component LDA. They accurately measured the longitudinal velocity (U) and vertical velocity (W) in an open channel with a two-color LDA system and then calculated the transverse velocity (V) from the equation of continuity on the condition of fully developed flow. Figure 2.4a shows the velocity vectors of the secondary currents measured by Nezu & Rodi (1985) in a narrow rectangular open channel. It can be noted that a pair of counter-rotating vortices are generated in the cross-stream plane. The upper-side vortex is called free-surface vortex and the lower-side vortex is called bottom vortex. These two vortices lead to formation of outer and bottom secondary flows as shown in Figure 2.4b.

Nezu et al. (1989) experimentally showed that there is a significant difference between the turbulence-driven secondary currents in duct flows and open channel flows. Tominaga et al. (1989) presented experiments on rectangular channels with different roughness conditions on the bed and walls and with different aspect ratios. They measured the three components of the velocity vector at several points in the cross section using an X-type hot-film sensor. For the case of smooth bed, their measurements showed a strong secondary circulation in the region near the side walls, with a steady decay toward the centre of the channel when the aspect ratio becomes large (b/h = 8). The corresponding rough bed experiments showed that the surface vortex near the side walls was much stronger and larger than in the smooth bed case.

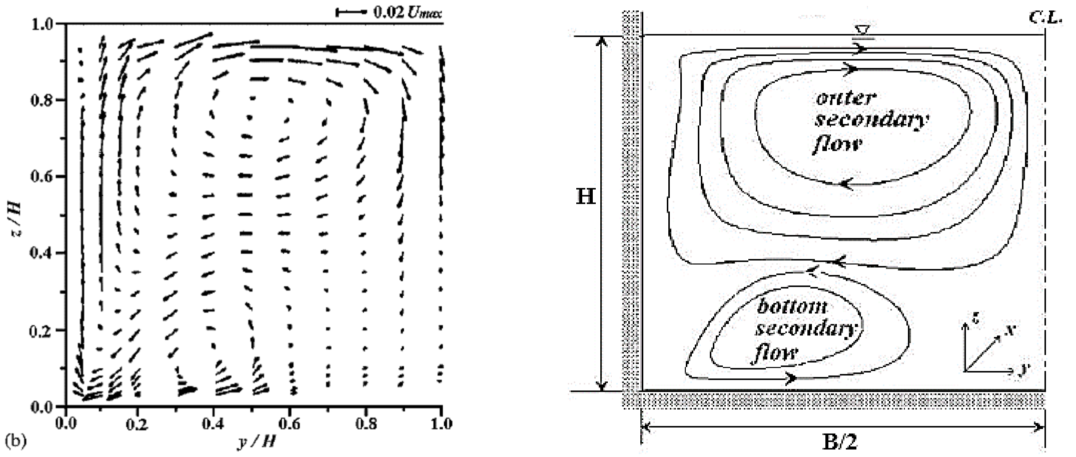

(a) measured by Nezu & Rodi (1985)

(b) Schematic view

Figure 2.4 Secondary flows in a rectangular open-channel.

Nezu & Nakagawa (1993) indicated, based on experimental results, that the free surface vortex contributes in transporting momentum and energy from the side wall toward the channel center near the free surface and then causes a considerable amount of momentum to transport from the free surface to the mid-depth. As a result, these large counter-rotating secondary cells produce the velocity dip where the maximum primary velocity occurs below the free surface.

The secondary currents are observed not only in rectangular channels, but also in the trapezoidal channels. Tominaga et al. (1989) measured three-dimensional flow in open smooth trapezoidal channels with different side slope angles and indicated to existence of secondary cells in all the channels considered. They observed that the maximum value of the secondary currents is of the same magnitude as that in the rectangular channel. Knight et al. (1994) investigated effects of secondary flows in straight trapezoidal channels on the boundary shear distributions, as shown in Figure 2.5. They found that the resulting distribution of boundary shear stress around the wetted perimeter can be influenced by the secondary vortices generated near the bottom and side walls. Knight et al. (2007) found that the number of secondary flow cells in a trapezoidal channel is dependent on the aspect ratio. For aspect ratios less than 2.2, the number of secondary cells are three, whereas for aspect ratios greater than 4, the number of secondary flow cells might be four.

Secondary currents may also occur in wide channels, as observed by Nezu & Rodi (1985) and Wang & Cheng (2006). They indicated that the secondary currents in the wide channel are usually located close to walls but in the central region they may totally disappear due to absence of spanwise variations in the bed shear stress. Rodriguez and Garcia (2008) observed the multicellular secondary motion in a very wide channel with a rough bed and smooth sidewalls. He attributed the generation of such multicellular structures to the considerable variation in roughness between a smooth glass wall and the rough gravel bed. Albayrak & Lemmin (2011) indicated that the effect of the aspect ratio on the dynamics of secondary currents in wide channels is significant, where the number of secondary current cells changes proportionally with the aspect ratio.

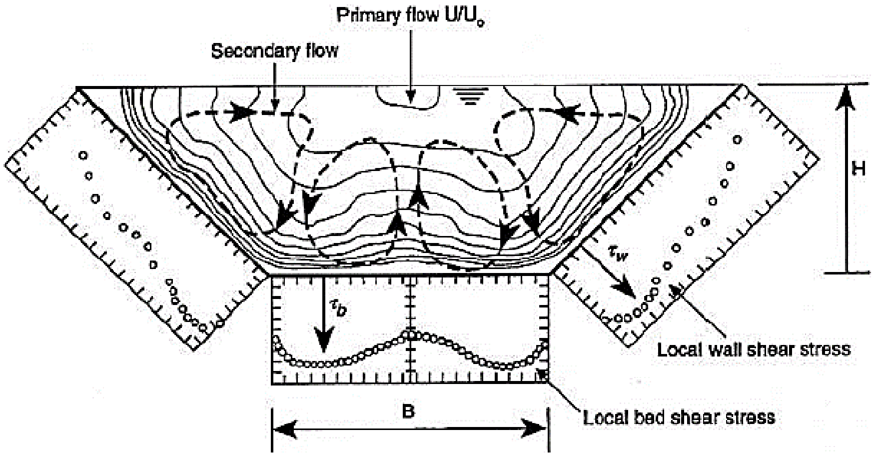

Figure 2.5 Isovels of primary and secondary flows with wall shear distribution (Knight et al. 1994).

Turbulence-driven secondary currents were also proved to exist in natural rivers by field measurements, (Nezu & Nakagawa, 1993; Sukhodolov et al., 1998).

Numerical simulations by many researchers using different three-dimensional models have been performed to predict the secondary currents and evaluate their effects on the primary flow in open channels, e.g.; Naot & Rodi (1982), Demuren & Rodi (1984), Cokljat & Younis (1995), Shi et al. (1999), Wu et al. (2000), Kang & Choi (2006) and Yang et al. (2013). Most of these works are reviewed in section (2.6) where numerical modelling of turbulent open channel flow is discussed.

On the basis of the experiments results presented above, it can be hypothesized that the secondary currents have a significant influence on the primary velocity distribution in straight open channels. Therefore, the existence of secondary currents and their effects have been considered in the investigation of the primary velocity distribution in straight rectangular channels.

2.3 Overbank flow in straight compound open channels

2.3.1 Flow structure and vorticity

Most natural rivers and engineered channels have floodplains that extend laterally away from the main channel, forming what is called a compound channel (Knight & Shiono 1996). When the flow in the main channel exceeds bankfull flow, the water occupies the adjacent floodplains and the overbank flow conditions occur. Overbank flow is somewhat different in a number of aspects from inbank flow. As a river changes from inbank to overbank flow, there is a significant increase in the complexity of the flow behaviour, even for relatively straight reaches. The complex overbank flow structure in a compound channel are schematically illustrated in Figure 2.6 (Shiono & Knight 1991).

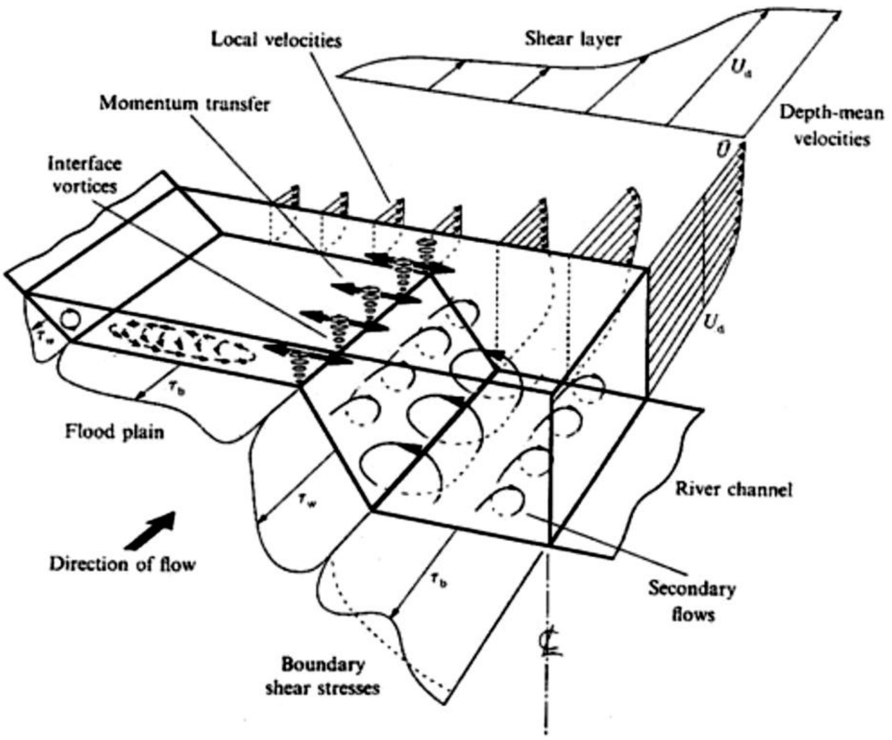

Figure 2.6 Flow structure in straight compound channels (Shiono and Knight, 1991).

When a complex turbulent overbank flow occurs, large vertical vortices develop at the interface between the main channel and the floodplain, as shown in Figure 2.6. These vertical vortices were first observed by Sellin (1964). He used a flow visualisation technique consisting of an aluminium powder scattered on the water surface and a camera moving downstream at a constant speed that is used to take photographs to the powder. Figure 2.7 provides an illustration for this type of large-scale vortices associated with overbank flows in compound channels. The difference in velocity between the main channel and the floodplain flows may produce strong lateral shear layers, which consequentially lead to the generation of the large-scale vortices, which also called planform vortices. These vortices transport the high momentum fluid from the main channel towards the floodplain. As a result, the conveyance in the main channel decreases while the conveyance in the adjacent floodplain increases (Myers, 1978; Wormleaton, Allen, & Hadjipanos, 1982; Knight & Demetriou, 1983; Shiono & Knight, 1991).

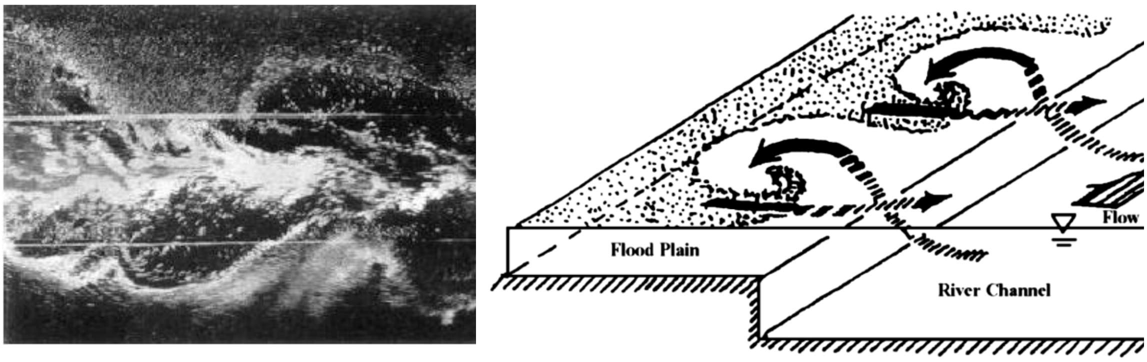

(a) (b)

Figure 2.7 Large vortices observed at the interfaces between the main channel and the floodplains: (a) Photo from Sellin experiments (1964), (b) Schematic illustration.

Ikeda et al. (2000) suggested that the planform vortices are induced by the shear instability. Based on his laboratory experiments, planform vortices were clearly observed in a laboratory flume which has a small relative depth ratio (*Dr*) of 0.18, as shown in Figure 2.8(a). For a relatively large depth ratio of 0.344, the periodic planform vortices disappear, and active intermittent boils were observed, as seen in Figure 2.8(b).

Particle Image Velocimetry (PIV) and Particle Tracking velocimetry (PTV) techniques have been employed to obtain the instantaneous flow field of the planform vortices, (Nezu, Nakagawa, & Saeki, 1994; Ikeda, Kuga, & Toda, 1995). Although the results from these experiments confirmed the existence of the large-scale motion, they were not sufficiently detailed to determine the mathematical explanation of this large-scale vortex. High resolution numerical simulations, in which the large-scale motion is resolved, have been performed by Ikeda et al. (2002), attempting to model the horizontal large-eddy in river flows.

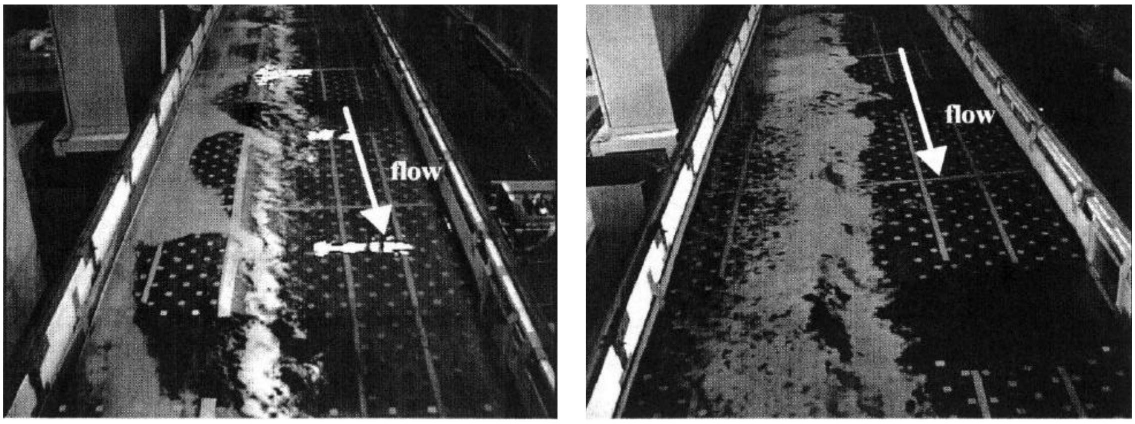

(a) *Dr* = 0.180 (b) *Dr* = 0.344

Figure 2.8 Horizontal vortices for different relative depths *Dr* (after Ikeda et al., 2000).

In addition to the planform vortices rotating about vertical axes, helical streamwise vortices rotating about horizontal axes can often be observed in compound channels with overbank flows (Figure 2.6). This vortices form is closely related with secondary flow of Prandtl's second kind. The existence of such vortices also play an important role in the momentum exchange, especially near the junction between the main channel (MC) and floodplain (FP), (Shiono & Knight 1988; Tominaga & Nezu 1991). The interaction of planform and streamwise vortices, and their effects on the primary flow are reviewed in the next section.

2.3.2 Secondary currents and their effects on the primary flow

Secondary currents in compound channels are generated by anisotropic turbulence and their patterns are influenced by many factors, including the channel geometry (such as aspect ratio and relative depth) and by the turbulence conditions (Shiono and Knight, 1991).

The nature of secondary currents in straight compound channels was investigated by Shiono and Knight (1989), Tominaga & Nezu (1991) and Nezu (1996) through a series of laboratory tests. Shiono and Knight (1989) investigated the influence of the shape of the cross-section on the secondary current circulations in symmetrical wide compound channels. According to their results, which are shown in Figure 2.9, they found that the shape of the cross section influences secondary current cells in the main channel, but has no significant effect on the secondary current cell that extends across the floodplain. For both rectangular and trapezoidal compound channels, two secondary current cells can be observed in the main channel. In the case of the rectangular main channel (Figure 2.9a), a large counter-clockwise cell exists in the upper region and a smaller clockwise cell exists in the left comer of the main channel. However, in the trapezoidal main channel, a smaller counter-clockwise secondary cell exists near the MC-FP junction and a larger clockwise cell covers most of the main channel as shown in Figure 2.9b.

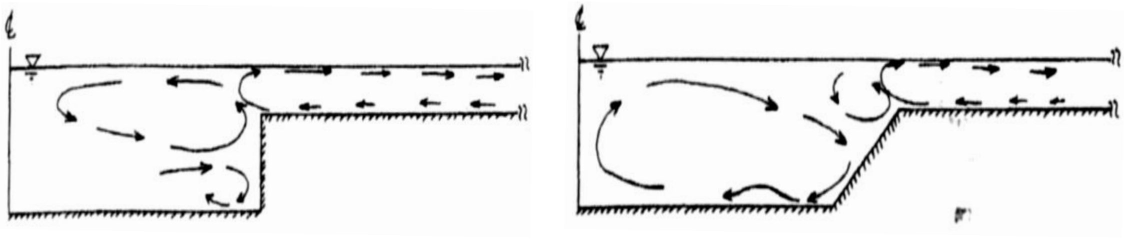

(a) rectangular main channel (b) trapezoidal main channel

Figure 2.9 Secondary currents in compound channels with two different cross-sections (Shiono & Knight, 1989).

Tominaga & Nezu (1991) investigated three-dimensional (3-D) turbulent flow in rectangular compound channels with various relative depths and roughnesses. In their experiment, they used a fiber-optic laser Doppler anemometer (FLDA) which have enabled them to accurately describe the secondary current velocities and their influences on the primary mean velocity field. Figure 2.10 shows the vector description of secondary flow velocities and corresponding isovels of primary flow velocity that were obtained from Tominaga & Nezu (1991) measurements. In all cases, a pair of secondary currents cells were recognized on both sides of the MC-FP junction. The vortex on the side of the floodplain was called the floodplain vortex, whereas the vortex on the side of the main channel was called the main-channel vortex. A free-surface vortex was also observed in the sidewall region of the main channel. It was found that under high relative depth, *Dr* = 0.75, the free-surface vortex prevailed over the main channel vortex and the floodplain vortex expanded in the vertical direction and reached the free surface. It was also observed that the roughness of the floodplain did not change the essential structure of secondary currents near the MC-FP junction, although it changed the size of longitudinal vortices.

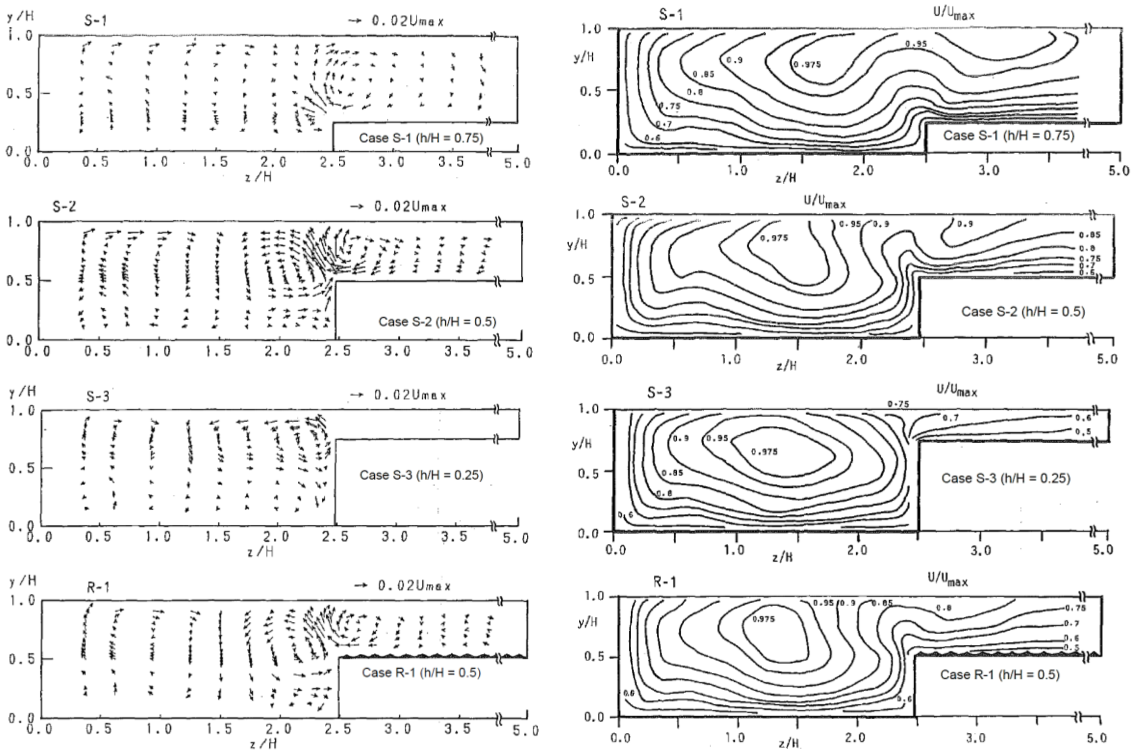

(a) Secondary current vectors (*V*, *W*) (b) Isovels of primary mean velocity (*U*)

Figure 2.10 Flow patterns for straight compound channels with different relative depths and roughnesses (Tominaga & Nezu, 1991).

From the results of the primary mean velocity (Figure 2.10), Tominaga & Nezu (1991) noted two remarkable features. One was the bulge from the junction towards the free surface, and the other was the velocity dip phenomenon, in which the maximum velocity appears below the free surface. Therefore, they suggested that the structure of the primary mean velocity is affected by the momentum transport due to the secondary currents.

Nezu (1996) extended the study of the secondary flows in compound channels to cover various geometries in terms of the main channel and floodplain widths. Their results, which are shown in Figure 2.11, coincided well with those of Tominaga and Nezu (1991). The inclined up-flow from the junction toward the free surface was also observed, i.e. the same feature as shown in Figure 2.10. It was found that as the floodplain width gets smaller, the up-flow tends to incline towards the main channel, which may be due to an effect from the side wall of the main channel.

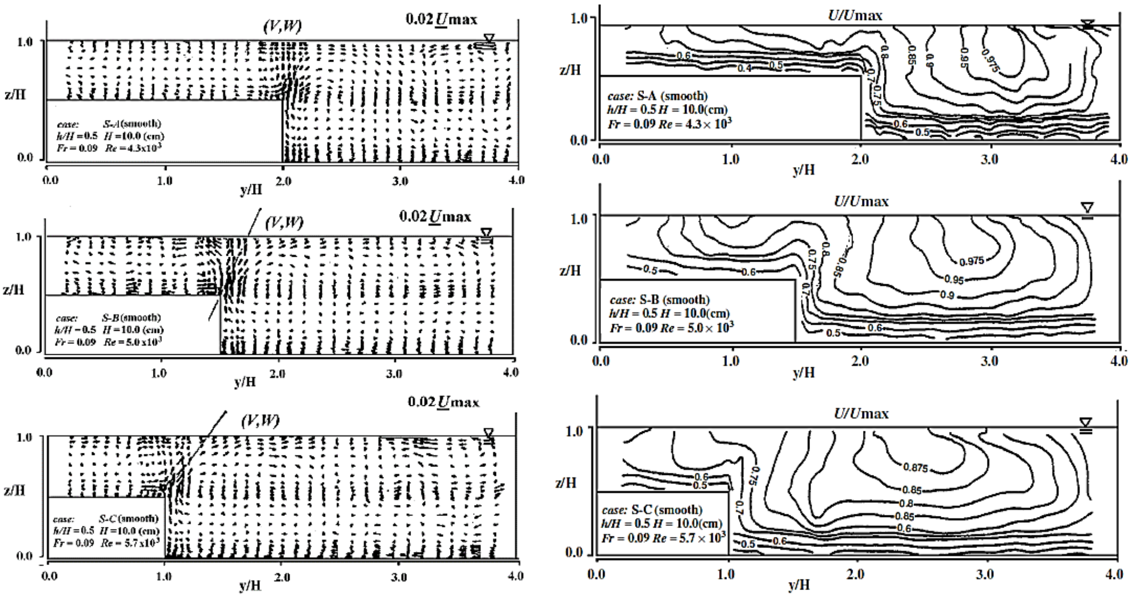

(a) Secondary flow velocities (b) Isovel lines of primary velocity

Figure 2.11 Secondary and primary flow velocities in compound channels with different floodplain width [LDA data measured by Nezu (1996)].

Secondary currents in compound channels were also accurately simulated by the use of different turbulence models, e.g. Naot et al. (1993), Thomas and Williams (1995), Sofialidis and Prinos (1998), Kang and Choi (2006), Cater and Williams (2008), Kara et al. (2012), Xie et al. (2013), Filonovich et al (2015) and Yang et al. (2017). Further review of the numerical modelling for turbulent flow in compound channels are given in section (2.4).

According to Tominaga and Nezu (1991), the maximum magnitude of is about 4% of the maximum longitudinal velocity in a compound channel. The magnitudes of secondary currents at the MC-FP junction in compound channels are usually about 5% of the bulk longitudinal velocity (Naot et al., 1993; Nezu, 1996). Although the magnitude is small, the secondary currents can greatly influence the flow behaviours, such as velocity and boundary shear stress, in the open compound channels (Naot et al., 1993). In this study, an investigation into the effects of the secondary currents on the velocity distributions and depth-averaged calculations are conducted by means of 3D CFD models.

2.3.3 Flow resistance due to friction

The flow resistance to flow in compound channel has been studied by many researchers. Lotter (1933), Einstein & Barbarossa (1952) and Krishnamurthy & Christensen (1972) proposed different formulae for predicting the composite roughness in compound channels.

One traditional approach used to estimate the conveyance capacities of compound channels is to subdivide the channel into a number of discrete sub areas. Then, the conveyance capacity for each sub area is calculated by using 1-D resistance equations (such as Manning equation) and the appropriate sub areas values for A, P, R, f and n. The individual conveyances are then summed to give the total discharge for the whole channel, (Chaudhry, 2008). The global resistance coefficients are known to vary with depth in most channel flows as indicated by Knight et al., (1989) and Myers et al. (1999). Therefore, one of the difficulties in applying 1-D resistance equations such as Manning equations is variation of Manning resistance coefficient (n) for overbank flow. The composite or global value of Manning coefficient ($n_{comp.}$) for the whole compound channel may decrease sharply just above bankfull level as shown in Figure 2.12, (Knight et al., 1989). This effect is entirely fictitious, due to abrupt changes in the hydraulic radius (R), and actually there is no any real change in channel roughness. This example shows the difficulties associated with predicting resistance coefficients for open channels, when flowing as overbank flow.

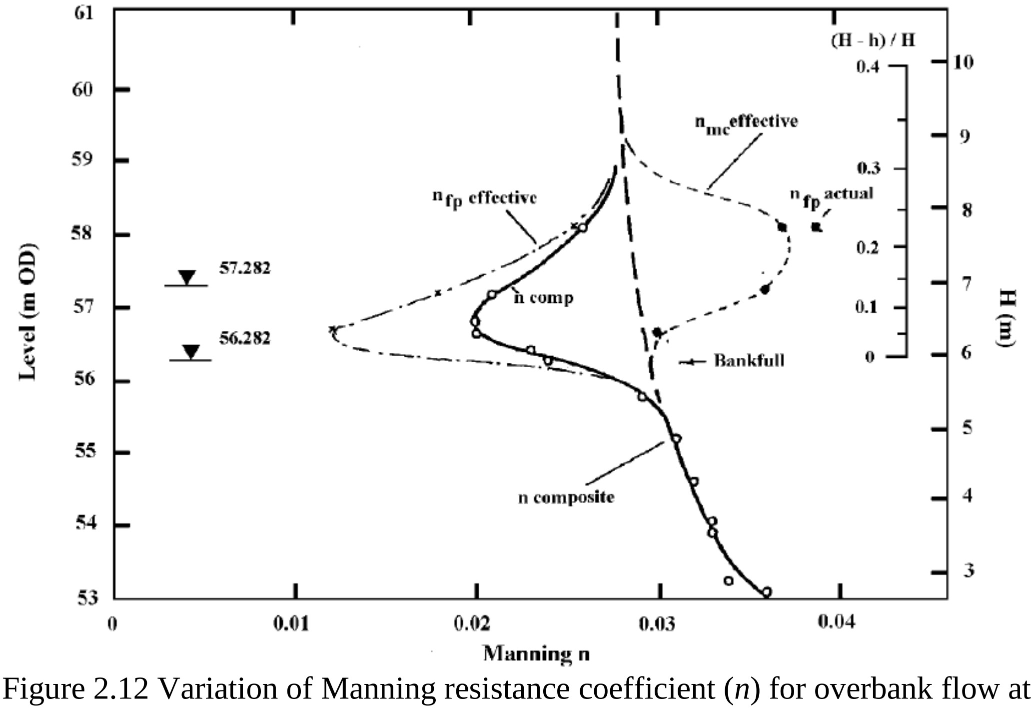

Figure 2.12 Variation of Manning resistance coefficient (n) for overbank flow at Montford, River Severn (Knight et al., 1989).

For practical purposes, flow resistance may be expressed as mean boundary shear stress (τ_o) which is traditionally linked to the section-mean velocity (U) and the global or overall friction factor (f) by an empirical, dimensionally valid relationship. However, in compound channel flows, the local boundary shear stress (τ_b) and its relationship to the cross section-average (τ_o) is difficult to determine theoretically, as indicated by (Knight, Yuen, & Al-Hamid, 1994). Therefore, care needs to be taken to distinguish between global and local friction factors, (Ikeda & McEwan2009). The two friction factor definitions, which commonly used in 1-D, 2-D and 3-D simulation models for compound open channel hydraulics, are often given as follows,

$$\tau_o = \left(\frac{f}{8}\right)\rho U^2 \quad \text{(globle for 1D model)} \tag{2.17}$$

$$\tau_b = \left(\frac{f_b}{8}\right)\rho U_d^2 \quad \text{(local/depth averaged for 2D model)} \tag{2.18}$$

$$\tau_b = \left(\frac{f_t}{8}\right)\rho u^2 \quad \text{(local/turbulence for 3D model)} \tag{2.19}$$

It should be noted that the depth-averaged friction factor defined in Eq. (2.18) implicitly include the effects of secondary flow and lateral shear because of using local values for velocities rather than section average values, (Knight et al., 2010). The local friction factor is a parameter that essentially relates the local boundary shear stress to the depth-averaged velocity. Therefore, it should consider the full three-dimensional flow effects throughout the depth of flow. This concept is attained using the Colebrook-White equation, given by Eq. (2.14).

2.3.4 Momentum transfer mechanisms

As presented earlier in this chapter, the velocity gradient between the fast-moving flow in the main channel and the slow-moving flow on the floodplains will cause strong mass and momentum transfers between them, leading to a very complex flow structure in the compound channel. Consequently, a significant lateral shear layer (mixing layer) will be created and various length scales vortices will be generated. The exchange of momentum taking place between the main channel and the floodplain acts as an apparent lateral shear stress that causes additional resistance to the flow, (Myers, 1978).

A number of studies have been devoted to prediction of the momentum exchange and determination of the apparent lateral shear stress generating at the mixing layer between the main channel and the floodplain. Knight & Demetriou (1983) have experimentally demonstrated that the apparent shear force acting on the vertical interface between the main channel and the floodplains increased rapidly for low relative depths and high floodplain widths. Baird & Ervine (1984) suggested a relationship relating the apparent shear stress with the mean velocity difference (ΔU) between the subsections for asymmetrical compound channels. Alavian and Chu (1985) proposed a mixing length approach to model the lateral turbulent shear stress, using the mixing layer width d as the length scale and the velocity difference between the channel and the floodplain (ΔU) as the velocity scale. Shiono & Knight (1991) found that there are three main mechanisms of momentum transfers in compound channels, including the bed-generated turbulence, lateral shear-generated turbulence and secondary currents. The bed-generated turbulence is a small-scale turbulence induced by the bottom resistance, while lateral shear-generated turbulence appears in the form of large-scale horizontal vortices. Lambert and Sellin (1996) employed a mixing length approach, using the water depth as a length scale. They suggested that the bed-generated turbulence plays a major role in momentum transfers. Ervine et al. (2000) modelled the momentum transfer by accounting for the secondary currents in combination with a formulation for the combined contributions of bed-generated and lateral shear-generated turbulence. Prooijen et al. (2005) investigated the momentum transfer in straight uniform compound channel, considering the different mechanisms that could play a role. They suggested that the momentum transfer is dominated by the horizontal planform vortices and the bottom turbulence, while secondary currents have a minor importance. Therefore, they proposed a new eddy viscosity model, in which the large-scale planform vortices and the bed-generated turbulence are incorporated.

In this research, the different mechanisms responsible for the momentum exchange in a straight compound channel are considered in investigating the hydraulic factors that influence on the primary velocity distributions. Subsequently, the eddy viscosity is used as a parameter to characterise the lateral momentum exchange due to the turbulence.

2.4 Numerical modelling of open channel flows

In this section, the numerical approaches used for modelling the turbulent flows in open channels are described briefly, focusing on numerical techniques involved in the computational fluid dynamics (CFD) applications. Practical and theoretical issues that need to be considered when applying the numerical models are also reviewed through the previous studies.

2.4.1 Three-dimensional numerical approach

Three-dimensional (3D) turbulence flow models (the basis of Computational Fluid Dynamics techniques, CFD) has increasingly used as an alternative and/or supplementary tool to the more traditional 1D and 2D approaches for modelling hydrodynamic and morphology problems in natural open channel flows, (Bates et al., 2005). 3D numerical CFD simulations may provide clearer explanations of the structure of the flow and the interactions of the key hydraulic components than do the traditional field and/or laboratory measurements.

The governing equations for 3D turbulent flows are basically in the form of a coupled set of partial differential equations, known as the Navier–Stokes equations (N-S). The Navier Stoke equations are based on the conservation laws of mass (*i.e.* continuity equation) and momentum (Newton's second law). The mass conservation for an incompressible fluid can be written in a Cartesian coordinate system as follows as follows (Hinze, 1975):

$$\frac{\partial u_i}{\partial x_i} = 0 \qquad (2.20)$$

The conservation of momentum in the absence of external sources of momentum can be given as follows:

$$\frac{\partial u_i}{\partial t} + \frac{\partial}{\partial x_j}(u_i u_j) = -\frac{1}{\rho}\frac{\partial p}{\partial x_i} + \frac{1}{\rho}\frac{\partial \tau_{ij}}{\partial x_i} \qquad (2.21)$$

where, i,j (=1,2,3) are index notations for Cartesian vector representations, u is the velocity, p is the pressure and τ_{ij} is the stress tensor.

The laminar-turbulent field can be physically described by Eq. (2.21) which may be solved directly using a method called direct numerical simulation (DNS). However, the DNS method is prohibitively difficult, because of the significantly different length and time scales in a turbulent field that need to be resolved. Consequently, the DNS solution requires a fine mesh resolution to resolve the smallest turbulence vortices, and usually this is not practical within the available computational resources, (Spalart, 2000 and Filonovich, 2015).

Large Eddy Simulation (LES) approach has recently been suggested to be a more realistic modelling tool instead of using the DNS method. In LES, a spatially filter function is applied to the 3D unsteady Navier–Stokes equations to resolve directly all scales of motion that are larger than the width of the filter. Smaller-scale motions, which is referred to as sub-grid scales, are typically modelled via a subgrid turbulence model. LES has been applied to solve hydraulic engineering problems by several researchers, (e.g. Thomas and Williams, 1995; Bradbrook et al., 2000; Cater & Williams, 2008; Kara et al., 2012 and Xie et al., 2013). Despite encouraging results obtained by LES simulations for moderate Reynolds number flows, LES would remain extremely costly in term of computer resources for domain with large dimension or at large Reynolds numbers (Xie et al., 2013; Chaouat, 2017).

Hence, the Reynolds-averaged Navier–Stokes (RANS) models that rely on Reynolds decomposition principle are used as a perfectly serviceable alternative for practical engineering computations. According to the Reynolds decomposition, instantaneous flow quantities, such as u_i, are decomposed in terms of a statistically stationary mean value (U_i) and a zero-mean, random turbulent fluctuation (u_i'). In RANS models, the governing equations for the mean flow quantities are derived by introducing the Reynolds decomposition into the instantaneous Navier–Stokes equations, Eqs. (2.20) and (2.21), and applying time averaging. For an incompressible and turbulent fluid flow, the Reynolds averaged Navier-Stokes (RANS) equations can be written in a Cartesian coordinate system as follows:

$$\frac{\partial U_i}{\partial x_i} = 0 \tag{2.22}$$

$$\frac{\partial U_i}{\partial t} + U_j \frac{\partial U_i}{\partial x_j} = -\frac{1}{\rho}\frac{\partial P}{\partial x_i} + \frac{\partial}{\partial x_j}\left[\nu\left(\frac{\partial U_i}{\partial x_j} + \frac{\partial U_j}{\partial x_i}\right)\right] - \frac{\partial}{\partial x_j}(\overline{u_i' u_j'}) \tag{2.23}$$

Due to the averaging operation, the resulting system of equations, i.e. RANS equations, contains six more unknowns than equations resulting in the system being not closed. These unknowns, which called Reynolds stresses ($\overline{u_i' u_j'}$), involve time-averaged products of fluctuating velocity components. To solve the closure problem of turbulence, different turbulence models are developed by which the Reynolds stresses are related to the mean property of the fluid flow.

Conceptually, the turbulence models are classified into two groups, specifically, Eddy-Viscosity Models (EVM) and Reynolds Stress Models (RSM) (Bates et al., 2005). The EVM models employ an additional transport equation for the turbulence kinetic energy (k) in conjunction with a transport equation for the rate of viscous dissipation (ε) or the specific dissipation rate (ω). On the other hand, RSM models provide one equation for each Reynolds stress as well as one equation for the dissipation of turbulent energy (ε or ω). The most used turbulent models for engineering calculations are presented in Table 2.1. More details on the theoretical formulations of these turbulence models are given in chapter 4. In the next subsection, CFD applications based on common RANS turbulence models are reviewed with emphasis on issues and challenges that are relevant to open channel flows.

Table 2.1 List of Popular Turbulence Models for engineering and environmental flows.

Model Classification	**Model Classification**
Eddy-Viscosity Models (EVM)	Standard k-ε (Launder and Spalding, 1974)
	RNG k-ε (Yakhot and Orszag, 1986)
	Realizable k-ε (Shih et al., 1995)
	LRN k-ω (Wilcox, 1994)
	SST k-ω (Menter, 1994)
Reynolds Stress Models (RSM)	LRR-IP (Launder, Reece & Rodi, 1975)
	LRR-IQ (Launder, Reece & Rodi, 1975)
	SSG (Speziale, Sarkar & Gatski, 1991)
	3D EARSM (Gatski & Speziale, 1993)
	BSL RSM (Menter, 2009)

2.4.2 CFD applications using RANS methodology

Growing in computing power encourages on using CFD modelling to perform extensive studies on the turbulent flows in open channels. In particular, CFD modelling based on various RANS models have frequently been used to simulate the turbulent structure in simple and compound open channels.

As in other engineering problems, the k-ε model has been the preferred choice and used by many researches for a wide variety of 3D open channel flows (e.g. Peric et al., 1988; Cheong & Xue, 1997; Fischer et al., 2000; Wu et al., 2003 and Rameshwaran & Naden, 2003). Although, the k-ε model was found to be applicable in certain situations with reasonable success, the model does not produce satisfactory results when anisotropy of turbulence and special effects like streamline curvature play an important role (Pezzinga, 1994; Cokljat & Younis, 1995a). This means, the k-ε model cannot reproduce directional effects of turbulent flows such as secondary motions of fluids.

For improving turbulence models based on the eddy viscosity concept, the linear strain rate is modified by including a nonlinear effect to account for the streamline curvature (Bernard & Wallace, 2002). The nonlinear RNG k-ε model is an example of such turbulence closures, which are often defined as anisotropic turbulence models. Pezzinga (1994) and Sofialidis & Prinos (1998) used the nonlinear k-ε model to predict open-channel flows with secondary currents. Although their modelling successfully predicted secondary currents in a compound channel, the mean flow and turbulence structure were not accurately simulated. For example, they found that the velocity-dip phenomenon can hardly be predicted by the nonlinear k-ε model used.

Naot and Rodi (1982) proposed a modelling approach, which is known as algebraic stress model (ASM), to numerically simulate open channel flows with secondary currents. The principal advantage of ASM approach is that the turbulent stresses are obtained from algebraic rather than differential equations, reducing the computational cost. Following Naot and Rodi (1982), many researchers simulated open channel flows using the ASM (Demuren & Rodi, 1984; Krishnappan & Lau, 1986 and Naot et al., 1993). However, because the ASM solves empirical relationships instead of solving the exact equations for Reynolds stresses, the simulated mean flow and turbulence structures are not sufficiently accurate (Naot et al., 1996).

Reynolds Stress Model (RSM) has been developed to overcome the weakness of the previous models. The RSM is a comprehensive model which is based on solving transport equations for the individual turbulent stress instead of using the eddy viscosity concept.

Reece (1977) was the first investigator who developed and used the RSM model to simulate the open channel flows. Later, Cokljat & Younis (1995a, 1995b) and Basara & Cokljat (1995) proposed a RSM model for numerical simulations of free surface flows in a rectangular channel and in a compound channel. They found that the RSM model used can give a good agreement between predicted and measured data. Kang and Choi (2006a) used RSM to simulate a straight open channel flow and Jing et al. (2009) to simulate meandering open channel flows. They indicated that RSM can successfully predict the velocity fields, secondary currents, wall shear stresses, and Reynolds stresses for both straight and meandering open channel flows. Filonovich et al. (2012) tested the performance of different

RSM models on straight compound channels and found that all RSM models can reproduce the complex flow pattern of primary velocity field, secondary currents and anisotropy of turbulence. However, they indicated that the performance of BSL RSM is better compared with the other RSM models.

In the light of the general review above, it can be concluded that the RSM models can predict the main turbulent features and the secondary motions in open-channel flows through accounting for the turbulence anisotropy effects. Furthermore, the RSM models are superior to eddy viscosity models because they can mathematically represent the physical processes of the free surface flow (Rodi, 2017). Therefore, the RSM model are used for the numerical simulations conducted in this study to understand the secondary flow and turbulence effects on the primary velocity distributions.

2.4.3 One-dimensional numerical approaches

The open channel flow can often be treated as one-dimensional (1D) rather than as a three-dimensional (3D) flow, which is considered in complex hydraulic problems. The governing equations of 1D numerical approaches are usually derived from three principles of conservation: momentum conservation, mass conservation and energy conservation laws. The derivation can be performed in various ways. The approaches found in the literature, (e.g. Chow, 1959; Chaudhry, 2008; Szymkiewicz, 2010) and others differ with respect to the formulation of the principle of conservation. However, the open channel flow equations are very often derived by balancing the fluxes and forces acting on the considered control volume, with an assumption of uniform velocity flow distribution over a channel cross-section. Next, when the governing equations are derived, some additional factors are introduced to correct the balanced quantity.

One-dimensional unsteady flow in an open channel can be described by the so-called Saint-Venant equations, which are based on momentum and mass conservation laws. These equations can be given as follows:

$$\frac{\partial A}{\partial t}+\frac{\partial Q}{\partial x}=q \tag{2.24}$$

$$\frac{\partial U}{\partial t}+\beta U\frac{\partial U}{\partial x}+g\frac{\partial h}{\partial x}+g(S_f-S_o)=0 \tag{2.25}$$

where t = time; x = longitudinal distance; A = cross-sectional area; Q = flow rate (= $U.A$); U = cross-sectional average flow velocity; h = flow depth; S_f = friction slop; S_o = bottom slope and q = lateral inflow (in most cases q is assumed to be neglected). The velocity correction coefficient (β), which is also called the Boussinesq coefficient or momentum correction coefficient, is usually applied in momentum equation (Eq. 2.25) to correct the error in momentum balance resulted from velocity averaging (Chanson, 2004).

In many practical applications the steady and gradually varied flow in open channels could be considered. Typical problem connected with this kind of flow is the determination of the flow profile behind a dam, which is also called backwater profile calculation. For such flow cases, the 1D energy equation derived from conservation of energy law is commonly used. The 1D energy equation is commonly written in the following form:

$$\left(h_1 + \alpha_1 \frac{U_1^2}{2g}\right) - \left(h_2 + \alpha_2 \frac{U_2^2}{2g}\right) = \Delta x\left(S_o - \overline{S_f}\right) \tag{2.26}$$

where h_1, h_2 = depth of flow at considered cross sections 1 and 2; U_1, U_2 = cross-sectional average velocities and α_1, α_2 = kinetic energy correction coefficients (also called Coriolis coefficients). The velocity correction coefficient (α) is introduced to correct the kinetic energy calculated using the average flow velocity U instead of the actual velocities.

The velocity distribution coefficients α and β can be defined from the comparison between the actual energy or momentum and the energy or momentum calculated with the averaged velocity U. Therefore, the coefficients α and β may be expressed as follows:

$$\alpha = \frac{1}{U^3 A}\int_A u^3 dA \tag{2.27}$$

$$\beta = \frac{1}{U^2 A}\int_A u^2 dA \tag{2.28}$$

The values of α and β coefficients increase with increase in non-uniformity of flow velocity distributions over cross-section (Chen, 1992). Therefore, these coefficients are used as indicators for the flow velocity distribution in the present research.

2.4.4 Velocity distribution coefficients

As mentioned in previous sections, the momentum and kinetic energy correction coefficients (β and α), which are also referred to as velocity distribution coefficients, reflect the extent of the nonuniformity for the velocity distribution over a cross section. In some limited cases these coefficients are assumed to be unity, however, in most situations, their values are often larger than unity. Based on this fact, the evaluation of velocity distribution coefficients and their effects on the 1D flow computations have been focused on in many previous studies.

In the past, there were many attempts by some researchers and engineers to find typical values for the velocity correction coefficients. Chow (1959) stated that for fairly straight prismatic channels, β varies approximately from 1.01 to 1.12, while α varies nearly from 1.16 to 1.47. He also indicated that for channels with complex cross sections, β and α may exceed 1.2 and 1.5, with their values varying quite rapidly from section to section in case of irregular alignment.

Some other researchers made attempts to suggest general formulas to estimate the values of the velocity correction coefficients instead of using typical values suggested in the classic textbook. Henderson (1966) assumed that for a linear velocity distribution α and β might be obtained from the following expressions:

$$\alpha = 1 + \varepsilon^2 \tag{2.29}$$

$$\beta = 1 + \frac{\varepsilon^2}{3} \tag{2.30}$$

and for logarithmic velocity distribution:

$$\alpha = 1 + 3\varepsilon^2 - 2\varepsilon^3 \tag{2.31}$$

$$\beta = 1 + \varepsilon^2 \tag{2.32}$$

in which ε = (U_{max}/U-1), U_{max} = maximum velocity and U = section mean velocity.

Strauss (1967) based on experimental studies, has given empirical formulae for computing α and β for general channel section based on the velocity distribution given by the following power law:

$$u = a.y^{1/m} \tag{2.33}$$

where u is the velocity at a point located at a height y from the bed, a is a constant and m is an exponent such that ($1 \le m \le \infty$). The application of Strauss's method is practically limited, because it is not always true that the same velocity distribution prevails along all the verticals of the cross-section. Li & Hager (1991) considered (β and α) as functions of U_{max}/U for the channel is implicitly assumed to be prismatic or two-dimensional and there is no flow separation. Li & Hager (1991) made also an attempt to relate (β and α) to boundary shear and to Manning's n.

In 1990's, some studies were conducted to investigate the significance of the velocity correction factors (β and α) in solving one-dimensional flow equations (Eqs. 2.25 and 2.26). Chen (1992) derived theoretical expressions of the momentum coefficient (β) and energy coefficient (α) for turbulent shear flow in wide open channels from the power law and compared them with their counterparts based on the logarithmic law. According to his results, he has drawn the following two conclusions: (1) a comparison of the corresponding expressions for (β) and (α) derived using both laws showed that their values differ only slightly within a valid range of small m; (2) use of a power-law-based (β) expression in the averaged equation of momentum could remove the inconsistent assumption of ($\beta = 1$) made in the equation and make improvement on the accuracy of the 1D flow computations. Xia & Yen (1994) conducted a sensitivity numerical analysis to probe the impact of the momentum correction coefficient (β) on the solution of the 1D Saint-Venant equations, Eq. 2.25. They found that there is always a difference in solutions between the nearly exact flow equations (i.e. for which $\beta > 1$) and the Saint-Venant equations for which the coefficient value is equal to unity. Also, their study indicated that the coefficient β has a greater impact on the solution for velocity than for depth. Fenton (2005) showed that neglecting the appropriate consideration of energy and momentum even in simple flow calculations might cause up to a 5-10% error. Thus, he indicated that α and β coefficients should be included in most applications in hydraulic practice. Costabile & Macchione (2010) highlighted the importance of the accurate evaluation of the momentum coefficient (Boussinesq coefficient) for the computation of flow variables (flow depth and flow rate) by using the 1D flow equations.

In addition, a series of laboratory experiments was performed by many researchers to investigate the effects of the flow parameters on the velocity distribution coefficients (α, β). Al-Khatib & Gogus (1999) suggested that the values of the coefficients α and β slightly decrease with increasing depth of flow and the influence of the main channel width on α and β values is almost negligible. Seckin et al. (2009) showed that α and β coefficients decreases with increases the total discharge of the compound channel as the flow become more stable at higher discharge. Luo (2012) indicated that the value of both the energy and momentum coefficients in smooth compound channels decrease with the increase of water depth and Reynold's number. Mohanty et al. (2013) proved that α could be related to β by an equation following a straight-line relationship. Hamidifar (2016) developed expressions for calculating the kinetic energy and momentum correction coefficients as a function of the flow relative depth and vegetation density.

Based on the previous studies reviewed above, it can be noted that the non-uniformity of velocity distribution, which can be expressed in terms of velocity distribution coefficients (α and β), should properly be considered in 1D flow formulations for obtaining accurate calculations. Furthermore, most previous studies focused on the flows in simple or compound open channels with smooth beds only, expressing the velocity distribution coefficients (α and β) as a function of few flow parameters. Therefore, as a part of this study, the velocity distribution coefficients are studied experimentally and numerically as a function of the whole flow regime classified according to the roughness and flow resistance.

2.5 Analytical models for velocity distribution

It is known that accurate predictions of mean velocity field for open channel flows can be obtained by applying sophisticated 3D models, which are based on Reynolds averaged Navier–Stokes (RANS) equations. However, it may be difficult and impractical to apply the 3D RANS models for engineering applications such as modelling flows in natural rivers. Furthermore, in most hydraulic problems, only the primary velocity distribution is of importance for hydraulic engineers. Therefore, instead of these 3D full RANS models, analytical models based on a simplified forms of RANS equations were proposed to predict the primary velocity distributions for both rectangular and compound channels. In this section, the development of these analytical models is briefly described, focusing on the theoretical considerations and related assumptions used in the development of such models. The full derivation of the analytical models used in the present study are discussed in more detail in chapter 5.

2.5.1 Analytical models for vertical distribution

Many analytical and semi analytical models have been proposed to predict the vertical distribution of the primary velocity in open channels as well as pipe flows. Such models were derived through integrating the RANS equations by assuming that the variations in the transverse direction at the centre of channels could be neglected. The proposed analytical models offered improvements to both the log and wake laws which were found to be unable to represent the flow features such as velocity-dip phenomenon (Guo & Julien, 2003).

Yang et al. (2004) proposed a dip-modified-log-law (DML-Law) based on the analysis of the Reynolds-averaged Navier-Stokes (RANS) equations. They assumed that the vertical component of secondary currents is generally in the downward direction and can be modeled using a linear relationship for simplicity of RANS equations. DML-law of Yang (2004) can be given as follows:

$$\frac{U}{u_*} = \frac{1}{k}\ln\frac{z}{z_o} + \frac{\mu}{k}\ln\left(1 - \frac{z}{h}\right) \tag{2.34}$$

where, z is vertical distance from bed, z_o is the distance at which the velocity is hypothetically equal to zero, u_* is shear velocity, h is the flow depth, k is the von Karman constant and μ is the dip-correction parameter which is a positive constant. The DML-law modified the log-law by adding the second term on the right-hand side of Eq. (2.34) that predicts the velocity dip position. The advantage of this law is that it contains only one parameter, i.e. μ, for dip-correction. Although the DML-law can predict dip-phenomena well for smooth uniform open channel flows, it fails to predict the velocity well in the rough channels (Guo & Julien, 2008; Bonakdari et al., 2008; Absi, 2011 and Lassabatere et al., 2012).

Guo and Julien (2008) proposed a modified-log-wake law (MLW-Law) which fits velocity profiles with a dip phenomenon. However, this law cannot be used for predictive applications since it requires measurements for velocity.

Lassabatere et al. (2012) proposed an analytical model for the streamwise velocity, on the basis of a specific formulation for the vertical velocity profile. Their proposed model was applicable to both rough and smooth flow regimes. However, the model is only applicable to the outer region and central part of channels.

Based on an analysis of the Reynolds-averaged Navier–Stokes equations and a log-wake modified eddy viscosity distribution, Absi (2011) proposed the dip-modified log-wake law (DMLW-law) which can be given as follows:

$$\frac{U}{u_*} = \frac{1}{k}ln\left(\frac{\xi}{\xi_o}\right) + \frac{2\Pi}{k}\sin^2\left(\frac{\pi}{2}\xi\right) + \frac{\mu}{k}ln(1 - \xi) \tag{2.35}$$

where, $\xi = z/h$, $\xi_o = z_o/h$ and Π is Coles parameter representing the strength of the wake. It was found that the DMLW-law can predict the velocity profiles for both smooth and rough flows. However, the dip correction is not sufficient for providing the accurate predictions and the appropriate values of strength parameter (Coles parameter) are also required.

In the present work, an in-depth study regarding the related assumptions of analytical DMLW-law is done. Using the detailed results obtained from the CFD modelling, a complete estimation of the model parameters associated with dip phenomenon and eddy viscosity are made to improve the analytical model accuracy.

2.5.2 Analytical models for depth-averaged distribution

Many studies have concerned with the prediction of the depth-averaged velocity and boundary shear stress in compound channels, e.g. Ervine & Ellis (1987); Shiono and Knight (1988, 1991); Lambert and Sellin (1996); Ervine et al. (2000). Based on these studies, a number of analytical approaches for modelling the depth-averaged velocity and the boundary shear stress distributions have been developed. However, the methodology proposed by Shiono and Knight (1991), which is based on Reynolds averaged Navier–Stokes (RANS) equation, is the most popular method and is widely used for modelling different cases associated with the compound channel flows. Therefore, this work concentrates only on the application of the Shiono and Knight methodology (SKM) to asymmetric compound channels that are considered here.

The basic form of Shiono and Knight method (SKM) that is widely used for depth-averaged calculations in simple and compound channel flows can be given as follows:

$$\rho g H S_o - \rho \frac{f}{8} U_d^2 \left(1 + \frac{1}{S^2}\right)^{\frac{1}{2}} + \frac{\partial}{\partial y}\left[\rho \lambda H^2 \left(\frac{f}{8}\right)^{1/2} U_d \frac{\partial U_d}{\partial y}\right] = \frac{\partial}{\partial y}\left[H(\rho UV)_d\right] \qquad (2.36)$$

where; f = Darcy-Weisbach friction factor, λ = dimensionless eddy viscosity; S = the channel side slope of the banks (1:S, vertical: horizontal), H = flow depth as a function of lateral distance y, and U_d, V_d = the depth-averaged streamwise and crosswise velocities. Solving Eq. (3.36) yields Ud as a function of y.

The term on the right-hand side of Eq. (2.36) accounts for the effect of the secondary flow on the primary flow. Shiono and Knight (1991) observed that the lateral gradient of the secondary flow term $[H(\rho UV)_d]$ decreases approximately linearly in the main channel and linearly increases on the floodplains, as shown in Figure (2.13). Therefore, they suggested that a constant value of secondary flow term, which is referred to as secondary flow parameter (Γ) can be allocated for main channel and floodplains. Thus, Eq. (2.36) can be rewritten as follows:

$$\rho g H S_o - \rho \frac{f}{8} U_d^2 \left(1 + \frac{1}{S^2}\right)^{\frac{1}{2}} + \frac{\partial}{\partial y}\left[\rho \lambda H^2 \left(\frac{f}{8}\right)^{1/2} U_d \frac{\partial U_d}{\partial y}\right] = \Gamma \qquad (2.37)$$

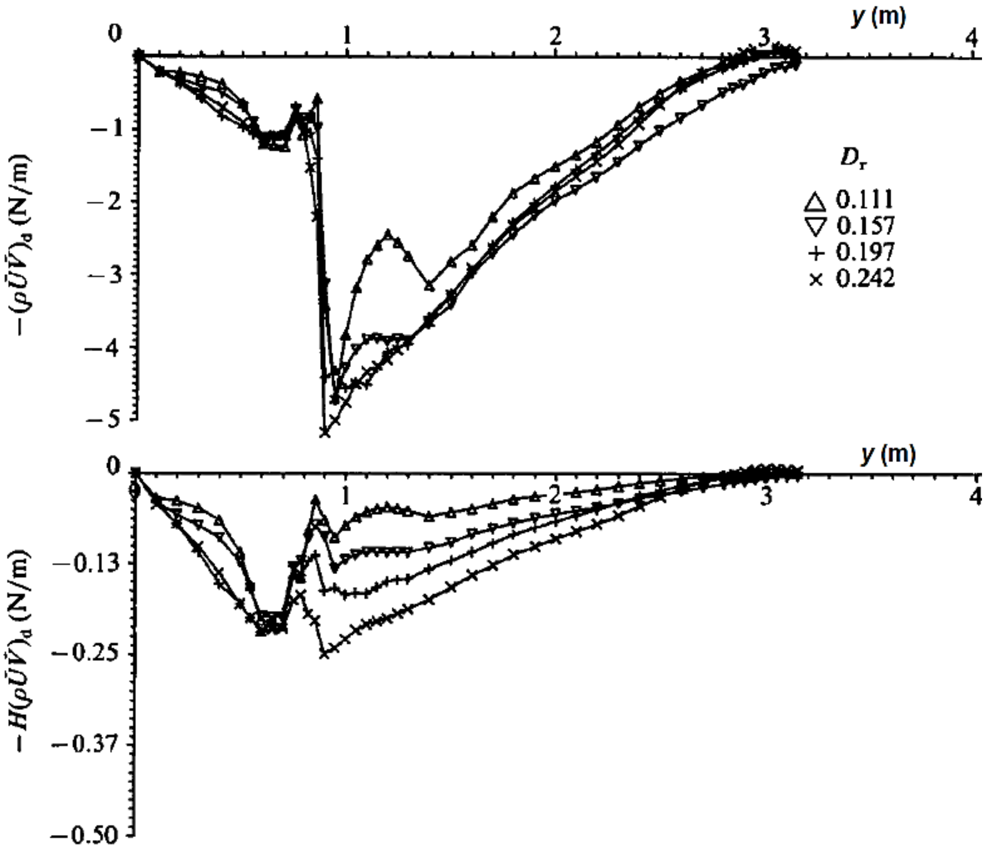

Figure 2.13 Lateral variation of apparent stress [$(\rho UV)_d$], and force per unit length [$H(\rho UV)_d$] due to secondary flows for different *Dr*, (Shiono and Knight, 1991).

Based on the SKM method, many investigations have been undertaken into flow in straight and meandering compound channels. For example, the SKM method has been applied to straight prismatic channels by Shiono & Knight (1991); Abril and Knight (2004); Liao and Knight (2007); Tang & Knight (2008); and Devi & Khatua (2016). Attempts have also been undertaken to use the SKM in modelling meandering channels (Liu et al. 2014) and non-prismatic channels (Rezaei & Knight 2009).

The accuracy of the SKM results was found to depend substantially on the three depth-averaged calibration coefficients, which include local bed friction (the Darcy-Weisbach friction factor) *f*; the dimensionless eddy viscosity λ and the transverse gradient of secondary flow term Γ. In the compound channel with wide floodplains, different methods have been suggested to calibrate each one of these three coefficients. The friction factor is often assumed to be constant in each panel and may be back calculated using ($f = 8\tau_b / U_d^2$), where the mean depth-averaged velocity U_d and shear stress τ_b are measured for each panel (Knight et al. 2007). The dimensionless eddy viscosity for the main channel (λ_{mc}) is usually taken as 0.07 for experimental channels and from 0.24 to 0.5 for natural channels (Shiono and Knight 1991). The value of the dimensionless eddy viscosity for the floodplain (λ_{fp}) is mostly predicted by the expression proposed by Abril and Knight (2004) and given as follows:

$$\lambda_{fp} = \lambda_{mc}(1.2D_r^{1.44} - 0.2) \tag{2.38}$$

where *Dr* is the relative depth and defined as the ratio between the flow depth of the floodplain to that of the main channel. The secondary flow parameter (Γ) can be defined as a fraction of the bed shear stresses ($\rho gHSo$), (Abril and Knight 2004). The simplification for the secondary flow term may also be made by expressing the term of V_d as a function of the U_d, (Ervine et al. 2000). The assumption is that the product of the local U_d and V_d velocities produce a profile that is similar to that of the squared depth-averaged streamwise velocity.

However, using the expressions suggested for a compound channel with wide floodplains to calculate the SKM parameters may not give the calibrated values that are proper for a compound channel with narrow floodplains. In this research, the conventional approaches discussed above are checked whether they can also be applicable to the compound channel with narrow floodplains and improved if necessary.

2.6 Summary

The previous sections have shown that that primary flows in simple and compound channels affected significantly by secondary flows, turbulence and roughness. For the inbank flow in a straight simple channel, secondary flows are generally generated due to the anisotropy of turbulence caused by the boundary conditions at the solid walls and at the free surface. Overbank flow in a straight compound channel is somewhat different in a number of aspects from inbank flow. The difference in velocity between the main channel and the floodplain flows may produce strong lateral shear layers, which consequentially lead to the generation of the large-scale vortices, which also called planform vortices. These vortices transport the high momentum fluid from the main channel towards the floodplain. In addition to the planform vortices rotating about vertical axes, helical streamwise vortices rotating about horizontal axes can often be observed in compound channels with overbank flows. The existence of such vortices also play an important role in the momentum exchange, especially near the junction between the main channel (MC) and floodplain (FP).

The open channel flow can often be treated as one-dimensional (1D) rather than as a three-dimensional (3D) flow, which is considered in complex hydraulic problems. For example, the one-dimensional unsteady flow in an open channel can be described by the so-called Saint-Venant equations, which are based on momentum and mass conservation laws. In other practical applications the steady and gradually varied flow in open channels could be considered. For such flow cases, the 1D energy equation derived from conservation of energy law is commonly used. The momentum and kinetic energy correction coefficients (β and α), which are also referred to as velocity distribution coefficients, are applied in momentum and energy equations to capture the 3D features of the flow and correct the errors resulted from velocity averaging. Based on the previous studies reviewed in this study, it can be noted that the non-uniformity of velocity distribution, which can be expressed in terms of velocity distribution coefficients (α and β), should properly be considered in 1D flow formulations for obtaining accurate calculations.

Furthermore, there are many analytical and semi analytical models have been proposed to predict the distribution of the primary velocity in both simple and compound open channels. Such models were derived through integrating the RANS equations by imposing specific assumptions for the secondary flows and turbulence. For the vertical velocity profile, the analytical dip-modified laws can be used, while Shiono and Knight method (SKM) is widely used for depth-averaged velocity distributions. The accuracy of the analytical models was found to depend substantially on the model parameters that account for the effects of secondary flows, turbulence and wall roughness.

Growing in computing power encourages on using Computational Fluid Dynamics (CFD) modelling to perform extensive studies on the turbulent flows in open channels. The 3D numerical simulations by the CFD may provide clearer explanations of the flow structure and the interactions of the key hydraulic components than do the traditional laboratory measurements. In the light of the review conducted in the present study, it can be concluded that the CFD model with Reynolds stress turbulence model (RSM) can predict the main turbulent features and the secondary motions in open-channel flows through accounting for the turbulence anisotropy effects. Furthermore, the RSM models can mathematically represent the physical processes of the free surface flow. Therefore, the RSM models are used for the numerical simulations conducted in this study to understand the secondary flow and turbulence effects on the primary velocity distributions.

In this study, by using the CFD modeling approach, a method for evaluating the velocity distribution coefficients (α and β), which play an important role in 1D numerical approach, is proposed. Also, methods for calibrating the key coefficients in analytical models of velocity distributions are suggested to improve the accuracy of these models for narrow open channel flows.

Chapter 3

Experimental Investigation

3.1 Introduction

Experiments performed in this study were conducted in a (0.3 m) wide by (8.6 m) long flume in the Hydraulics Laboratory of the School of Computing, Science & Engineering (CSE) at the University of Salford. Velocity distributions and their non-uniformity were investigated for flows in rectangular and compound channels with different roughness regimes. Three flow regimes in terms of the roughness (smooth, transitional and rough regimes) were established by changing roughness configurations of the bed. The details of the experimental procedure and some typical data are described in this chapter, while the results are presented and discussed in Chapters 6 and 7.

3.2 Experimental facilities

3.2.1 Flume setup

All experiments were conducted in a glass-sided tilting Arm-Field flume with a stainless-steel bed. The typical flow section was rectangular with working dimensions of 0.30 m in width, 0.45 m in depth. The flume was composed of a channel, inlet tank and discharge tank as shown in Figure 3.1. The flume was also provided with a closed flow circulating system with a series of water sump tanks located on the floor and connected with each other. Water circulation was carried out by the centrifugal pump mounted beneath the flume, drawing water from the series of interconnected sump tanks. The flow was regulated using a manual control valve. The flow rate was measured using an electromagnetic flow-meter (EMFM) and displayed on a digital readout located on the front of the electrical console.

The flume was provided with a small manual moving cart that works as a carriage to move the point gauge and to hold the velocity measurement device along the entire length of the flume. The flume was marked with a millimeter scale to help in identifying the location of the carriage and the measuring devices. A tail gate located at the downstream end of the flume was used to adjust tail water levels. A hand wheel on the end jacking pedestal, which allows the slope of the channel bed to be varied, was used for setting the slope of the bed.

For convenience the actual slope was displayed on an indicator adjacent to the hand wheel. The scale was calibrated to give a slope value of one in (scale reading), e.g. a value of 200 on the scale corresponds to a slope of 1 in 200, or 0.005 m/m.

(a) inlet with pump (b) discharge unit with sump tanks

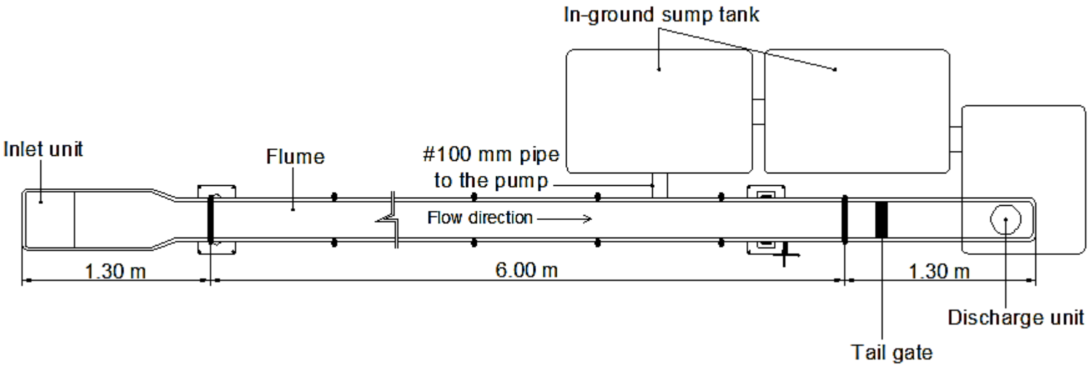

(c) Schematic diagram of the laboratory flume

Figure 3.1 Photos and diagram for the laboratory flume used.

3.2.2 Velocity measuring devices

The main velocity measuring device used in this study is the Pitot Tube. In this section, only a general description and operating principle for the velocity instrument are given. The subsequent sections provide more detailed information about the set up and use of this device.

A Pitot tube with inner diameter of 1.0 mm and with 4 holes (φ 0.75 mm), as shown in Figure 3.2, was used in the experiments of both rectangular and compound channels. It was used to obtain vertical velocity profiles, depth-averaged velocity profiles, and isovel line patterns.

The Pitot tube was connected to the low-range digital pressure transducer (Comark C9551/SIL, 0 to ± 140mbar), to measure the pressure difference (Δp) between the static and dynamic pressures. The opening at the tip of the tube records the stagnation pressure (total pressure, P_t) which is the sum of static and dynamic pressures (P_s+ P_v), while the side openings record the static pressure (P_s) as illustrated in Figure 3.2c. The difference of the two measurements gives the dynamic pressure which is recorded by the transducer as a differential head (in mmH_2O) with approximate accuracy (±0.1 mm). The point velocity then can be calculated from the following equation derived based on Bernoulli principle:

$$u = \sqrt{2g\Delta h} \tag{3.1}$$

where u is local velocity of water at Pitot tube point, g is acceleration due to gravity and Δh is differential head measured using the pressure transducer.

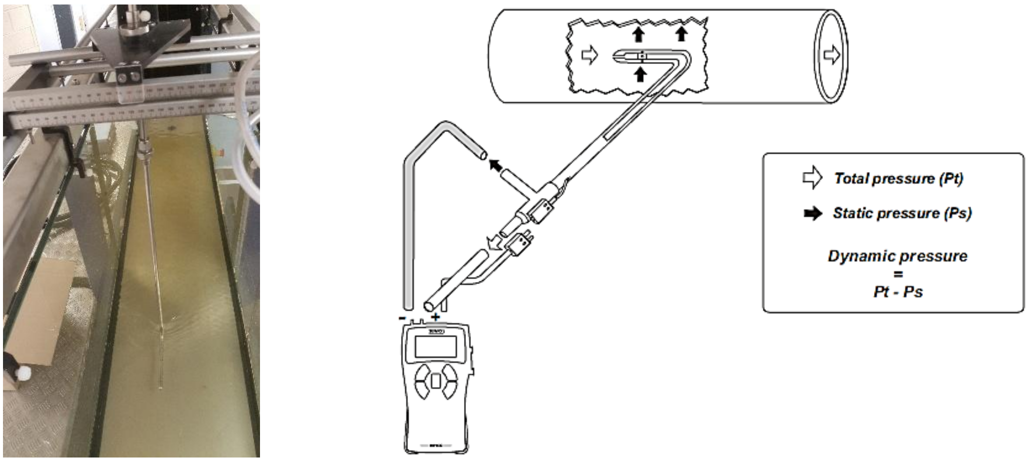

(a) (b)

Figure 3.2 Photo and schematic of the Pitot tube.

3.3 Test program

The experimental program was designed to study various aspects of velocity distributions for inbank and overbank flows with different flow regimes in terms of roughness conditions. Therefore, two sets of experiments were conducted on two channel configurations that have different hydraulic and roughness characteristics for collecting the experimental data. One of the channels had a rectangular section to simulate the inbank flow condition, while the other had a compound section constructed inside the flume to represent the overbank flow condition. The main objectives and some details for all experiments considered in this study are summarised in Table 3.1. The description of experiments is given in the next following sections.

Table 3.1 Summary for sets of experiments.

Set No.	Number of tests	Flow condition	Objectives	Test #	Bed condition	Roughness regime
1	12	uniform flow rectangular channel	Investigating vertical velocity distributions in rectangular channels under different roughness regimes by measuring and calculating the following hydraulic parameters: 1-velocity distribution coefficients (α, β) 2-section mean velocity (U) 3-maximum velocity (U_{max}) 4-Roughness Reynolds number (Re^*) 5-aspect ratio ($Ar = B/H$) 6-vertical profile of eddy viscosity (ν_t) 7-secondary currents (U_{sec})	S6	smooth ($K_s \approx 0.15$ mm)	hydraulically smooth ($Re^* < 5$)
				S10		
				S15		
				S20		
				T6	rough ($K_s \approx 1.5$ mm)	transitionally rough ($5 < Re^* < 70$)
				T10		
				T15		
				T20		
				R6	rough ($K_s \approx 8.0$ mm)	fully rough ($Re^* > 5$)
				R10		
				R15		
				R20		
2	12	uniform flow asymmetric compound channel	Investigating lateral velocity distributions in compound channels under different roughness regimes by measuring and calculating the following hydraulic parameters: 1-velocity distribution coefficients (α, β) 2-depth-average velocity (U_d) 3-Roughness Reynolds number (Re^*) 4-relative friction factor (f_{mc}/f_{fp}) 5-relative depth (Dr) 6- lateral eddy viscosity (ε_{yx}) 7-secondary currents (U_{sec})	CS0.25	main channel smooth, floodplain smooth	hydraulically smooth ($Re^* < 5$)
				CS0.33		
				CS0.40		
				CS0.50		
				CT0.25	main channel smooth, floodplain rough (K_s=1.5mm)	transitionally rough ($5 < Re^* < 70$)
				CT0.33		
				CT0.40		
				CT0.50		
				CR0.25	main channel smooth, floodplain rough (K_s=8mm)	fully rough ($Re^* > 5$)
				CR0.33		
				CR0.40		
				CR0.50		

3.4 Experimental setup

3.4.1 Experimental setup for rectangular channel flows

The first set of experiments was concerned with investigating the combined effects of the bed roughness, secondary currents and turbulence characterised by the eddy viscosity on velocity distributions of flows in rectangular channels. Moreover, these experiments were undertaken to provide a basis for studying the potential relationship between the velocity distribution coefficients (α and β), which are taken as indicators for non-uniformity of velocity distributions, and the flow regime in terms of roughness conditions described by Re^*. The effects of the secondary currents and the eddy viscosity on the non-uniformity of the velocity distribution were also examined based on the results from these experiments alongside numerical results obtained by CFD simulations.

In this set of experiments, three different bed roughness elements were used to cover all hydraulically defined roughness regimes that might occur in engineered or natural open channels. Experimental conditions for the first set of test cases are given in Table 3.2.

Table 3.2 Flow and channel conditions for rectangular channel experiments.

Case **[#]**	**Flow depth** H **[cm]**	**Aspect ratio** Ar **[---]**	**Flow rate** Q **[l/s]**	**Mean bulk velocity** U **[m/s]**	**Global shear velocity** U_* **[m/s]**	**Reynolds number** Re **(x10^4)** **[---]**	**Roughness height** K_s **[mm]**	**Roughness Reynolds number** Re^* **[---]**
S6	6.0	5.0	5.22	0.290	0.0145	4.95	0.15	2.8
S10	10.0	3.0	11.39	0.380	0.0172	9.08	0.15	3.4
S15	15.0	2.0	21.17	0.470	0.0192	14.06	0.15	3.8
S20	20.0	1.5	32.86	0.548	0.0205	18.70	0.15	4.0
T6	6.0	5.0	4.13	0.229	0.0145	3.92	1.5	28.8
T10	10.0	3.0	9.33	0.311	0.0172	7.44	1.5	34.1
T15	15.0	2.0	17.42	0.387	0.0192	11.57	1.5	38.2
T20	20.0	1.5	26.14	0.436	0.0205	14.88	1.5	40.8
R6	6.0	5.0	3.12	0.174	0.0145	2.96	8.0	144.4
R10	10.0	3.0	7.36	0.245	0.0172	5.87	8.0	170.8
R15	15.0	2.0	14.92	0.332	0.0192	9.91	8.0	191.0
R20	20.0	1.5	24.59	0.410	0.0205	14.00	8.0	204.2

$Ar = B/H$, $U = Q/A$, A = the cross-sectional area of the flow, $U^* = \sqrt{gRS_o}$, R = hydraulic radius, $Re = 4U_mR/v$, $Re^* = U^* Ks/v$, v = Kinematic Viscosity of water.

Experiments were classified into three groups. In the first group, which includes test cases S6 to S20 in Table 3.2, the smooth stainless bed surface of the flume was used for establishing a hydraulically smooth condition for which $Re^* < 5$. In the second group, which consists of experiments T6 to T20, an anti-slip sheet of 1.5 mm thick was used to roughen the channel bed. The equivalent sand roughness K_s of this rough bed was estimated to be the same magnitude as the sheet thickness. Therefore, the values of R^* for cases of second group were laying in the range of transitional roughness conditions ($5 < Re^* < 70$). The cases of third group, i.e. R6 to R20, represented the fully rough flow regime for which $Re^* > 70$. The rough bed used in third group experiments were generated using a single layer of grains ($D_{84} = 8.0$ mm) affixed to an aluminium plate having the same width as that of the flume bed. D_{84} is the particle diameter so that 84% of the particles in the total grain-size distribution are smaller than D_{84}. The equivalent sand roughness height for the fully rough cases was estimated to be the same order of magnitude as D_{84}. Figure 3.3 shows roughness elements used for generating all roughness conditions considered in the first set of experiments.

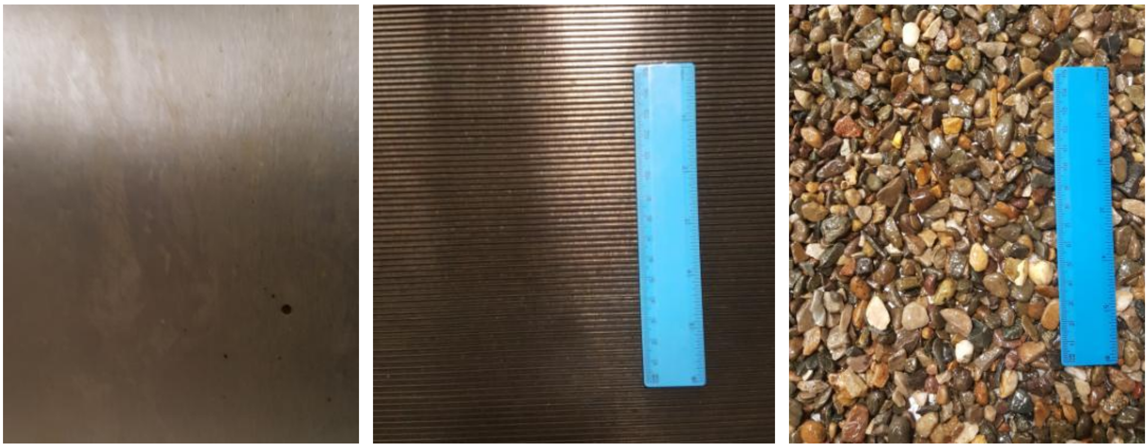
(a) Smooth (b) Transitionally rough (c) Full rough

Figure 3.3 Bed surfaces for test cases of flows in rectangular channels.

All experiments within this set were performed at four different uniform flow depths (6, 10, 15 and 20 cm) with a fixed-bed slope of 0.0005. The flow depth H was changed with keeping the channel width invariant to examine the effect of aspect ratio (Ar) on secondary currents. The adopted flow depths provide the range of aspect ratios from 1.5 to 5, covering the same range as for narrow rectangular channels. In the narrow channels where $Ar < 5$, strong secondary currents are developed and their effect on the primary flows is thought to be significant. Therefore, this range of Ar values was selected for rectangular channel experiments. Figure 3.4 shows roughness conditions for all rectangular channel experiments considered in the present study.

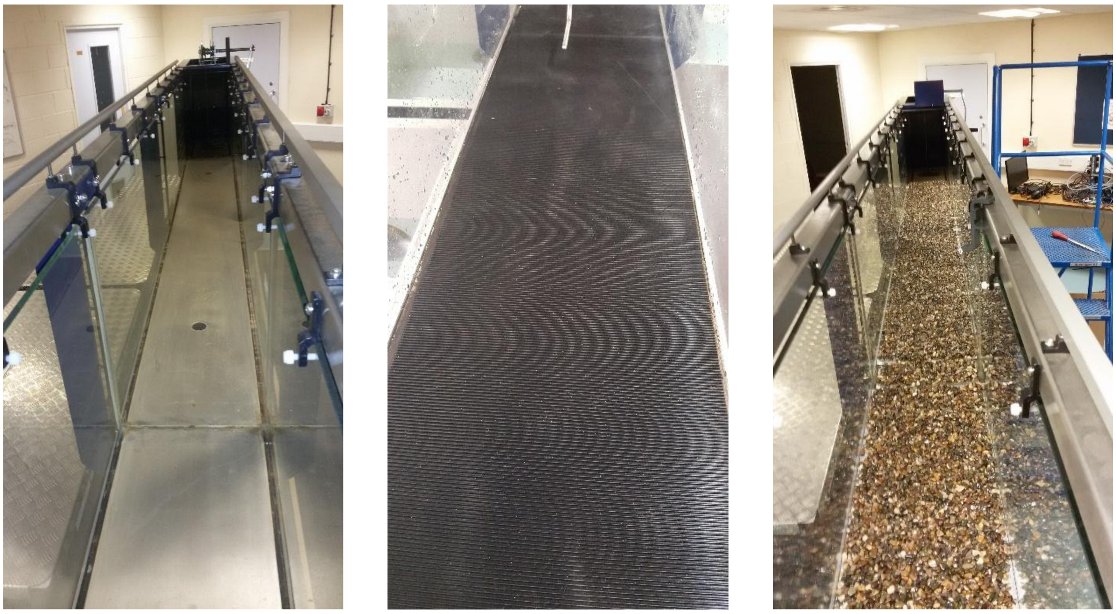
(a) smooth (b) Transitionally rough (c) Fully rough

Figure 3.4 Photos showing roughness conditions of rectangular channels.

3.4.2 Experimental setup for compound channel flows

The second set of experiments was undertaken for investigating the effect of all energy loss mechanisms including roughness, secondary currents and turbulence on depth-averaged velocity distributions in overbank flows. Also, this set was conducted to provide a basis for exploring the relationship between the non-uniformity of velocity distribution described by α or β and between the parameters that characterize secondary currents, eddy viscosity and friction in compound channels.

This set of experiments was carried out in the same flume used for the first set, but an asymmetric compound section was constructed from plywood plates inside the flume to simulate overbank flow conditions. The cross-section configuration is shown in Figure 3.5. The compound section consists of a rectangular main channel of width (b) 0.20 m and a single adjacent rectangular flood plain of width 0.10 m.

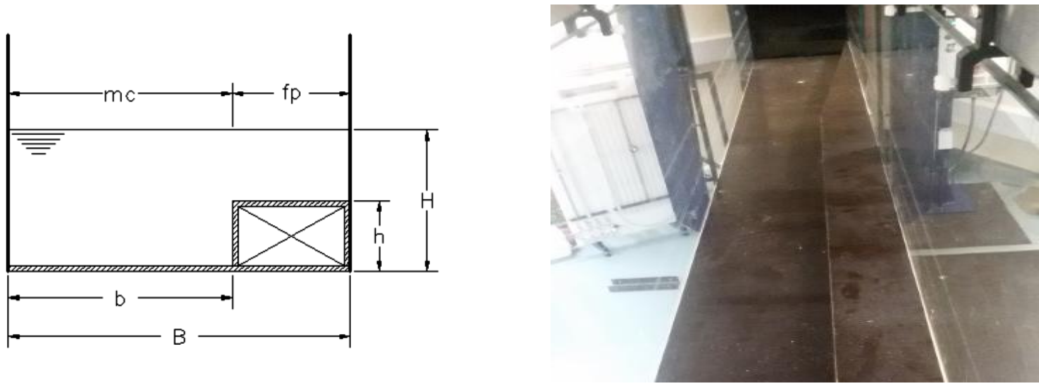

(a) (b)

Figure 3.5 Compound channel configurations used in second set of experiments.

Test cases within the second set were classified according to the bed roughness into three groups. Experimental conditions for all test cases are given in Table 3.3. In the first group, which includes the cases CS0.25 to CS0.50, both the main channel and the floodplain had smooth boundaries and the height of the floodplain (*h*) was 60 mm. In these smooth floodplain cases, the Manning coefficients (*n*) in the main channel and floodplain were estimated as about 0.010 from the normal depth measurements. The total flow depth was varied between 80 mm to 120 mm to cover a range of relative depth *Dr* [= (*H*-*h*)/*H*] from 0.25 to 0.50. The relative depth was selected as a key experimental parameter in compound channel flows on the basis that the interaction between the floodplains and the main channel is known to be depth dependent. An upper limit of 0.5 was chosen on the grounds that *Dr* values in most practical flow cases are equal to or lower than this limit.

Table 3.3 Flow and channel conditions for the compound channels experiments.

Case [#]	Dr [---]	H_{mc} [mm]	$K_{s,mc}$ [mm]	H_{fp} [mm]	$K_{s,fp}$ [mm]	Q [l/s]	**Average** Re^* [---]
CS0.25	0.25	80.0	0.2	20.0	0.2	6.09	2.9
CS0.33	0.33	90.0	0.2	30.0	0.2	7.49	3.1
CS0.40	0.40	100.0	0.2	40.0	0.2	9.01	3.3
CS0.50	0.50	120.0	0.2	60.0	0.2	12.40	3.7
CT0.25	0.25	80.0	0.2	20.0	1.5	5.28	28.6
CT0.33	0.33	90.0	0.2	30.0	1.5	6.57	31.3
CT0.40	0.40	100.0	0.2	40.0	1.5	7.99	33.4
CT0.50	0.50	120.0	0.2	60.0	1.5	11.21	36.7
CR0.25	0.25	100.0	0.2	25.0	8.0	6.60	122.9
CR0.33	0.33	112.0	0.2	37.0	8.0	8.11	133.7
CR0.40	0.40	125.0	0.2	50.0	8.0	9.90	142.8
CR0.50	0.50	150.0	0.2	75.0	8.0	13.79	156.1

The cases considered in the second group (i.e. CT0.25 to CT0.50) had a rough bed on the bottom of the floodplain while the main channel was kept smooth. The bed of the floodplain was roughened by the same anti-skid sheet that was used for rectangular channel experiments. The equivalent sand roughness K_s of this rough bed was about 1.5 mm. The average values of $Re*$ ($= \overline{U}_* K_s/\nu$) for cases CT0.25 to CT0.50 were then ranged from 28 to 36, which lie in the range of transitionally rough regime (i.e., $5 < Re* < 70$). $\overline{U}_*$ is the averaged value of the shear velocity in the main and floodplain channels. The height of the floodplain (h) was 60 mm. The flow depth was varied between 80 mm and 120 mm to provide the range of relative depth from 0.25 to 0.50.

The cases considered in the third group (i.e. CR0.25 to CR0.50) had a rough floodplain while the main channel was smooth. Gravel particles with D_{84} of approximately 8.0 mm are pasted closely over the bed of the floodplain to create a rough surface. Since the great part of gravel has a size of the same order of magnitude as D_{84}, so the equivalent sand grain roughness height (K_s) for the floodplain can be estimated to be 8.0 mm. For the smooth main channel, K_s was calculated based on the Manning's n to be 0.20 mm. The height of the floodplain (h) was 75 mm. The total flow depth was varied between 100 mm and 150 mm to cover the similar range of relative depth that was provided for first and second groups. In all test cases, the bed slope of the channels was fixed at about 0.0070 m/m. Figure 3.6 shows the roughness conditions of channels used in the second set of experiments.

(a) smooth floodplain (b) transitional floodplain (b) rough floodplain

Figure 3.6 Photos showing roughness conditions of compound channels.

3.5 Experimental procedure

3.5.1 Determination of bed slope (S_o)

The bed slope was chosen to be 0.0005 for rectangular channel flows experiments (i.e. the first set of experiments). This is partly, because the chosen slope is hydraulically defined as a mild slope, and partly because with that slope a wide range of flow depths can be established within the flow capacity of the pump used to supply water for the flume. The pump used has a flow capacity of 35 l/s. For compound channel flows experiments (the second set of experiments), a slope of 0.0007 was chosen, which is nearly the same order of magnitude as that for most natural rivers. Added to this fact, by doing the experiments on the channel with this slope, it was found that all required flow depths can practically be set under the available flow capacity provided by the water pump.

Before proceeding with the flume slope setting, the slope mechanical system of the flume was checked to ensure it gives accepted values when using its slope scale. For checking purposes, a simple method was adopted by using a transparent plastic tube filling with water. By this method, the slope of the channel bed was calculated from measuring the depth of water in the plastic tube at two points which were specified at the upstream and downstream ends of the channel. With knowing the difference of water depth and the longitudinal distance between the points, the slope can easily be calculated. The slope recorded from slope scales on the flume (S_r) and the slope obtained by the checking method (S_o) are plotted in Figure 3.7. After comparing the slope values taken from the slope scale of the flume with those obtained experimentally, the following calibration equation can be proposed based on the regression analysis:

$$S_o = 1.0508S_r - 8 * 10^{-5}, \ R^2 = 0.9992 \tag{3.2}$$

The slope taken from the slope scale of the flume was then modified according to the calibration equation to give the required slope with an accepted order of accuracy.

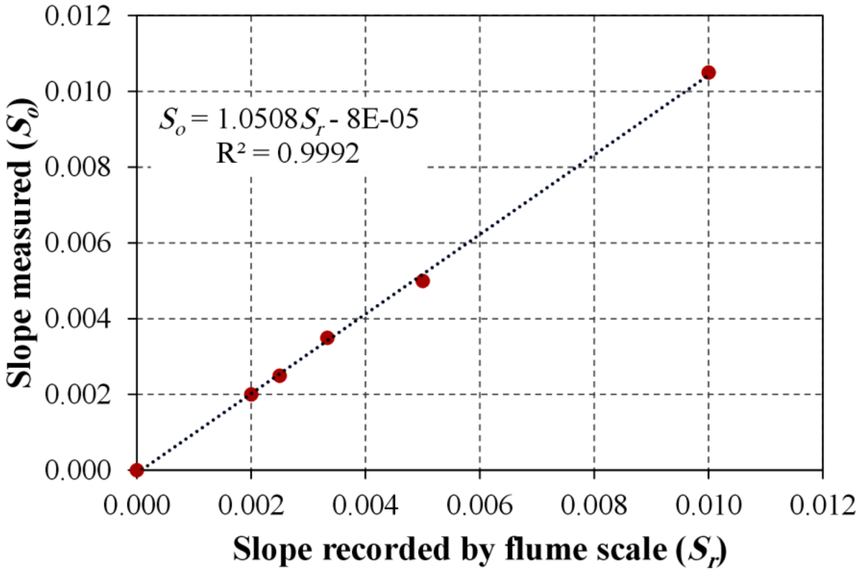

Figure 3.7 Bed slop calibration.

3.5.2 Determination of channel roughness

As mentioned in a previous section, the experiments considered in this study were performed on rectangular and compound channels under three different roughness conditions. A smooth bed and two roughened beds were used to generate three roughness regimes based on the roughness Reynolds number (*Re**) which is a function of the equivalent sand roughness height (K_s). Furthermore, K_s is a prerequisite parameter for numerical prediction models that are used in the present study. Hence, it is important to determine equivalent sand roughness height K_s correctly and precisely for all beds of experimental channels under investigation.

For rough experiments in rectangular channels, the equivalent sand roughness K_s was estimated based on grain analysis results. According to the British Standard BS 882, sieve analysis was performed for the aggregates used in roughening the bed to find out its particle size distribution and other necessary properties such as D_{50}, D_{84} and geometric standard deviation (σ_g). The percent finer range for the tested materials is shown in Figure 3.8.

In general, the gravel or ball diameter can be taken as K_s for uniform roughness case, and for non-uniform gravel beds, K_s is estimated to be the mean diameter (D_{50}). However, equivalent sand roughness may vary with grain non-uniformity and increase with increasing geometric standard deviation of the grain size distribution, (Cheng, 2015). Thus, for rough rectangular channels considered here, the K_s was estimated as D_{84} (i.e about 8.0 mm) because of a relatively high non-uniformity for the aggregates used (σ_g =1.3).

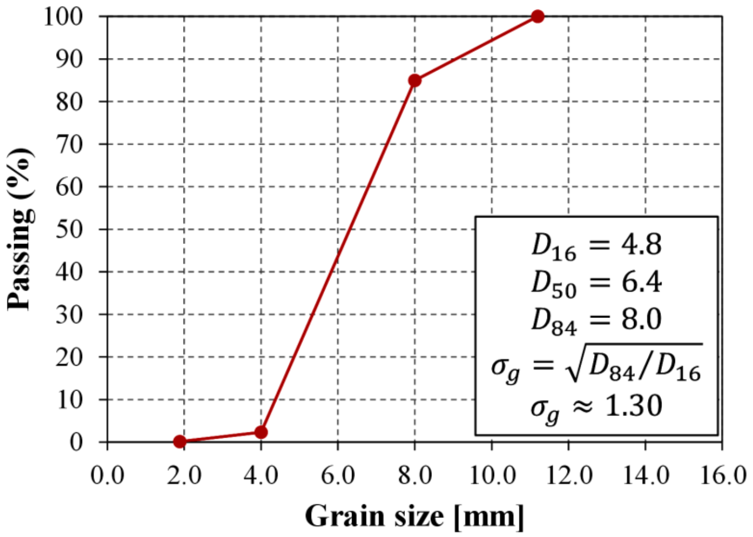

Figure 3.8 Particle size distribution of aggregates used for rough cases.

Since the anti-slip sheet used to generate the transitional rough bed had uniform protrusions, so the equivalent sand roughness height for transitional rough cases can be estimated as the same magnitude as the sheet height (i.e. 1.5 mm).

For experiments in smooth rectangular channels, the Manning coefficient n was firstly obtained from the experimental data for uniform flow over a smooth bed. The equivalent roughness height K_s was then calculated from the relationship proposed by Ackers (1991):

$$K_s = \left(8.25\sqrt{g}n\right)^6 \tag{3.3}$$

The Manning coefficients in the cases S6 to S20 were all about 0.009. Hence, the equivalent roughness height K_s calculated by Eq. (3.3) was 0.15 mm. It is found that in most river flow cases, Manning's *n* has less variation with discharge (Ladson et al. 2013). Therefore, the value of *n* was assumed to be constant for all discharges considered here.

The values of roughness heights K_s obtained from rectangular channel experiments were also adopted as resistance coefficients for compound channel experiments in the present study. The procedure of determining the roughness coefficients in compound channels based on inbank flow calculation has been adopted by many previous investigators, e.g. Myers and Brennan (1990) and Atabay and Knight (2006).

3.5.3 Establishment of uniform flow

The first and second sets of experiments were conducted under uniform flow conditions. Uniform flow by definition, implies that the water surface and energy gradient are parallel to the bed of the channel. The ability to establish and recognize uniform flow in a laboratory flume is difficult due to limited flume length and water surface irregularities. However, the best approximation under these conditions is when the average water surface line lies at the correct distance above the bed level and both the water and bed levels have the same slope. The flow was adjusted to achieve uniform flow at a specified normal depth by using an adjustable tailgate at the downstream end of the flume.

In order to make setting the uniform flow easier, different flow rates with a range of 2.0 to 30.0 l/s were pre-determined, then normal depth corresponding for each flow rate was determined for getting stage-discharge curves. These curves then used to find the flow rate for any depth in the experiments.

The following procedure was adopted in establishing the uniform flow and finding the normal depth for rectangular channel experiments. For a given discharge predetermined by adjusting the inlet valve, the tailgate was raised or lowered to achieve various M1 or M2 profiles, where M1 and M2 are customary textbook symbols for water surface profiles in open channel flow on a mild slope. M1 profile flow decelerates in the downstream direction, while M2 profile flow accelerates in the downstream direction. By using the point gage, the water surface elevation was measured at three points along the centreline of the channel. The normal depth was then determined by taking the mean of flow depths at a point where both M1 and M2 water surface profiles asymptotically approach one to another in the upstream direction, which was generally about 1.0 m downstream of the channel entrance. Finally, each discharge was plotted against the corresponding normal depth to obtain the stage-discharge curves as shown in Figure 3.9. The same procedure is also followed to establish the uniform flow in the compound channel experiments. Figure 3.10 shows the stage-discharge curves for flow cases in smooth, transitional and rough compound channels.

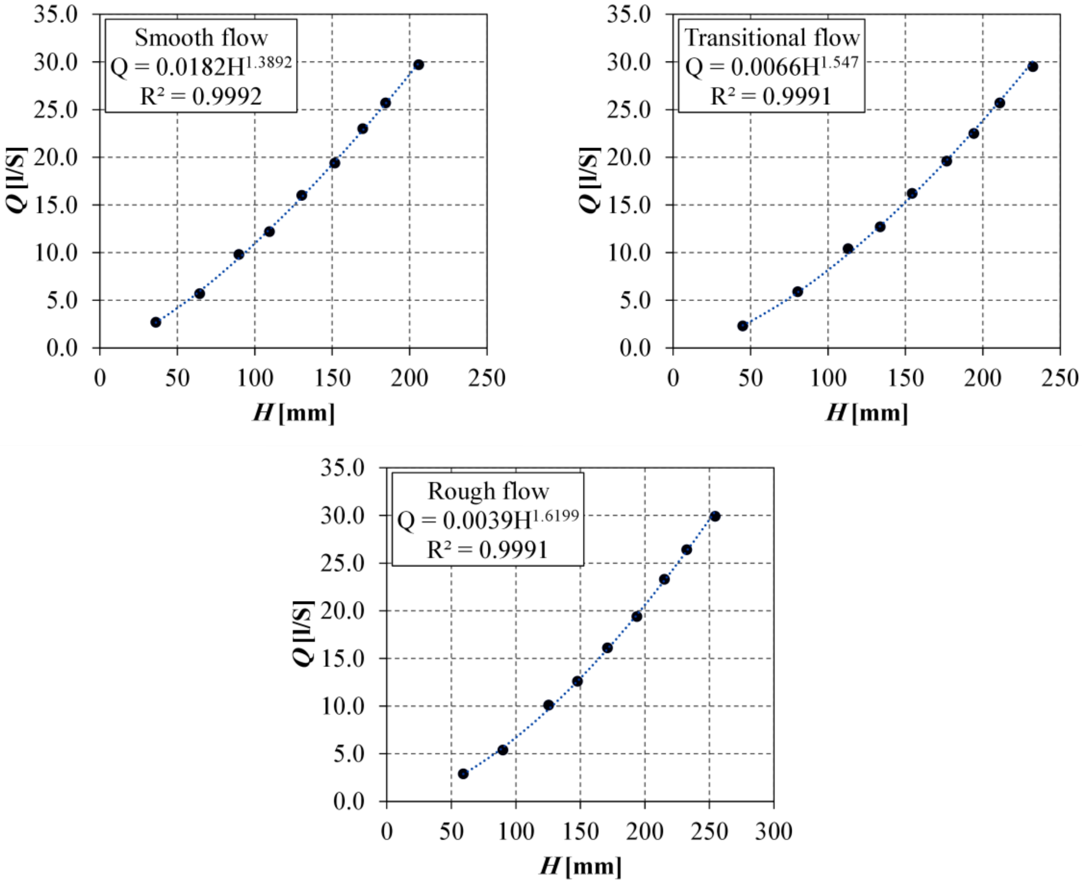

Figure 3.9 Stage-discharge curves for rectangular channel flows.

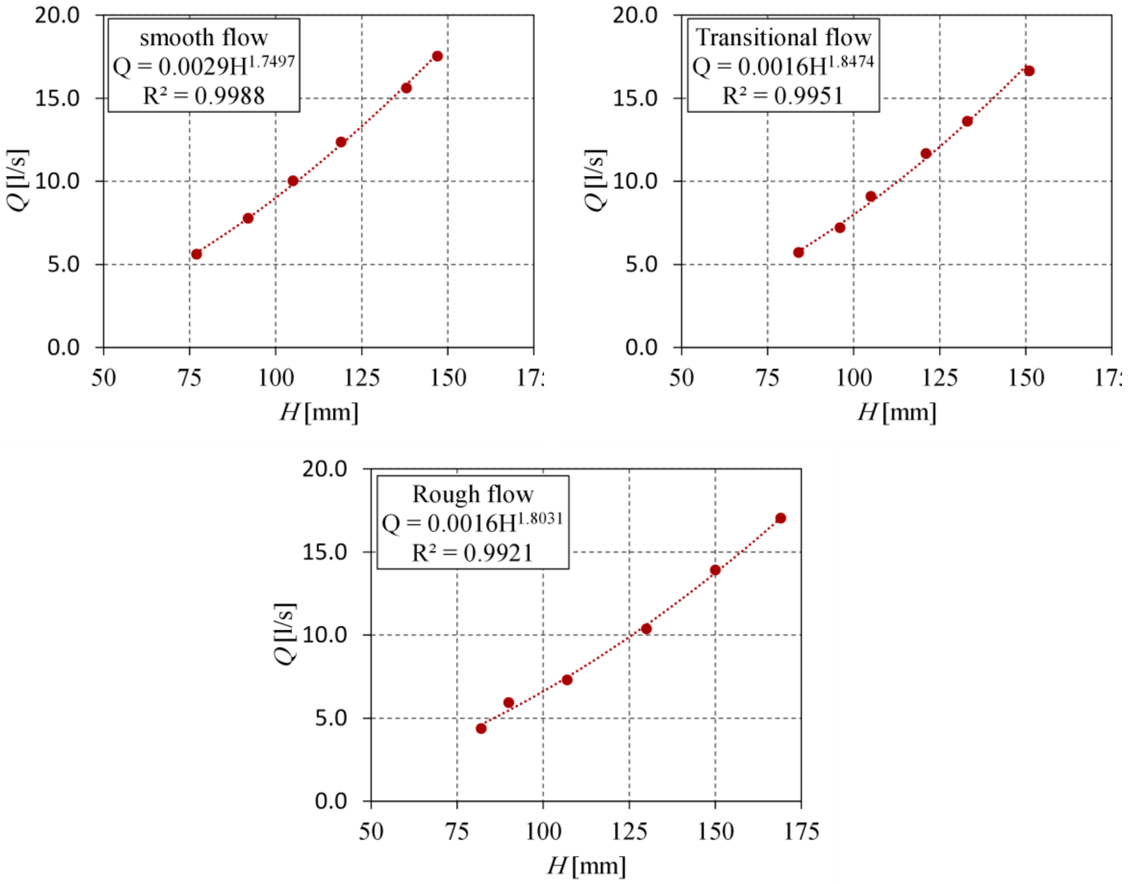

Figure 3.10 Stage-discharge curves for compound channel flows.

3.5.4 Taking velocity measurements

In all the experiments on rectangular and compound channel flows, a micro-Pitot tube with an internal diameter of 1.0 mm in conjunction with a pressure transducer was used to measure velocity. The Pitot tube was fixed to a main scale attached to a vernier scale with least count of 0.1mm. Testing section located at 6.5 m downstream from the inlet was selected for measuring the point velocities across the channel section. This is because at that distance there were negligible entrance effects and the fully developed flow could nearly be established.

In rectangular channel experiments, the point velocities were measured across the entire cross section by dividing the working section into grid every 20 mm laterally and every 10 mm vertically as shown in Figure 3.11a. The velocity was taken at each point over a 10 second interval and averaged over 60s. The velocity distributions were then integrated over the flow section to calculate the mean section velocity (U_m) and the integrated discharge (Q_m) by using Eqs. (3.3) and (3.4) below:

$$U_m = \frac{1}{A}\int u dA \cong \frac{1}{A}\sum_{1}^{n} u_i \Delta A_i \tag{3.4}$$

$$Q_m = U_m A \tag{3.5}$$

where A is the cross-sectional area, ΔA_i is the representative area of the point at which the velocity u_i is measured, and n is the number of measurements. The discharge, Q_m, which is obtained by integration of the point velocities, was compared with those recorded by the electro-magnetic flow meter (EMFM). The percentages of deviations should be within 3%, otherwise the experiments were repeated.

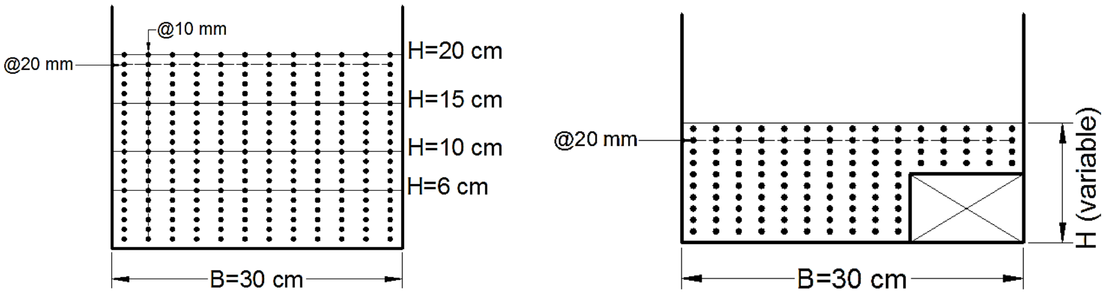

(a) Rectangular channel

(b) Compound channel

Figure 3.11 Velocity measurement grids.

For experiments in the compound channels, fifteen vertical velocity profiles spaced laterally 20 mm apart were measured to obtain the depth-averaged velocity distribution over the entire cross section (Figure 3.11b). In the main channel, ten points measurements equally spaced along each vertical profile were taken to obtain the depth-averaged velocity in this region. For each vertical profile in the floodplain, depth-averaged velocity was established from a point velocity measurement at an elevation of 0.4 times the flow depth. The resulting measured velocity distributions when integrated over the cross section should produce discharges (Q_m) that are within ±3 percent of the discharges measured by the calibrated electro-magnetic flow meter (EMFM) in the flume supply pipes. Figure 3.12 and Figure 3.13 show photos for some of the experiments carried out on rectangular and compound channels for taking velocity measurements. Examples of velocity measurements obtained from some of the experiments are presented in Appendix A.

The velocity distribution coefficients were also calculated based on the velocity distributions data as is described in the next section.

Figure 3.12 Photographs for some experiments on rectangular channels.

Figure 3.13 Photographs for some experiments on compound channels.

3.6 Calculation methods for experimental parameters

3.6.1 Velocity distribution coefficients

As mentioned previously, the energy and momentum coefficients (α, β) reflects the extent of non-uniform distribution of the velocity over a cross section. Therefore, velocity distribution coefficients were chosen in this study as indictors for describing the non-uniformity of velocity distributions. The energy coefficient is defined by:

$$\alpha = \frac{\int_A u^3 dA}{U^3 A} \tag{3.6}$$

and the momentum coefficient by:

$$\beta = \frac{\int_A u^2 dA}{U^2 A} \tag{3.7}$$

in which u is the velocity at a point in the cross section, U is the mean velocity through the cross section computed by Eq. (3.4).

In this study, α and β were calculated based on the point velocities obtained from the measurements in rectangular and compound channels. After taking velocity measurements, a cross section of the channel was divided into subareas with a small size. In rectangular channel cases, the subarea had a depth of 10 mm and a width of 25 mm. In compound channel cases, the width of subarea was 20mm while its depth was 1/10 of the flow depth. The variation of flow velocity in each subarea is small. Therefore, each subarea was assumed to have the same flow velocity throughout. In such a case, the integration of Eqs. (3.6) and (3.7) can be replaced by summation as follows:

$$\alpha \approx \frac{\sum_{i=1}^{n}(u_i^3 \Delta A_i)}{U^3 A} \tag{3.8}$$

$$\beta \approx \frac{\sum_{i=1}^{n}(u_i^2 \Delta A_i)}{U^2 A} \tag{3.9}$$

3.6.2 Shear velocity

The shear velocity (u_*) is the most fundamental velocity scale by which the mean velocity and turbulence quantities are usually normalised. In open channel flow, the shear velocity is often determined from direct measurements of boundary shear stress (τ_b) based on the following basic equation:

$$u_* = \sqrt{\tau_b/\rho} \tag{3.10}$$

Using the Preston tube (Preston, 1954; Patel, 1965) is a simpler technique to measure the boundary shear stress. Although the Preston tube technique can be successfully used on smooth surfaces, some problems arise when using on a rough surface. The additional parameters relating to the surface roughness condition make developing a calibration chart for a rough surface more complicated than that for a smooth surface (Wu & Rajaratnam, 2000).

When the bed shear stress is difficult to be measured directly, it can be correlated with the average measured velocity. In the present work, the boundary shear stress (τ_b) was calculated from the square law of the depth-averaged velocity (U) using:

$$\tau_b = C_f \rho U^2 \tag{3.11}$$

The parameter C_f is expressed in terms of a roughness parameter (Darcy-Weisbach factor, f) as follows:

$$C_f = f/8 \tag{3.12}$$

The shear velocity u_* was then calculated according to the above equations, using the measurements of the velocity taken in the rectangular and compound experiments.

Chapter 4

CFD Modelling of Channel Flows

4.1 Introduction

In the present study, the computational fluid dynamic (CFD) models were applied to simulate the flow in the rectangular and compound channels that were used in the experiments. The 3D numerical CFD models were developed and run using CFX package (v.15). The detailed CFD results were used as part of an investigation to understand the significance of secondary flows and turbulent eddy viscosity in calculations of primary velocity distributions.

This chapter presents the fundamental governing equations of fluid flow used in CFD schemes. Various turbulence models adopted in the modelling of turbulent flows are also discussed which will help in selecting a turbulence model that fits the flow cases under investigation. Then the boundary conditions and input parameters required for application of CFD models are presented in detail.

4.2 Theoretical basis of CFD modelling

4.2.1 Governing equations

The numerical modelling using computational fluid dynamics (CFD) involves the solution of the Navier–Stokes (N-S) equations, which are derived based on the laws of conservation of mass and momentum within a moving fluid. For a turbulent flow of an incompressible and Newtonian fluid, Navier–Stokes equations can be formulated as follows:

Continuity equation (the conservation of mass),

$$\frac{\partial u_i}{\partial x_i} = 0 \tag{4.1}$$

Momentum equation (the conservation of momentum),

$$\frac{\partial u_i}{\partial t} + \frac{\partial}{\partial x_j}(u_i u_j) = -\frac{1}{\rho}\frac{\partial p}{\partial x_i} + \frac{1}{\rho}\frac{\partial \tau_{ij}}{\partial x_i} \tag{4.2}$$

where u_i (i = 1, 2, 3) are the instantaneous velocity components, p is the instantaneous pressure and τ_{ij} (i,j = 1, 2, 3) are the components of the viscous stress tensor. For a Newtonian fluid the stress tensor can be related to the rate of strain tensor as follows:

$$\tau_{ij} = \rho\nu(\frac{\partial u_i}{\partial x_j} + \frac{\partial u_j}{\partial x_i}) \tag{4.3}$$

in which ν is the kinematic viscosity of the fluid.

Based on the Reynolds decomposition approach, instantaneous velocity components and pressure can be expressed into a mean value (U_i, P) plus a random fluctuating part (u_i', p') to account for turbulence. By relying on the Reynolds decomposition and applying time averaging to the instantaneous N-S equations (Eqs. 4.1 and 4.2), the Reynolds-averaged Navier–Stokes (RANS) equations are obtained as follows:

$$\frac{\partial U_i}{\partial x_i} = 0 \tag{4.4}$$

$$\frac{\partial U_i}{\partial t} + U_j \frac{\partial U_i}{\partial x_j} = -\frac{1}{\rho}\frac{\partial P}{\partial x_i} + \frac{\partial}{\partial x_j}\left[\nu\left(\frac{\partial U_i}{\partial x_j} + \frac{\partial U_j}{\partial x_i}\right)\right] - \frac{\partial}{\partial x_j}(\overline{u_i' u_j'}) \tag{4.5}$$

The Reynolds-averaging operation produces nine extra unknown quantities ($-\overline{u_i' u_j'}$) as a consequence of the non-linearity of the advection term, the second term in Eq. (4.2). These quantities comprise the so-called Reynolds stress tensor. Since ($\overline{u_i' u_j'}$) equals ($\overline{u_j' u_i'}$), the Reynolds stress tensor is symmetric and, thus, has only six independent components. This means, the Reynolds-averaging of the N-S equations introduced six new unknowns into the governing equations. Therefore, a mathematical closure model is needed for these six new unknowns. This usually involves the solution of additional transport equations known as a turbulence model.

4.2.2 Turbulence models for the RANS equations

Since the Reynolds stress is not known a priori, the Reynolds averaged Navier–Stokes (RANS) equations (4.4 and 4.5) are not closed, unless a model that relates the Reynolds stress tensor ($-\overline{u_i' u_j'}$) to the global mean property of the fluid flow is provided. This has prompted the development of various turbulence models and some of these will be discussed in the next sections.

Two general closure strategies are typically adopted to develop practical turbulence models for engineering calculations (Rodi, 2017). The first strategy is based on the eddy-viscosity concept, whereas the second modelling strategy relies on Second-Moment Closure (SMC) approach. A brief description of both turbulence modelling methods is given herein in order to justify why the turbulence models based on the second strategy (SMC) was chosen for 3D numerical simulations in the present study.

4.3 Eddy-Viscosity turbulence models

Eddy Viscosity Models (EVM), which are also called the first order models, are based on an analogy between laminar and turbulent flow. This analogy is referred to as the generalized Boussinesq hypothesis. Following Boussinesq's assumption, the components of the Reynolds stress tensor are assumed to vary linearly with the mean rate of strain tensor as follows:

$$-\overline{u_i'u_j'} = \nu_t \left(\frac{\partial U_i}{\partial x_j} + \frac{\partial U_j}{\partial x_i} \right) - \frac{2}{3} k \delta_{ij} \tag{4.6}$$

where k is the turbulence kinetic energy (=$\overline{u_i'u_i'}/2$), δ_{ij} is the unit tensor (Kronecker's delta), and ν_t is the turbulent eddy viscosity. Unlike its molecular counterpart, i.e. kinematic viscosity ν, the eddy viscosity is a property of the flow not of the fluid. Therefore, it depends on flow quantities and vary in space and time. In eddy viscosity models, ν_t is expressed as the product of a turbulence length scale (ℓ_t) and a turbulence velocity scale (u_t) as follows:

$$\nu_t = \ell_t u_t \tag{4.7}$$

Depending on the approach adopted to calculate these scales, the eddy viscosity models can be classified in three general categories: zero-equation models, one-equation models and two-equation models.

4.3.1 Zero-equation models

These models, which are also called as algebraic eddy-viscosity models, specify both scales (ℓ_t,u_t) in terms of an explicit algebraic relation. Algebraic models rely on Prandtl's famous mixing-length hypothesis. For a simple 2D boundary layer flow, Prandtl (1925) proposed the following expression for the Reynolds shear stress:

$$\overline{u_1' u_2'} = \nu_t \frac{dU_1}{dx_2} = \ell_t^2 \left|\frac{dU_1}{dx_2}\right| \frac{dU_1}{dx_2} \tag{4.8}$$

For 3D flows, the mixing-length model can be generalized to give a general formulation of ν_t:

$$\nu_t = 2\ell_t^2 \sqrt{S_{ij} S_{ij}}, \ \ S_{ij} = \frac{1}{2}\left(\frac{\partial U_j}{\partial x_i} + \frac{\partial U_i}{\partial x_j}\right) \tag{4.9}$$

The mixing-length (ℓ_t) is an empirical quantity and needs to be specified using input from experiments. It is often assumed to be proportional to some characteristic length scale of the flow such as hydraulic depth.

The mixing-length assumption is valid only when the turbulence is in local equilibrium and, thus, the model is limited to calculate mean properties and turbulent shear stress for very simple 2D flows (Durbin and Reif, 2011). Therefore, the zero equation models were not used for modeling 3D turbulent flows under investigation in this work.

4.3.2 One-equation models

One-equation models employ one additional Partial Differential Equation (PDE) for the velocity scale and specify the length scale algebraically. In such models, the transport equation for the Turbulence Kinetic Energy (k) is used to calculate a local turbulence velocity scale ($u_t \approx \ k^{1/2}$). The turbulent eddy viscosity is typically computed from the following equation:

$$\nu_t = c_\mu k^{1/2} \ell_t \tag{4.10}$$

where c_μ is a constant that be determined empirically. The one-equation models lack accuracy when predicting the turbulent viscosity in complex open channel flows, therefore, they were not used for 3D numerical simulations within this study.

4.3.3 Two-equation models

As implied by their name, two-equation models employ two additional transport equations to calculate the turbulence velocity and length scales. Most such models employ the same transport equation for the turbulence kinetic energy (k) to calculate a local turbulence velocity scale. However, various two-equation closures differ from each other by the variable that is used to determine the turbulence length scale or equivalently the dissipation of the turbulence kinetic energy (ε). The actual rate of dissipation *ε* and the specific dissipation rate, ($\omega = \varepsilon/k$, dissipation per unit kinetic energy) are the most commonly used variables for defining the turbulence length scale (Rodi, 2017). Thus, in this study, only the turbulence models based on these two definitions of length scale is discussed in some details.

4.3.3.1 The k- ε model

The *k*-*ε* model is the most popular and widely used turbulence model, therefore it is incorporated in most commercial CFD codes. The model, which was originally proposed by Jones and Launder (1972) and later developed by Launder and Spalding (1974), employs a modelled equation for the turbulence kinetic energy *k* in conjunction with a transport equation for the rate of viscous dissipation *ε*. The equations of the standard *k*-*ε* model read as follows:

$$\frac{\partial k}{\partial t} + U_j \frac{\partial k}{\partial x_j} = P_k - \varepsilon + \frac{\partial}{\partial x_j}\left(\frac{\nu_t}{\sigma_k}\frac{\partial k}{\partial x_j}\right) \tag{4.11}$$

$$\frac{\partial \varepsilon}{\partial t} + U_i \frac{\partial \varepsilon}{\partial x_j} = \frac{\varepsilon}{k}(C_{\varepsilon 1}P_k - C_{\varepsilon 2}\varepsilon) + \frac{\partial}{\partial x_j}\left(\frac{\nu_t}{\sigma_\varepsilon}\frac{\partial \varepsilon}{\partial x_j}\right) \tag{4.12}$$

$$\nu_t = C_\mu\left(k^{1/2}\right)\left(\frac{k^{3/2}}{\varepsilon}\right) = C_\mu \frac{k^2}{\varepsilon} \tag{4.13}$$

where P_k is the production of the turbulence kinetic energy by mean shear, which is modeled using the following equation:

$$P_k = \nu_t\left(\frac{\partial U_i}{\partial x_j} + \frac{\partial U_j}{\partial x_i}\right)\frac{\partial U_i}{\partial x_j} \tag{4.14}$$

The standard values of the constants in the above equations are given as follows (Launder and Sharma, 1974):

$$\sigma_k = 1, \qquad \sigma_\varepsilon = 1.3, \qquad C_\mu = 0.09, \qquad C_{\varepsilon 1} = 1.44, \qquad C_{\varepsilon 2} = 1.92 \tag{4.15}$$

It should be mentioned that the modelled *ε*-equation, Eq. (4.12), is based entirely on empirical physical reasoning and dimensional arguments, (Bates, Lane, & Ferguson, 2005).

The main shortcoming of the standard *k*- *ε* model is it produces a large turbulent viscosity because of its assumption of isotropy in the turbulence fluctuations. Therefore, this model frequently produces inaccurate predictions in some turbulent fluid flows (Mohammadi and

Pironneau, 1994). In addition, the *k-ε* model equations are valid only sufficiently far from solid boundaries, where such model is found to predict the wrong behavior for *k* and *ε* near the solid walls (low Reynolds Number region). For this reason, a near wall treatment is needed for the *k-ε* models through using the wall function formulation.

As the weaknesses of the standard *k-ε* model have become known, improvements have been made to the model to improve its performance. Two of these improved *k-ε* models are the renormalization group (RNG) *k-ε* model and realizable *k-ε* model (Yakhot and Orszag, 1986 and Shih et al., 1995). The RNG *k-ε* model includes refinements that account for low-Reynolds number effects and rapidly strained flows. The realizable *k-ε* model differs from the standard *k-ε* model in containing an alternative formulation for the turbulent viscosity.

4.3.3.2 The k-ω model

The *k-ω* model solves two transport equations, one for the turbulent kinetic energy (*k*) and another for the turbulent frequency (*ω* = *ε*/*k*). The stress tensor is then computed from the eddy viscosity concept. The *ω*-equation was originally proposed by Kolmogorov (1942) who employed similar physical reasoning and dimensional arguments as those involved in the derivation of the ε-equation. However, the modern version of the *k-ω* model was proposed by Wilcox (1988), which can take the following formulations, (ANSYS Inc., 2013):

$$\frac{\partial k}{\partial t} + U_j \frac{\partial k}{\partial x_j} = \nu_t \left(\frac{\partial U_i}{\partial x_j} + \frac{\partial U_j}{\partial x_i} \right) \frac{\partial U_i}{\partial x_j} - \beta^* k\omega + \frac{\partial}{\partial x_j}\left[(\nu + \sigma^* \nu_t) \frac{\partial k}{\partial x_j} \right] \qquad (4.16)$$

$$\frac{\partial \omega}{\partial t} + U_j \frac{\partial \omega}{\partial x_j} = \alpha \frac{\omega}{k} \nu_t \left(\frac{\partial U_i}{\partial x_j} + \frac{\partial U_j}{\partial x_i} \right) \frac{\partial U_i}{\partial x_j} - \beta \omega^2 + \frac{\partial}{\partial x_j}\left[(\nu + \sigma \nu_t) \frac{\partial \omega}{\partial x_j} \right] \qquad (4.17)$$

$$\nu_t = \frac{k}{\omega} \qquad (4.18)$$

$$\alpha = \frac{5}{9}, \qquad \beta = \frac{3}{40}, \qquad \beta^* = \frac{9}{100}, \qquad \sigma = \frac{1}{2}, \qquad \sigma^* = \frac{1}{2} \qquad (4.19)$$

It should be referred that the *k-ω* model includes a low Reynolds number extension for the near-wall turbulence so that it does not require wall functions, although wall functions can be incorporated when necessary.

It is found that the two equations models, such as *k-ε* model and *k-ω* model, fail to predict any evidence of secondary flow in the case of prismatic channels such as those that are considered in this work, (Knight D., 2005). This is because these models assume that the turbulence is isotropic, whereas turbulence is known to be anisotropic. Hence, the models falling under this category were not employed for conducting the 3D simulations during this project.

4.4 Second-Moment Closure (SMC) models

In such models, also known as Reynolds Stress models (RSM), the components of the Reynolds stresses needed to close the RANS Equation, Eq. (4.5), are obtained by directly solving transport equations for the individual Reynolds stresses and an additional dissipation equation for the turbulence length scale (Rodi, 1993). The exact form of the Reynolds stress transport equations may be derived by taking moments of the instantaneous N-S equations. This process involves multiplying the exact momentum equations by a fluctuating property, and then applying time-averaging. Unfortunately, several terms in the exact equation are unknown and modeling assumptions are required to close the equations.

The exact transport equation for the Reynolds stresses in Cartesian tensor notation reads as (*e.g.* Pope, 2000):

$$\underbrace{\frac{\partial \overline{u_i' u_j'}}{\partial t} + U_k \frac{\partial \overline{u_i' u_j'}}{\partial x_k}}_{\text{(I)}} = \underbrace{P_{ij}}_{\text{(II)}} + \underbrace{DT_{ij}}_{\text{(III)}} + \underbrace{DL_{ij}}_{\text{(IV)}} + \underbrace{\Phi_{ij}}_{\text{(V)}} - \underbrace{E_{ij}}_{\text{(VI)}} \tag{4.20}$$

The various terms in the above equations can be interpreted as follows:

(I) Convection of Reynolds stresses by the mean flow.

(II) Production of turbulence (P_{ij}) by mean shear. This term sustains turbulence by extracting energy from the mean flow and is given as follows:

$$P_{ij} = -u_i' u_k' \frac{\partial U_j}{\partial x_k} - u_j' u_k' \frac{\partial U_i}{\partial x_k} \tag{4.21}$$

(III) Turbulent diffusion (DT_{ij}) due to velocity and pressure fluctuations (ten new unknowns). This term is written as follows:

$$DT_{ij} = -\frac{\partial}{\partial x_k}\left(\rho \overline{u_i' u_j' u_k'} + \overline{p' u_i'}\delta_{jk} + \overline{p' u_j'}\delta_{ik}\right) \tag{4.22}$$

(IV) Diffusion of Reynolds stresses via molecular mixing (DL_{ij}):

$$DL_{ij} = \frac{\partial}{\partial x_k}\left(\nu \frac{\partial \overline{u_i' u_j'}}{\partial x_k}\right) \tag{4.23}$$

(V) Pressure-strain redistribution term (Φ_{ij}) (six new unknowns). This term acts to drive the turbulence toward an isotropic state by redistributing the Reynolds stresses and can be expressed as follows:

$$\Phi_{ij} = \overline{p\left(\frac{\partial u_i'}{\partial x_j} + \frac{\partial u_j'}{\partial x_i}\right)} \tag{4.24}$$

(VI) Viscous dissipation of Reynolds stresses (E_{ij}) (six new unknowns):

$$E_{ij} = 2\mu \overline{\frac{\partial u_i'}{\partial x_k}\frac{\partial u_j'}{\partial x_k}} \tag{4.25}$$

Terms (I), (II) and (IV) contain only mean velocity components and the Reynolds stresses, thus, they do not require modelling when Eq. (4.20) is used to close the mean flow equation (Eq. 4.5). On the other hand, terms (III), (V) and (VI) introduce 22 new unknowns into the governing equations, thus they need to be modeled to close the equations.

There are three standard Reynolds stress models in which the ε equation has been used to provide the length scale. These are commonly known as LRR-IP, LRR-QI and SSG. The LRR-IP and LRR-QI models were developed by Launder, Reece and Rodi (1975), whereas the SSG model was developed by Speziale, Sarkar and Gatski (1991). These models only differ in the formulation used for modelling the pressure-strain term. In LRR-IP and LRR-QI models, the pressure-strain correlation is linear, while the SSG model uses quadratic relation for the pressure-strain correlation.

In addition to the standard models, which are based on ε-equation to calculate turbulence dissipation rate, there are two other Reynolds stress models that use the ω-equation as the length scale-determining equation. They are Omega Reynolds Stress (SMC-ω) and Baseline Reynolds stress models (BSL-RSM). The advantage of the ω-equation is that it allows for a more accurate near wall treatment and switch automatically from a wall function to a low-Reynolds number formulation based on the grid size.

In general, Reynolds Stress or Second Moment Closure (SMC) models physically include the effects of streamline curvature, sudden changes in the strain rate, anisotropic Reynolds stress and secondary flows (Cokijat, 1993). This means, Reynolds stress models (RSM) are more appropriate choice for flows with sudden changes in strain rate or secondary flows and may be preferred over the turbulence models based on the eddy viscosity approximation. Therefore, to simulate the turbulent flows in the open channels considered in the present work, it is necessary to implement a turbulence model which is falling under this category. Nevertheless, it was reported that for wall bounded flows, Reynolds stress models based on *ε*-transport equation (i.e. LRR-IP, LRR-Q and SSG) might have a poor performance compared with Omega Based Reynolds Stress Models (SMC- ω and BSL-RSM), (Knight, 2005). For this reason, the *ω* based RSM models have been considered during this project for performing 3D CFD numerical simulations.

4.4.1 Omega-Based Reynolds Stress Models

As explained previously, Omega Based Reynolds Stress Models are preferred over other RSM models based on *ε*-transport equation for wall bounded flow. This is because, *ω*-equation allows for a more accurate treatment to near wall region. In this type of turbulence models, the modeled equations based on the exact equation (Eq. 4.20) for the Reynolds stresses can be written as follows (ANSYS Inc., 2013):

$$\frac{\partial \rho \overline{u_i' u_j'}}{\partial t} + U_k \frac{\partial \rho \overline{u_i' u_j'}}{\partial x_k} = P_{ij} + \Phi_{ij} + \frac{\partial}{\partial x_k}\left[\left(\mu + \frac{\mu_t}{\sigma_k}\right)\frac{\partial \overline{u_i' u_j'}}{\partial x_k}\right] - \frac{2}{3}\beta' \rho \omega k \delta_{ij} \tag{4.26}$$

The pressure-strain (Φ_{ij}) tensor is modeled by the following constitutive relationship:

$$\begin{aligned}\Phi_{ij} = \beta' C_1 \rho \omega \left(-\overline{u_i' u_j'} + \frac{2}{3} k \delta_{ij}\right) - a' \left(-P_{ij} - \frac{2}{3} P \delta_{ij}\right) \\ - \beta'' \left(-D_{ij} - \frac{2}{3} P \delta_{ij}\right) - \gamma' \rho k \left(S_{ij} - \frac{1}{3} S_{kk} \delta_{ij}\right)\end{aligned} \tag{4.27}$$

The production tensor of Reynolds stresses is given by:

$$P_{ij} = -\rho \overline{u_i' u_k'} \frac{\partial U_j}{\partial x_k} - \rho \overline{u_j' u_k'} \frac{\partial U_i}{\partial x_k}; \quad P = 0.5 P_{kk} \tag{4.28}$$

The tensor D_{ij} is given by:

$$D_{ij} = -\rho \overline{u_i' u_k'} \frac{\partial U_k}{\partial x_i} - \rho \overline{u_j' u_k'} \frac{\partial U_k}{\partial x_j} \tag{4.29}$$

The coefficients for the model are:

$$\beta' = 0.09;\ \alpha' = \frac{8+C_2}{11};\ \beta'' = \frac{8C_2-2}{11};\ \gamma' = \frac{60C_2-4}{55};\ C_1 = 1.8;\ C_2 = 0.52 \tag{4.30}$$

The omega Reynolds stress model uses the following equation for *ω*:

$$\frac{\partial(\rho\omega)}{\partial t} + U_k\frac{\partial(\rho\omega)}{\partial x_k} = \alpha\rho\frac{\omega}{k}P_k + \frac{\partial}{\partial x_k}\left[\left(\mu + \frac{\mu_t}{\sigma}\right)\frac{\partial\omega}{\partial x_k}\right] - \beta\rho\omega^2 \tag{4.31}$$

The following coefficients are applying with Eq. (4.31):

$$\sigma = 2;\ \beta = 0.075;\ \alpha = \frac{5}{9} \tag{4.32}$$

The main problem with the standard *k*-*ω* model is its strong sensitivity to freestream conditions. Therefore, the Baseline Reynolds stress model (BSL-RSM) was developed, which is based on the *ω*-equation used in the Baseline (BSL) *k*-*ω* model proposed by Menter (1994).

In BSL-RSM model, the coefficients *α* and *β* of the standard *ω*-equation (Eq. 4.31), as well as the turbulent Prandtl number *σ* are blended between values from two sets of constants, corresponding to the *ω* based mode constants and the *ε* based model constants. Hence, the following equation is employed for *ω*:

$$\begin{aligned}\frac{\partial(\rho\omega)}{\partial t} &+ U_k\frac{\partial(\rho\omega)}{\partial x_k} \\ &= \alpha_3\rho\frac{\omega}{k}P_k + \frac{\partial}{\partial x_k}\left[\left(\mu + \frac{\mu_t}{\sigma_3^*}\right)\frac{\partial\omega}{\partial x_k}\right] - \beta_3\rho\omega^2 \\ &+ (1-F)2\rho\frac{1}{\sigma_3\omega}\frac{\partial k}{\partial x_k}\frac{\partial\omega}{\partial x_k}\end{aligned} \tag{4.33}$$

Based on BSL *k*-*ω* model proposed by Menter (1994), the equation for *ω* (Eq. 4.33) has two sets of constants, one corresponding to the *ω* zone:

$$\sigma_1^* = 2;\ \sigma_1 = 2;\ \beta_1 = 0.075;\ \alpha_1 = 0.553 \tag{4.34}$$

and the other to the *ε* zone:

$$\sigma_2^* = 0.856;\ \sigma_2 = 1;\ \beta_2 = 0.0828;\ \alpha_2 = 0.440 \tag{4.35}$$

The two sets of coefficients are blended by smooth linear interpolation using the weight function *F*, (Menter 1994):

$$\phi_3 = F\phi_1 + (1-F)\phi_2 \tag{4.36}$$

where $F = tanh\,(arg^4)$ with:

$$arg = min\left\{max\left(\frac{\sqrt{k}}{\beta'\omega y}, \frac{500\upsilon}{y^2\omega}\right), \frac{4\rho k}{CD_{k\omega}\sigma_{k\varepsilon}y^2}\right\} \tag{4.37}$$

and

$$CD_{k\omega} = max\left(2\rho\frac{1}{\sigma_{k\varepsilon}\omega}\frac{\partial k}{\partial x_j}\frac{\partial \omega}{\partial x_j}, 10^{-10}\right) \tag{4.38}$$

The turbulent viscosity (μ_t) in the diffusion terms of the main equations 4.26 and 4.33 is calculated in the same way as in the Wilcox model (1988):

$$\mu_t = \rho\frac{k}{\omega} \tag{4.39}$$

The Omega-Based Reynolds stress models have been used in simulating different open channel flow cases and its predictions were in a very good agreement with the measurements, e.g. Cokljat & Younis (1995a & 1995b); Morvan et al., (2002); Kang & Choi (2004); Jing et al., (2009); and Filonovich et al., (2015). However, BSL-RSM model is preferred over the Omega Reynolds stress model in engineering applications that includes free surface flow problems. For this reason, BSL-RSM model has been only used in the present study.

4.5 Setting up and running the CFD simulations

4.5.1 The software CFX

The commercially available ANSYS-CFX software (2013) has been used to solve the governing equations described above. ANSYS-CFX is a general purpose Computational Fluid Dynamics (CFD) software that combines an advanced solver with powerful pre- and post-processing capabilities. The solver uses an unstructured Finite Element based Finite Volume method for both structured and unstructured meshes. The CFD package used in this study consists of three software modules that take a geometry, mesh and physical information required to perform a CFD analysis and pass them to the CFX-solver to solve the governing equations and tender the flow field. An example of CFX input file for one of the flow simulations performed in the present research is given in Appendix B. The results of simulations can be processed and displayed by Post-processor component. Data flow through CFX package is shown in Figure 4.1.

All categories of turbulence models are available for use in the CFX software like eddy-viscosity two equations models and RSM models. As was discussed in a previous section, BSL-RSM model is preferred over the others due to its accuracy in predicting the secondary currents. Therefore, this type of turbulence model was selected to simulate the turbulence flows considered in this project. The following subsections give details of the procedure used for applying ANSYS-CFX packages to perform 3D CFD simulations.

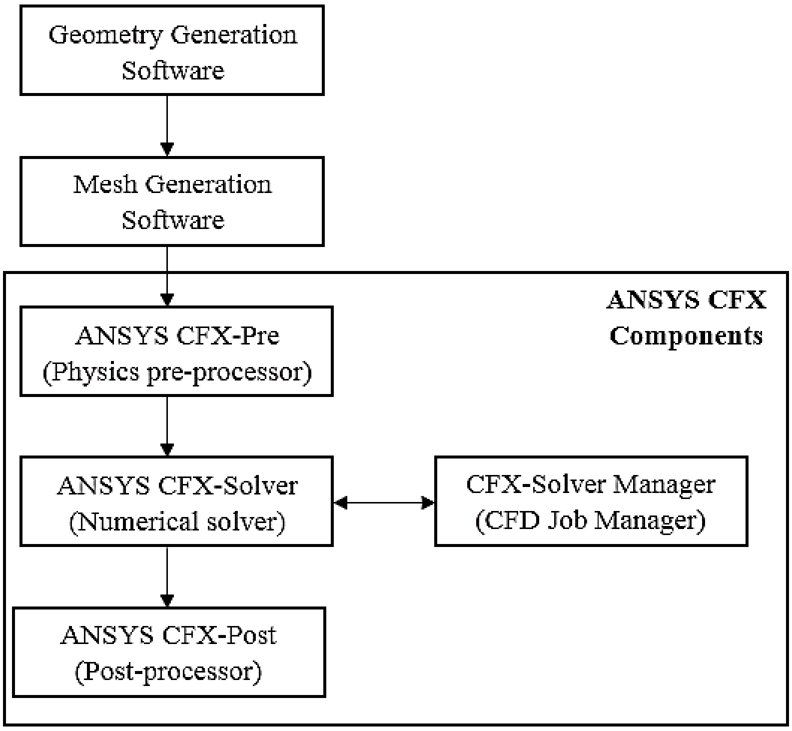

Figure 4.1 Data flow by CFX software.

4.5.2 Constructing the Geometry

3D numerical simulations were performed on two computational geometries for modelling the rectangular channel flows (investigated in first sets of experiments), and the compound channel flows (investigated in second set of experiments). Geometries of both models were constructed by using Geometry element in workbench of ANSYS 15.0. The approach adopted in creating the geometry was to create the upstream cross-section in the first place and then extended it in the streamwise direction to construct a prismatic channel.

The rectangular geometry, which was constructed in the CFX-Pre. component, had six faces as shown in Figure 4.2a. These faces would be utilized for applying the boundary conditions to the computational domain. In all cases, the width of the domain (Ly) was fixed at 0.3m, i.e. identical to the channel width, and its length in streamwise direction (Lx) was

0.1m. The depth of the domain (*Lz*) was varied from 0.06m to 0.2m according to its magnitude in the corresponding experiment.

The compound geometry, which was constructed for simulating compound channel flows, had eight faces as illustrated in Figure 4.2b. The dimensions of the computational domain were similar to those of compound sections used for experiments CS, CT and CR. The main channel was 0.2m wide, while the width of the floodplain was 0.1 m. The height of the internal wall (*h*) between the main channel and the floodplain was 0.06 m in CS and CT cases and 0.075m in CR cases. The total depth of the domain (*H*) was varied to provide the range of relative depth ratios (*Dr*) from 0.25 to 0.50, covering the same range of *Dr* values as that in the experiments.

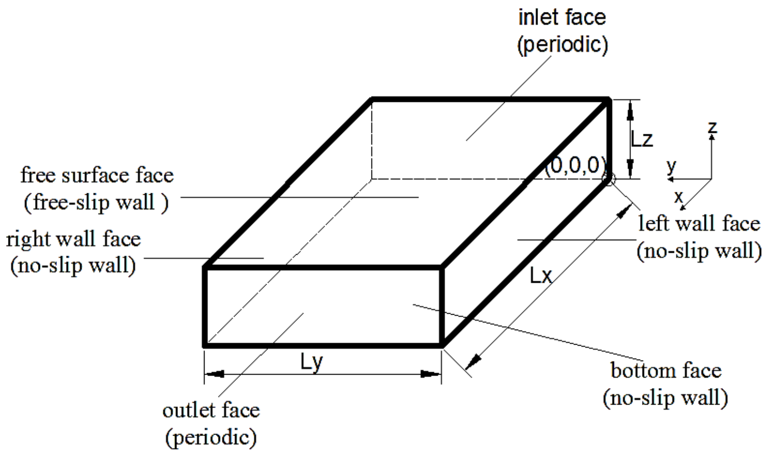

(a) Rectangular channel simulations

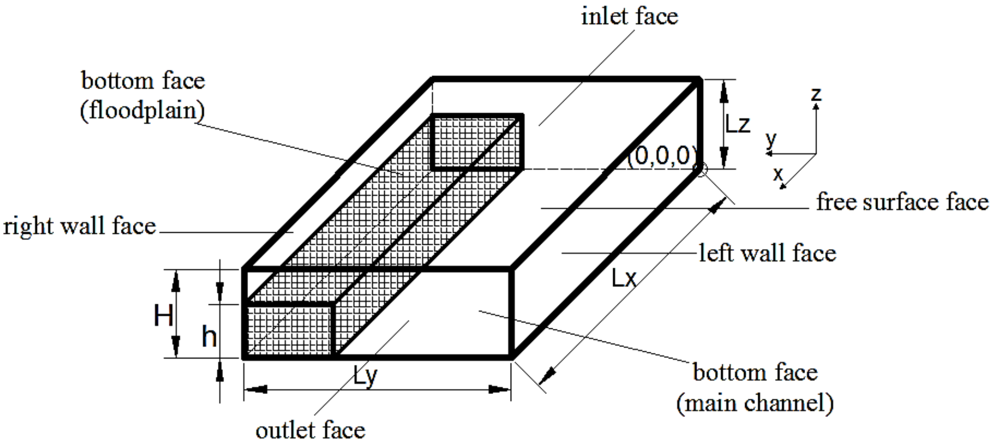

(b) Compound channel simulations

Figure 4.2 Schematic of domain geometry and boundary conditions.

4.5.3 Generating the mesh

The mesh generation involves subdividing the geometry into smaller elements known as cells. Hexahedral cells were used for the generation of meshes in all simulations, where the domain is represented by series of six-sided polyhedron with rectangular faces. This type of mesh cells was utilized because it is relatively easy to implement with regular geometries such as the cases considered in this work.

To ensure that the mesh does not negatively influence the accuracy of simulation results, a mesh or grid independence study was carried out first. During this study, three mesh structures were generated for the biggest computational domains of rectangular and compound channels, i.e. the cases S20 and CS0.50, as shown in Table 4.1.

Table 4.1 Mesh structures used for grid independence study.

Case simulated	**Number of Nodes**		
	Coarse mesh	**Medium mesh**	**Fine mesh**
Rectangular Channel (S20)	129830	148967	167761
Compound Channel (CS0.50)	96179	112209	134651

Small discrepancies were observed after comparing the predicted results for key parameters (mean streamwise velocity and Reynolds stresses) between the medium and fine mesh. The maximum differences between these two mesh levels were less than 3% for the rectangular channel simulation and 3.2% for compound channel simulation. Therefore, it could be concluded that the fine mesh level was sufficient for obtaining grid-independent solutions. All results predicted by CFD modelling were obtained based upon the fine mesh. An illustration of the mesh structures generated for both channel configurations is shown in Figure 4.3 and Figure 4.4.

In addition, it is important to provide a sufficiently fine mesh in the regions where the flow may experience rapid change in key variables such as velocity. For example, sufficient mesh resolutions are required near walls to resolve the large change in velocity in the wall normal direction. A non-dimensional distance (z^+) is often used to define mesh so that the z^+ for the cells nearest the wall lie within a certain range. z^+ is a function of the normal distance from the wall to the first node, the flow velocity and viscosity. The specific criteria of the z^+ depends upon the turbulence model that is selected to make the flow modelling. When using low-*Re* models (such as turbulence models based on the ω-equation), the average $z^+ < 2$ should be adopted to ensure capturing the laminar sub-layer. and low-Reynolds number grids, without a loss in accuracy. This certainly helps in reducing the level of the refinement.

On the other hand, when using wall function models (such as turbulence models based on the ε-equation), the z^+ value should ideally be above 15 to avoid incorrect modelling of the buffer layer and the laminar sub-layer, (Bates, Lane, & Ferguson, 2005). However, CFX software offers the automatic wall treatment which allows a gradual switch between wall functions.

Based on the above considerations, the automatic treatment was applied with BSL-RSM turbulence model in this work to reduce the resolution requirements. Also, the generated mesh was fined to a level so that z^+ was around 15 to ensure that the first grid point is located within the log-law region when wall function is implemented.

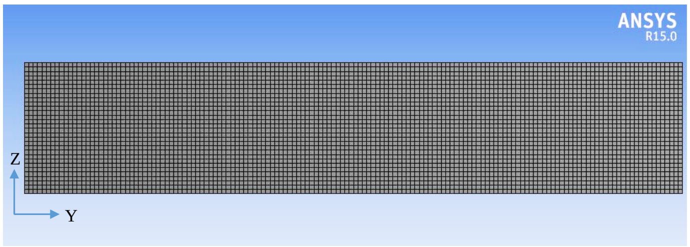

(a) Mesh for cases: S-6, T-6 and R-6

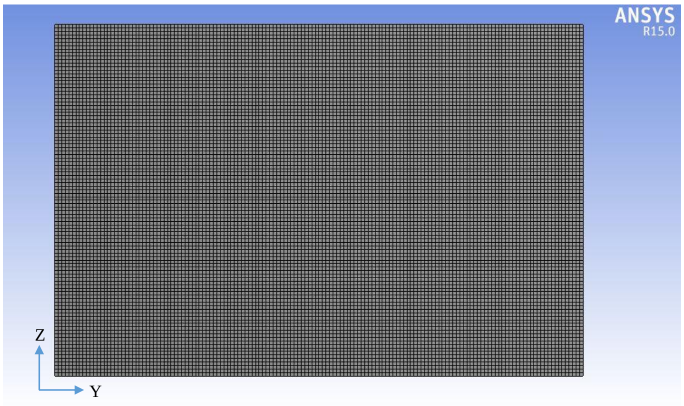

(b) Mesh for cases: S-20, T-20 and R-20

Figure 4.3 Illustrative mesh cross section for rectangular channel cases

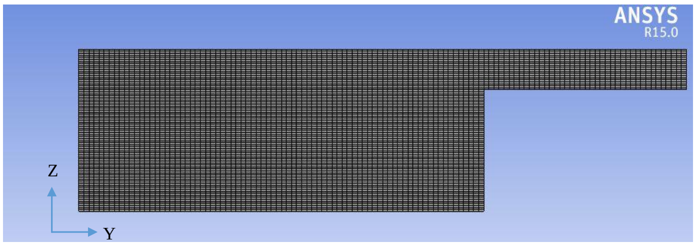

(a) Mesh for cases: CS0.25, CT0.25 and CR0.25

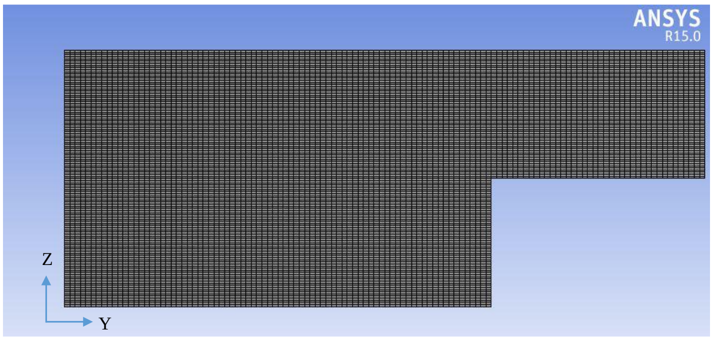

(b) Mesh for cases: CS0.5, CT0.5 and CR0.5

Figure 4.4 Illustrative mesh cross section for compound channel cases

4.5.4 Defining the boundary conditions

Boundary conditions is required on all the boundaries of the computational domain to set the properties of domain surfaces, and to fully define the physical characteristics of the flow domain. The boundary conditions applied to the domain surfaces must reflect the actual conditions of the flow that is being modelled, although this task is not always simple. Also, any inaccuracy in estimating the boundary conditions may affect the accuracy and even the correctness of the numerical solution. If the boundary conditions are not applied correctly, it may cause the effort of choosing a sophisticated turbulence model to collapse, (Bates, Lane, & Ferguson, 2005). Therefore, care needs to be taken over the choice of the boundary conditions to be imposed for each surface of the computational domain.

As indicated previously, two series of simulations have been conducted during this project, the first series were to simulate the uniform flow in rectangular channels, while the second series were for modelling the uniform flow in compound channels. The simulations conducted on these uniform flow cases were based on modelling the flow as a single phase of water. The boundary conditions implemented for the simulations of uninform flows in both the rectangular and compound channels are summarized in Table 4.2.

4.5.4.1 Inlet and outlet locations

The simulations conducted as part of this project are based on modelling a uniform fully developed flow (i.e. zero gradients of all flow variables, except for the pressure). Under such flow conditions, it can be assumed that the flow is statistically homogenous in streamwise direction (i.e. flow characteristics at upstream and downstream boundaries are coincident). Thus, for the inlet and outlet locations of computational domain, the periodic boundary conditions were applied in the streamwise direction. As a consequence of employing the periodic boundary conditions the solution obtained was not varying along the length of the flow domain. Therefore, much shorter channel lengths coupled with fewer cells were used along the streamwise direction.

Table 4.2 Boundary conditions applied for uniform flow simulations

Location	**Boundary condition applied**
Inlet (flow in)	Periodic boundary condition with constant pressure gradient (*dp/dx*)
Outlet (flow out)	
Right sidewall	No-slip wall (smooth)
Left sidewall	No-slip wall (smooth)
Bed wall	No-slip wall (smooth or rough depending on the case being simulated)
Free surface	Free-slip wall with zero gradient for turbulent kinetic energy (k).

In the periodic motion, the flow is driven by a constant pressure gradient (dp/dx). Therefore, a constant pressure gradient was applied as a momentum source (M_x) in the governing equations to drive the flow in the streamwise direction, as follows:

$$dp/dx \equiv M_x = \rho g S_o \tag{4.40}$$

By applying the periodic boundary condition, the flow depth was specified at the same values recorded in the experiments while no value of discharge was needed to be assigned. In this way, a velocity distribution calculated by the CFD will be consistent with the flow depth, channel shape and wall roughness specified previously. The discharge obtained from the predicted velocity was then compared with the experimentally measured value. The differences between the computed and measured flow rates was found to be less than (∓3%).

4.5.4.2 Treatment of free surface

For steady fluid flows, an approximate fixed lid approach can be specified to represent the water surface. Hence, this approach was adopted so that the position of the free surface can be specified at the depth measured experimentally. In all simulations conducted in this study, the free-slip condition with the modified free surface treatment proposed by Rodi (1993) was imposed on the free surface boundary. Through this approach, the value of dissipation (ε) at the free surface is specified based on the free surface value of the turbulent kinetic energy (k) obtained from the zero-gradient condition. The reason for imposing this type of boundary condition was to reproduce the effect of the velocity dip. Also, using this boundary condition helps to mimic the damping of turbulent fluctuations by the surface.

4.5.4.3 Treatment of channel walls

For the channel walls, including the bed and side walls, the no-slip wall boundary conditions were imposed for all test cases simulated in the present work. However, the details of the wall boundary conditions were different depending upon the type of wall surface, which should be set either smooth or rough. For hydraulically rough walls, the equivalent sand-grain roughness (K_s) was required as an input parameter for proper modelling of the surface roughness effects. For the cases of hydraulically smooth walls, the contribution of sand grain size to roughness was negligible, therefor the sand-grain roughness was not specified. The method by which the CFX software models the effect of wall roughness is presented in the next section.

4.5.5 Modelling of roughness effect

Surface roughness have a significant effect on flow computations, practically for the simulation of rough cases. The appropriate modelling of surface roughness effects is therefore essential for accurate predictions. The roughness causes the wall shear stress to increase due to increase in turbulence production. Furthermore, the wall roughness breaks up the viscous sub-layer in turbulent flows, particularly in fully rough flows. To account for these effects, the CFX has developed a rough wall treatment based on the formulation of the wall law for rough flows, with downward shift in the logarithmic velocity profile as shown in Figure (4.5). The law of wall for rough flow is given by CFX as follows:

$$U^{+} = \frac{1}{k}\ln(z^{+}) + B - \Delta B \tag{4.41}$$

where $U^+ = U/u_*$, $z^+ = zu_*/\nu$, k = 0.41 is the von Karman constant and B = 5.2. ΔB is the shift in the velocity profile due to the roughness effect. In CFX code the downward shift (ΔB) can be calculated based on the equivalent sand-grain roughness height (K_s) as follows:

$$\Delta B = \frac{1}{k} ln(1 + 0.3K_s^+) \tag{4.42}$$

where K_s^+ is the dimensionless roughness height and is defined as:

$$K_s^+ = \frac{K_s u_*}{\nu} \tag{4.43}$$

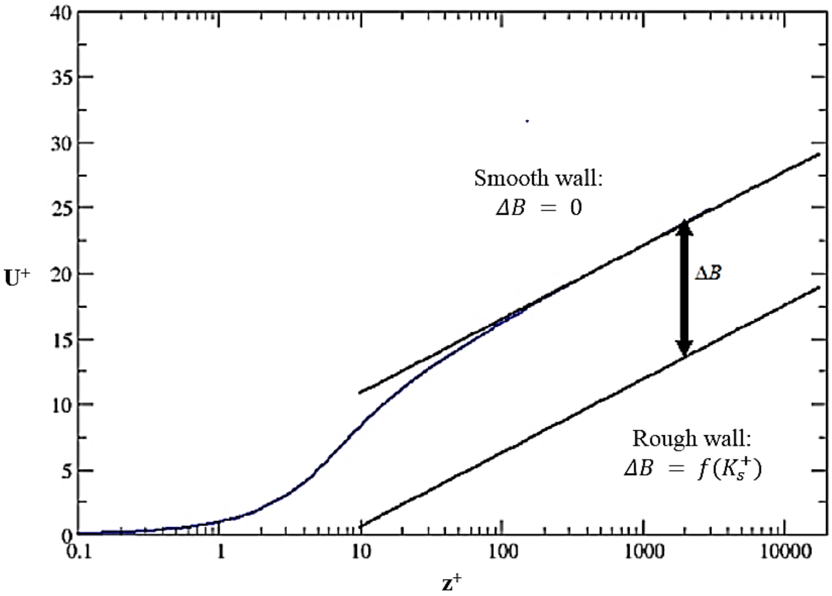

Figure 4.5 Downward Shift of the Logarithmic Velocity Profile.

In addition to modifying the wall function for rough flows, the distance of the nearest grid to the wall is also shifted by 50% of the height of the roughness elements to account for the blockage effect caused by the surface roughness (ANSYS Inc., 2013).

In this study, the automatic rough wall treatment provided by CFX code was used for modelling turbulence and roughness effects. Based on this way, the viscous sublayer formulation has either a limited or neglected influence on the near wall treatment for rough walls. For rough flows considered in the present work, the equivalent sand-grain roughness height was needed to be specified as input in CFX solver. Therefore, roughness height of K_s = 1.5 mm is used in transitional flow simulations and 8 mm in rough flow simulations. The input roughness parameters K_s have the same values as that was estimated in the corresponding transitional and rough flow experiments described earlier in chapter 3.

4.5.6 Solver control and convergence criteria

ANSYS CFX uses an element-based finite volume method, which first involves discretizing the spatial domain using a mesh. The mesh is then used to construct finite volumes, which are used to conserve relevant quantities such as mass, momentum, and energy. In all CFD simulations performed in the present work, High Resolution scheme was selected to calculate the advection terms in the discrete finite volume equations. This higher order numerical scheme was used because it gives the most accurate result with no difficulties in obtaining a converged solution (ANSYS Inc., 2013).

Because all test cases considered here were modelled as steady state problems, therefore, unsteady effects have been averaged and time-dependent solutions were not obtained. However, an initial condition was needed as an initial guess to the flow conditions to make the solver start the simulation. To initialize the flow, a mean velocity was specified over the whole inlet plane. The inlet mean velocities were taken from the experimental average values. In addition, a medium turbulence intensity (5%) was defined in the inlet of the flow domain as the initial conditions for the turbulence. This option is recommended by previous studies when any information about the inlet turbulence is not available (Kang & Choi, 2004; Jing et al., 2009 and Filonovich et al., 2015). Also, the automatic time step calculation algorithm that is part of the software was used to control and calculate the time scale automatically by the solver. Although the automatic option may lead to a slower convergence, but it was selected because this option tends to be conservative and the appropriate time scale is more difficult to be obtained manually.

Before the solution stage, convergence criteria need to be defined and key flow quantities should be specified to monitor during the simulation. In this study, the reliable convergence was considered to be achieved when the root mean square (RMS) residual of main variables in mass and momentum equations dropped below the residual target value. A low residual target ($<10^{-7}$) was defined for solution convergence in all simulations. Using such low convergence criteria was important for the secondary terms to stabilize and required to obtain accurate solution for turbulence shear stresses. In addition, the average velocity (U) and average shear stress on the channel walls (τ_o) were also monitored and used as additional convergence criteria. The monitor points specified within CFX needed to reach nearly a constant value to assume that the simulation is met all convergence criteria. Figure 4.6 and Figure 4.7 show convergence plots for some of the simulations conducted in this work.

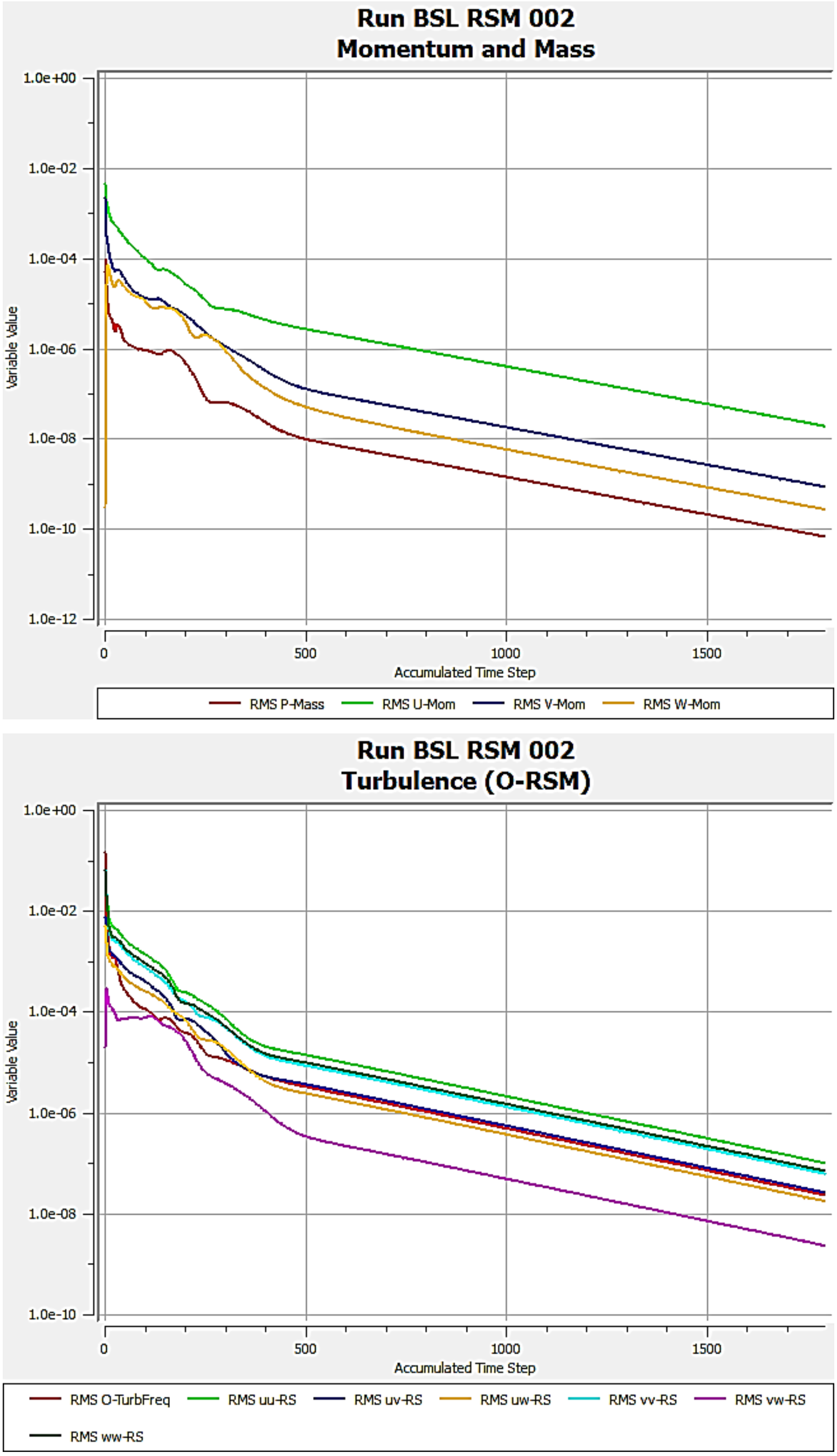

Figure 4.6 The convergence criteria: Root mean square (RMS) residual.

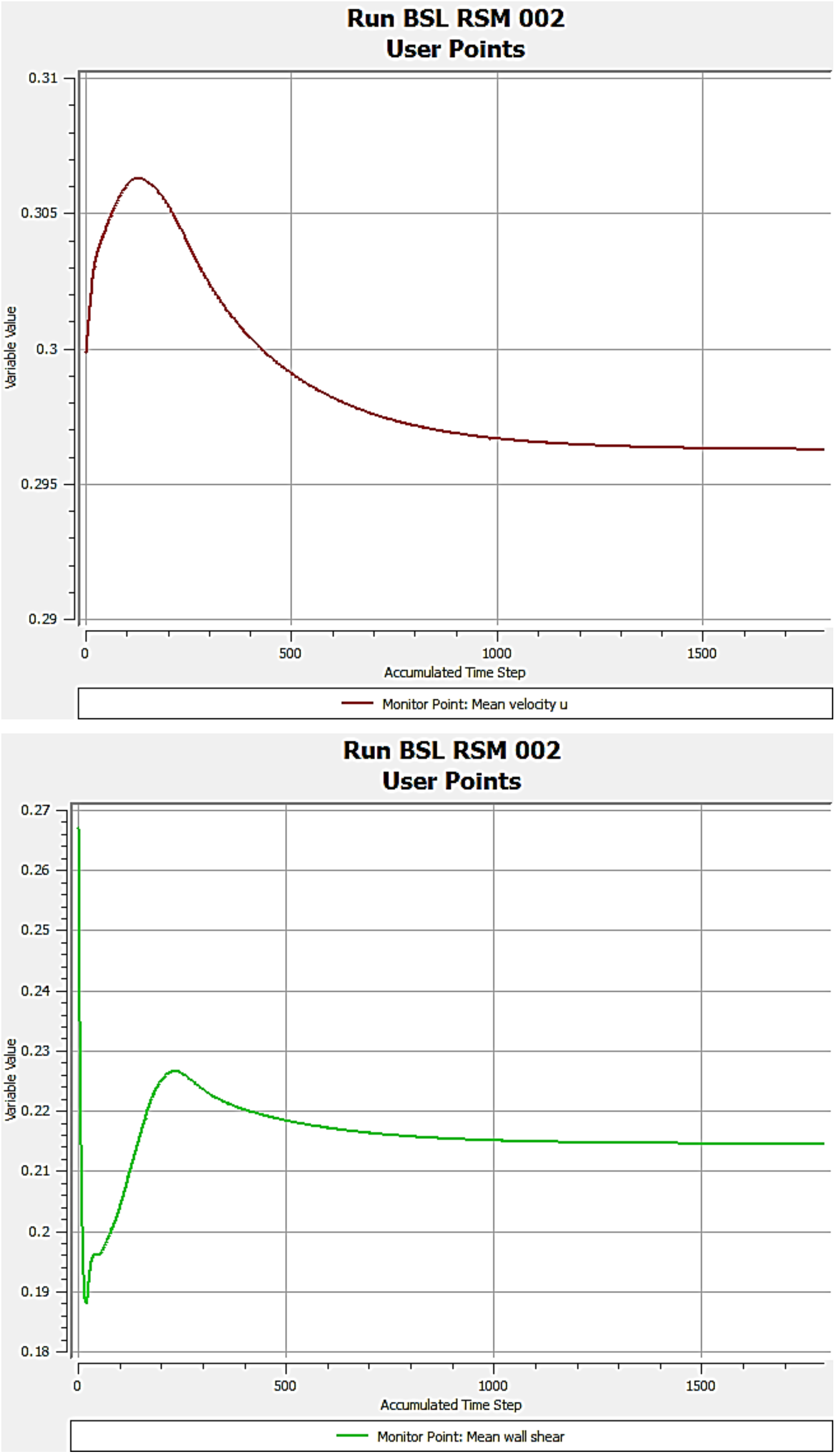

Figure 4.7 The convergence criteria: Monitor points for mean velocity and wall shear.

Chapter 5

Analytical Models for Velocity Distributions

5.1 Introduction

In this chapter, the formulation and analysis of various models based on the analytical solution of the simplified Navier-Stokes equations are given. These models are widely applied to engineering problems in open channel flows because of their simplicity compared to the 3D modeling approaches. The effects of bed friction, vertical and lateral turbulence and secondary flows are substantially considered when the analytical models are derived. Therefore, the focus in this chapter is on the methods and assumptions used to model the effects of these three features of the flow.

5.2 Analytical models for velocity distribution in rectangular channels

5.2.1 Simplified Reynolds Averaged Navier–Stokes Equations

For steady state flow the RANS momentum in the streamwise direction and continuity equation can be written relative to the frame of reference shown in Figure 4.2, as follows:

$$\begin{aligned} U\left(\frac{\partial U}{\partial x}\right)+V\left(\frac{\partial U}{\partial y}\right)+W\left(\frac{\partial U}{\partial z}\right) &\\ = gS_o+\nu\left(\frac{\partial^2 U}{\partial x^2}+\frac{\partial^2 U}{\partial y^2}+\frac{\partial^2 U}{\partial z^2}\right)+\frac{\partial}{\partial x}(-\overline{u'u'}) &\\ +\frac{\partial}{\partial y}(-\overline{u'v'})+\frac{\partial}{\partial z}(-\overline{u'w'}) & \end{aligned} \tag{5.1}$$

$$\frac{\partial U}{\partial x}+\frac{\partial V}{\partial y}+\frac{\partial W}{\partial z}=0 \tag{5.2}$$

where U, V, and W = mean velocity in the streamwise (x), lateral (y), and vertical (z) directions, respectively; $(-\overline{u'u'})$, $(-\overline{u'v'})$, and $(-\overline{u'w'})$ = Reynolds stress tensor components; and ν = fluid kinematic viscosity. Assuming a uniform and fully developed flow, Eqs. (5.1) and (5.2) can be easily combined to lead to (Yang et al., 2004):

$$\left(\frac{\partial UV}{\partial y}\right)+\left(\frac{\partial UW}{\partial z}\right)=gS_o+\nu\left(\frac{\partial^2 U}{\partial y^2}+\frac{\partial^2 U}{\partial z^2}\right)+\frac{\partial}{\partial y}(-\overline{u'v'})+\frac{\partial}{\partial z}(-\overline{u'w'}) \tag{5.3}$$

Considering the central part of the channel, the vertical gradients ($\partial/\partial z$) are dominating and then all derivatives with respect to y can be assumed negligible. Therefore Eq. (5.3) can be simplified as follows:

$$\frac{\partial UW}{\partial z} = gS_o + \nu\frac{\partial^2 U}{\partial z^2} + \frac{\partial}{\partial z}(-\overline{u'w'}) \tag{5.4}$$

Integrating Eq. (5.4) in the vertical direction over an interval from a point z to the entire depth h and rearranging its terms yields:

$$\nu\frac{\partial U}{\partial z} - \overline{u'w'} - UW = gS_o(h - z) \tag{5.5}$$

When Eq. (5.4) was integrated to get Eq. (5.5), the boundary conditions applied at the free surface were: vertical component, W, equals zero and both the differentiation term and the velocity fluctuation in vertical direction was set to zero at h.

Since for large values of z the viscous shear stress ($\nu\,\partial U/\partial z$) is small compared to the turbulent shear stress ($-\overline{u'w'}$) (Absi, 2008), Eq. (5.5) becomes:

$$-\overline{u'w'} = gS_o(h - z) + UW \tag{5.6}$$

Equation (5.6) can be rewritten after the shear velocity u_* is defined as a function of the bed slope ($\sqrt{ghS_o}$):

$$-\overline{u'w'} = u_*^2\left(1 - \frac{z}{h}\right) + UW \tag{5.7}$$

Equation (5.7) can further be simplified by dividing with u_*^2 :

$$\frac{-\overline{u'w'}}{u_*^2} = \left(1 - \frac{z}{h}\right) + \frac{UW}{u_*^2} \tag{5.8}$$

In most simplified RANS approaches, two additional assumptions were often imposed on Eq. (5.7) to get an analytical solution. One for approximating the secondary flow term (UW) and the other for modelling the Reynolds shear stress ($-\overline{u'w'}$).

Due to the secondary flow effect, the maximum velocity come to below the water surface. This phenomenon, which is called the velocity dip, occurs in narrow open-channels where the aspect ratio of the channel width to water depth (*B/h*) < 5. Thus, to account for the influence of secondary currents on the velocity distribution calculation, the analytical model should be capable of predicting the velocity-dip feature. Furthermore, Yang et al. (2004) found that secondary current velocity w in the outer region is generally in the downward direction, thus the third term in Eq. (5.8) can be modelled using a linear relationship, i.e.,

$$\frac{UW}{u_*^2} \approx \mu \frac{z}{h} \tag{5.9}$$

where μ is a coefficient representing the effect of secondary current on velocity distribution and called dip-correction parameter.

On the other hand, the Boussinesq assumption is frequently used to model the Reynolds shear stress as following:

$$-\overline{u'w'} = \nu_t \frac{dU}{dz} \tag{5.10}$$

where ν_t is the eddy viscosity. Substituting Eq. (5.9) and Eq. (5.10) into Eq. (5.8), the following partial differential equation (PDE) is obtained:

$$\frac{dU}{dz} = \frac{u_*^2}{\nu_t}\left[\left(1 - \frac{z}{h}\right) - \mu \frac{z}{h}\right] \tag{5.11}$$

Equation (5.11) is the simplified form to RANS equations which is used as a basic equation to obtain the analytical solution for the mean velocity profile in rectangular channels with uniform flows. Depending upon the models by which the eddy viscosity is expressed, different analytical formulations for calculating the velocity distribution can be obtained from the simplified RANS equation, Eq. (5.11). The analytical models based on the simplified RANs equation are known as dip-modified laws, because they can be used to predict the velocity dip phenomenon in open channels.

5.2.2 Dip-modified laws

5.2.2.1 Dip-modified log law (DML-law)

Velocity distribution can be obtained by integrating Eq. (5.11) with a known profile for the eddy viscosity $\nu_t(z)$. Parabolic model for the eddy viscosity can be employed to define $\nu_t(z)$ in Eq. (5.11). The widely used expression of the parabolic model is:

$$\nu_t = \kappa u_* z\left(1 - \frac{z}{h}\right) \tag{5.12}$$

where k is the Von Karman constant (≈0.41). By using Eq. (5.12), Eq. (5.11) can be expressed as follows:

$$\frac{dU}{dz} = \frac{u_*}{kz}\left[1 - \mu\frac{\left(\frac{z}{h}\right)}{\left(1 - \frac{z}{h}\right)}\right] \tag{5.13}$$

Integration of Eq. (5.13) gives:

$$\frac{U}{u_*} = \frac{1}{k}\left[\ln\left(\frac{z}{z_o}\right) + \mu\ln\left(\frac{1 - \frac{z}{h}}{1 - \frac{z_o}{h}}\right)\right] \tag{5.14}$$

where z_o is the distance from the bed at which the velocity is hypothetically equal to zero. Since $z_o/h \ll 1$, with defining $z/h = \xi$ and $z_o/h = \xi_o$, Eq. (5.14) can be simplified further to give:

$$\frac{U}{u_*} = \frac{1}{k}\left[ln\left(\frac{\xi}{\xi_o}\right) + \mu\, ln(1 - \xi)\right] \tag{5.15}$$

Equation (5.15) is known as dip-modified log law (DML-law), which was first suggested by Yang et al. (2004). DML-law predicts the velocity-dip phenomenon by the term $\mu\, ln(1 - \xi)$, which includes the dip-correction parameter μ. This law returns into the classical log law if $\mu = 0$.

5.2.2.2 Dip-modified log wake law (DMLW-Law)

Instead of parabolic model, the approximation for eddy viscosity distribution given by Nezu and Rodi (1986) can be employed in the simplified RANS Equation, Eq. (5.11), to drive a law for the velocity distribution. Nezu and Rodi (1986) suggested their model for eddy viscosity based on the log-wake law and it can be written as:

$$\nu_t = \kappa u_* h\left(1 - \frac{z}{h}\right)\left[\frac{h}{z} + \pi\Pi\sin\left(\pi\frac{z}{h}\right)\right]^{-1} \tag{5.16}$$

where Π is the wake strength parameter. In the outer region (*z/h* > 0.2), the log-law deviates from experimental data, and this deviation is accounted for by adding Coles (1956) wake function. Hence, it is thought that using the eddy viscosity model based on the wake function could probably improve the performance of dip modified law that is derived from the simplified RANS equation. Using eddy viscosity model given by Nezu and Rodi (1986), i.e. Eq. (5.16), instead of the parabolic profile, the ordinary differential equation, Eq. (5.11), for velocity distribution leads to:

$$\frac{dU}{dz} = \frac{u_*}{kh}\left[1 - \mu\frac{\left(\frac{z}{h}\right)}{\left(1-\frac{z}{h}\right)}\right]\left[\frac{h}{z} + \pi\Pi\sin\left(\pi\frac{z}{h}\right)\right] \tag{5.17}$$

In dimensionless form, Equation (5.17) can be rewritten as follows:

$$\frac{dU}{d\xi} = \frac{u_*}{k}\left(1 - \mu\frac{\xi}{1-\xi}\right)\left[\frac{1}{\xi} + \pi\Pi\sin(\pi\xi)\right] \tag{5.18}$$

Integration of Eq. (5.18) for $\xi_o \ll 1$ gives:

$$\frac{U}{u_*} = \frac{1}{k}ln\left(\frac{\xi}{\xi_o}\right) + \frac{2\Pi}{k}\sin^2\left(\frac{\pi}{2}\xi\right) + \frac{\mu}{k}ln(1-\xi) - \frac{\mu\pi\Pi}{k}\int_{\xi_o}^{\xi}\frac{\xi}{1-\xi}\sin(\pi\xi)\,d\xi \tag{5.19}$$

Equation (5.19) is called the full dip-modified-log-wake law (fDMLW-law), in which the last term on the right-hand side needs to be integrated using the trapezoidal or Simpson rules. For wide open-channels (*Ar* > 5), $\mu \to 0$, and the fDMLW-law reverts to log-wake law because the 3rd and 4th terms will vanish (Absi, 2011). As the 4th term is relatively small compared with the other terms in Eq. (5.19), this term can be considered negligible, giving the expression for the velocity distribution as:

$$\frac{U}{u_*} = \frac{1}{k}ln\left(\frac{\xi}{\xi_o}\right) + \frac{2\Pi}{k}\sin^2\left(\frac{\pi}{2}\xi\right) + \frac{\mu}{k}ln(1-\xi) \tag{5.20}$$

Equation (5.20) is referred as the simple dip-modified-log-wake law (sDMLW-law). This equation differs from the (fDMLW-law, Eq. 5.19) only by truncating the integral term for simplicity. The DMLW-laws have the advantage of accounting for the combined effects of the secondary current and the wake turbulence strength in the outer region. Therefore, in 3D open-channel flows with secondary currents, the DMLW-laws may predict the velocity distribution better than DML-law.

5.2.3 Model parameters

In this study, the predictive capability of the analytical DMLW-law, given by Eq. (5.20), is further assessed against experimental data for rectangular channels with different roughness regimes. Based on an analysis of eddy viscosity distributions and secondary currents obtained from 3D CFD simulations, the model parameters (i.e. wake strength Π and dip-correction parameter μ) were calibrated to improve the performance of the analytical model derived from the simplified RANS equation, Eq. (5.11).

5.3 Analytical model for depth-averaged velocity in compound channels

5.3.1 Depth-Averaged Reynolds Averaged Navier–Stokes Equations

In a prismatic open channel, the equation for the stream wise component of momentum in a steady flow may be combined with the continuity equation to give:

$$\rho\left[\frac{\partial UV}{\partial y}+\frac{\partial UW}{\partial z}\right]=\rho g S_o+\frac{\partial}{\partial y}(-\rho\overline{u'v'})+\frac{\partial}{\partial z}(\rho\overline{u'w'}) \tag{5.21}$$

where (U, V, W) are the mean velocity components in the x (stream wise), y (lateral) and z (normal to bed) directions respectively; (u', v', w') are turbulent fluctuations of velocity with respect to the mean, ρ is the density of water, g is the gravitational acceleration and S_o is the bed slope. The depth-averaged momentum equation can be obtained by integrating Eq. (5.21) over the water depth, H, assuming $W(H) = W(0) = 0$, as given by Shiono and Knight (1991):

$$\rho g H S_o+\frac{\partial H\bar{\tau}_{yx}}{\partial y}-\tau_b\sqrt{1+\frac{1}{s^2}}=\frac{\partial[H(\rho UV)_d]}{\partial y} \tag{5.22}$$

in which τ_b is the bed shear stress, s is the side slope (1:s = vertical: horizontal), and

$$(\rho UV)_d=\frac{1}{H}\int_0^H(\rho UV)dz \quad\text{and}\quad \bar{\tau}_{yx}=\frac{1}{H}\int_0^H(-\rho\overline{u'v'})dz \tag{5.23}$$

Based on the commonly used eddy viscosity assumptions, the depth-averaged Reynolds stress ($\bar{\tau}_{yx}$) can be given as follows:

$$\bar{\tau}_{yx}=\rho\bar{\varepsilon}_{yx}\frac{\partial U_d}{\partial y} \quad\text{and}\quad \bar{\varepsilon}_{yx}=\lambda u_* H \tag{5.24}$$

where $\bar{\varepsilon}_{yx}$ is depth-averaged eddy viscosity, λ is the dimensionless eddy viscosity coefficient and u_* (=$\sqrt{\tau_b/\rho}$) is the local shear velocity. Using the customary flow resistance relationship that relates local boundary shear stress (τ_b) with the depth-mean velocity (U_d) and the Darcy-Weisbach friction coefficient (f), τ_b can be computed by:

$$\tau_b = \rho \frac{f}{8} U_d^2 \quad \text{or} \quad U_* = \sqrt{\frac{f}{8}} U_d \tag{5.25}$$

Then, substituting Eq. (5.24) and Eq. (5.25) into (5.22) yields:

$$\rho g H S_o - \rho \frac{f}{8} U_d^2 \sqrt{1 + \frac{1}{s^2}} + \frac{\partial}{\partial y}\left[\rho \lambda H^2 \sqrt{\frac{f}{8}} U_d \frac{\partial U_d}{\partial y}\right] = \frac{\partial}{\partial y}[H(\rho UV)_d] \tag{5.26}$$

Based on experimental results, the shear stress due to secondary flow, $(\rho UV)_d$, is assumed to vary approximately linearly with respect to y (Shiono and Knight, 1991). Therefore, the lateral gradient of the secondary flow force per unit length may be written as:

$$\frac{\partial}{\partial y}[H(\rho UV)_d] = \Gamma \tag{5.27}$$

where Γ is a dimensionless secondary flow parameter which is different for each part of the flow. Considering Γ defined by Eq. (5.27), the final depth-averaged equation for RANS can be obtained as follows:

$$\rho g H S_o - \rho \frac{f}{8} U_d^2 \sqrt{1 + \frac{1}{s^2}} + \frac{\partial}{\partial y}\left[\rho \lambda H^2 \sqrt{\frac{f}{8}} U_d \frac{\partial U_d}{\partial y}\right] = \Gamma \tag{5.28}$$

An analytical solution to Eq. (5.28) for the lateral distribution of depth-mean velocity has been obtained by Shiono and Knight (1988, 1991).

5.3.2 Analytical solution for depth-averaged velocity

In the analytical method, which is used throughout this research, the cross section is divided into sub-areas (panels) with constant depth domains as shown in Figure 5.1. For a sub-area with a constant water depth H, the U_d distribution can analytically be obtained from Eq. (5.28) as follows:

$$U_d = [A_1 e^{\gamma y} + A_2 e^{-\gamma y} + k]^{1/2} \tag{5.29}$$

where:

$$k = \frac{8gS_oH}{f}(1-\beta) \tag{5.30}$$

$$\gamma = \sqrt{\frac{2}{\lambda}}\left(\frac{f}{8}\right)^{\frac{1}{4}}\frac{1}{H} \tag{5.31}$$

$$\beta = \frac{\Gamma}{\rho g H S_o} \tag{5.32}$$

A_1 and A_2 are integration constants and can be determined by considering the relevant boundary conditions.

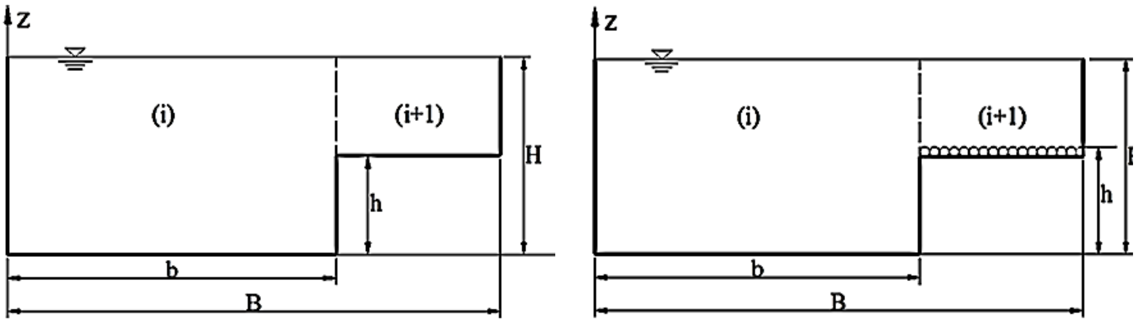

(a) with smooth floodplain (b) with rough floodplain

Figure 5.1 Cross-section of compound channel divided into panels

Different boundary conditions are usually used to determine the unknown A_1 and A_2 constants. At the remote edges of the channel, the no-slip condition holds where the velocity can be assumed to be equal to zero, thus:

$$(U_d)_{y=0}^{(i)} = (U_d)_{y=B}^{(i+1)} = 0 \tag{5.33}$$

At the interface between two adjacent panels, the following different forms of boundary conditions can often be applied (Knight, 2013):

Form [A]: The continuities of the depth-averaged velocity and of the lateral gradient of velocity, i.e.,

$$\begin{gathered} (U_d)_{y=b}^{(i)} = (U_d)_{y=b}^{(i+1)} \\ \left(\frac{\partial U_d}{\partial y}\right)_{y=b}^{(i)} = \left(\frac{\partial U_d}{\partial y}\right)_{y=b}^{(i+1)} \end{gathered} \tag{5.34}$$

Form [B]: The continuities of the depth-averaged velocity and of the lateral gradient of $H(y)U_d$, i.e.,

$$\begin{gathered}(U_d)_{y=b}^{(i)} = (U_d)_{y=b}^{(i+1)} \\ \left(\frac{\partial HU_d}{\partial y}\right)_{y=b}^{(i)} = \left(\frac{\partial HU_d}{\partial y}\right)_{y=b}^{(i+1)}\end{gathered} \tag{5.35}$$

Form [C]: The continuities of the depth-averaged velocity and of the apparent shear force per unit length, i.e.,

$$\begin{gathered}(U_d)_{y=b}^{(i)} = (U_d)_{y=b}^{(i+1)} \\ \left(\frac{1}{2}\rho\lambda H^2 \frac{\partial U_d^2}{\partial y}\right)_{y=b}^{(i)} = \left(\frac{1}{2}\rho\lambda H^2 \frac{\partial U_d^2}{\partial y}\right)_{y=b}^{(i+1)}\end{gathered} \tag{5.36}$$

Form [D]: The continuities of the depth-averaged velocity and of the continuity of unit force with the boundary shear force along the internal wall, i.e.,

$$\begin{gathered}(U_d)_{y=b}^{(i)} = (U_d)_{y=b}^{(i+1)} \\ \left(\phi \frac{\partial U_d^2}{\partial y}\right)_{y=b}^{i} = \left(\phi \frac{\partial U_d^2}{\partial y}\right)_{y=b}^{i+1} - h\tau_w\end{gathered} \tag{5.37}$$

where:

$$\phi = \frac{1}{2}\rho\lambda H^2\sqrt{f/8} \; and \; \tau_w = \rho f_w (U_d^2)_{y=b}/8 \tag{5.38}$$

The boundary Forms [A]–[C] are physically reasonable for trapezoidal compound channels, and good predictions can be obtained by using these forms (e.g., Ervine et al. 2000; Shiono and Knight 1991). However, for a rectangular compound channel, as shown in Figure 5.1, the flow depth at the internal vertical wall between the main channel and its floodplains is discontinuous. Therefore, the apparent shear force (ASF) at the conjunction is not continuous because of the existence of the boundary shear force along the internal wall, (Knight et al. 2004). This indicates that Form [C] is not physically reasonable in the case of a rectangular compound channel. Knight et al. (2004) indicated that the ASF is discontinuous over the vertical wall and the discontinuity is equal to the shear force on this wall. Based on that, Tang and Knight (2008) proposed the form [D] of boundary conditions by considering the boundary shear force along the internal wall. However, determining the boundary shear force along the internal wall is particularly difficult and challenging. To check whether the boundary conditions described by form [D] can give good predictions for depth-averaged velocity, they were verified in this study by the experimental data.

By applying the boundary conditions [D], the following set of linear equations is obtained in which the *A* coefficients in Eq. (5.29) are the unknowns:

$$\begin{bmatrix} 1 & 1 & 0 & 0 \\ 0 & 0 & e^{\gamma_2 B} & e^{-\gamma_2 B} \\ e^{\gamma_1 b} & e^{-\gamma_1 b} & -e^{\gamma_2 b} & -e^{-\gamma_2 b} \\ (\phi_1\gamma_1 + \rho f_w D/8)e^{\gamma_1 b} & -(\phi_1\gamma_1 - \rho f_w D/8)e^{-\gamma_1 b} & -\phi_2\gamma_2 e^{\gamma_2 b} & \phi_2\gamma_2 e^{-\gamma_2 b} \end{bmatrix} \begin{bmatrix} A_1 \\ A_2 \\ A_3 \\ A_4 \end{bmatrix} = \begin{bmatrix} -k_1 \\ -k_2 \\ k_2 - k_1 \\ -\rho f_w D k_1/8 \end{bmatrix} \qquad (5.39)$$

Once the *A* coefficients are defined, the lateral variation of depth-averaged velocity across the channel can be obtained from Eq. (5.29). The MATLAB Code that was developed for the analytical solution of the depth-averaged velocity is shown in Appendix C.

5.3.3 Model parameters

The value of friction factor (*f*) for each panel should be obtained along with the values of dimensionless eddy viscosity, λ, and secondary flow term, Γ, through calibration. The accurate prediction of depth averaged velocity depends on proper estimation of the three calibration parameters in the model (i.e. *f*, λ, and Γ). In this study, the predictive capability of the analytical solution given by Eq. (5.29) is assessed against experimental data for an asymmetric compound open channel. Detailed Computational Fluid Dynamics (CFD) results were used to compute the detailed and averaged eddy viscosity and secondary currents in compound channels with different roughness regimes. Based on the CFD results, expressions were proposed to calibrate the three parameters (*f*, λ, and Γ) for narrow compound channels having different floodplain roughnesses.

Chapter 6

Results for Rectangular Channel Flows

6.1 Introduction

In this chapter, the results obtained from the CFD modelling for the rectangular channels were validated and described in conjunction with the findings of the first set of experiments. First, the CFD model was validated by comparing the computed results with experimental data. Next, the primary flow in a rectangular channel was investigated by examining the effects of boundary roughness, secondary flow and turbulence on the non-uniformity of the velocity distribution. Then, expressions for calculating the parameters that represent the secondary flow and turbulence effects were developed to improve the performance of the analytical model (DMWL-law) for smooth and rough flows. Finally, the application of the analytical model (DMWL-law) to narrow open channels with different roughness conditions was assessed.

6.2 Verification and validation of CFD computations

6.2.1 Conservation of momentum calculation

To verify the CFD computations, a conservation of momentum calculation was performed for each case. For Rectangular channel cases, the average shear stress, τ_o, is calculated as:

$$\tau_o = \frac{1}{P}\int_P \tau dl = \frac{1}{P}[2h\tau_w + b\tau_b] \tag{6.1}$$

where τ_w and τ_b are the average wall and bed shear stress computed by the CFD software, and P is the wetted perimeter of the channel. Assuming uniform flow the average shear stress at the boundaries of the channel is analytically given by:

$$\tau_o = \rho g S_o R \tag{6.2}$$

where R is the hydraulic radius (= A/P). To verify that the momentum balance is established, the following equality should hold:

$$2h\tau_w + b\tau_b = \rho g S_o A \tag{6.3}$$

It can be seen from Table 6.1, the conservation of momentum is satisfied by the CFD model for all cases simulated in this research.

Table 6.1 Conservation of momentum calculation for CFD simulations.

Case [#]	H [m]	B [m]	τ_w [pa]	τ_b [Pa]	$2h\tau_w + b\tau_b$ [computed]	$\rho g S_o A$ [analytical]
S6	0.06	0.30	0.199	0.215	0.088	0.088
S10	0.10	0.30	0.293	0.296	0.147	0.147
S15	0.15	0.30	0.368	0.357	0.218	0.221
S20	0.20	0.30	0.440	0.416	0.301	0.294
T6	0.06	0.30	0.121	0.247	0.089	0.088
T10	0.10	0.30	0.191	0.367	0.148	0.147
T15	0.15	0.30	0.257	0.469	0.218	0.221
T20	0.20	0.30	0.312	0.552	0.290	0.294
R6	0.06	0.30	0.091	0.258	0.088	0.088
R10	0.10	0.30	0.143	0.394	0.147	0.147
R15	0.15	0.30	0.204	0.539	0.223	0.221
R20	0.20	0.30	0.248	0.643	0.292	0.294

6.2.2 Computed primary flow velocity

To validate the primary flow patterns obtained using CFD simulations, vertical profiles and contours of the computed primary velocity for smooth, transitional and rough cases were compared with those measured. Figure 6.1 shows the comparison between the numerically predicted and the experimentally measured primary mean velocity profiles at the centreline of the channel for all rectangular flow cases considered in this work. It can be seen that the predicted vertical distribution of mean velocity (U) by the CFD using the RSM turbulence model is very close to the experimental measurements for all flow depths and for all roughness regimes. Figure 6.1 also indicates that the maximum velocity tends to appear below the free surface in the deeper channel cases with smaller aspect ratios (i.e. Ar = 1.5, 2.0). The same phenomena (i.e. dip phenomena) can be observed by both experimental and numerical data. However, for high flow cases, CFD predictions appear to slightly deviate from the experimental data at the near-surface zone as shown in 6.1c and 6.1d. This is most probably due to the free surface boundary condition imposed here, which accounts for free surface effects on turbulence and secondary flow but not exactly on the primary flow. Nonetheless, it has been verified that the slight differences, which are noticed between the computed and measured velocity profiles at this small zone, has no considerable impact on the velocity distribution over the entire cross section. Therefore, it can generally be stated that the CFD model fairly reproduced the velocity profile over the entire flow depth for all cases, and this is essential for the accurate prediction of the magnitudes and patterns of the other velocity components (*V* and *W*) as well as the secondary flow.

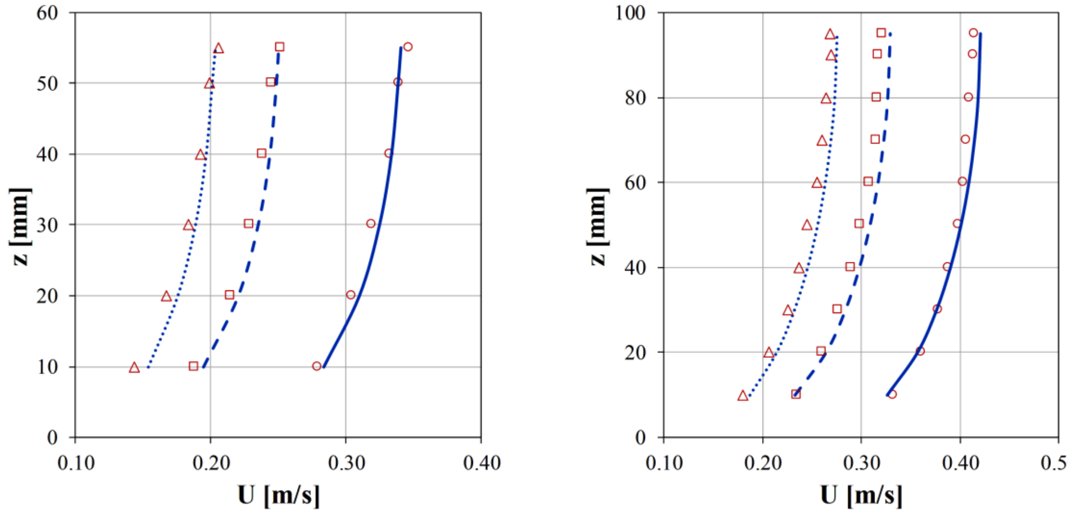

(a) *H* = 6 cm, *Ar*=5.0 (b) *H* = 10 cm, *Ar*=3

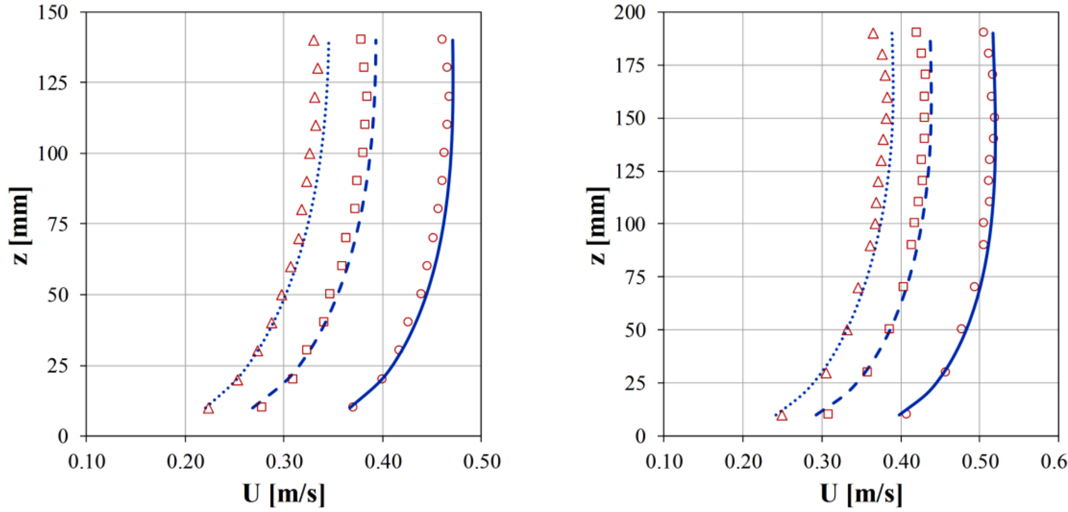

(c) *H* = 15 cm, *Ar*=2.0 (d) *H* = 20 cm, *Ar*=1.5

Experiment: ○ smooth regime □ transitional regime △ rough regime

Simulation: —— smooth regime - - - transitional regime ········ rough regime

Figure 6.1 Velocity profile at the center line of the rectangular channel for all cases.

The simulated and measured primary velocity contours are compared in Figure 6.2 and Figure 6.3 for the two aspect ratios. The first figure plotted is for the cases of the largest aspect ratio (*Ar* = 5.0) while the second one is for the smallest aspect ratio (*Ar* = 1.5). The velocity values in both figures were normalized by the maximum velocity of each flow case. Only velocity contours for half of the geometry has been displayed because of the symmetry in the velocity distribution along the centre of the channel.

A reasonably good agreement between the numerical and experimental data for the primary flow has been obtained in terms of the general patterns of the velocity and the magnitudes of velocities. It can clearly be seen in both simulated and measured results for velocity how the contour of higher velocity rises up towards the free surface when the roughness of channel bed increases. From Figure 6.2, the approximate location of the velocity contour that has a value of 0.95 U/U_{max} occurs at $z/H = 0.50$ for smooth case (S6) compared with $z/H = 0.60$ for the rough case (R6). This implies that the CFD model, with RSM turbulence closure and shifted log-law methods, can successfully capture the blockage effects of the rough surfaces on the primary flow. For the cases with the aspect ratio of $Ar = 1.5$ (Figure 6.3), the position of maximum velocity appears about $0.4H$ below the free surface when the flow regime is hydraulically smooth. When the flow regime is fully rough, the position of maximum velocity from the free surface reduces to about $0.2H$. This fact coincides well with the data for open channel flows which were obtained using an LDA system by Nezu and Rodi (1985).

The influence of the secondary current on the primary velocity contours is obviously predicted by the CFD simulations. There is some indication of bulging of velocity contours in the CFD results, where the contours tend towards the corner at the bottom due to the secondary currents. The bulging in the velocity contours is more visibly in the deep flow cases, i.e. with the smallest aspect ratio, as the secondary currents are expected to be stronger. In addition, it can be noticed that the contours of the simulated velocity are not normal to the free surface which conforms to the boundary conditions used. The results from the CFD model, which used RSM turbulence model in combination with the modified boundary condition supplied by CFX, verify that the maximum velocity lies beneath the free surface. Such a feature has also been observed experimentally as shown in Figure 6.3. It could therefore be argued that the CFD model with RSM turbulence closure adopted in this study can reproduce the primary flow over different boundary roughnesses.

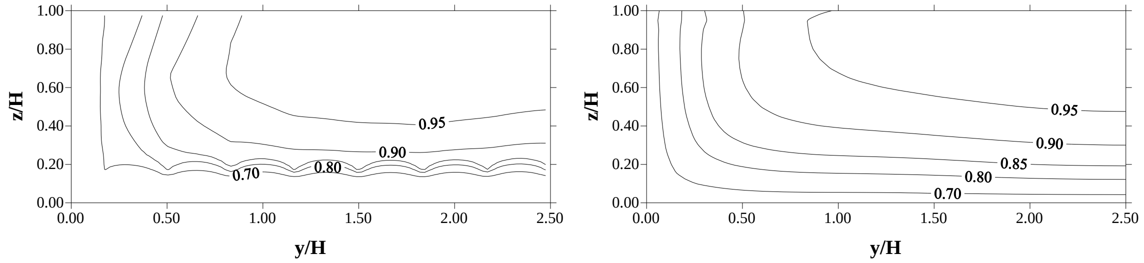

(a) S6 (Experiment)   (b) S6 (simulation)

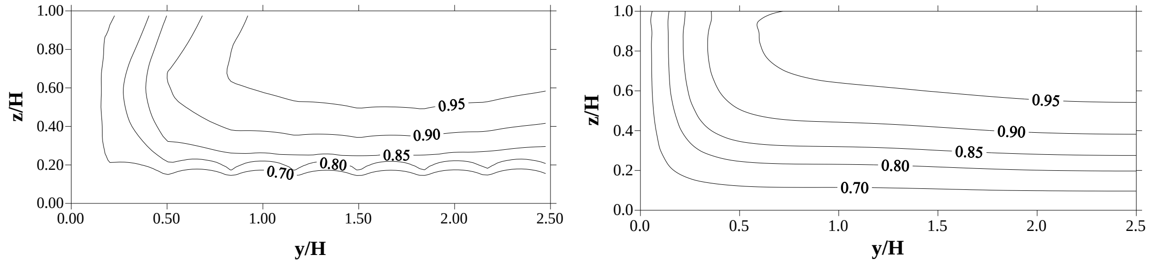

(a) T6 (Experiment)   (b) T6 (simulation)

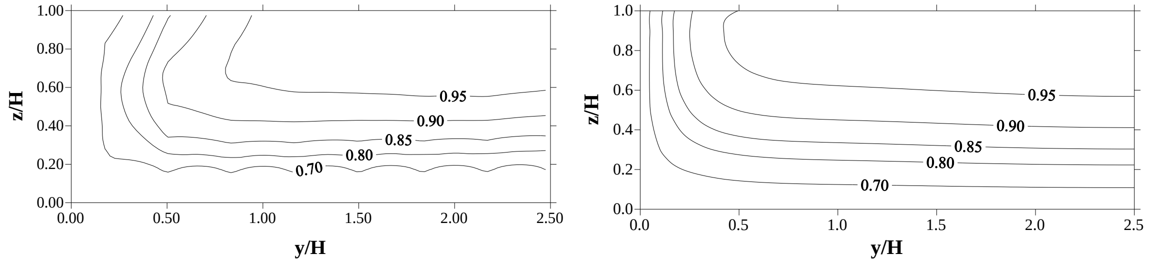

(a) R6 (Experiment)   (b) R6 (simulation)

Figure 6.2 Primary velocity contours for test cases of the largest aspect ratio (A_r = 5).

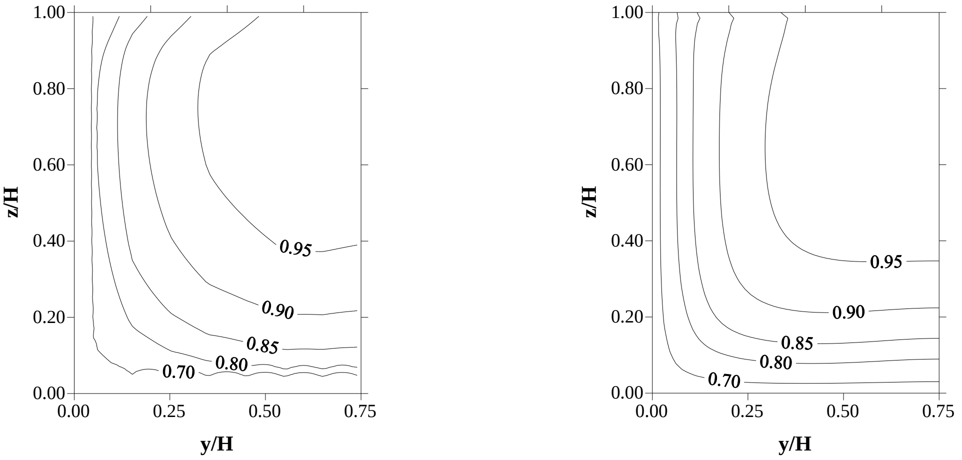

(a) S20 (Experiment) (b) S20 (simulation)

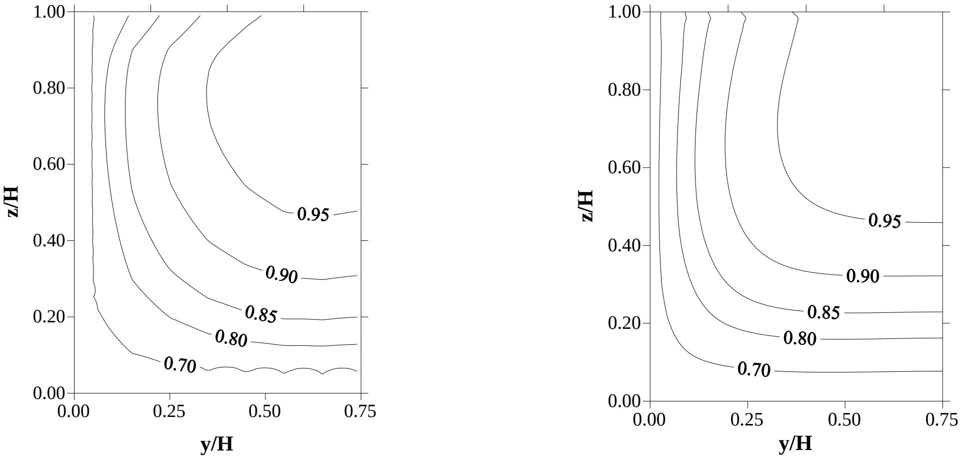

(a) T20 (Experiment) (b) T20 (simulation)

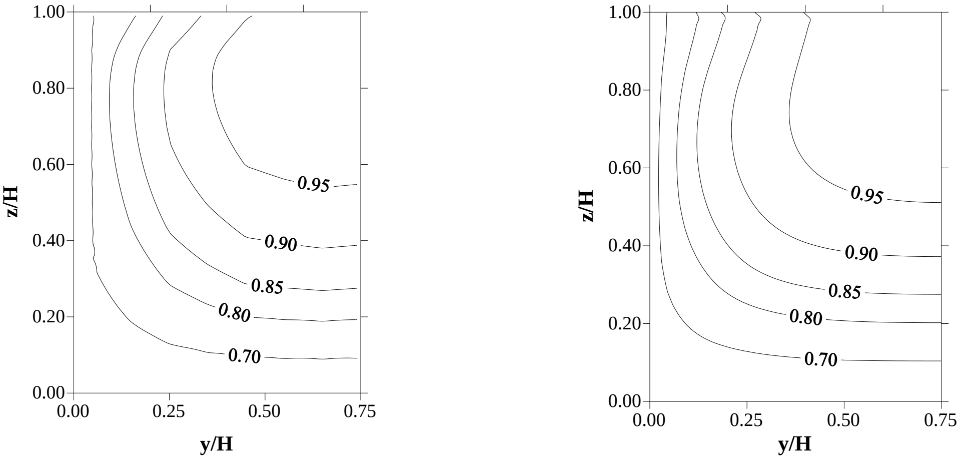

(a) R20 (Experiment) (b) R20 (simulation)

Figure 6.3 Primary velocity contours for test cases of the smallest aspect ratio (A_r = 1.5).

6.3 Results for secondary currents

6.3.1 Patterns and magnitudes of secondary currents

Secondary current vectors for the smooth case of $Ar = 2.0$ predicted by the present CFD model are given in Figure 6.4. The results from the present work are compared with experimental measurements by Tominaga et al. (1989) and LES data by Shi et al. (1999) for a rectangular channel that has similar value of Ar.

The general pattern and the magnitudes of the secondary currents predicted by the present CFD model are seen to be consistent with measured and LES numerical results. For the present model (Figure 6.4c), the magnitude of the secondary flows is relatively small, with many points having values that equal to or less than 2% of the primary velocity. These results fairly agree with previous results obtained by Tominaga et al. (1989), and Shi et al. (1999) shown in Figures 6.4a and 6.4b. In all figures, two cells of secondary currents can be observed, one is located near the free surface (called as the free surface vortex) and the other is near the bottom (called as bottom vortex). However, there are slight differences between the locations and sizes of secondary vortices obtained by the numerical simulations (Figure 6.4b and 6.4c) and those measured in the experiments (Figure 6.4a). In the present simulation, the free surface vortex appears to be closer to the side wall. This is probably because the flow conditions in the present work are not exactly same as that in the experiments used for the comparison.

Figure 6.5 and 6.6 show the numerically obtained secondary flow vectors normalized by U_{max} for the smooth, transitional and fully rough regimes with different aspect ratios (Ar). For all flow cases, it can clearly be seen that the pair of vortices (i.e., free-surface and bottom vortices) are generated near the side wall and the bottom bed. Also, Figures 6.5 and 6.6 show that when the aspect ratio of the channel becomes larger, the spanwise scale of the bottom vortex increases and reaches about $1.5H$. The length scale of the free-surface vortex is nearly confined to about $0.5H$ for all flow cases in regardless of whether the aspect ratio is small or large. The pattern of secondary currents predicted for flow cases considered here is reasonably similar to that observed in some literature studies, e.g. Nezu and Rodi (1985) and Tominaga & Nezu, (1989).

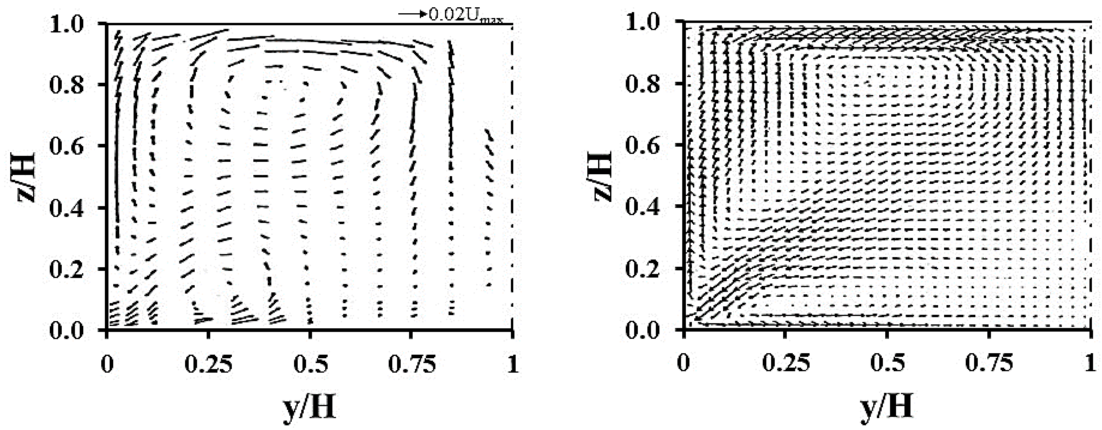

(a) Exp. (Tominaga et al. 1989)

(b) LES (Shi et al. 1999)

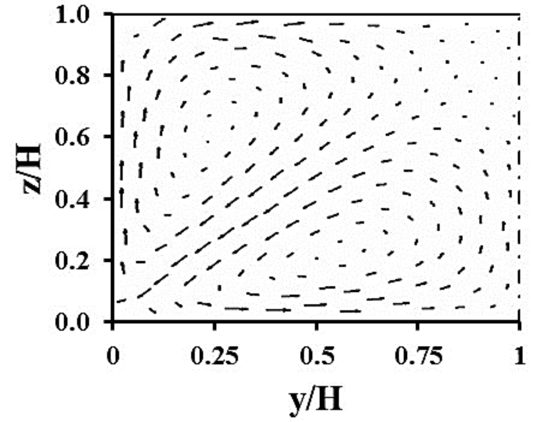

(c) RSM (Present work)

Figure 6.4 Measured and simulated secondary currents vectors for rectangular channel flows with aspect ratio $Ar = 2.0$.

In terms of the magnitude of the secondary currents, the maximum magnitudes of the secondary currents computed by CFD modelling are averaged about $0.023U_{max}$ for smooth cases. These magnitudes are nearly close to the LDA data of Nezu and Rodi (1985) who estimated the maximum secondary currents to be about 0.020 U_{max}. The values of the maximum secondary currents in rough channel flows are somewhat greater than the value obtained in smooth channel flow. For the condition of rough bed, cases T and R, the free-surface vortex becomes stronger near the side wall than in the smooth rectangular channel as shown in Figure 6.5 and 6.6. Hence, the maximum secondary velocity is of about $0.034U_{max}$ for the transitional cases and $0.050U_{max}$ for rough cases. These magnitudes are in line with the measurements of McLean (1981) and Tominaga et al., (1989) in rough open channel flows.

In the light of the above mentioned, it can be concluded that the present CFD simulation correctly predicts the complex features of secondary currents in terms of the number and locations of secondary cells. The maximum magnitudes of secondary currents for all cases simulated are given in Table 6.2. The results in Table 6.2 indicates that the magnitude of secondary currents increases with decrease in aspect ratio, i.e. increase in flow depth.

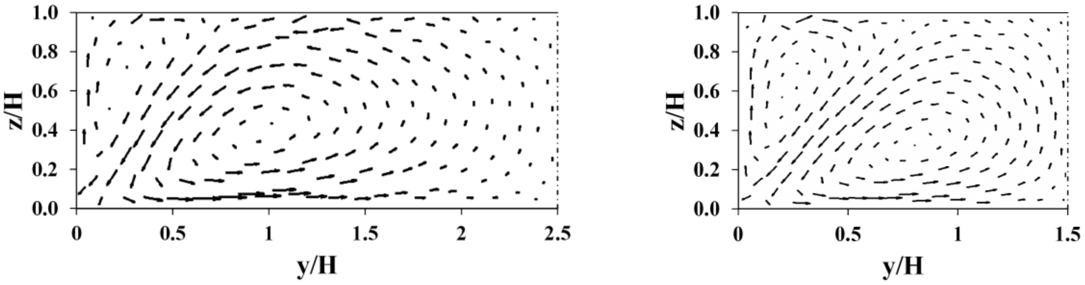

(a) S6 (*Ar* = 5) (b) S10 (*Ar* = 3.0)

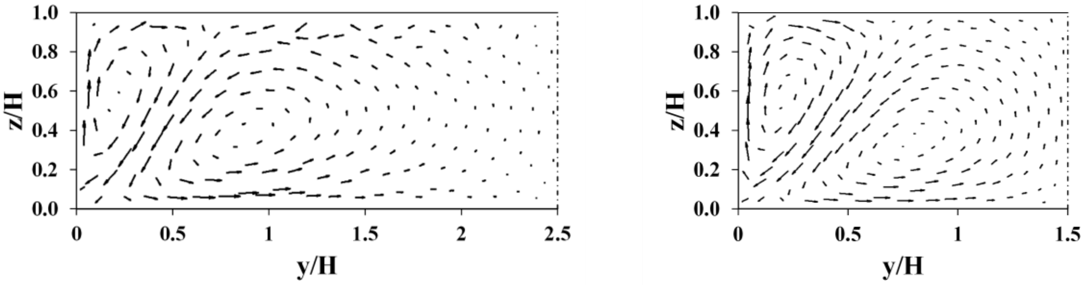

(a) T6 (*Ar* = 5) (b) T10 (*Ar* = 3.0)

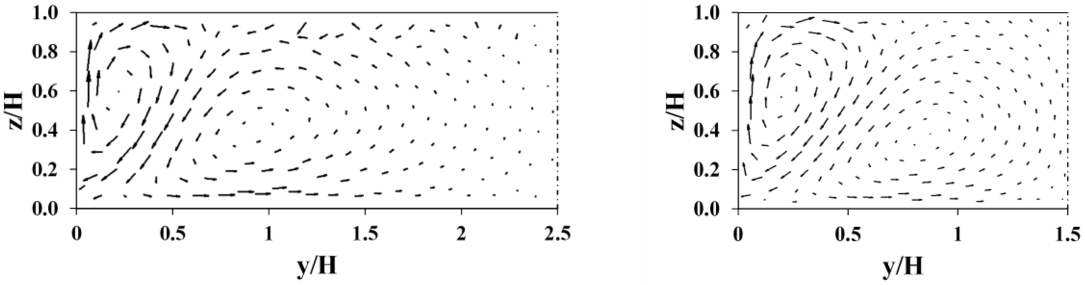

(a) R6 (*Ar* = 5) (b) R10 (*Ar* = 3.0)

Figure 6.5 Secondary currents for flow cases *H*= 6 cm and *H*= 10 cm.

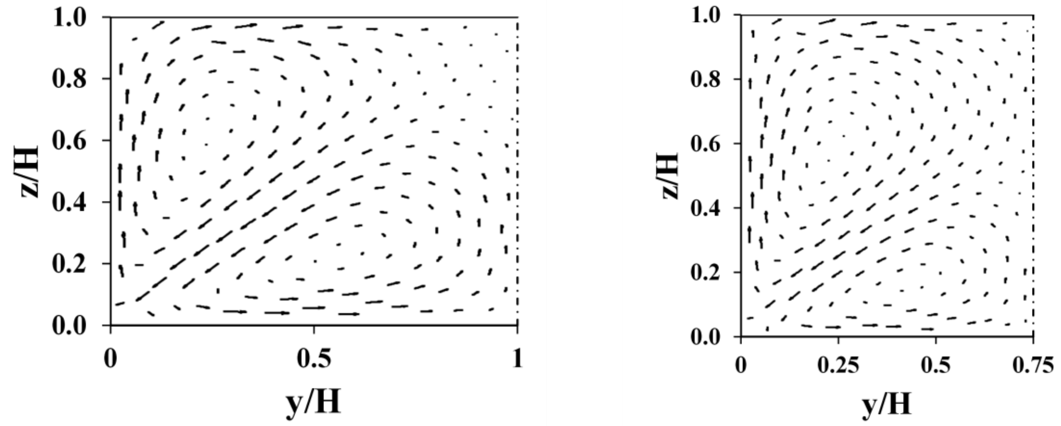

(a) S15 (*Ar* = 2) (b) S20 (*Ar* = 1.5)

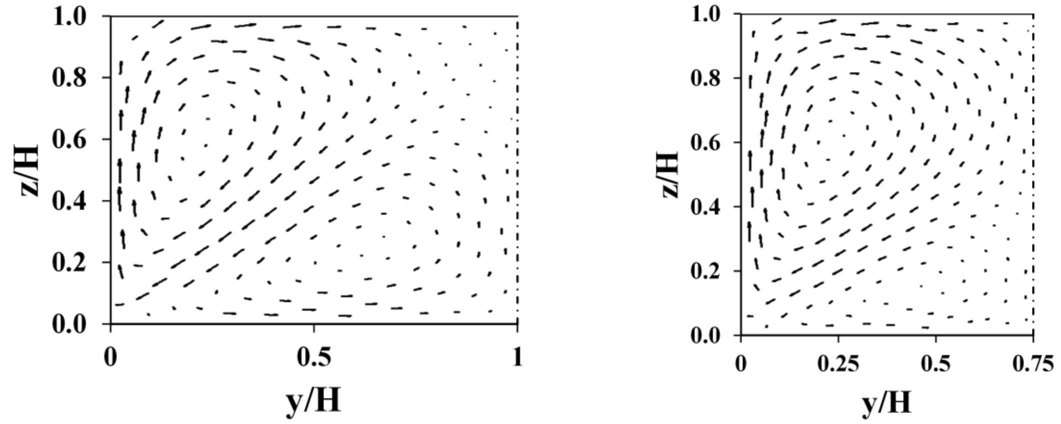

(a) T15 (*Ar* = 2) (b) T20 (*Ar* = 1.5)

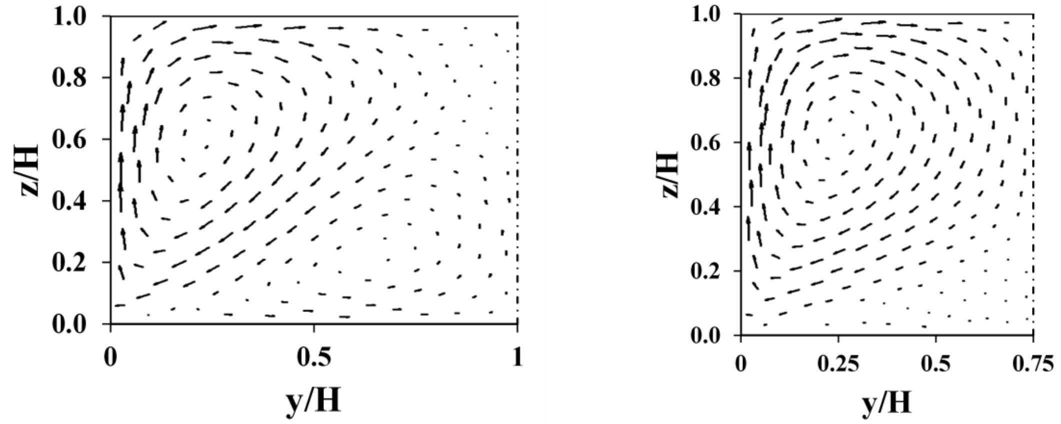

(a) R15 (*Ar* = 2) (b) R20 (*Ar* = 1.5)

Figure 6.6 Secondary currents for flow cases *H*= 15 cm and *H*= 20 cm.

Table 6.2 Maximum magnitude of secondary velocity for all cases simulated

Depth	***Ar***	**Max.U_{sec} (10^{-2}) [m/s]**			**Max.U_{sec} /U_{max}**		
H [cm]	**B/H**	**Smooth**	**Transitional**	**Rough**	**Smooth**	**Transitional**	**Rough**
6.0	5	0.676	0.844	1.154	0.020	0.034	0.057
10.0	3	0.937	1.140	1.441	0.022	0.035	0.052
15.0	2	1.173	1.351	1.625	0.024	0.034	0.046
20.0	1.5	1.307	1.516	1.803	0.025	0.034	0.045
				Average	0.023	0.034	0.050

6.3.2 Production mechanism of secondary currents

It is known that the turbulence anisotropy is the main reason for generation of turbulence-driven secondary currents. In Figure 6.7, the secondary currents vectors are plotted together with the normalised turbulence anisotropy contours $[(\overline{vv}-\overline{ww})/U_*^2]$ to illustrate the strong interconnection between turbulence anisotropy and secondary currents. For the sake of brevity, only the cases of *Ar* = 2 are considered. The computed results of $(\overline{vv}-\overline{ww})$ is highly consistent with those for rectangular channels experiments conducted by Tominaga. et al (1989) and shown in Figure 6.8. It can be noticed that $(\overline{vv}-\overline{ww})$ have the maximum positive values at the bed and the maximum negative values at the sidewall.

The location of the equilibrium or zero line, which represents the locations of points where $\overline{vv}$ and $\overline{ww}$ are equal, is of particular interest here. From Figure 6.7, the increase of the bed roughness imparts an asymmetry to the flow, leading the line of zero turbulence anisotropy moving towards the side wall. Because of that, in rough bed case the contour lines near the side wall are close to each other and the values of the normal-stress anisotropy increase rapidly from zero to maximum value over a short distance. Therefore, the gradients of the normal-stress anisotropy are high, and hence the strong secondary velocities generated there. These results are well matched with the measurements of previous works (e.g. Tominaga. et al 1989). Differences in the positive maximum values of the turbulence anisotropy, which occur at the bottom, are also shown based on the roughness of the bed. The positive maximum value of $[(\overline{vv}-\overline{ww})/U_*^2]$ is about 0.90 for smooth case S15 compared to 1.20 in rough case (R15). This reflects the impact of the bed roughness on the turbulence anisotropy and consequently on the secondary motion.

(a) S15

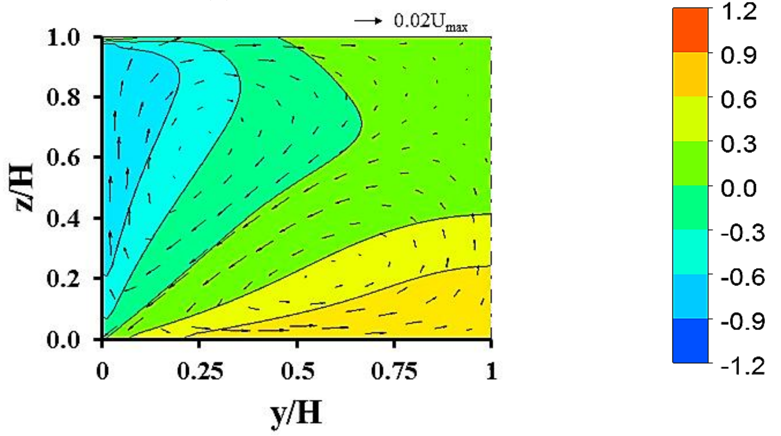

(a) T15

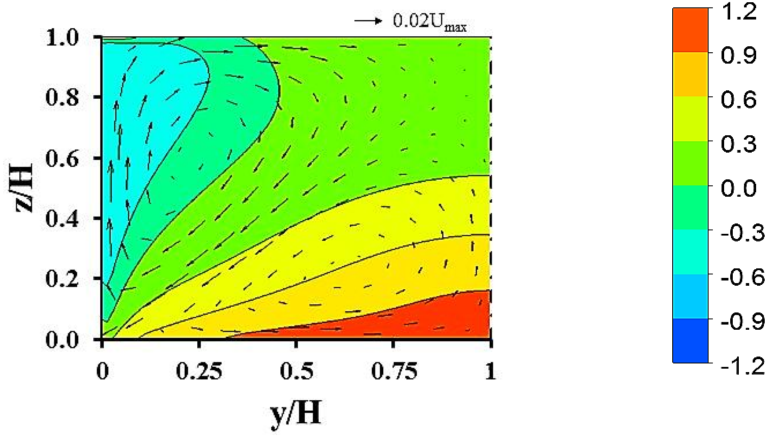

(a) R15

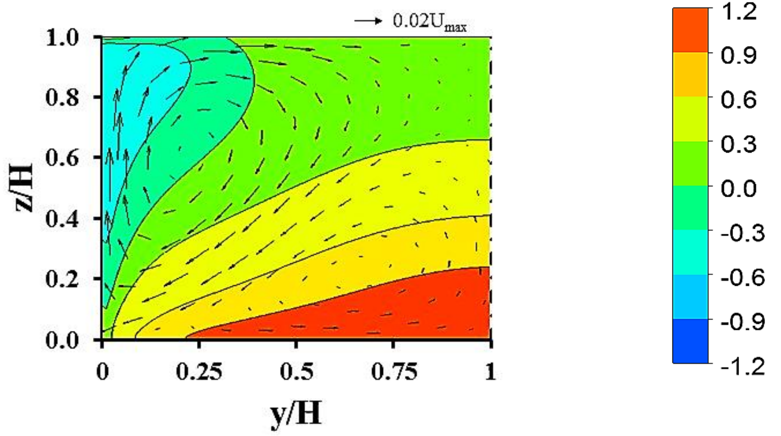

Figure 6.7 Secondary current velocity vectors and turbulence anisotropy for flow cases with *Ar* = 2.0.

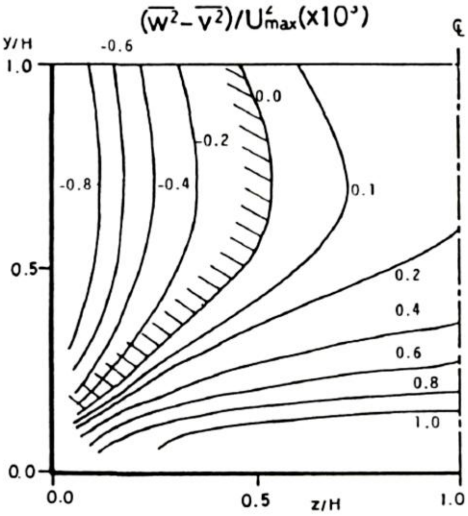

Figure 6.8 Measured turbulence anisotropy $(\overline{vv}-\overline{ww})$ for rectangular open channel flow by Tominaga et al (1989).

6.4 Results for Turbulence characteristics

6.4.1 Turbulence intensities

Turbulence measurements were not performed in the experiments conducted in this study, so the turbulence intensities computed by CFD simulations were analysed based on some assumptions. The computed turbulence intensity was also compared with experimental measurements by Grass (1971). The main purpose of this analysis is to verify the prediction of the CFD for turbulence features and Reynolds shear stress, which can be used to calculate the eddy viscosity.

Most of the available analytical attempts to describe the vertical distribution of turbulence intensities use the assumption of an equilibrium between turbulence production and dissipation. This assumption leads to the followings universal profiles proposed by Nezu & Nakagawa (1993) for laboratory open-channel flows:

$$\frac{u_{rms}}{u_*}=D_u\exp(-C_k\frac{z}{h}) \tag{6.4}$$

$$\frac{w_{rms}}{u_*}=D_w\exp(-C_k\frac{z}{h}) \tag{6.5}$$

where u_{rms} ($\sqrt{\overline{u'u'}}$) and w_{rms} ($\sqrt{\overline{w'w'}}$) are turbulence intensities in streamwise and vertical direction represented in the form of root mean square (RMS); D_u, D_w, and C_k are empirical parameters which for laboratory open-channel flows were determined experimentally to be equal to 2.30, 1.27, and 1.0, respectively (Nezu and Nakagawa, 1993).

The CFD results of streamwise and vertical turbulence intensities were verified by comparing with the semi-theoretical equations given by Eqs. (6.4) and (6.5) and with experimental data from Grass (1971). Turbulence measurements of experiments, corresponding to hydraulically smooth and rough boundary conditions (K_s =9 mm) were used for comparison in this study. The roughness conditions in Grass experiments are nearly similar to those in the present study.

Figures (6.9) and (6.10) represent the vertical distributions of u_{rms} and w_{rms} for smooth and rough cases respectively. For smooth cases (S6 and S20), Figure (6.9) indicates that CFD results for u_{rms} and w_{rms} fairly agree with both values measured by Grass (1971) and calculated by Nezu & Nakagawa (1993) equations. However, some deviations between computed CFD and theoretical values for u_{rms} occur in the region close to the boundary wall, $z/h < 0.4$, which may be due to difficulties in modelling the strong effect of the wall on the turbulence there. The figure also shows that the predicted values of the vertical intensity (w_{rms}) is dampened as the free surface is approached, reflecting the suppression of vertical eddy movement. In turn, near to the free surface the streamwise intensity (u_{rms}) is nearly a constant. This coincides well with turbulent motion near the surface described by Hunt (1984).

For rough flows (R6 and R20), Figure (6.10) indicates that the compatibility of the computed values for u_{rms} and w_{rms} to the universal equations (Eqs. 6.4 and 6.5) is almost similar to that of smooth flows. Also, the degree of agreement between CFD predictions and measurement data of Grass (1971) is reasonably high in the region near the bed, $0.2 < z/h < 0.6$. However, in high flow case (R20) the computed values of intensities show a slight disagreement with universal profiles in some region. In spite of some deviations between CFD predictions and universal equations for turbulence intensity, it can be suggested that the CFD simulations generally give reasonably accurate results for turbulence motion in smooth and rough channels.

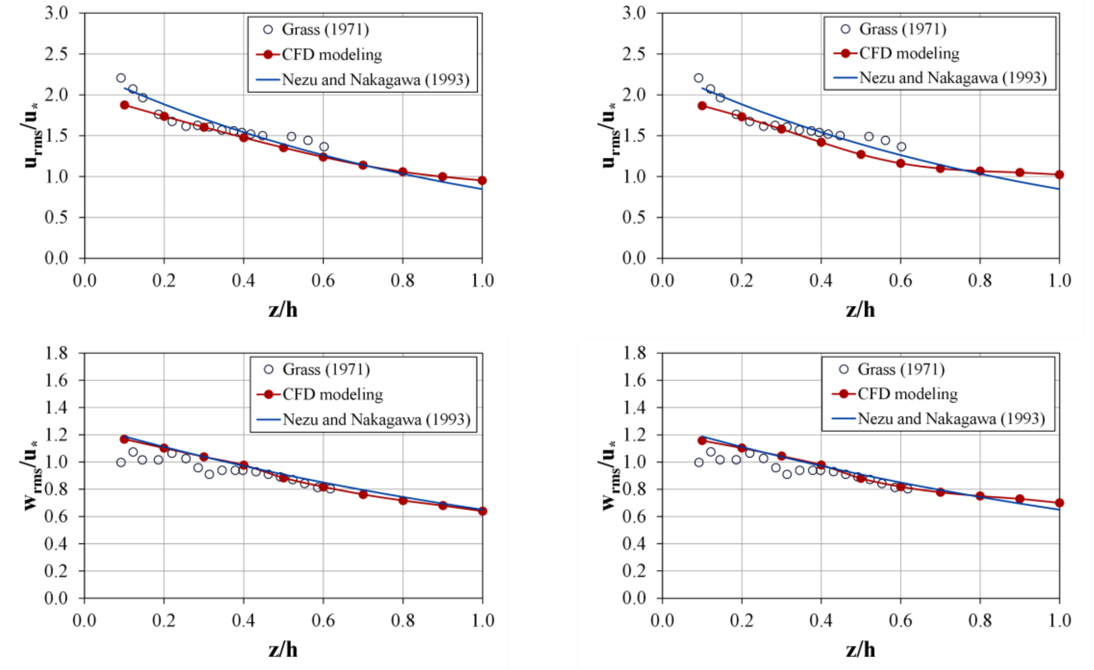

(a) S6 (b) S20

Figure 6.9 streamwise and vertical components of turbulence intensity for smooth flows.

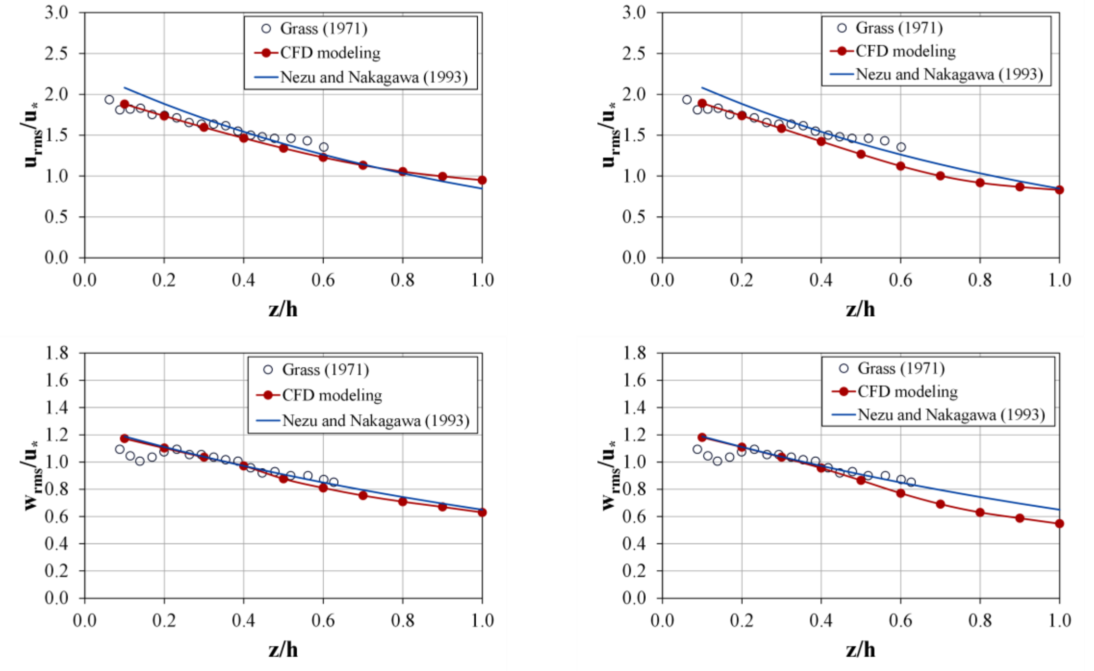

(a) R6 (b) R20

Figure 6.10 Streamwise and vertical components of turbulence intensity for rough flows.

6.4.2 Numerical calculation of eddy viscosity

In the present study, the turbulent eddy viscosity (ν_t) for all smooth, transitional and rough flow cases were computed by making use the CFD results. The eddy viscosity was used as a parameter describing the turbulence strength of the flows. The turbulent eddy viscosity ν_t was calculated in the CFD post-processor from the definition equation of the eddy viscosity:

$$\nu_t = \frac{-\overline{u'w'}}{dU/dz} \tag{6.6}$$

where the Reynolds stresses ($-\overline{u'w'}$) and the velocity gradients (dU/dz) are readily obtainable from the CFD simulations. The measured values of $-\overline{u'w'}$ may show considerable scatter and could not be measured accurately near the bed and the free surface (Nezu and Rodi, 1985). This gives a justification for using numerical simulation to compute the eddy viscosity.

To check the applicability of CFD model for calculation of the eddy viscosity profiles, the vertical distributions of the eddy viscosity computed by the CFD were compared against the experimental results of Nezu and Rodi (1986). Figure 6.11 compares the predicted and measured distributions of the normalised turbulent eddy viscosity (ν_t/HU_*) along the centreline for smooth and rough cases which have the smallest and largest aspect ratios. The runs P-1 and P-4 in Nezu and Rodi experiments were selected for comparison purposes because the Reynolds numbers (*Re*) for these experiments fall within the same range as that for the flow cases considered in the present study.

For the smallest aspect ratio cases (S20 and R20), the agreement between the numerical prediction by the CFD and the measured profile by Nezu and Rodi (1986) appears to be satisfying, irrespective of the roughness conditions. However, for the cases of the largest aspect ratio (S6 and R6), there is some differences between the numerical and experimental data, where the model over-predicts the turbulent eddy viscosity in the near free surface region. This may be attributed to numerical diffusion associated with grid discretisation and the treatment of the water surface which may not give rigorous correction for the reduction of length scale at this region. Nevertheless, an encouraging qualitative agreement between model predictions and corresponding measured results is considered to be achieved. In both numerical and experimental results, the eddy viscosity is zero at the bed and at the free surface and has a maximum value at the mid-depth of the flow.

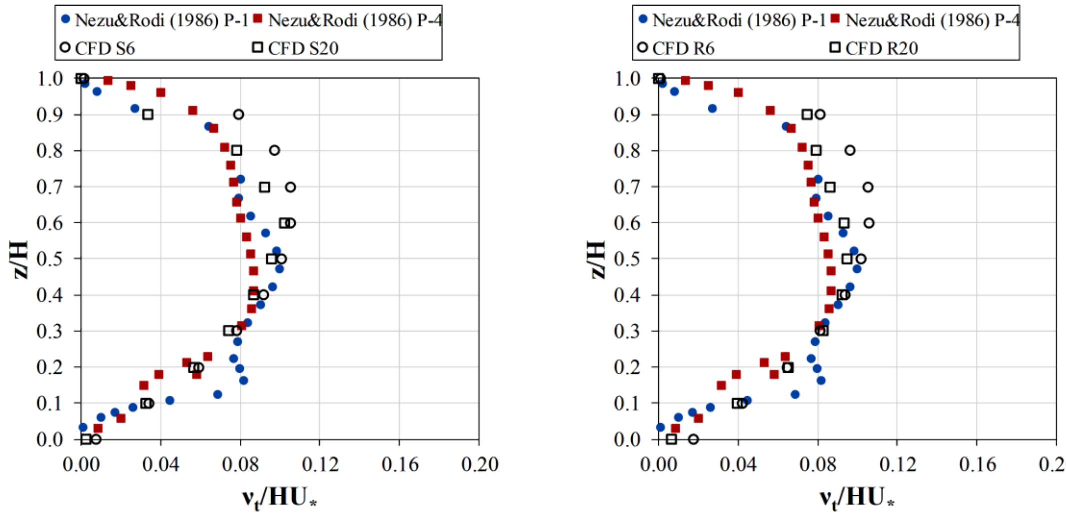

(a) Smooth flows

(b) Rough flows

Figure 6.11 Distribution of eddy viscosity: Comparison between CFD and experimental results

6.4.3 The relationship between the eddy viscosity and wake strength

As stated in previous sections in the present study, the wake strength parameter has a significant effect on the analytical calculations for velocity distributions. Therefore, in this section a numerical analysis was carried out to find out the relationship between the eddy viscosity and the wake strength parameter.

According to Nezu and Rodi (1986), the eddy viscosity can be calculated by the following semi-theoretical equation:

$$\frac{\upsilon_t}{u_* H} = k\left(1-\frac{z}{H}\right)\left[\frac{H}{z}+\pi\Pi\,sin\left(\pi\frac{z}{H}\right)\right]^{-1} \tag{6.7}$$

where Π is the Coles' wake strength parameter. Nezu and Rodi (1986) proved that the value of Π depends on the shear Reynolds number ($R_h^* = Hu_*/\upsilon$), as shown in Figure 6.12. The figure indicates that at smaller values of R_h^*, Π increases rapidly with the Reynolds number but remains constant at Π = 0.2 beyond $R_h^* > 2000$. Based on this fact, the following equation, which expresses the dependency of the wake strength parameter Π on the roughness conditions of the flow, was suggested in this study:

$$\Pi = 0.1243\ln(R_h^*) - 0.7445 \tag{6.8}$$

Equation (6.8) was used to estimate the values of Π that are needed for calculating the theoretical profiles of the eddy viscosity from Eq. (6.7).

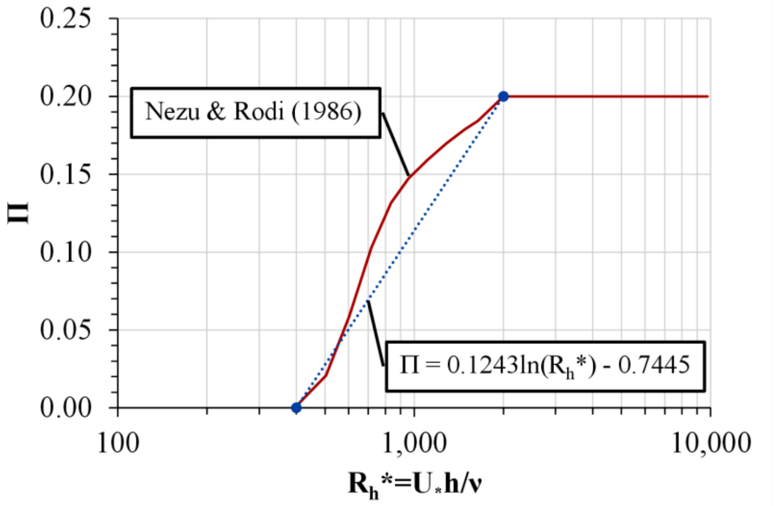

Figure 6.12 The relationship between wake strength parameter and R_h^*.

Figures 6.13, 6.14 and 6.15 show the distributions of (υ_t/Hu_*) obtained by the CFD model for all cases together with the theoretical curves according to Eq. (6.7). The solid lines represent the theoretical curves based on Π calculated from Eq. (6.8), while the dashed lines are the theoretical curves based on a constant Π = 0.2.

For low flow cases, i.e. H = 6 and 10 cm, it can be seen that the prediction for the eddy viscosity is closer to theoretical curves based on Π < 0.20 than curves with constant Π = 0.2. In contrast, for high flows (H = 15 and 20 cm) the predicted eddy viscosity profiles are asymptotic to theoretical curves calculated by a constant Π with a value of 0.2. The CFD results confirm the fact indicated by Nezu and Rodi (1986) that the parameter Π has a significant influence on the distribution of the eddy viscosity over the flow depth. The dependence of ν_t on Π is resulted from the dependence Π on the shear Reynolds number R_h^*. Therefore, the value of Π increases from 0 to 0.2 as R_h^* increases, giving better agreement between the CFD and theoretical profiles. On the other hand, the value of Π should be remain constant at 0.2 for high flows with large R_h^* > 2000, to obtain closer theoretical profiles to CFD predictions.

The average magnitude of the vertical eddy viscosity for all the CFD results was found to be roughly equivalent to the value calculated by the theoretical approach when Eq. (6.8) was used for calculating Π. Table 6.3 shows the variations between the CFD and the based-theoretical model results for average normalized eddy viscosity (ν_t/ν). In general, the variations lie within the range (3% - 13%). This could fairly justify using the average values of v_t obtained by the CFD simulations as indicators of turbulence effects on the non-uniformity of velocity.

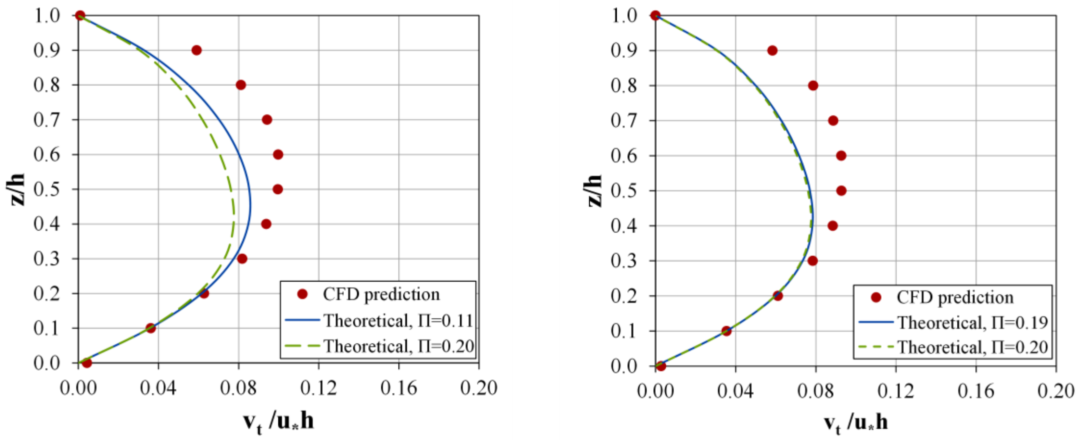

(a) S6 (H = 6 cm)

(b) S10 (H = 10 cm)

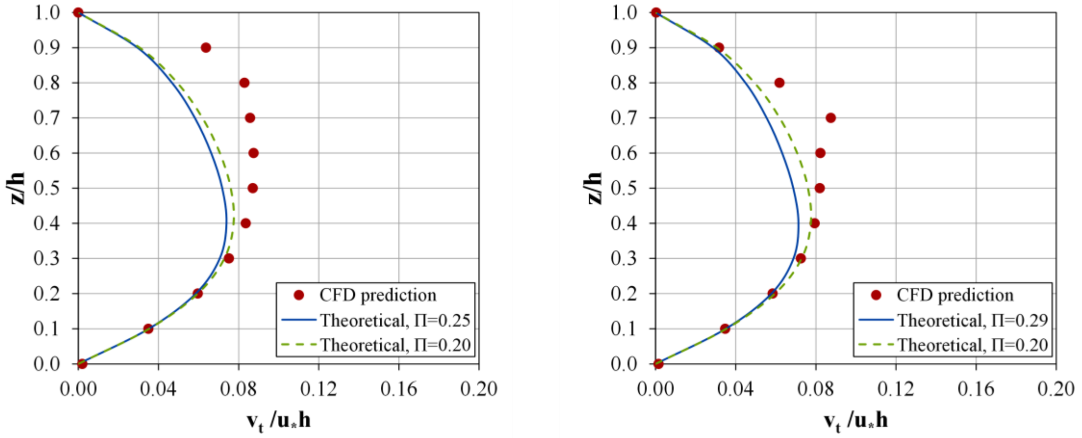

(c) S15 (H = 15 cm)

(d) S20 (H = 20 cm)

Figure 6.13 Distribution of eddy viscosity for smooth cases

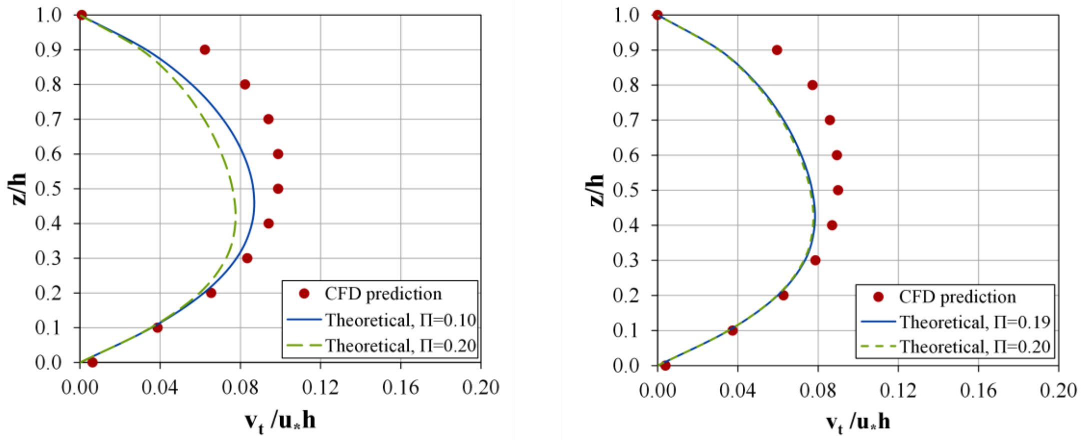

(a) T6 (H = 6 cm)

(b) T10 (H = 10 cm)

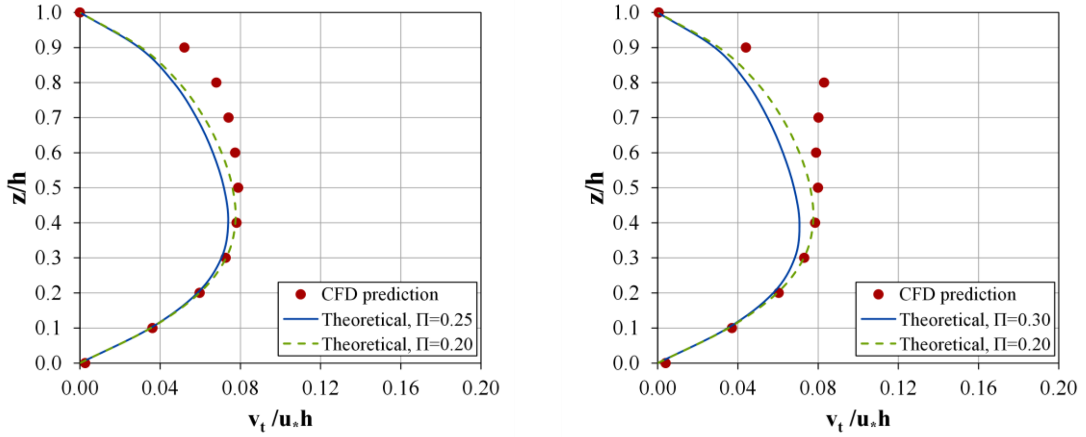

(c) T15 (H = 15 cm)

(d) T20 (H = 20 cm)

Figure 6.14 Distribution of eddy viscosity for transitional cases

Table 6.3 Average normalized eddy viscosity (v_t/v) for all flow cases.

Case	Average normalized eddy viscosity (v_t/v)		Error
[#]	CFD computations	Theoretical	[%]
S6	55.06	50.23	9
S10	101.00	89.43	11
S15	159.68	143.11	10
S20	203.63	204.15	0
T6	52.19	47.44	9
T10	98.69	88.26	11
T15	151.36	149.97	1
T20	224.93	216.37	4
R6	56.08	48.91	13
R10	105.02	91.50	13
R15	168.84	159.94	5
R20	231.49	224.28	3

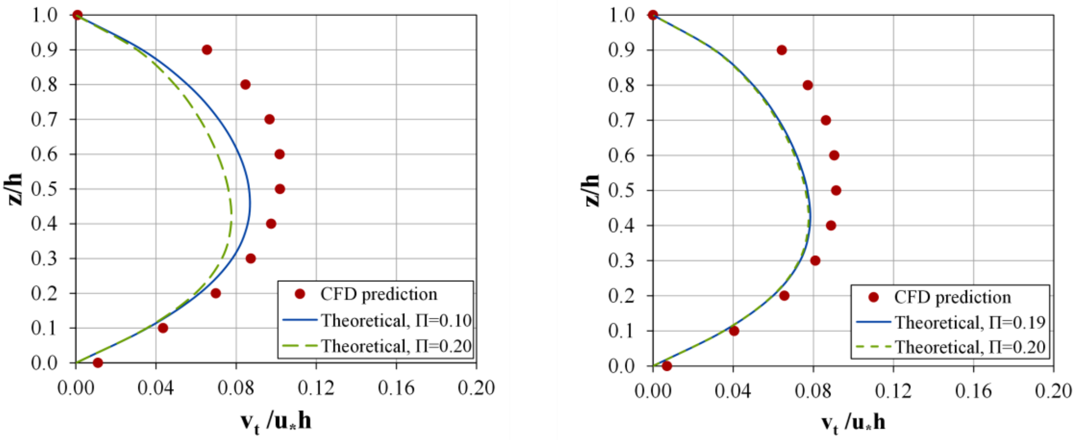

(a) R6 (H = 6 cm) (b) R10 (H = 10 cm)

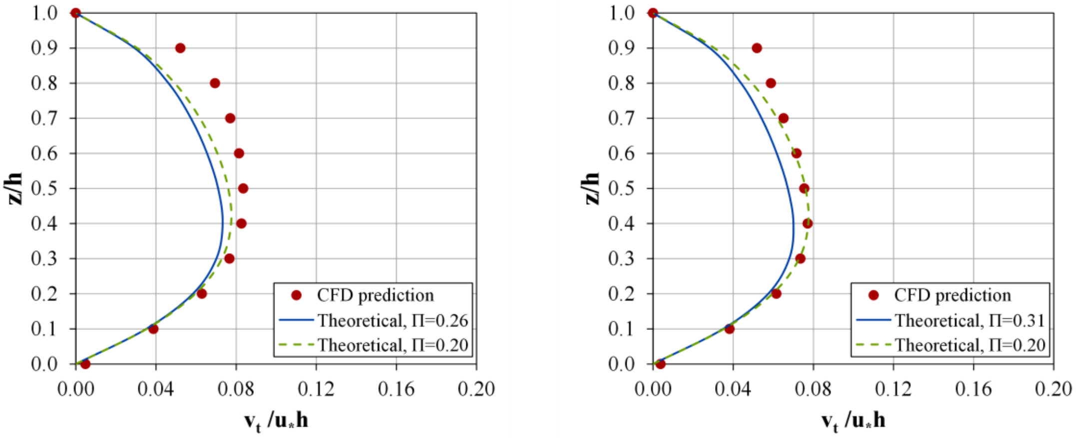

(c) R15 (H = 15 cm) (d) R20 (H = 20 cm)

Figure 6.15 Distribution of eddy viscosity for rough cases

6.5 Velocity distribution and its non-uniformity

Based on the facts explained in previous sections, the effect of the roughness and the turbulence structures on the velocity distributions were found to be considerable. In the present study an analysis was made to explore the links between the velocity distribution and the flow regimes in terms of the roughness and turbulence conditions. During the analysis, the velocity distribution coefficients (α, β) were used as indictors to the non-uniformity of the velocity distribution.

For all test cases considered in this work, the velocity distribution coefficients (α, β) were plotted against the aspect ratio (*Ar*) as shown in Figure 6.16. In general, the figure indicates that for a given flow depth (i.e. *Ar* is constant), increasing the roughness causes α and β coefficients to increase. The values of α are ranging from 1.07 to 1.16 in fully rough regimes while α values are varying from 1.05 to 1.13 in the corresponding smooth flow cases. The similar trend can be seen for β values, where β lies within a range of (1.013 – 1.032) in smooth flows and (1.022 - 1.045) in rough flows. This means that the non-uniformity of the velocity distribution in the cases of fully rough flow regimes (i.e $Re^* > 70$) is more considerable than those in hydraulically smooth and transitionally rough flow cases ($Re^* < 70$). On the other hand, for specific flow regime (i.e. constant Re^*), the velocity distribution coefficients (α, β) increase with increase in aspect ratio *Ar*. This is suggested to be related to the effects of secondary currents and turbulence conditions.

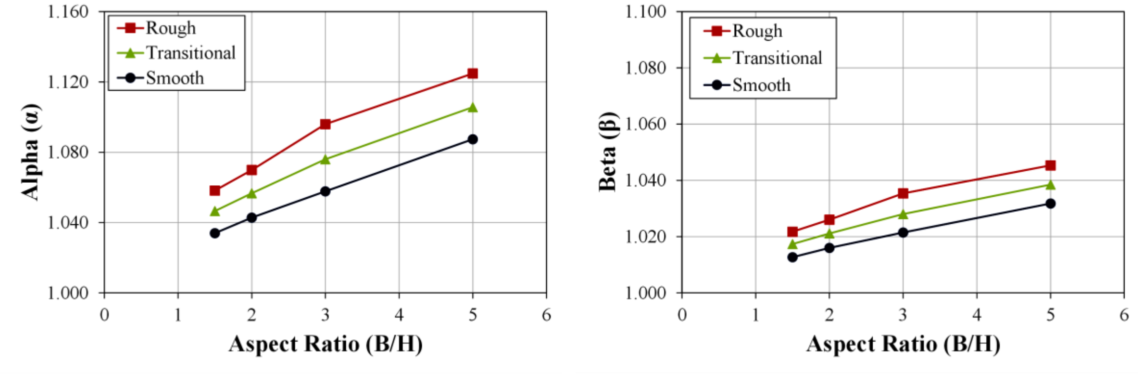

(a) (b)

Figure 6.16 Velocity distribution coefficients (α, β) for all flow regimes.

It is known that generating the turbulence and the secondary currents in rectangular open channels is largely relying on the geometrical properties of the channel, particularly the aspect ratio. Variations α and maximum secondary currents (U_{sec}) with aspect ratio (*Ar*) are shown in Figure 6.17. The figure suggests that for both smooth and rough regimes the values of α increase with increase in the aspect ratio. However, the values of U_{sec} appear to follow reverse trends, where they decrease with increasing the aspect ratio. The reason is when the aspect ratio is small, i.e. the channel is narrow and the flow depth is high, the secondary currents are strong and their effect on the uniformity of velocity distributions is much more than that of the bed roughness. This, in turn, leads to more uniform distribution for velocity and less values for α. In the case of low flows with large values of *Ar*, the secondary currents are less and their effects on the velocity distribution become weaker compared with that of the bed roughness. Therefore, the velocity distributions are less uniform and α values become smaller because of the dominant effect of the bed roughness.

The same effect can be seen in Figure 6.18 for turbulence strength on the uniformity of velocity distribution. Figure 6.18 represents the variations of the velocity coefficient (α) and the normalised eddy viscosity (ν_t/ν) with aspect ratio *Ar*. The figure shows that the velocity distribution coefficient α increases while the eddy viscosity decreases with increase in *Ar*. This clearly suggest that the decrease in the turbulence strength in the cases of large *Ar*, i.e. low flows contribute to increase the non-uniformity of the primary velocity distribution and subsequently the velocity coefficients increase.

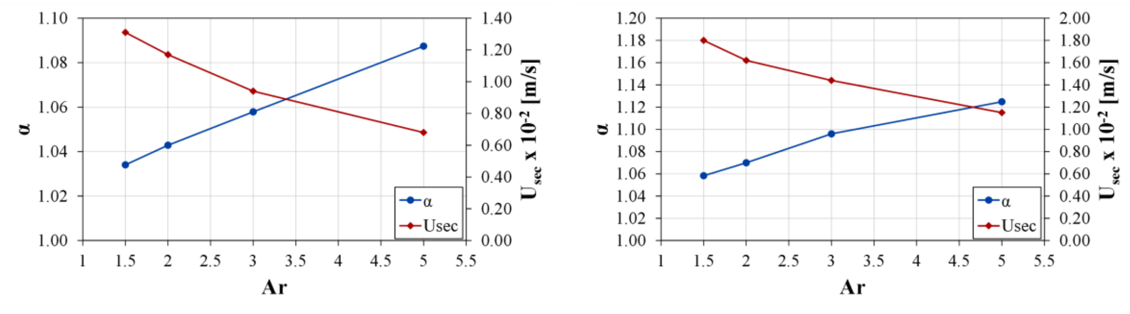

(a) smooth flow (b) rough flow

Figure 6.17 Variations of α and U_{sec} with aspect ratio *Ar*.

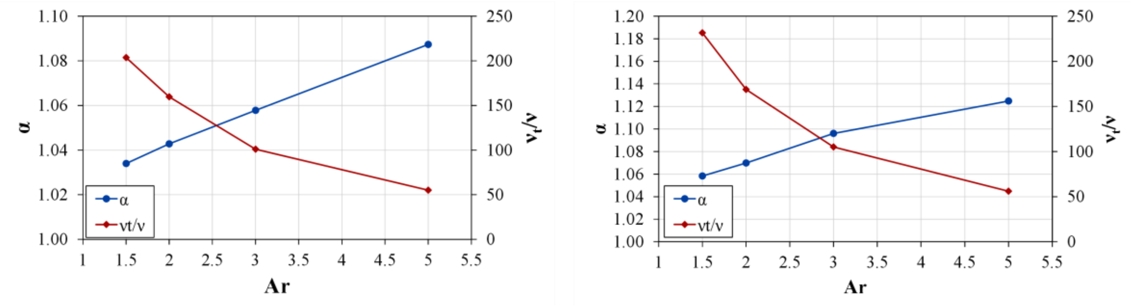

(a) smooth flow (b) rough flow

Figure 6.18 Variations of α and ν_t with aspect ratio *Ar*.

Based on the facts above, it can be concluded that the velocity distribution coefficients (*α* or *β*) can be related to both Roughness Reynolds number (*Re**) and aspect ratio (*Ar* = *B/H*). Figure 6.19 shows the coefficients *α* plotted as a function of the roughness Reynolds number (*Re**) for different aspect ratio (*Ar*), ranging from 1.5 to 5. The figure shows that the relation of the velocity coefficient α to the logarithm of *Re** appears clearly linear and can be expressed as:

$$\alpha = C \log Re^* + D \tag{6.9}$$

where *C* = slope of a line and *D* = intercept of a line. From Figure 6.19, it is also clear that the slopes of all lines for all *Ar* values are nearly similar. Therefore, it can be suggested that *C* = constant. However, there is a different intercept for each line with a specific *Ar*. Thus, it can be claimed that *D* is a function of *Ar*. The values of the parameters *C* and *D* were determined according to Figure 6.19 and given in Table 6.4. The equation provides a relationship by which the non-uniformity of velocity distribution can be measured as a function of the flow regime in terms of roughness, turbulence and secondary currents.

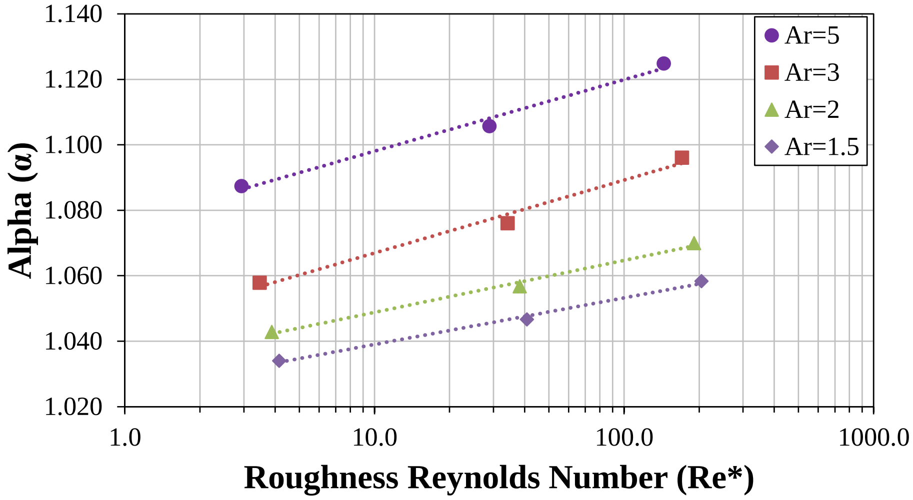

Figure 6.19 Alpha as a function of *Re** and *Ar*.

Table 6.4 The coefficients of equation (6.9) developed in the present study.

Ar	**C**	**D**
5	0.008	1.076
3	0.008	1.044
2	0.008	1.033
1.5	0.008	1.024

6.6 Application of the analytical model to rectangular channels

6.6.1 Discussion of model parameters

In the analytical model (dip-modified log wake law) used in the present study, two parameters need to be characterized. They are the wake strength parameter Π, and the dip correction factor μ. The value of Π can serve as an indicator for the influence of the turbulence, while μ can be considered to represent the effect of the secondary currents on the primary velocity distribution.

Several researchers, e.g. Absi (2011) and Kundu and Ghoshal (2012), showed that the value of Π has a significant effect on velocity predictions obtained by analytical solutions based on the log wake low. Therefore, the values of Π should be estimated carefully. In open channel flows, the value of Π seems to be not universal where many researchers suggested different values of Π. Cebeci and Smith (1974) indicated that Π increases with the Reynolds number, suggesting a constant value of Π = 0.55 at high Reynolds numbers. Coleman (1981) obtained an average value of Π as 0.19, Steffler et al. (1985) as 0.08 – 0.15, and Kirkgöz (1989) as 0.1. Cardoso et al. (1989) recommended a relatively small wake strength parameter (Π ≈ 0.08) for uniform flow in a smooth open channel. Nezu and Rodi (1986) studied the behaviour of Π in flows with different friction Reynolds numbers ($R_h^* = HU_*/\nu$). They indicated that Π increases from zero with the friction Reynolds number R_h^* and take a nearly constant value Π = 0.2 at $R_h^* > 2000$.

The numerical analysis of the eddy viscosity ν_t conducted in the present study demonstrated the dependence of ν_t on Π and confirmed the relation of Π with R_h^*. Therefore, the equation proposed here (Eq. 6.8), which is based on Nezu and Rodi (1986) results, was used to estimate the value of Π from knowing the value of R_h^* for each flow case.

The value of dip correction factor μ can be determined from the distance of the maximum velocity from the bed as follows (Wang et al., 2001):

$$\mu = \frac{1}{\xi_{dip}} - 1 \qquad (6.10)$$

where ξ_{dip} is normalized distance of maximum velocity from the channel bed (z_{max}/H). Experiments have shown that ξ_{dip} is mainly related to the lateral position (y/H) of the measured velocity profiles in the channel (Wang et al., 2001 and Yang et al., 2004). Hence, Yang et al. (2004) proposed an empirical formula for the dip correction factor and can written as follows:

$$\mu = C_1 \exp(-C_2 \frac{y}{H}) \qquad (6.11)$$

At the centreline of the channel, y is equal to 0.5B. Equation (6.11) has been derived for smooth flow regime with $C_1 = 1.3$ and $C_2 = 1.0$.

When applying Eq. (6.11) to smooth flow cases considered here, the estimated values of μ appear to be close to those calculated by Eq. (6.10) based on the measured distance of maximum velocity as shown in Figure 6.20. However, Figure 6.20 also shows that the parameter C_1 in Eq. (6.11) should be reduced from 1.3 to 1.1 to make the equation applicable for rough flow cases. Therefore, Eq. (6.11) was used to calculate μ in smooth, transitional and rough flows, but with different value of C_1 as listed in Table 6.5.

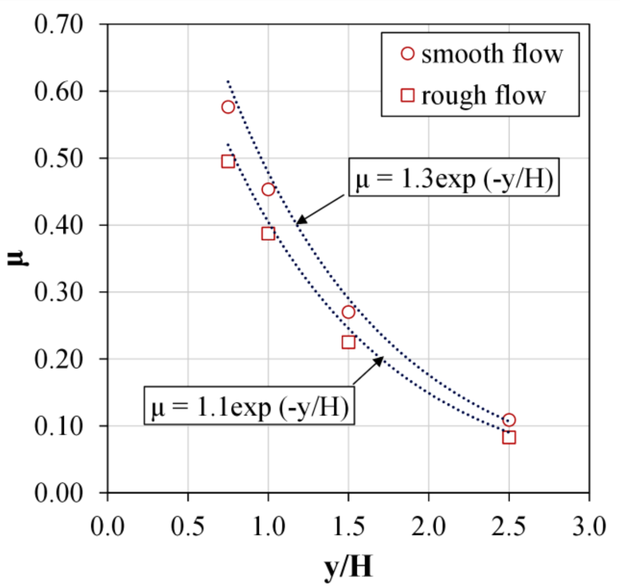

Figure 6.20 Relationship between μ and z/H for smooth and rough flow cases.

Table 6.5 Values of C1 and C2 parameters of Eq. (6.11) corresponding to each flow regime.

Flow regime	C1	C2
Smooth	1.3	1.0
Transitional	1.2	1.0
Rough	1.1	1.0

The validity of the equations proposed for estimating the values of Π and μ are tested in the next section throughout applying the analytical model to the flow cases considered in the present study.

6.6.2 Comparison with experimental data

The analytical dip-modified log wake law (DMLWL) given by Eq. (5.19) was used to obtain the velocity distribution for all flow cases considered in this study. When the analytical model was applied, the wake strength parameter, Π, and dip correction factor, μ, were determined using Eqs. (6.8) and (6.11), respectively, based on experimental data. The values of Π and μ calculated by Eqs. (6.8) and (6.11) are summarised in Table 6.6.

Table 6.6 Values of Π and μ used in the analytical model for rectangular channel flows.

Case No.	Re_h^*	Π from Eq. (6.8)	μ from Eq. (6.11)
S6	947.62	0.11	0.11
S10	1825.03	0.19	0.29
S15	2947.68	0.25	0.48
S20	4205.07	0.29	0.61
T6	885.72	0.10	0.10
T10	1801.23	0.19	0.27
T15	3089.01	0.25	0.44
T20	4456.81	0.30	0.57
R6	913.16	0.10	0.09
R10	1867.41	0.19	0.25
R15	3294.32	0.26	0.40
R20	4768.19	0.31	0.52

Figures (6.21), (6.22) and (6.23) compare the predicted velocity profiles obtained by the dip-modified log wake law (DMLWL) with the experimental data of smooth, transitional and rough flow cases. In all Figures, two values of Π were used, one was calculated from the equation (6.8) proposed in this study and the other value is assumed to be a constant as 0.2.

The application of the analytical model (DMLWL) to smooth cases (Figure 6.21) shows that the model is generally able to reproduce the experimental velocity distributions. Also, it can be seen that the dip-phenomena in high flow cases, i.e. S15 and S20, is reasonably modelled by the analytical model together with μ calculated by Eq. (6.11). However, there is some differences between the predicated and measured velocities in the upper part of the flow ($z/H > 0.7$). These differences may be attributed to imperfections of the measuring technique, as velocity measurements are difficult to measure in accurate way near the free surface.

Furthermore, it should be noted that the value of Π plays an important role in obtaining accurate solutions for velocity distributions. For low flow cases (S6 ~ S10), where the friction Reynolds number is less than 2000, the analytical profiles with Π calculated by Eq. (6.8) are more consistent with the experimental data than the profile based on a constant value of Π, i.e. Π = 0.2. In contrast, Figure 6.21 clearly shows that the value of Π has no influence on the analytical solutions for high flow cases (S15 and S20), i.e. the cases with high friction Reynolds number (Re_h^*). For these flow cases, the velocity profiles obtained analytically do not agree well with the experimental data when Π calculated from Eq. (6.8) were used. However, when Π remains constant at 0.20, the analytical profiles for velocity improved and come closer to the experimental profiles. These results confirm the suggestion of depending the eddy viscosity and then Π on the friction Reynolds number Re_h^* up to a certain value (< 2000). After this limit of Re_h^*, Π takes a constant value at 0.2 even though Re_h^* increases.

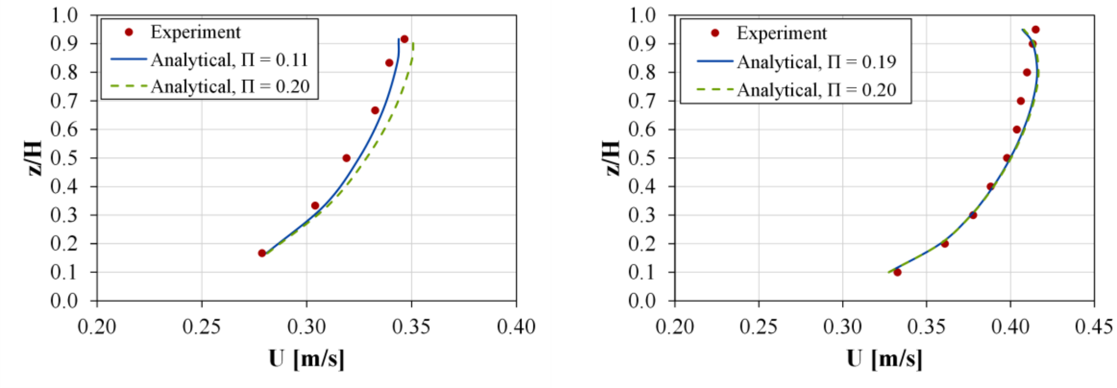

(a) S6 (H = 6 cm)

(b) S10 (H = 10 cm)

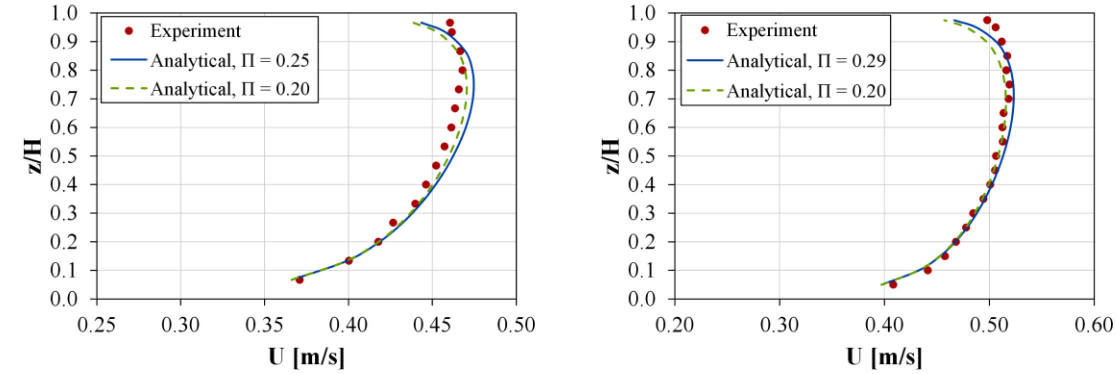

(c) S15 (H = 15 cm)

(d) S20 (H = 20 cm)

Figure 6.21 Comparison between analytical and experimental vertical distributions of *U* for smooth flow cases.

For comparison, the application of the analytical model to the transitional and rough flow cases has also been undertaken, as illustrated in Figures (6.22) and (6.23). Both figures show that the analytical model can successfully predict velocity distributions for flows over rough surfaces. It is also clear from the two figures that the DMLWL is able to predict the maximum velocity and its position with an accepted degree of accuracy. This means that the modification made on Eq. (6.11) by reduce the value of C_1 make the equation applicable to calculate the dip correction factor μ in smooth and rough flows as well. In addition, Figures (6.22) and (6.23) show the same influence of Π on the analytical results that was shown in smooth flow cases. The figures indicate that using Π based on Eq. (6.8) gives good predicted velocity profiles in the cases of low flows (T6, R6). But for high flows (T20, R20), keeping Π constant at 0.20 lead to the best agreement between the analytical and experimental results. This clearly illustrates the effects of friction on estimating the value of Π and then on the results of the analytical solutions.

In summary, the results indicate that the methods suggested in the present study to calibrate the parameters (Π and μ) may provide efficiency to the application of the analytical model for rectangular channel flows under different flow regimes.

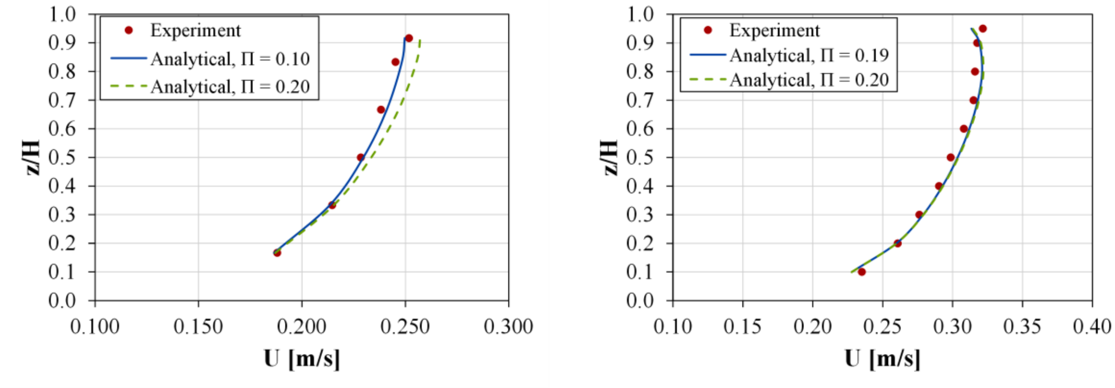

(a) T6 (H = 6 cm)

(b) T10 (H = 10 cm)

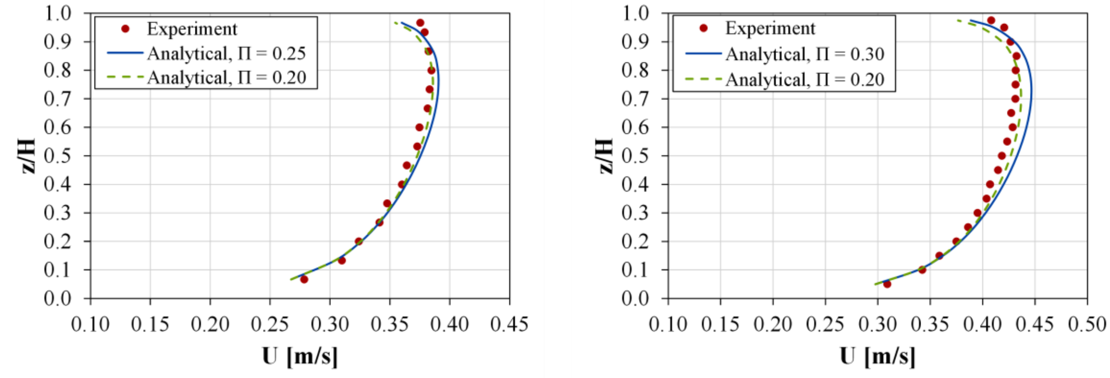

(c) T15 (H = 15 cm)

(d) T20 (H = 20 cm)

Figure 6.22 Comparison between analytical and experimental vertical distributions of *U* for transitional flow cases.

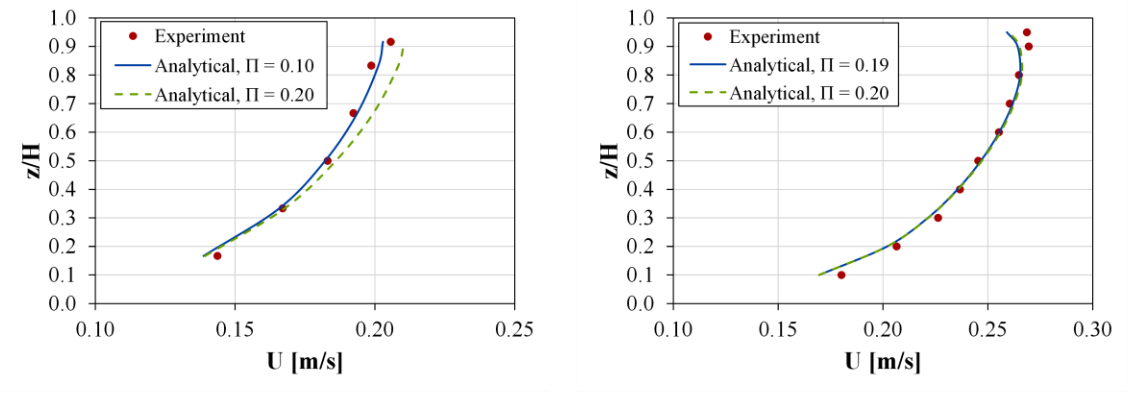

(a) R6 (H = 6 cm)

(b) R10 (H = 10 cm)

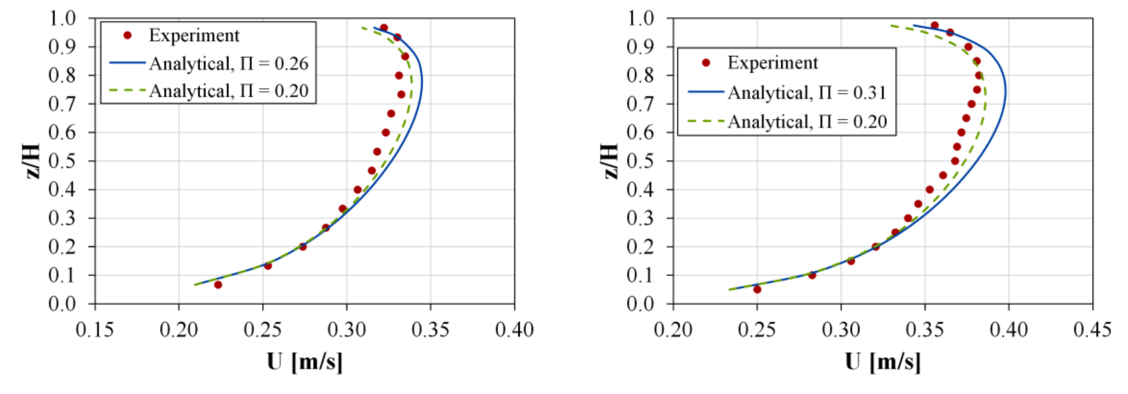

(c) R15 (H = 15 cm)

(d) R20 (H = 20 cm)

Figure 6.23 Comparison between analytical and experimental vertical distributions of *U* for rough flow cases.

Chapter 7

Results for Compound Channel Flows

7.1 Introduction

In this chapter, the predicted CFD results for the compound channel flows were validated and described in accordance with the findings obtained by the second set of experiments. First, the CFD results for primary and secondary flows was validated by comparing the computed results with experimental data. second, numerical analysis of momentum transfers due to the turbulence and secondary flows was carried out. Third, the primary flow in a compound channel was investigated by examining the effects of boundary roughness, secondary flow and turbulence on the velocity distribution coefficients (α and β). Finally, the application of the analytical model (SKM) to a compound channels with a narrow floodplain was assessed and improved by developing the expressions used for calibrating the parameters of the eddy viscosity and secondary currents.

7.2 Verification of CFD results

7.2.1 Results for primary flow

In this section, the vertical and lateral distributions of the primary velocity obtained numerically by the CFD model were compared with the experimental results to verify that the CFD model can reproduce the primary velocity fields for the flow cases considered in this study.

Figure 7.1 shows the comparison between the measured and predicted primary velocity profiles at different locations for two test cases, namely CS0.40 and CR0.40. In the case CS0.40, the compound channel has a smooth floodplain, while the floodplain is rough in the case CR0.40. It can be seen that the computed mean velocity profiles agree reasonably well with the measured data for both simulated cases. However, the CFD model predicts the velocity profiles more accurately at some locations than does at other locations. For example, the velocity profiles are better predicted near the wall (y/B = 0.2) and the middle of the main channel (y/B = 0.3) than at the location (y/B = 0.5) near the junction between the main channel and floodplain. It is known that the prediction and also measurements of the flow features are rather hard at a location in the junction zone. Therefore, this may be a reason for the differences between the predicted and the measured profiles at locations within the junction zone. Figure 7.1 also shows that the primary velocity in the main channel is greatly affected by the wall while it is not in the floodplain. Both CFD and experiment results indicate that the maximum velocity occurs below the free surface at the location near the wall due to the wall effects. On the other hand, in the floodplain, the primary velocity increases significantly with flow depth.

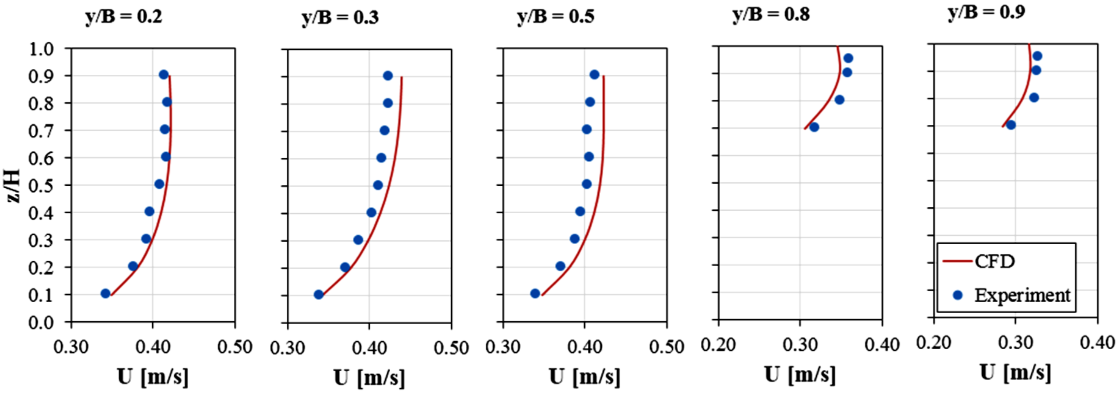

(a) Case CS0.40

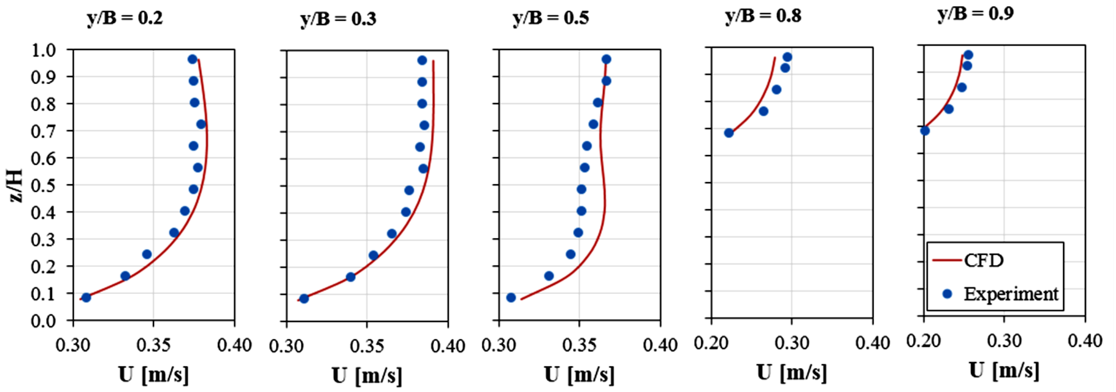

(b) Case CR0.40

Figure 7.1 Vertical distribution of primary velocity at different locations.

Figures 7.2, 7.3 and 7.4 show the comparison between the predicted and measured lateral distribution of the depth-averaged velocity for all test cases. The agreement between the predicted and measured data is reasonably well for all cases, indicating the CFD model can acceptably reproduce the lateral distribution of the depth-averaged velocity. However, it should be noted that the predicated results for velocity over the floodplain is not as the same level of the accuracy as that in the main channel. This little difference in predictive ability for the velocity over the floodplain can be argued if the error for the experimental results in this region is also considered.

Based on the comparisons above, it can be concluded that the numerically predicted primary flow is very close to the experimental measurements and this is essential for the accurate prediction of the overall magnitude and variations of the other velocity components (*V* and *W*) as well as the secondary flow.

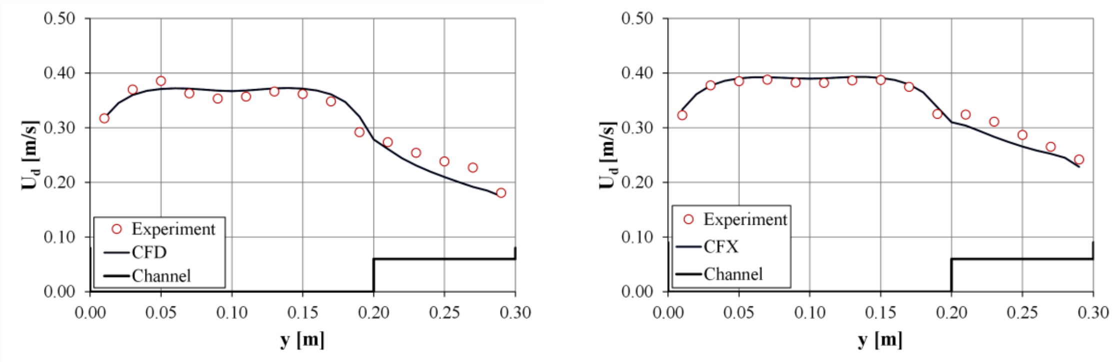

(a) CS0.25 (*Dr* = 0.25)

(b) CS0.33 (*Dr* = 0.33)

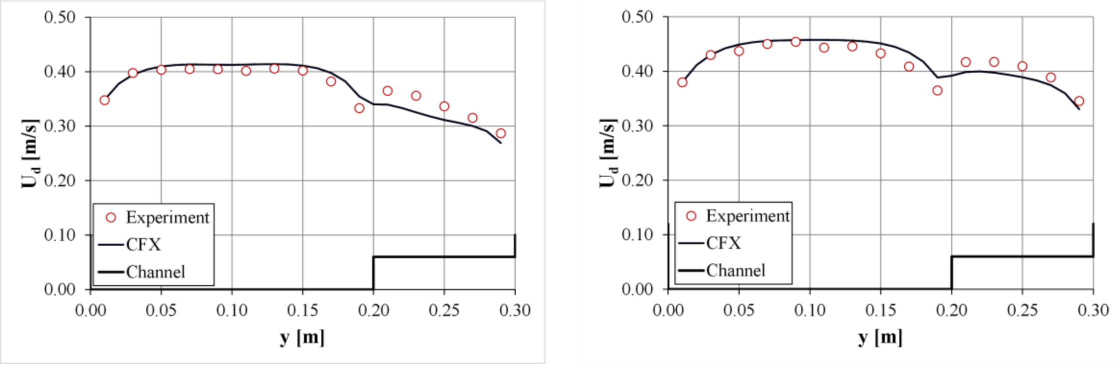

(c) CS0.40 (*Dr* = 0.40)

(d) CS0.50 (*Dr* = 0.50)

Figure 7.2 Lateral distribution of primary velocity for smooth floodplain cases.

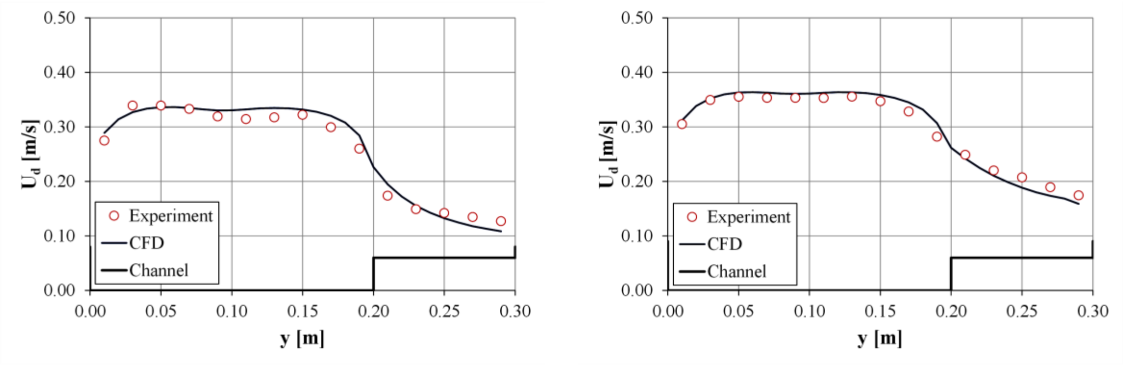

(a) CT0.25 (*Dr* = 0.25)

(b) CT0.33 (*Dr* = 0.33)

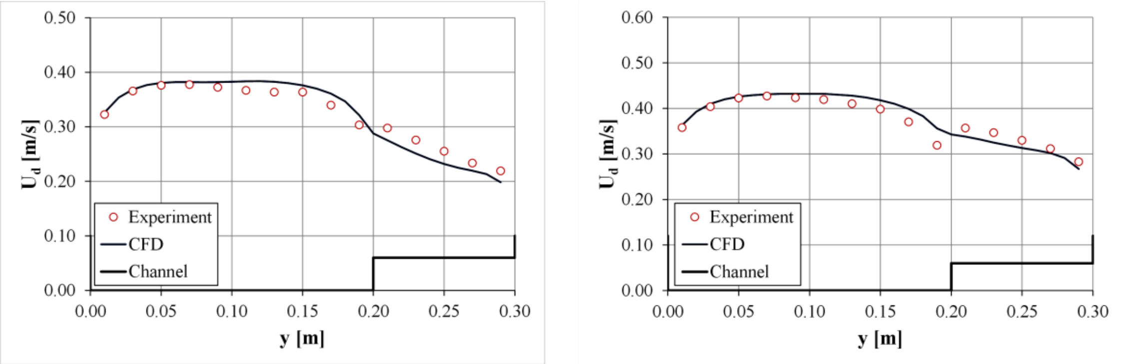

(c) CT0.40 (*Dr* = 0.40)

(d) CT0.50 (*Dr* = 0.50)

Figure 7.3 Lateral distribution of primary velocity for transitionally rough floodplain cases.

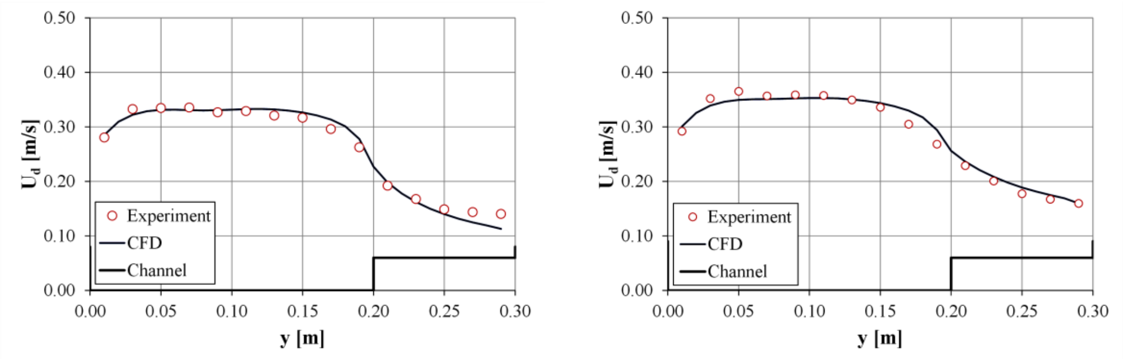

(a) CR0.25 (*Dr* = 0.25)

(b) CR0.33 (*Dr* = 0.33)

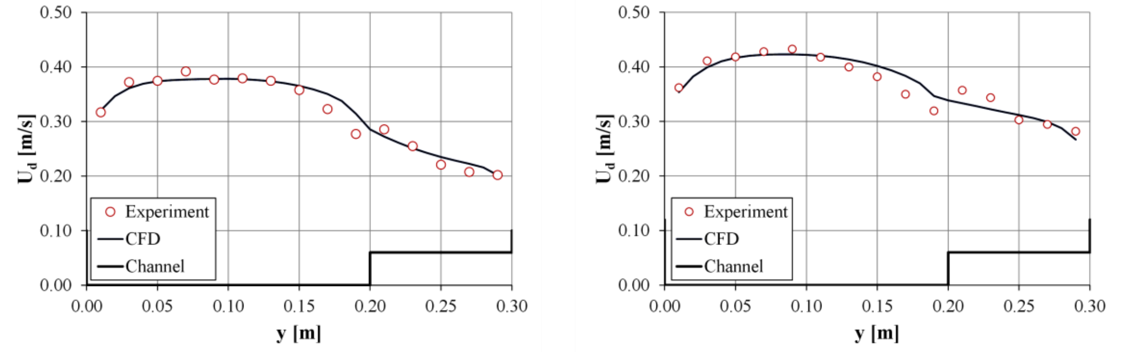

(c) CR0.40 (*Dr* = 0.40)

(d) CR0.50 (*Dr* = 0.50)

Figure 7.4 Lateral distribution of primary velocity for fully rough floodplain cases.

7.2.2 Results for secondary flow

Figures 7.5 and 7.6 show the secondary current vectors for smooth and transitionally rough floodplain cases with relative depth *Dr* = 0.50, i.e. the cases CS0.50 and CT0.50. In these figures the CFD solutions for secondary currents were compared with the experimental results obtained by Tominaga and Nezu, (1991) from experiments on compound channels have similar relative depth and roughness conditions to the channels used in the present study. In both figures, it can be seen that typical patterns of secondary flow in a compound channel are well predicted. Strong inclined secondary currents near the junction edge between the main channel and floodplain and twin vortices at each side of the junction clearly apparent in the CFD predictions as in the experimental results. These pair of vortices are called the main-channel vortex and the flood-plain vortex. Also, it should be noted that the floodplain vortex slightly moves towards the main channel in the cases of rough floodplain. This feature is seen in both numerical and experimental results, but it is clearer in the CFD results than in the experiment. The movement of the secondary cell over the floodplain to main channel side may be attributed to the roughness effects.

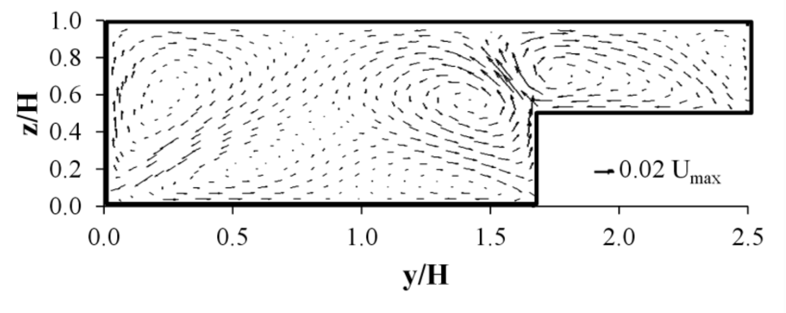

(a) CFD model (present study)

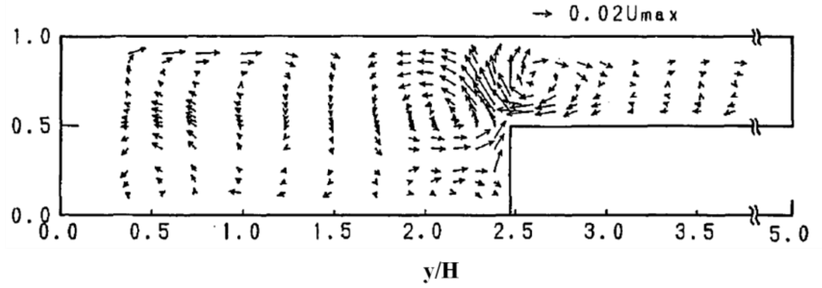

(b) Experiment (Tominaga and Nezu, 1991)

Figure 7.5 Predicted and measured secondary flow for smooth floodplain case.

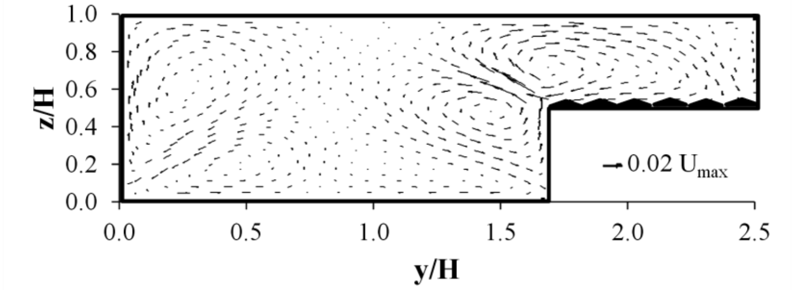

(a) CFD model (present study)

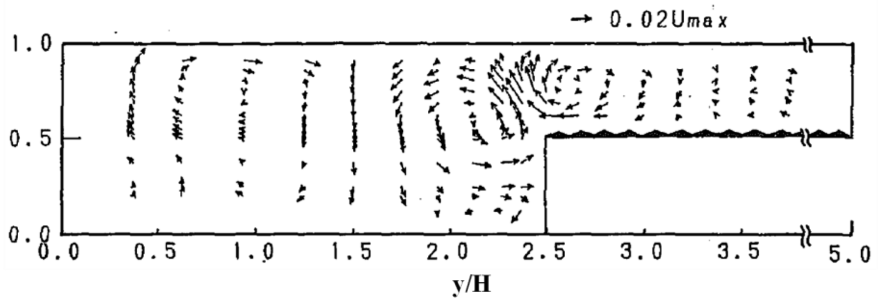

(b) Experiment (Tominaga and Nezu, 1991)

Figure 7.6 Predicted and measured secondary flow for transitionally rough floodplain case.

The magnitude of the computed secondary flows is very small compared with the primary flow, with many points being characterized by values of less than 2% of the maximum primary velocity (U_{max}). The maximum magnitudes of secondary velocity for all cases simulated are found to be within the range (3.5% to 5.5%) of the maximum mean streamwise velocity. These results are nearly of the same order of the secondary velocities (about 5%) estimated by Tominaga & Nezu, (1991).

As a conclusion of this comparisons, the CFD simulation fairly predicts the complex features of secondary currents in terms of the number and locations of secondary cells observed in many literature studies, e.g. Tominaga & Nezu, (1991) and Nezu and Nakagawa (1993).

7.3 Impact of roughness conditions on secondary currents

The comparisons of the secondary currents for smooth, transitional rough, and fully rough floodplain are given in Figures 7.7 and 7.8. The first figure shows the vector description of the secondary currents which are obtained from CFD simulation for the cases CS0.25, CT0.25 and CR0.25, which have the smallest relative depth, i.e. $Dr = 0.25$. Irrespective of the roughness conditions of the floodplain, a pair of secondary cells can be recognized on both sides of the interface between the main channel and floodplain. However, the core of the main channel vortex shifts towards the internal wall of the channel and to below away from the water surface in the rough floodplain case. When the floodplain is rough, as in cases CT0.25 and CR0.25, the floodplain vortex becomes larger and extends inside the main channel, causing the main channel vortex to shift towards the bottom of the channel. This is suggested to be a consequence of the effect of the rough bed of the flood plain on the secondary filed structures. The same behaviour of the main channel and floodplain vortices can be seen in the cases of the high flow with larger $Dr = 0.50$, as shown in figure 7.8. But the size of secondary cells in these cases are larger than those in the low flow with $Dr = 0.25$. The same effect for the roughness on the patterns of the secondary vortices was found by Tominaga and Nezu (1991) in the rectangular compound channel.

The shift in secondary vortices may consequently affected the mean streamwise velocity contours as shown in Figures 7.7 and 7.8. From the figures, it can be seen that the velocity contour of the primary velocity within the junction zone bulges horizontally when the floodplain is transitionally or fully rough.

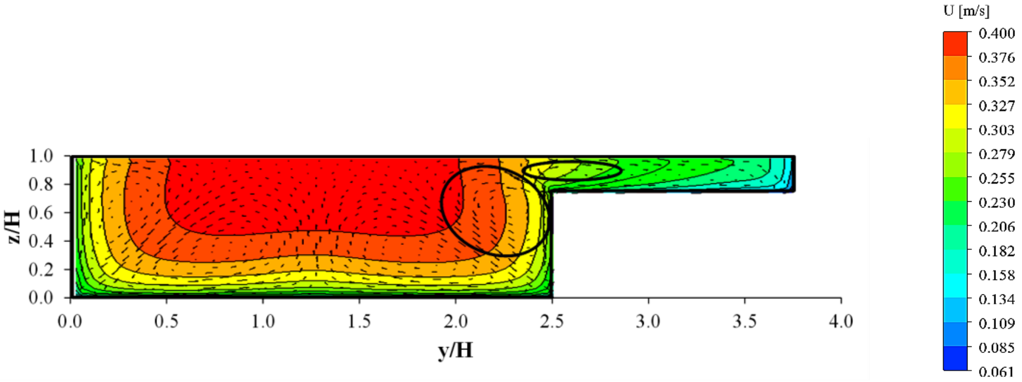

(a) CS0.25

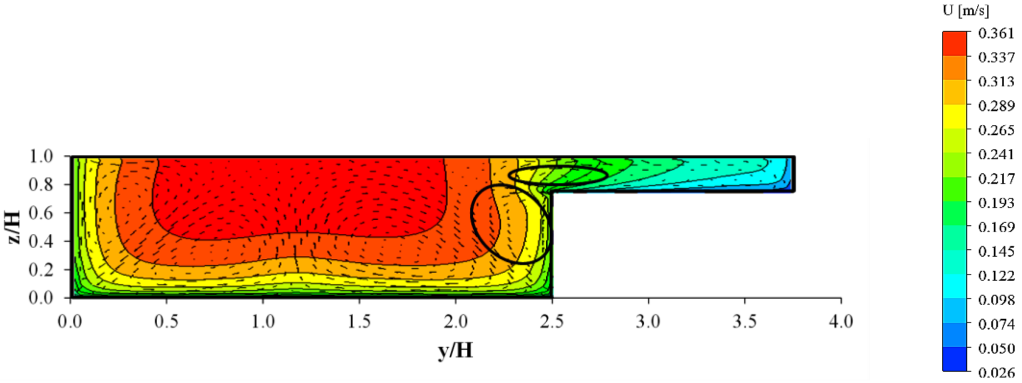

(b) CT0.25

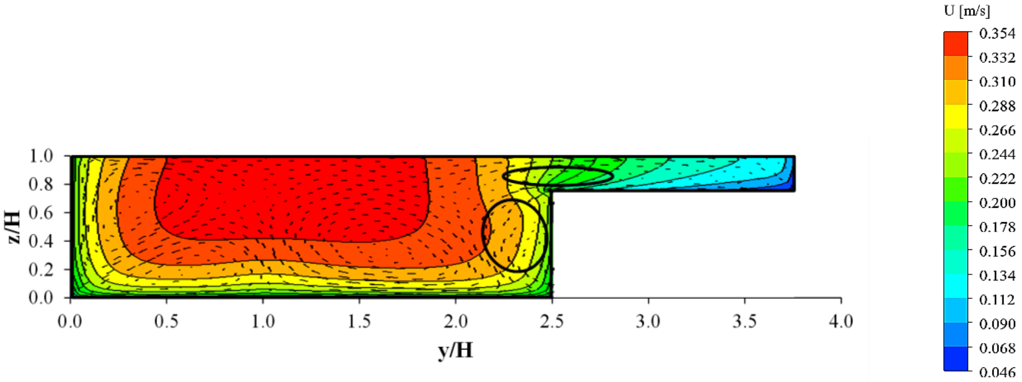

(c) CR0.25

Figure 7.7 Impact of roughness conditions on secondary currents in cases of *Dr* = 0.25.

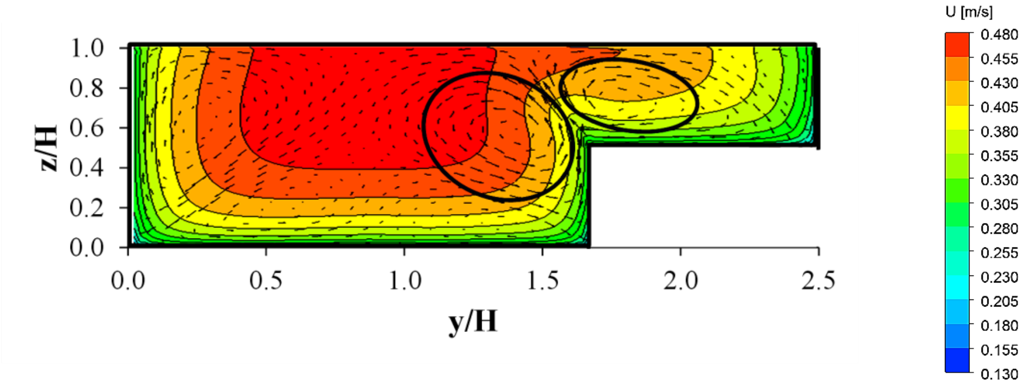

CS0.50

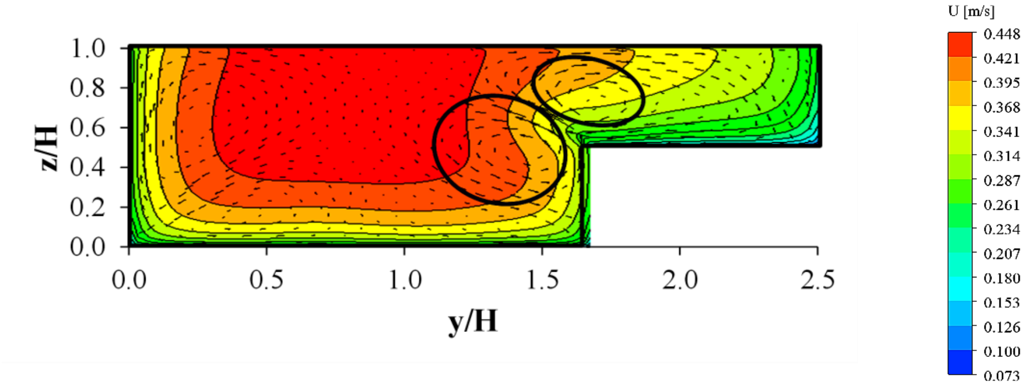

CT0.50

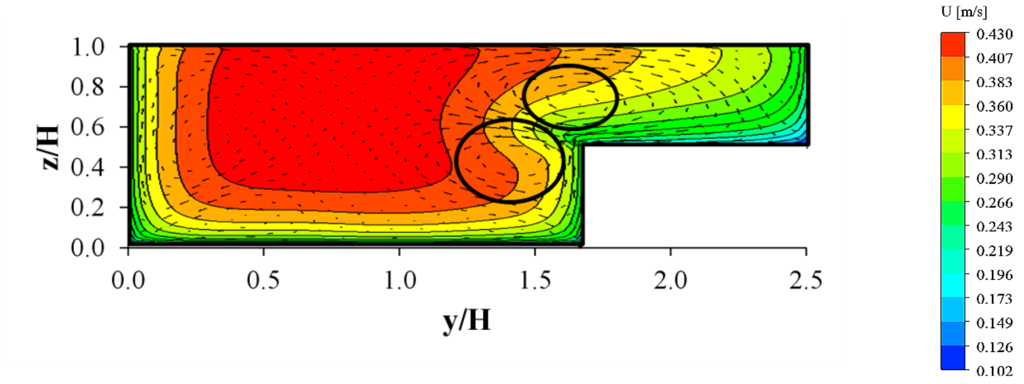

CR0.50

Figure 7.8 Impact of roughness conditions on secondary currents in cases of *Dr* = 0.50.

7.4 Numerical analysis of momentum transfers due to turbulence

The lateral Reynolds stress ($\tau_{yx} = -\rho\overline{u'v'}$) is also of significance on the primary flow because it is directly related to the lateral momentum transfer. In this section, the depth-averaged Reynolds shear stress ($\bar{\tau}_{yx}$) and depth-averaged eddy viscosity (ε_t) were calculated from the measurements of the velocity and friction data based on some assumptions. The calculated results of $\bar{\tau}_{yx}$ and ε_t were then compared with those numerically obtained from CFD simulations to check the approach used. An analysis was also made to investigate the effects of the floodplain roughness conditions on the depth-averaged eddy viscosity, which can be used as a parameter to characterise the lateral momentum exchange in the shear layer.

7.4.1 Computation method of depth-averaged Reynolds shear stress

The depth-averaged Reynolds shear stress is related to the depth-averaged eddy viscosity and the velocity gradient through the following equation:

$$\bar{\tau}_{yx} = \rho\varepsilon_t \frac{\partial U}{\partial y} \tag{7.1}$$

Using the mixing layer approach, Alavian and Chu (1985) proposed a model by taking the effects of both the bed-generated turbulence and shear-generated turbulence into account. Based on the Alavian and Chu model, Prooijen et al (2005) recently adopted the eddy viscosity concept and proposed a similar model. This eddy viscosity model was developed from experimental data and therefore it is expected to be applicable in similar experimental conditions such as those in this work. Therefore, the model by Prooijen et al. (2005) was used in the present study.

According to Prooijen et al. (2005), both bottom turbulence and lateral shear contribute to the eddy viscosity. The depth-averaged eddy viscosity (ε_{tb}) due to the bottom turbulence and that (ε_{ts}) due to the lateral shear can be modelled as follows:

$$\varepsilon_{tb} = \lambda_{tb}\left(\frac{f}{8}\right)^{1/2} U_d H \tag{7.2}$$

$$\varepsilon_{ts} = \frac{H_m}{H}(0.08\delta)^2 \left|\frac{\partial U_d}{\partial y}\right| \tag{7.3}$$

where λ_{tb} is the dimensionless depth-averaged eddy viscosity, U_d is the depth-averaged longitudinal velocity, f is the friction factor, H_m is the mean value of the water depth in the main channel and on the floodplain and δ is the width of the shear layer. For a laboratory flume, the value of λ_{tb} was assumed as 0.07 (Rameshwaran & Shiono 2006).

The width of the shear layer (δ) is determined from the distance between the positions $y_{75\%}$ and $y_{25\%}$, as follows:

$$\delta = 2|y_{75\%} - y_{25\%}| \tag{7.4}$$

where $y_{75\%}$ is the position at which $U(y_{75\%}) = \overline{U}_f + 0.75(\overline{U}_c - \overline{U}_f)$ and $y_{25\%}$ is the position at which $U(y_{25\%}) = \overline{U}_f + 0.25(\overline{U}_c - \overline{U}_f)$. $\overline{U}_c$ and $\overline{U}_f$ are the maximum velocity in the main channel and the floodplain respectively.

Velocity gradient ($\partial U_d/\partial y$) is calculated from two adjacent depth-averaged velocities from the following approximate formula:

$$\frac{\partial y}{\partial x} \approx \frac{U_{d,i} - U_{d,i-1}}{dy} \tag{7.5}$$

where $U_{d,i}$ and $U_{d,i-1}$ are depth-averaged velocities at $y = y_i$ and $y = y_{i-1}$.

By considering both the bed-generated turbulence and shear-generated turbulence the depth-averaged eddy viscosity (ε_t) can be expressed as follows:

$$\varepsilon_t = \varepsilon_{tb} + \varepsilon_{ts} \tag{7.6}$$

Eddy viscosity and Reynolds shear stress were calculated using the above methods based on raw experimental data for velocity, water depth and bed friction.

7.4.2 Lateral distribution of depth-averaged eddy viscosity

The lateral distributions of the depth-averaged eddy viscosity (ε_t) in compound channel cases with *Dr* of 0.25 and 0.50 are shown in Figures 7.9 and 7.10. In the figures, the eddy viscosity (ε_{tb}) calculated by considering the bed-turbulence contribution only are also presented. From Figure 7.9, the depth-averaged eddy viscosities (ε_t), considering the shear and bed turbulence contributions, are larger than those calculated without accounting for the shear contribution (ε_{tb}). It can also be seen that the eddy viscosities at the main channel/floodplain junction increase significantly when the floodplain is rough, indicating an increase in the lateral shearing between the main channel and floodplain flows. The increase of the floodplain roughness changes the primary velocity gradient and then this increases the lateral shear and generation rate of the turbulent energy.

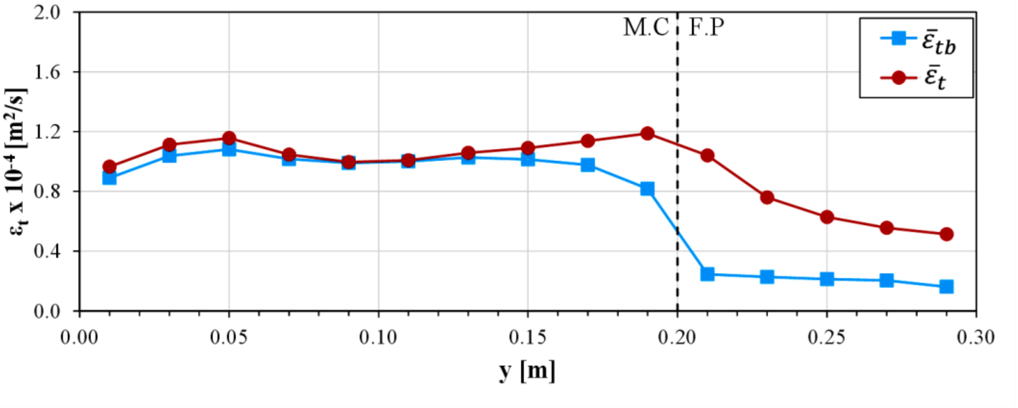

(a) Smooth floodplain (CS0.25)

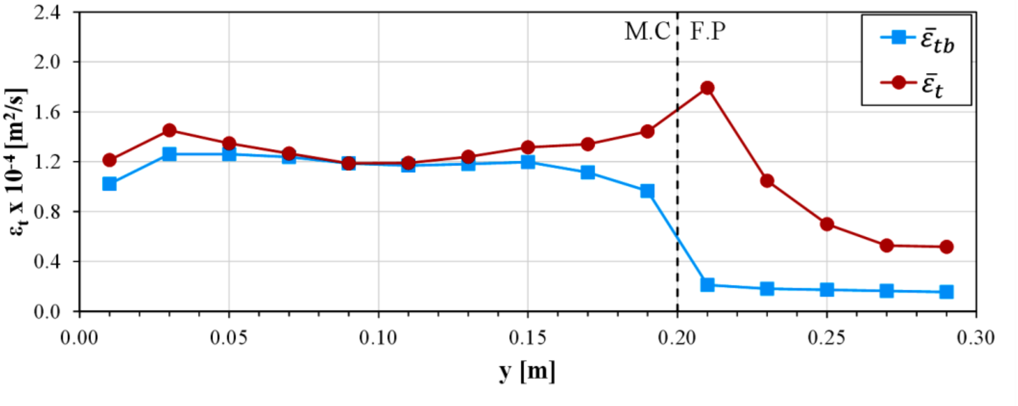

(b) Transitional floodplain (CT0.25)

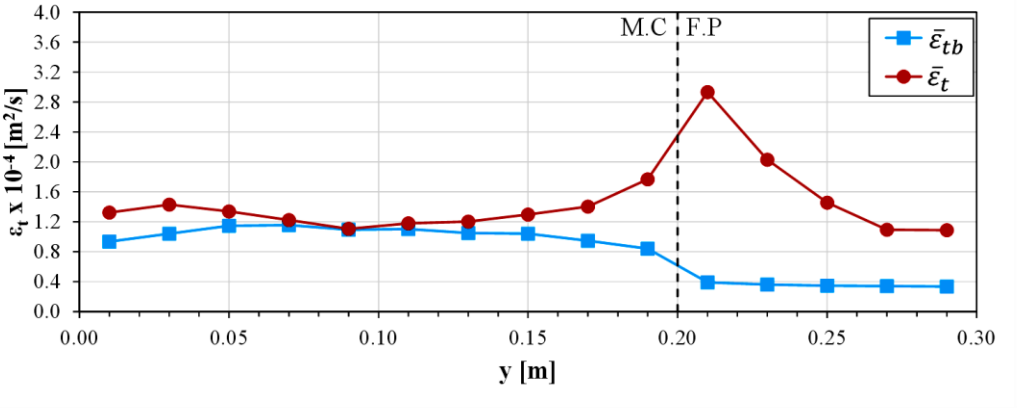

(c) Rough floodplain (CR0.25)

Figure 7.9 Lateral distribution of depth-averaged eddy viscosity for cases of *Dr* = 0.25.

From Figure 7.10, the eddy viscosities (ε_t) for the high flow cases (*Dr* = 0.50) behave in a different manner to those for low flow cases (*Dr* = 0.25). The distributions of ε_t, which are calculated based on the combined effects of the bed and shear generated turbulence, diverge slightly from the distribution of ε_{tb}, which calculated by accounting for the bed generated turbulence only. This indicates that the contribution of the lateral shear to the eddy viscosity is limited even in the case of the rough floodplain, i.e. CT0.5 and CR0.5.

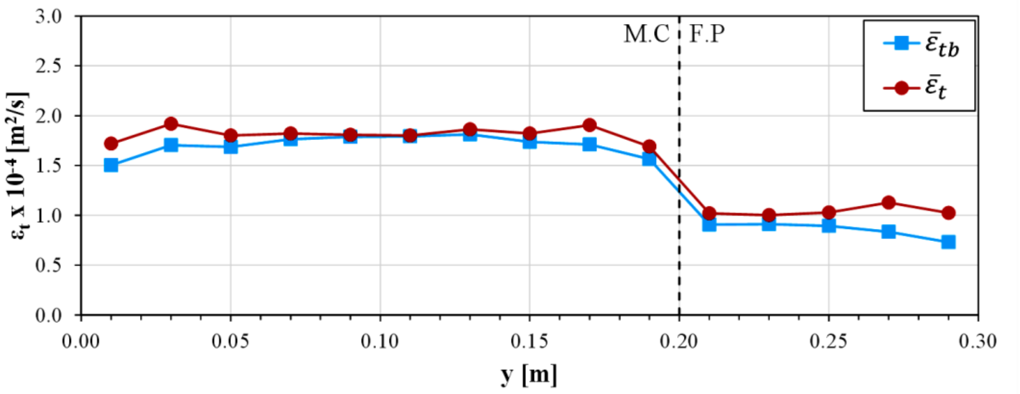

(a) Smooth floodplain (CS0.50).

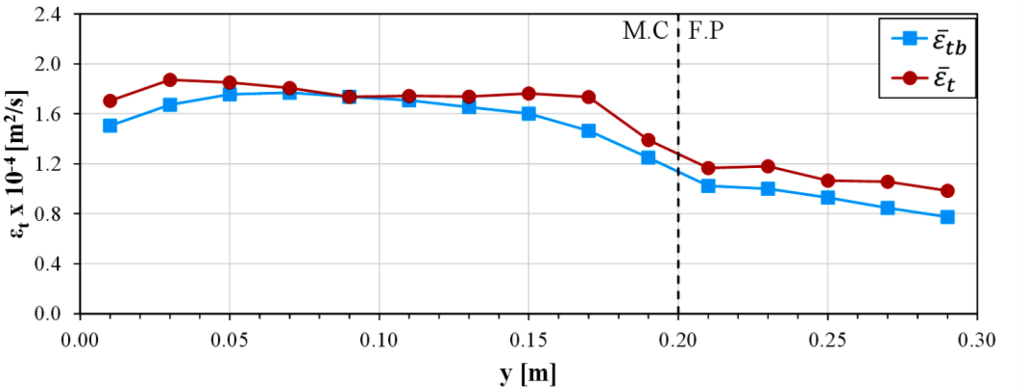

(b) Transitional floodplain (CT0.50).

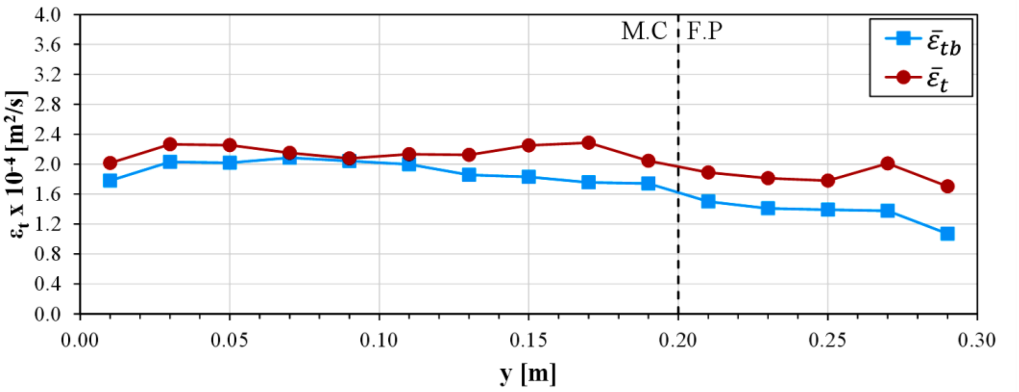

(c) Rough floodplain (CR0.50).

Figure 7.10 Lateral distribution of depth-averaged eddy viscosity for cases of *Dr* = 0.50.

The mean values of the eddy viscosities (ε_t and ε_{tb}) in the main channel and the floodplain for the cases of small and large *Dr* are given in Table 7.1. The results in Table 7.1 indicate that the effect of roughness in small relative depth cases (*Dr* = 0.25) is to change the mean value of the eddy viscosity ε_t in the main channel from 1.08 to 1.33 m^2/s and in the floodplain from 0.70 to 1.72 due to increasing the lateral shear. In the cases of the larger relative depth, the change of the mean values of ε_t due to roughness effects is relatively small with values varying from 1.73 to 2.16 m^2/s in main channel and from 1.04 to 1.84 m^2/s in flood plain region. It should be noted that the mean eddy viscosity calculated based on only bottom turbulence also increase in both flow regions when the roughness of floodplain increase. This is not surprising because ε_{tb} is defined as function of the friction parameter (*f*) which is large for the rough floodplain cases. The results of Table 7.1 also illustrate that the mean values of the eddy viscosity in both flow regions, i.e. the main channel and the floodplain, are increased when the lateral shear-generated turbulence contribution is included in calculating the eddy viscosity.

Table 7.1 Mean values of the eddy viscosity in cases of small and large *Dr* (10^{-4} m^2/s).

		Main channel		Floodplain	
Case	*Dr*	ε_t	ε_{tb}	ε_t	ε_{tb}
CS0.25	0.25	1.08	0.99	0.70	0.18
CT0.25	0.25	1.30	1.04	0.92	0.21
CR0.25	0.25	1.33	1.16	1.72	0.35
CS0.50	0.50	1.73	1.61	1.04	0.86
CT0.50	0.50	1.81	1.71	1.09	0.92
CR0.50	0.50	2.16	1.91	1.84	1.35

The above results of eddy viscosity indicate that the shear contribution to the eddy viscosity is very important when the flow is shallow with small relative depth, i.e. *Dr* = 0.25. The results also show that the effect of the lateral shear on the eddy viscosity increase in the compound channel with rough floodplain.

7.4.3 Lateral distribution of depth-averaged Reynolds stress

The lateral distributions of the depth-averaged Reynolds stress ($\bar{\tau}_{yx}$) for smooth and rough floodplain cases with two different relative depths (*Dr* = 0.25 and 0.50) are shown in Figures 7.11 and 7.12. The later distributions of $\bar{\tau}_{yx}$ that obtained from the CFD simulations were also compared with those calculated by the experiment-based method for verification purposes. Equations 7.1 to 7.6 were used in calculating $\bar{\tau}_{yx}$ based on the experimental results of the velocity and bed friction.

In the case of *Dr* =0.25, i.e. Figure 7.11, the predicted CFD value is almost similar to the one calculated experimentally for the three roughness conditions. With an increase of the floodplain roughness, the predicted and experimentally calculated values of τ_{yx} increase in the lateral shear region. The same degree of agreement between the predicted and experimentally calculated lateral distributions of τ_{yx} can also be seen for the case of large *Dr* (= 0.50). However, in the case of small *Dr*, i.e. CS0.25 – CR0.25, the peak of the depth-averaged Reynolds stress is slightly different in terms of the magnitude and the position, where the CFD model underestimates the peak value at the interfacial region. This underestimation of the Reynolds stress in the interfacial region may be caused by the fact that the approximate method used for calculating eddy viscosity relies on the approximation of the velocity gradients. It is suggested that the present turbulence model (BSL-RSM model) can predict the depth-averaged with an accepted degree of accuracy because such model solves transport equations of Reynolds stresses directly. Therefore, the present turbulence model (RSM model) can be used to estimate the momentum transfers due to the secondary currents, as is presented in the next section.

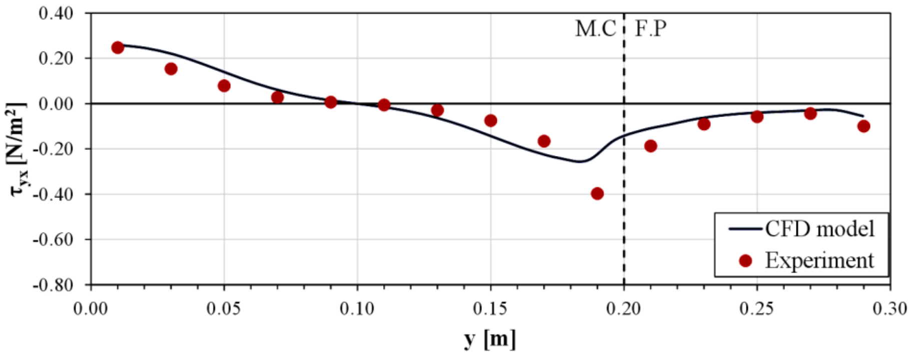

(a) Smooth floodplain (CS0.25)

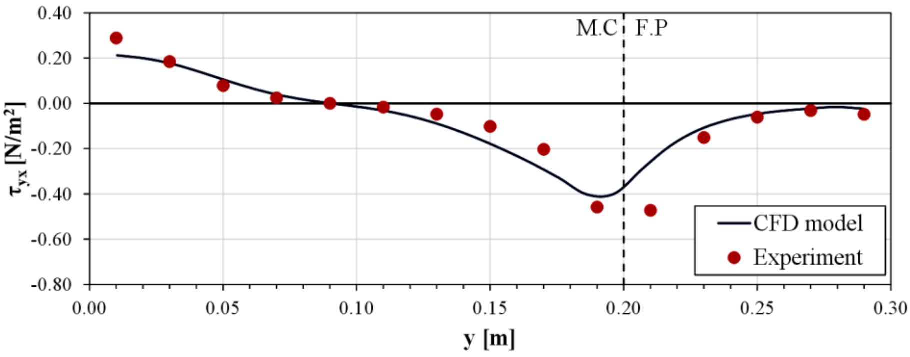

(b) Transitional floodplain (CT0.25)

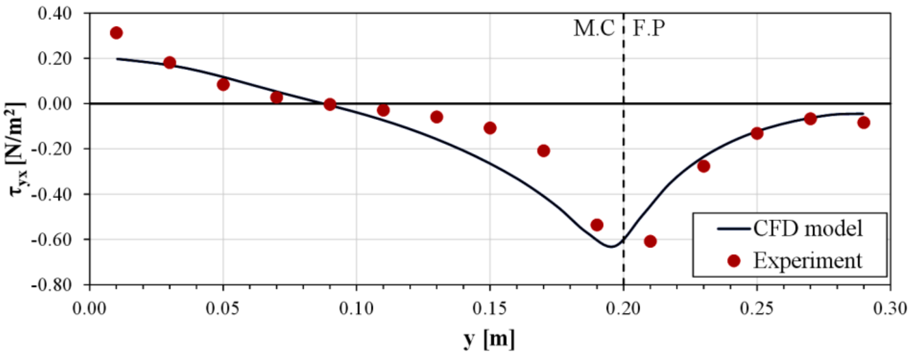

(c) Rough floodplain (CR0.25)

Figure 7.11 Lateral distribution of depth-averaged Reynolds stress (τ_{yx}) for Cases of *Dr* = 0.25.

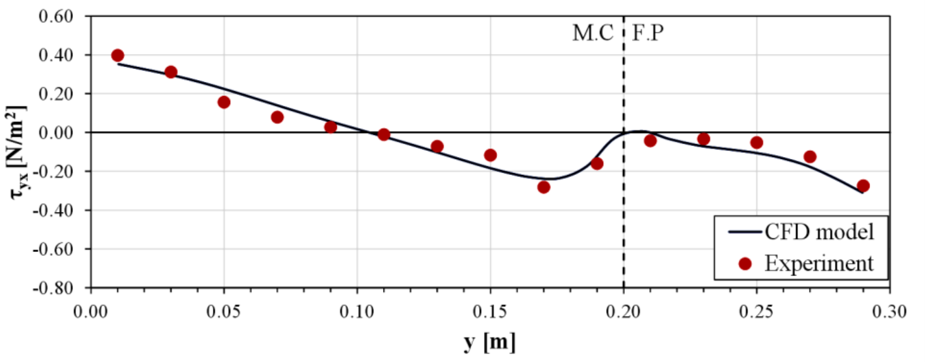

(a) Smooth floodplain (CS0.50)

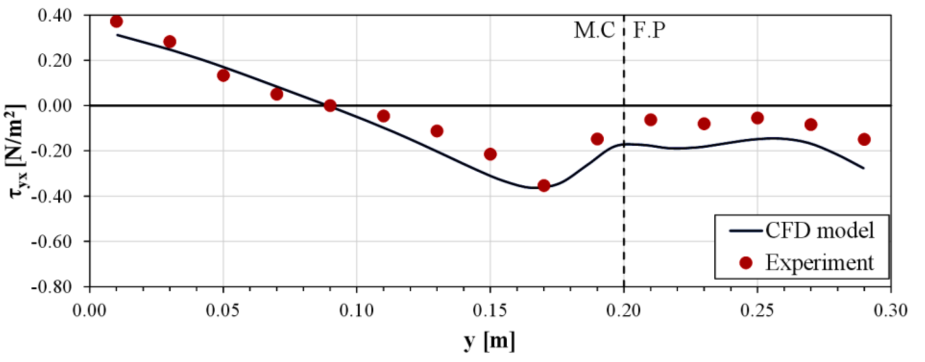

(b) Transitional floodplain (CT0.50)

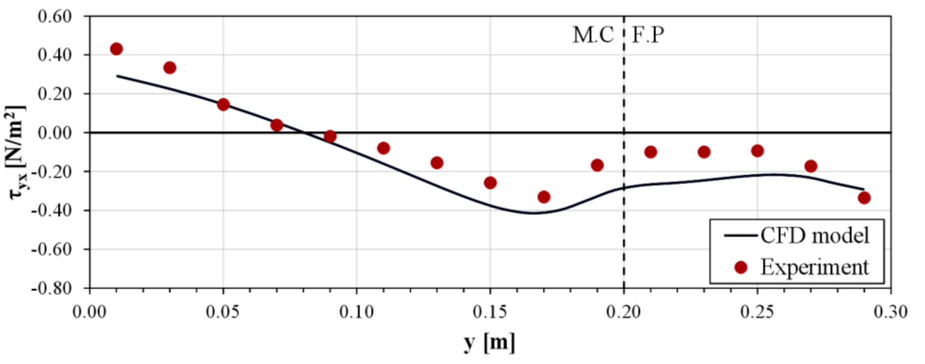

(c) Rough floodplain (CR0.50)

Figure 7.12 Lateral distribution of depth-averaged Reynolds stress (τ_{yx}) for Cases of *Dr* = 0.50.

7.5 Numerical analysis of momentum transfers due to secondary flow

The secondary flow effects on lateral momentum transfer were estimated indirectly based on the CFD simulations because of the difficulty in measuring the secondary flow with sufficient accuracy. It was clarified in a previous section that the simulated secondary flow has a structure is fairly similar to the observed one.

The secondary flow contribution to momentum transfers was calculated by the following equation, using the detailed results obtained from the CFD simulations:

$$-(\rho UV)_d = -\frac{1}{H}\int_0^y (\rho g H S_o - \tau_b)dy - \tau_{yx} \tag{7.7}$$

The results obtained from Eq. (7.7) for apparent shear stress due to the secondary flow $[-(\rho UV)_d]$ are shown in Figure 7.13. Only the cases with three different relative depths (*Dr* = 0.25, 0.33, 0.50) are shown. For each relative depth *Dr*, the results for three cases of different floodplain roughness were compared together.

The profiles of $[-(\rho UV)_d]$ show the linearly descending feature at the interfacial zone that is quite similar to the experimental results obtained by Shiono & Knight (1991), but the magnitudes are different because of the differences in the geometrical properties. It can be seen that the apparent shear stress due to the secondary flow decreases from the left wall, reaches the maximum negative value at y ≈ 0.20 m, i.e. at the edge of the floodplain and then increases towards the right wall. In the main channel the profile of $[-(\rho UV)_d]$ is nearly constant for y < 0.15 m. However, near the junction between the main channel and the floodplain (0.15 < y < 0.20 m) the distribution decreases significantly to the maximum negative value, possibly indicating the presence of a strong secondary flow cells as shown by Figure 7.7 and 7.8 in a previous section.

Figure 7.13 also shows that the maximum value of $[-(\rho UV)_d]$ increases as the relative depth increases. For example, the maximum magnitudes in smooth floodplain cases CS0.25, CS0.33 and CS0.50 are -0.78, -0.85 and -0.96 N/m^2, respectively. This indicates that the contribution of the secondary flow to the momentum transfer is stronger under the conditions of higher flow depth, i.e. larger *Dr*. The results in Figure 7.13 also shows that when the floodplain is roughened, the profile shapes of $[-(\rho UV)_d]$ on the main channel do not differ significantly from those for smooth floodplain cases. This indicate that the influence of the floodplain roughness on the secondary current in the main channel is not considerable. However, the profile of $[-(\rho UV)_d]$ in the floodplain appears to be influenced by the increase of roughness over the floodplain. The variation of $[-(\rho UV)_d]$ in rough floodplain cases is larger than that shown for smooth floodplain cases. This indicates that the effect of the roughness on the secondary current is more important in the floodplain, but is less important in the main channel.

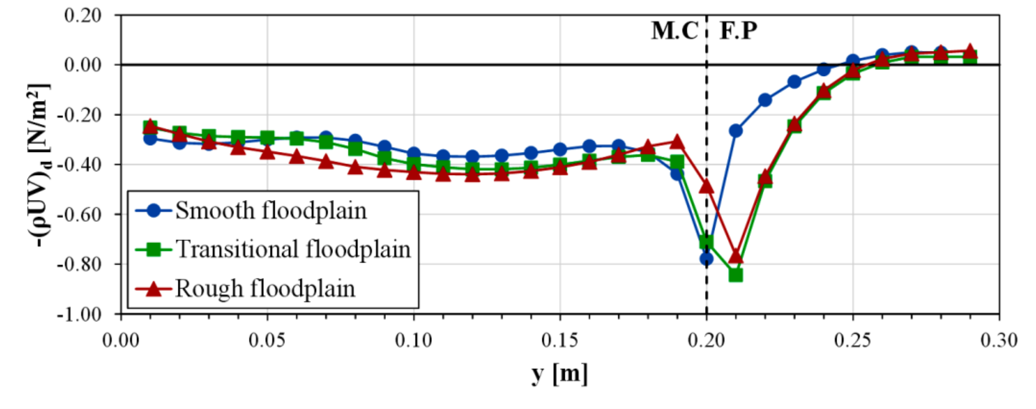

(a) Cases CS0.2, CT0.25 and CR0.25 (*Dr* = 0.25).

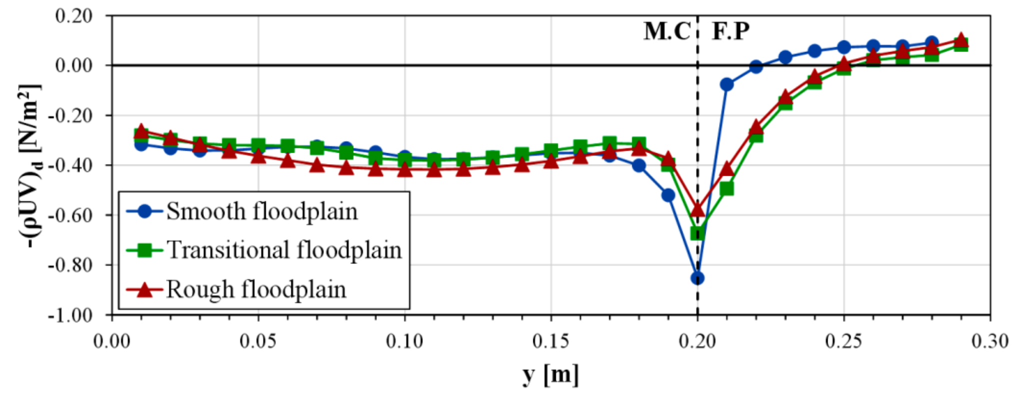

(b) Cases CS0.33, CT0.33 and CR0.33 (*Dr* = 0.33).

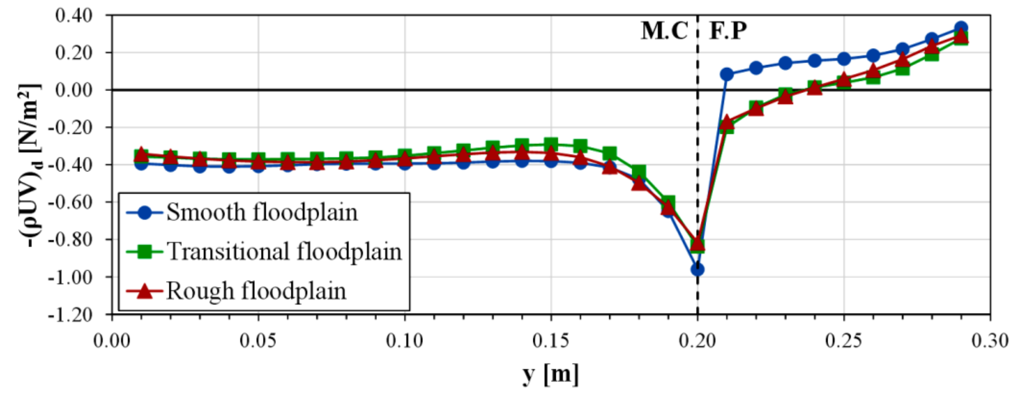

(c) Cases CS0.50, CT0.50 and CR0.50 (*Dr* = 0.50).

Figure 7.13 Lateral distribution of apparent stress due to secondary flows for different *Dr*.

7.6 Non-uniformity of velocity distributions in compound channels

To examine how the velocity distribution in the compound channel flows could be influenced by the geometry factors and roughness conditions, the velocity distribution coefficients (α, β) for all test cases were calculated based on the velocities obtained from the experiments. As mentioned previously, test cases considered in the present work includes three different types of roughness conditions for the floodplain so that three flow regimes are established. These flow regimes are smooth (cases CS-0.25 to CS0.50), transitionally rough (cases CT0.25 to CT0.50), and fully rough (cases CR0.25 to CR0.50).

Figures 7.14 and 7.15 show the variations of the energy (α) and momentum (β) coefficients, respectively, for different values of flow relative depth and floodplain roughness. It can be seen in the two figures that for all roughness conditions, the maximum magnitudes of α and β occur for the lowest values of the relative depth *Dr*, whereas the minimum magnitudes of α and β correspond to the highest values of the relative depth. This indicates that the values of α and β decrease as the relative depth increases. According to Figure 7.14, the α takes a value of 1.078 for the case CS0.25 that has the smallest relative depth (Dr = 0.25) and smooth floodplain, then reach to 1.057 for the case CS0.50 that has the largest relative depth (Dr = 0.50) and smooth floodplain. Similar trends for the values of α can be seen for the cases with transitional and rough floodplains. As shown in Figure 7.15, the values of the momentum correction coefficient β also decrease as the values of the relative depths increase, irrespective of the roughness conditions of the floodplain flows. For example, for smooth floodplain cases, the values of β lower from 1.038 at the smallest relative depth (Dr = 0.25) to 1.02 at the largest relative depth (Dr = 0.50).

The results in Figures 7.14 and 7.15 also shows that the roughness conditions have a significant effect on the values of the velocity distribution coefficients (α and β). For the cases of rough floodplain, the values of α and β are larger than those for the cases of smooth floodplain. For example, the value of α equals to 1.125 for the case CR0.25 in which the floodplain is fully rough, while the value of a is less at 1.078 in the case CS0.25 which have the same value of *Dr* but smooth floodplain.

Based on the results above, it can be concluded that the velocity distribution is described as more non-uniform in the cases of low flows and fully rough floodplain.

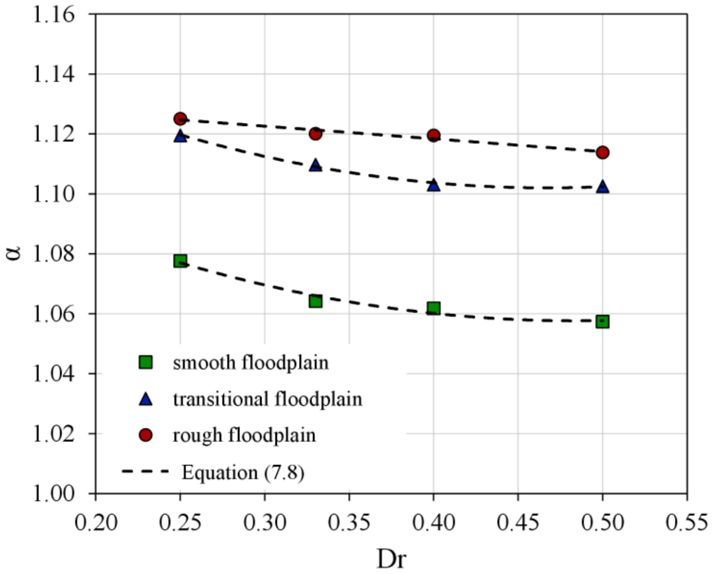

Figure 7.14 Variations of the kinetic energy coefficient (α) against *Dr* for different floodplain roughness conditions.

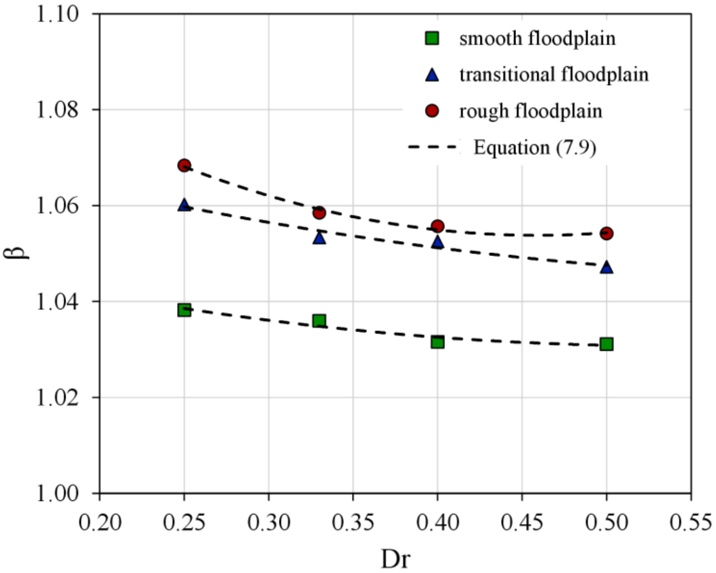

Figure 7.15 Variations of the momentum correction coefficient against Dr for different floodplain roughness conditions.

Using regression analysis, some equations were fitted to the experimental data and the energy and momentum coefficients were correlated to the flow relative depth for each roughness flow regimes. The equations obtained from the analysis of velocity distribution coefficients (α and β) take the general polynomial forms as follows:

$$\alpha = A_\alpha Dr^2 - B_\alpha Dr + C_\alpha \tag{7.8}$$

$$\beta = A_\beta Dr^2 - C_\beta Dr + C_\beta \tag{7.9}$$

The coefficients (A_α, B_α and C_α) in Eq. (7.8) and (A_β, B_β and C_β) in Eq. (7.9) depends on roughness conditions over the floodplain. Based on the results of the experiments conducted in the present work, the equations proposed for estimating α and β are summarized in table 7.2. These equations can be used to explain the effects of the relative depth and roughness factors on the non-uniformity of the velocity distributions in a compound channel flows. It should be noted that the empirical equations given in Table 7.2 are applicable only over the range of hydraulic conditions mentioned in this work. If these equations are intended to use for different flow conditions, calibration process needs to be made to evaluate the coefficients in Eq. (7.8) and (7.9).

Table 7.2 Proposed equations to determine the coefficients of α and β in compound channels.

Roughness Conditions	Equations for α and β	Correlation coefficient (R2)
Smooth floodplain	$\alpha = 0.3543Dr^2 - 0.3428Dr + 1.1406$	0.97
	$\beta = 0.0932Dr^2 - 0.1006Dr + 1.0579$	0.95
Transitional floodplain	$\alpha = 0.3754Dr^2 - 0.3508Dr + 1.1839$	0.99
	$\beta = 0.0807Dr^2 - 0.1094Dr + 1.082$	0.97
Rough floodplain	$\alpha = -0.0025Dr^2 - 0.0405Dr + 1.135$	0.96
	$\beta = 0.3272Dr^2 - 0.3003Dr + 1.1227$	0.99

7.7 Application of analytical model

7.7.1 Calibration of model parameters

7.7.1.1 Friction factor (f)

To be able to apply the analytical model given by Eq. (5.28) effectively, the values of local friction factor *f* for each flow region needs to be known. The bed friction factor across the channel can be determined based on the roughness height K_s. Rameshwaran and Shiono (2007) reformulated the Colebrook–White equation and suggested the following resistance relationship for compound channels:

$$f = \left[-2\log\left(\frac{3.02\upsilon}{\sqrt{128gH^3S_o}} + \frac{K_s}{12.3H}\right)\right]^{-2} \tag{7.10}$$

Equation (7.10) was applied to Series 8 carried out on a rectangular compound channel in the Flood Channel Facility (FCF) operated at Hydraulics Research Ltd, Wallingford, England (Shiono and Knight, 1991). The calculated values of the local friction factor across the section for two relative depths of 0.25 and 0.30 are shown in Figure 7.16. From the figure, it is seen that the friction factors calculated agree reasonably well with the experimental data, indicating that the friction factor f can be estimated using Eq. (7.10). Therefore, in the present work, the values of f for main channel and floodplain regions were calculated by using Eq. (7.10) based on the values of K_s estimated experimentally for each test case.

For the smooth flow cases, where the equivalent roughness height K_s did not measure directly, the values of K_S were calculated from the Manning coefficient n by the following relationship (Ackers, 1991):

$$K_s = \left(8.25\sqrt{g}n\right)^6 \tag{7.11}$$

Table 7.3 presents the values of f which are calculated for all test cases to use in the analytical model.

Table 7.3 Friction factor f for all test cases.

Case	f_{mc}	f_{fp}	**Case**	f_{mc}	f_{fp}	**Case**	f_{mc}	f_{fp}
CS0.25	0.0181	0.0296	**CT0.25**	0.0201	0.0505	**CR0.25**	0.0188	0.0946
CS0.33	0.0175	0.0252	**CT0.33**	0.0194	0.0408	**CR0.33**	0.0182	0.0719
CS0.40	0.0169	0.0227	**CT0.40**	0.0188	0.0353	**CR0.40**	0.0176	0.0588
CS0.50	0.0160	0.0198	**CT0.50**	0.0178	0.0290	**CR0.50**	0.0167	0.0452

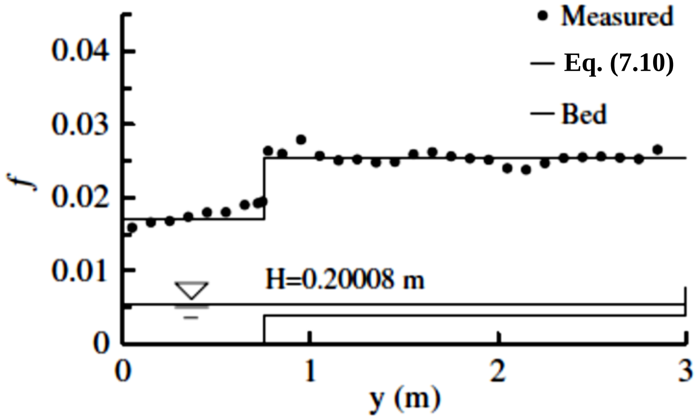

(a) *Dr* = 0.25

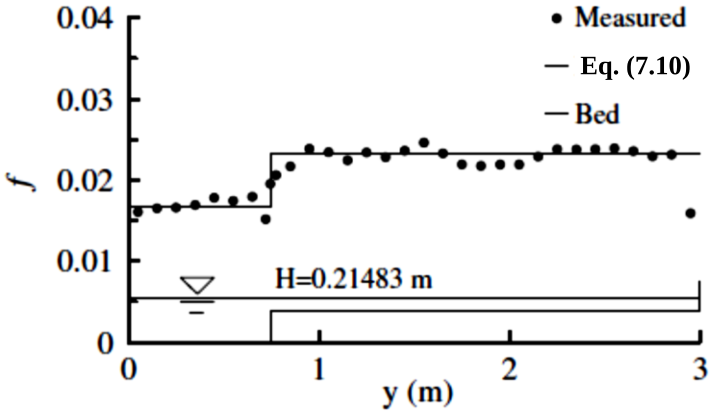

(b) *Dr* = 0.30

Figure 7.16 Measured and predicted friction factor f across a section based on the rectangular compound channel of FCF.

7.7.1.2 Dimensionless eddy viscosity (λ)

The values of the eddy viscosity coefficient used in the analytical model must be properly selected by considering the bed and lateral shear effects to give satisfactory flow predictions. Therefore, the depth-averaged eddy viscosities defined by Eq. (7.6) and shown in Figures 7.9 and 7.10 were used to determine the dimensionless eddy-viscosity coefficients, λ $(= \varepsilon_t / u_* H)$. The lateral distribution of λ across the section are shown in Figure 7.17 for all flow cases, with smooth, transitional and rough floodplains. In the figure, the horizontal solid lines represent the averaged values of λ per panel for flow cases with the smallest relative depth (i.e. *Dr* = 0.25), while the horizontal dashed lines are the average value for the largest relative depth cases, with *Dr* = 0.50.

From Figure 7.17, it can be observed that the values of λ in the main channel are approximately constant irrespective of the relative depth and roughness conditions. The average values of λ in the main channel are about 0.07 for all *Dr*, which corresponds closely to the standard depth-averaged value suggested by Shiono and Knight (1991) for experimental channels. The figure also shows that the values of λ are higher in the floodplain than in the main channel, with higher values being observed in the floodplain for smaller relative depths. This indicate the dependence of λ in the floodplain on the relative depth (*Dr*). It should be noted that the value of λ does not change significantly with change of floodplain roughness, indicating no clear dependence of λ on the roughness of the floodplain.

As discussed above, λ values increase on the floodplain and the degree of increase is related to the value of the relative depth, *Dr*. Shiono and Knight (1991) proposed an expression that relates the ratio of the floodplain and main channel values ($\lambda_{fp}/\lambda_{mc}$) to the *Dr*, as follows:

$$\lambda_{fp}/\lambda_{mc} = (2Dr)^{-4} \tag{7.12}$$

This relationship is only valid within the range 0.1 < *Dr* < 0.25 and related to the geometry of the channel by which the equation 7.12 was derived.

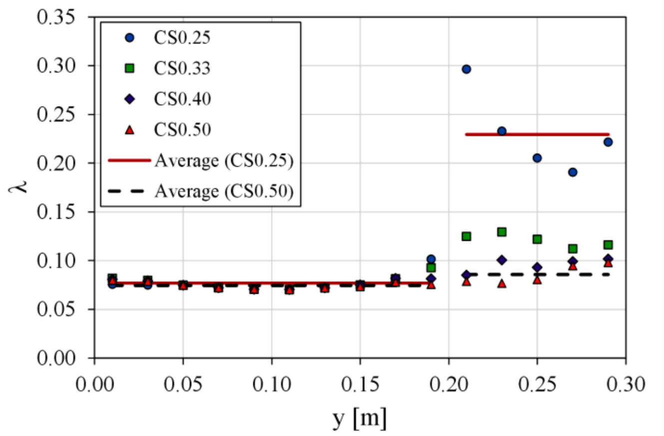

(a) Smooth floodplain cases

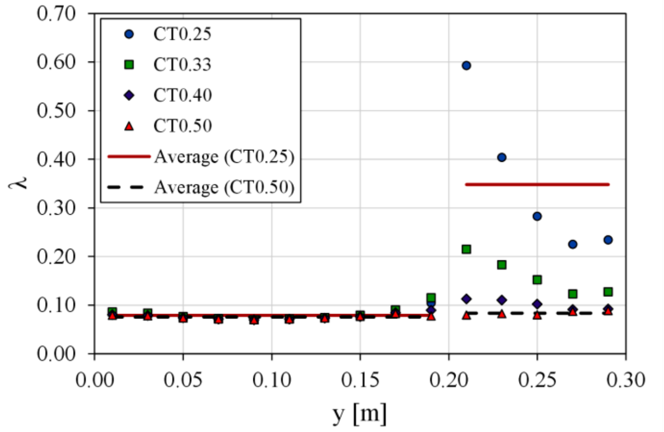

(b) Transitional floodplain cases

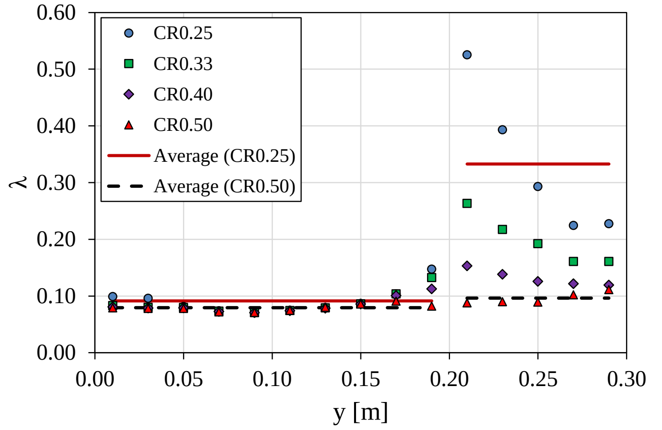

(c) Rough floodplain cases

Figure 7.17 Lateral distribution of dimensionless eddy viscosity coefficient (λ) for all test cases.

To check the equation (7.12) for the channel geometries tested in this study, which have *Dr* ranging from 0.25 to 0.50, the values of $\lambda_{fp}/\lambda_{mc}$ calculated from Eq. (7.12) and those obtained from Figure 7.17 were plotted together in Figure 7.18. From the figure, it is seen that the calibration equation (7.12) gives much greater values for $\lambda_{fp}/\lambda_{mc}$ ratios than those obtained directly from the depth-averaged eddy viscosity, particularly at low relative depths. Therefore, in the present study the following general relationship between the ratio ($\lambda_{fp}/\lambda_{mc}$) and the relative depth (*Dr*) was suggested to estimate the value of λ in the floodplain:

$$\lambda_{fp}/\lambda_{mc} = a(2Dr)^b \tag{7.13}$$

where *a* and *b* are constants which are different with respect to the channel geometry. Figure 7.18 shows that Eq. (7.13), with a = 0.90 and b = -2, gives $\lambda_{fp}/\lambda_{mc}$ ratios that are better fitted to the values calculated experimentally. Therefore, Eq. (7.13) with a = 0.90 and b = -2 was used for calibrating the value of λ in the narrow floodplain considered in the study.

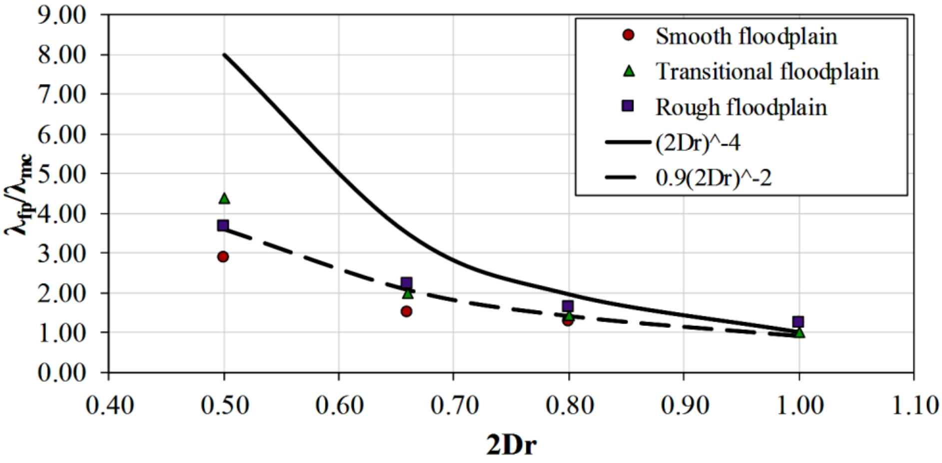

Figure 7.18 Eddy viscosity ratio ($\lambda_{fp}/\lambda_{mc}$) as a function of *Dr*.

7.7.1.3 Secondary currents coefficient

Figure 7.13 has already shown that the distribution of the lateral momentum transfers due to the secondary flow $[-(\rho UV)_d]$ is approximately linear in all regions, except in the junction region between the main channel and the floodplain. This implies that the secondary flow term Γ $[= \partial H(\rho UV)_d/\partial y]$ may be considered as a constant for a constant-depth *H(y)* domain, but it is different for the main channel and the floodplain. Since Γ has the same dimensions of ρgHS_o, it may be assumed to be expressed as:

$$\Gamma = k\rho g H S_o \tag{7.14}$$

where k is defined as the secondary flow coefficient and is different in the main channel and the floodplain regions.

Based on the lateral distributions of $[-(\rho UV)_d]$ shown in Figure 7.13, the secondary flow coefficients were calculated for each flow case as follows:

$$k = \frac{\partial H(\rho UV)_d/\partial y}{\rho g H S_o} \tag{7.15}$$

The calculated values of k for the cases of smooth, transitional and rough floodplain are shown in Figure 7.19. The results in the figure indicate that for a given roughness condition the secondary flow coefficients may be considered as constants in each flow region irrespective of the relative depth. However, it should be noted that secondary flow coefficient k in the floodplain is larger for the cases of rough floodplain. From Figure 7.19, the mean values of the secondary flow coefficients for the floodplain are about -0.21, -0.32, and -0.36 for smooth, transitional and rough floodplain cases respectively. For the main channel the values of k are nearly constant at 0.20 for all flow cases. This indicates that secondary flow coefficient k varies from panel to panel and depend on the bottom roughness.

In the present study, the values of k presented in Figure 7.19 were used in the application of the analytical model to compound channels with narrow floodplain. However, the values of k are related to the channel geometry. For example, Shiono and Knight (1991) suggested the values of k_{mc} = 0.15 and k_{fp} = -0.25 for a channel with wide floodplain. In case of the lateral distribution of the secondary flow term $[-(\rho UV)_d]$ is not known, the value of k may be determined by tuning the model until it gives a good depth-averaged velocity distribution compared with the experimental data.

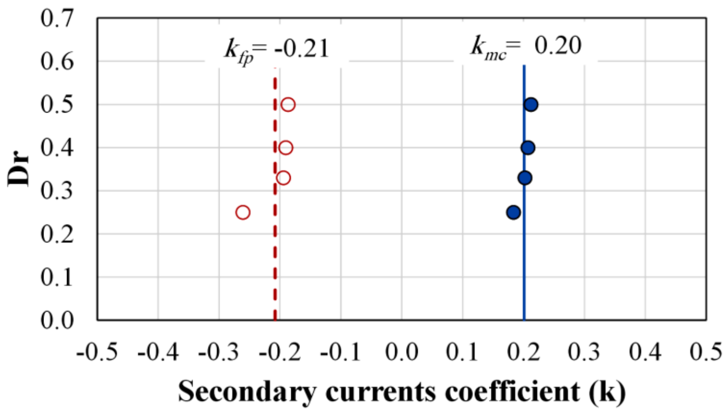

(a) Smooth floodplain cases

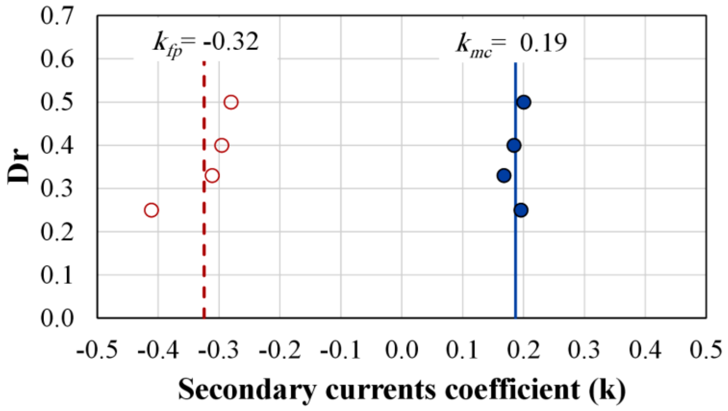

(b) Transitional floodplain cases

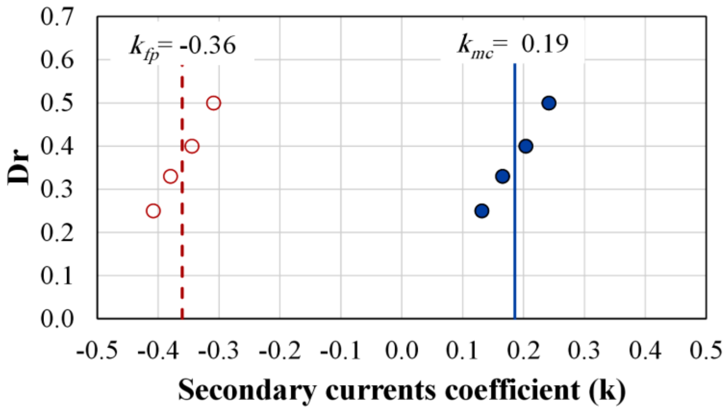

(c) Rough floodplain cases

Figure 7.19 Variation of secondary flow coefficient k with relative depth for main channel and floodplain.

7.7.2 Comparisons with experimental data

The analytical model described earlier has been applied to the test cases of smooth floodplain (CS0.25 – CS0.50), transitional floodplain (CT0.25 – CT0.50), and rough floodplain (CR0.25 – CR0.50). For all simulations, the proposed calibration expressions and values for the friction factor (f), the dimensionless eddy viscosity parameter (λ) and the secondary flow coefficients (k) are used. f was estimated by Eq. (7.10), λ was calibrated based on the equation (7.13) suggested in the present study, and k values for the main channel and floodplain were taken as the values calculated in Figure 7.19.

The predicted results of the depth-averaged velocity for both the proposed calibration method and the traditional calibration method proposed by Shiono and Knight (1991) are compared with the experimental data in Figures 7.20, 7.21 and 7.22. The predicted profiles based on the present calibration values of λ and k are indicated by the solid lines and those based on the traditional method values are indicated by dashed lines.

From Figures 7.20 to 7.22, it can be seen that the prediction of velocity for the floodplain is underestimated when the eddy viscosity (λ) and secondary flow (k) parameters are calibrated based on their traditional method given by Shiono and Knight (1991). However, the figures also indicate that the predicted results can be improved when the eddy viscosity and secondary flow coefficients are calibrated by the equations and values suggested in the present study. This is probably because the traditional expression (Eq. 7.12) for calibrating the effect of the eddy viscosity was suggested for shallow flows in wide channels. Therefore, the traditional calibration equation gives large values for λ in the floodplain region, leading to a reduction in the predicted velocity in this flow region. The values of λ calibrated by the proposed equation (Eq. 7.13) are smaller to reflect the reducing in the lateral shear in flow cases with higher depths and narrow floodplain, which are considered in the current study. Thus, the predicted results of the velocity (U_d) based on the present calibration method are in a closer agreement with the experimental data than those produced from the traditional calibration method.

Figures 7.20 to 7.22 also indicate that the velocity for the main channel is reasonably well predicted when the proposed or the traditional calibration methods are used. This is because the same values of λ and approximately comparable values of k were used in both methods for the main channel panel.

From Figures 7.20 to 7.22, the predicted values of U_d using the traditional calibration method comes closer to the predicted values by the present calibration method in the high flow cases with large relative depths. This is not surprising because both the proposed and the traditional calibration methods give almost equal values of λ as shown in Figure 7.18.

In the rough floodplain cases (Figure 7.22), the differences between the predicated values of U_d based on the traditional calibration expressions and those based on the present calibration expressions are larger than that in the smooth floodplain cases (Figure 7.20). this is thought to be that the traditional values of the secondary flow coefficient k are assumed to be same in the smooth and rough cases without considering the effect of the roughness on the secondary flow. However, the calculations conducted in the present work for the secondary flows indicate that the secondary flow coefficient k in the floodplain increase as the roughness height increases as shown in Figure 7.19.

In summary, the agreement between the analytical and experimental values of U_d improves considerably when the proposed calibration expression for λ and calibrated values for k are adopted.

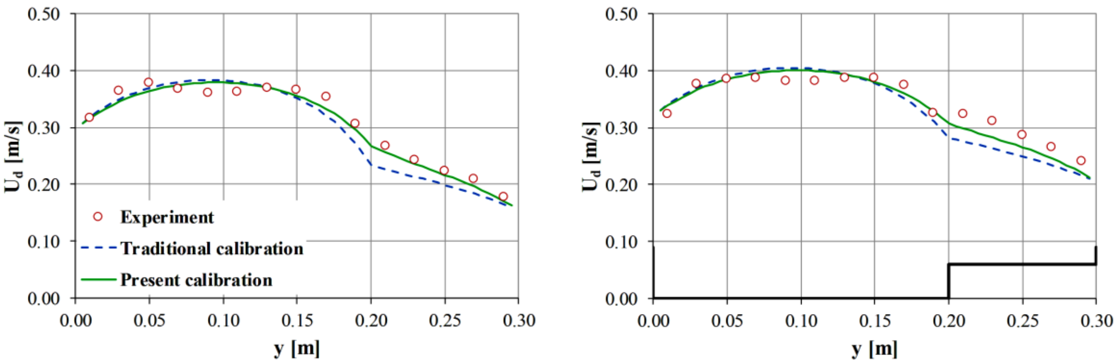

CS0.25 CS0.33

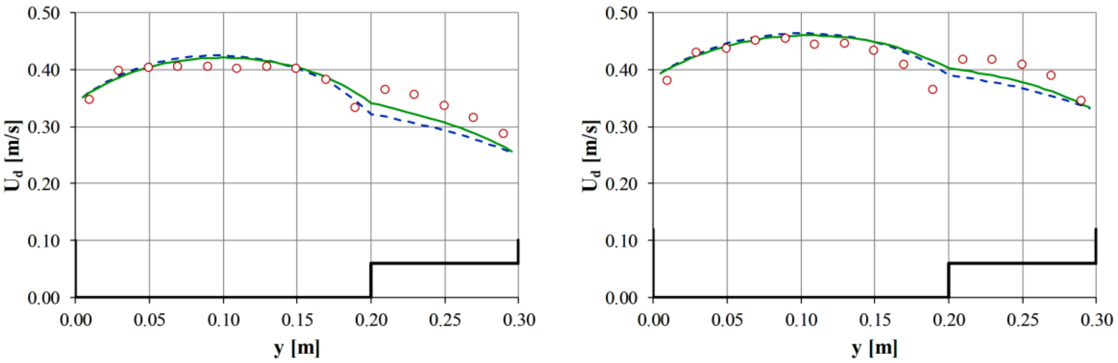

CS0.40 CS0.50

Figure 7.20 Comparison between analytical and experimental lateral distributions of U_d for smooth floodplain cases (solid lines represent the present calibration method, while the dashed lines represent the traditional calibration method).

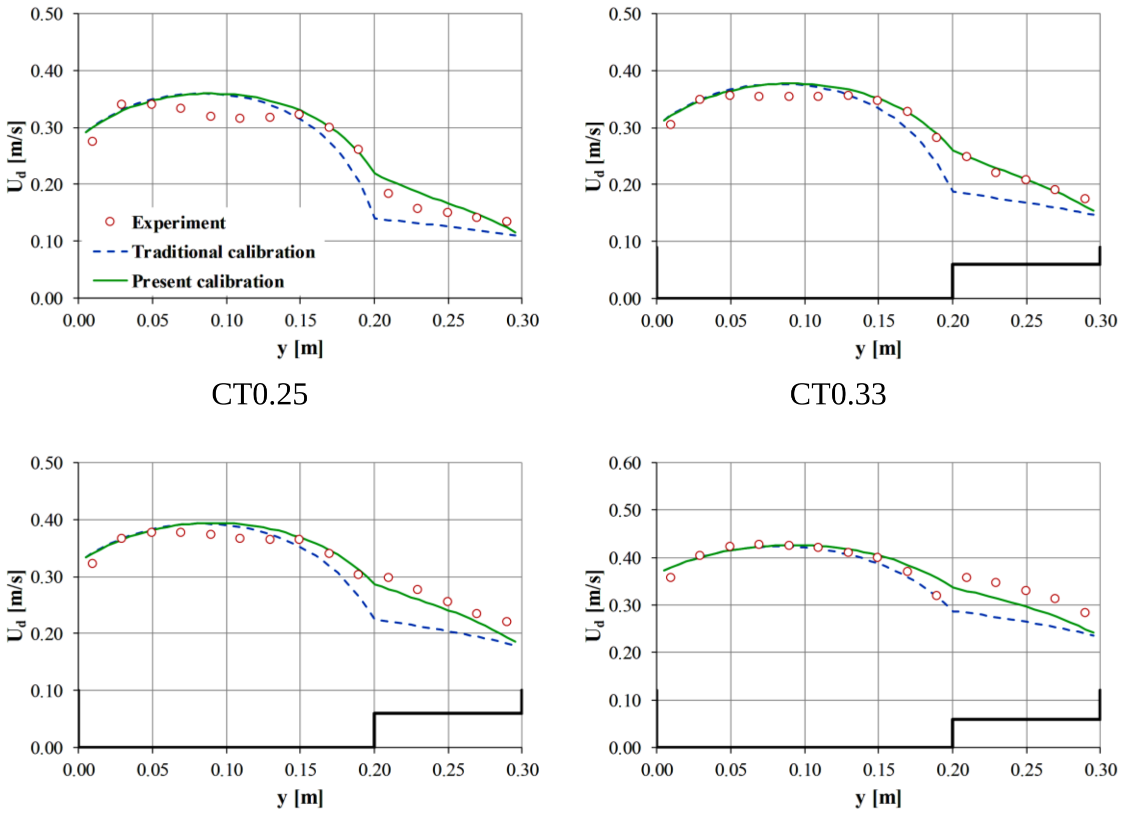

CT0.25

CT0.33

CT0.40

CT0.50

Figure 7.21 Comparison between analytical and experimental lateral distributions of U_d for transitional floodplain cases (solid lines represent the present calibration method, while the dashed lines represent the traditional calibration method).

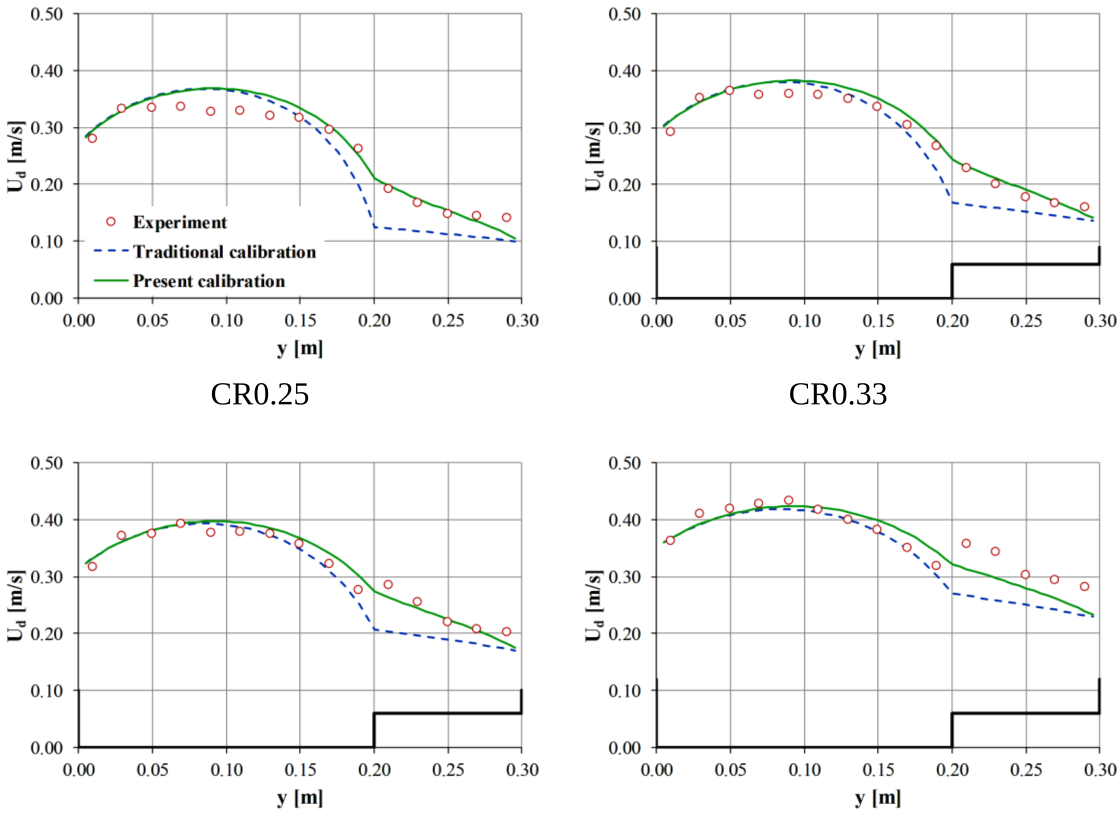

CR0.25

CR0.33

CR0.40

CR0.50

Figure 7.22 Comparison between analytical and experimental lateral distributions of U_d for rough floodplain cases (solid lines represent the present calibration method, while the dashed lines represent the traditional calibration method).

Chapter 8

Conclusions and Recommendations

8.1 Research summary

This study focused largely on the velocity distribution of the primary flow in rectangular and compound open channels under different flow regimes in terms of roughness conditions. A series of laboratory experiments was conducted for open channel flows with three artificial bed surfaces to establish three different regimes, namely the hydraulically smooth, transitionally rough and fully rough. The detailed Computational Fluid Dynamics (CFD) results were also used as part of an investigation in the significance of assumptions about secondary flows and turbulent eddy viscosity in calculations of velocity distributions.

In the experimental investigation, two sets of experiments were conducted on two channel configurations that have different hydraulic and roughness characteristics for collecting the experimental data. One of the channels had a rectangular section to simulate the inbank flow condition, while the other had a compound section constructed inside the flume to represent the overbank flow condition.

In the numerical study, the computational fluid dynamic (CFD) models were applied to simulate the flow in the rectangular and compound channels that were used in the experiments. The 3D numerical CFD models were developed and run using CFX package (v.15). The numerical CFD model developed in this study was created based on the Reynolds stress turbulence models (RSM). The RSM model was preferred over the other turbulence models due to its accuracy in predicting the secondary currents.

This chapter includes two parts. In the first part, the findings from all experimental and numerical works are presented. whereas, the second part discusses the possible improvements that can be suggested for both the numerical and experimental investigations conducted in this study.

8.2 Research Findings and Contributions

The combination of the results obtained experimentally and numerically for rectangular channel flows leads to the following findings with respect to the velocity distributions and their calculations:

1. Based on the experimental measurements for the velocity distributions, the effect of the roughness on the velocity distributions in outer region was found to be considerable. The experimental results have shown that increasing the roughness causes the velocity distribution coefficients (α and β) to increase, even though the flow depth (H) and the aspect ratio ($Ar = B/H$) are constant. Therefore, the non-uniformity of the velocity distribution in the cases of fully rough flow regimes (i.e $Re* > 70$) is more considerable than those in hydraulically smooth and transitionally rough flow cases ($Re* < 70$).
2. On the other hand, for specific flow regime (i.e. constant $Re*$), the velocity distribution coefficients (α, β) was found to increase with increase in aspect ratio Ar. This is suggested to be related to the effects of secondary currents and turbulence conditions.
3. The results obtained from the CFD confirmed that the Reynolds Stress Model (RSM) used as the turbulence model can predict the main features of secondary currents and turbulence. However, the predicted results were found to be influenced by the boundary conditions imposed on the flow domain, particularly on the free surface and the walls.
4. Based on the experiments and the numerical simulations conducted in this study, it was found that the velocity distribution coefficients (α or β) can be related to both Roughness Reynolds number ($Re*$) and aspect ratio (Ar) through a logarithmic relationship, which its general form can be given as Eq. (6.9). This equation can be used to estimate the energy coefficient (α) and momentum coefficient (β) when 1D modelling is used for solving the engineering hydraulic problems.
5. The effects of the secondary currents and the wake contribution were found to play an important role in the calculation of the velocity distribution by the analytical models that based on simplified Reynolds Averaged Navier–Stokes (RANS) equations. Therefore, the analytical model called the dip-modified log wake law (DMLW-law) was used in this study because it accounts for the effects of both the secondary currents and wake strength by two calibration parameters. These two parameters the dip correction factor (μ) and the wake strength parameter (Π).
6. The expressions used for estimating the dip correction factor (μ) in smooth flows was found to be not accurate for the rough flows. Therefore, in this study, the conventional expression given by Eq. (6.11) was modified to be applicable for rough flow cases.
7. This study confirmed that the dependency of the wake strength parameter Π on the roughness conditions of the flow as suggested by Nezu and Rodi (1986). Based on this fact, an expression was proposed to use in estimating the wake strength parameter when applying the analytical model (DMLW-law).

8. The results indicated that the expressions suggested in the present study to calibrate the parameters (Π and μ) may provide efficiency to the application of the analytical model (DMLW-law) for rectangular channel flows under different flow regimes.

On the basis of the investigations concerning velocity distributions in narrow compound channels, the following conclusions are drawn.

1. Based on the velocity measurements obtained from the experiments conducted in this study, the velocity distribution coefficients (α and β) in the compound channel flows was found to be influenced by the geometry and roughness conditions. The results of the energy (α) and momentum (β) coefficients for the compound channel flows showed that the velocity distribution is described as more non-uniform in the cases of low flows and fully rough floodplain.
2. The results showed that the energy (α) and momentum (β) coefficients vary with the variations of the flow relative depth (Dr) and the floodplain roughness. Using the regression analysis, it was found that the energy and momentum coefficients can be correlated to the flow relative depth for each roughness flow regimes by polynomial (quadratic) equations such as Eqs. (7.8) and (7.9).
3. The numerical analysis of the secondary flows and depth-averaged eddy viscosity confirmed the significance of the secondary flow and momentum transfer between the main channel and floodplain on the depth-averaged velocity distribution.
4. In this study the analytical SKM model developed by Shiono and Knight (1988, 1991) was applied for depth-averaged velocity calculations. The SKM model relies on three parameters, namely friction factor (f), dimensionless eddy viscosity (λ), and secondary flow term (Γ). It was found that the application of SKM model with the traditional expressions for the three parameters (f, λ, Γ) does not fit to the compound channel with narrow floodplains such as the channels used in the present study. Therefore, the detailed Computational Fluid Dynamics (CFD) results were used to modify the traditional expressions so that they can be used to calibrate the model parameters (f, λ, and Γ) for narrow compound channels having different floodplain roughnesses.
5. The agreement between the analytical and experimental distributions of the depth-averaged velocity improved considerably when the modified calibration expression for λ and new computed values for Γ were adopted. This means that the expressions for λ, and Γ parameters proposed in the present study can give better prediction for the narrow

compound channel flow than when the traditional expressions of the model parameters are used.

8.3 Study limitations and further research

The main conclusions given in the previous section may lead to the better understanding of the primary velocity distribution and its calculation in the straight rectangular and compound channels. However, the following future research recommendations are suggested for the findings of this research to be improved:

1. The expressions proposed in the present study for estimation of the velocity distribution coefficients can only be used for straight prismatic channels. Therefore, it is suggested that further investigations should be made to extend the applications of these expressions to natural channels and other laboratory channels with different sinuosity, geometry and surface conditions.
2. The effects of the secondary currents and the momentum transfers were found to have an important influence on the velocity distributions, particularly in compound channels. Further detailed studies under different flow conditions should be carried out to investigate these effects on the calculations of the primary velocity distribution.
3. For the analytical formulations used for velocity calculation in rectangular channels, further experimental study is required to generalise the expression proposed for the velocity-dip and wake effects in other single channels with different shapes.
4. For the analytical model used for velocity calculation in compound channels, the expressions developed for calibrating the parameters of secondary flow and eddy viscosity were only applied to the flow cases considered in the present study. Therefore, further detailed studies under different flow conditions should be carried out generalise these expressions for different engineering applications
5. Turbulence measurements were not carried out in the flow cases tested in the present work. Therefore, further study is needed to explore the effect of the turbulence on the velocity distribution more accurately.

References

Abril, J. B., & Knight, D. W. (2004). Stage-discharge prediction for rivers in flood applying a depth-averaged model. *Journal of Hydraulic Research, 42*(6), 616-629.

Absi, R. (2008). Comments on "turbulent velocity profile in fully-developed open channel flows". *Environmental fluid mechanics, 8*(4), 389-394.

Absi, R. (2011). An ordinary differential equation for velocity distribution and dip-phenomenon in open channel flows. *Journal of Hydraulic Research, 49*(1), 82-89.

Ackers, P. (1991). Hydraulic design of straight compound channels. Rep. SR 281, Hydraulics Research Ltd., Wallingford, U.K.

Alavian, V., & Chu, V. H. (1985). Turbulent exchange flow in shallow compound channel. *Proce. 21st Cong. IAHR, Melbourne, Australia, 3,* 446-451.

Albayrak, I., & Lemmin, U. (2011). Secondary currents and corresponding surface velocity patterns in a turbulent open-channel flow over a rough bed. *Journal of Hydraulic Engineering, 137*(11), 1318-1334.

Al-Khatib, I. A., & Göğüş, M. (1999). Momentum and kinetic energy coefficients in symmetrical rectangular compound cross section flumes. *Turkish Journal of Engineering and Environmental Sciences, 23*(3), 187-198.

Andersson, B., Andersson, R., Håkansson, L., Mortensen, M., Sudiyo, R., & Van Wachem, B. (2011). *Computational fluid dynamics for engineers*. Cambridge University Press.

ANSYS, A. (2013). Version 15.0; ANSYS. *Inc.: Canonsburg, PA, USA November*.

Asnaashari, A., Akhtari, A. A., Dehghani, A. A., & Bonakdari, H. (2016). Experimental and numerical investigation of the flow field in the gradual transition of rectangular to trapezoidal open channels. *Engineering Applications of Computational Fluid Mechanics, 10*(1), 272-282.

Atabay, S., & Knight, D. W. (2006). 1-D modelling of conveyance, boundary shear and sediment transport in overbank flow. *Journal of Hydraulic Research, 44*(6), 739-754.

Baird, J. I., & Ervine, D. A. (1984). Resistance to flow in channels with overbank flood-plain flow. In *Channels and Channel Control Structures* (pp. 561-574). Springer, Berlin, Heidelberg.

Basara, B., & Cokljat, D. (1995). Reynolds-Stress Modeling of Turbulent Flows in Meandering Open Channels. *ASME-PUBLICATIONS-FED, 221*, 27-32.

Bates, P. D., Lane, S. N., & Ferguson, R. I. (Eds.). (2005). *Computational fluid dynamics: applications in environmental hydraulics*. John Wiley & Sons.

Bernard, P. S., & Wallace, J. M. (2002). *Turbulent flow: analysis, measurement, and prediction*. John Wiley & Sons.

Bonakdari, H., Larrarte, F., Lassabatere, L., & Joannis, C. (2008). Turbulent velocity profile in fully-developed open channel flows. *Environmental Fluid Mechanics*, *8*(1), 1-17.

Bradbrook, K. F., Lane, S. N., Richards, K. S., Biron, P. M., & Roy, A. G. (2000). Large eddy simulation of periodic flow characteristics at river channel confluences. *Journal of Hydraulic Research*, *38*(3), 207-215.

BS 882. Specification for aggregates from natural sources for concrete. British Standards Institution, London, United Kingdom, 1992.

Cardoso, A. H., Graf, W. H., & Gust, G. (1989). Uniform flow in a smooth open channel. *Journal of Hydraulic Research*, *27*(5), 603-616.

Cater, J. E., & Williams, J. J. (2008). Large eddy simulation of a long asymmetric compound open channel. *Journal of Hydraulic Research*, *46*(4), 445-453.

Cebeci, T., & Smith, A. M. O. (1974). *Analysis of Turbulent Boundary Layers*, Academic Press, Inc., New York.

Chaouat, B. (2017). The State of the Art of Hybrid RANS/LES Modeling for the Simulation of Turbulent Flows. *Flow, Turbulence and Combustion*, *99*(2), 279-327.

Chaudhry, M. H. (2008). *Open-Channel Flow.* New York, NY: Springer Science.

Chen, C. L. (1992). Momentum and energy coefficients based on power-law velocity profile. *Journal of Hydraulic Engineering*, *118*(11), 1571-1584.

Cheng, N. S. (2015). Representative grain size and equivalent roughness height of a sediment bed. *Journal of Hydraulic Engineering*, *142*(1), 06015016.

Cheong, H. F., & Xue, H. (1997). Turbulence model for water flow over two-dimensional bed forms. *Journal of Hydraulic Engineering*, *123*(5), 402-409.

Chow, V. (1959). *Open Channel Hydraulics.* New York, US: McGraw-Hill Book Company.

Cokijat, D. P. (1993). *Turbulence models for non-circular ducts and channels* (Doctoral dissertation, City University London).

Cokljat, D., & Younis, B. A. (1995a). Second-order closure study of open-channel flows. *Journal of hydraulic engineering*, *121*(2), 94-107.

Cokljat, D., & Younis, B. A. (1995b). Compound-channel flows: A parametric study using a Reynolds-stress transport closure. *Journal of Hydraulic Research*, *33*(3), 307-320.

Colebrook, C. F., & White, C. M. (1937). Experiments with fluid friction in roughened pipes. *Proc. R. Soc. Lond. A*, *161*(906), 367-381.

Coles, D. (1956). The law of the wake in the turbulent boundary layer. *Journal of Fluid Mechanics*, *1*(2), 191-226.

Costabile, P., & Macchione, F. (2010). The role of Boussinesq's coefficient in computing flood propagation in compound channels. In *Proc. First European IAHR Congress, Edinburgh, Scotland*.

Demuren, A. O., & Rodi, W. (1984). Calculation of turbulence-driven secondary motion in non-circular ducts. *Journal of Fluid Mechanics*, *140*, 189-222.

Devi, K., & Khatua, K. K. (2016). Prediction of depth averaged velocity and boundary shear distribution of a compound channel based on the mixing layer theory. *Flow Measurement and Instrumentation*, *50*, 147-157.

Durbin, P. A., & Reif, B. P. (2011). *Statistical theory and modeling for turbulent flows*. John Wiley & Sons.

Einstein, H. A., & Barbarossa, N. L. (1952). *River channel roughness* (Vol. 117). USA: Transactions of the American Society of Civil Engineers.

Einstein, H., & Li, H. (1958). Secondary currents in straight channels. *Eos, Transactions American Geophysical Union*, *39*(6), 1085-1088.

Ervine, D. A., & Ellis, J. (1987). Experimental and computational aspects of overbank floodplain flow. *Earth and Environmental Science Transactions of The Royal Society of Edinburgh*, *78*(4), 315-325.

Ervine, D. A., Babaeyan-Koopaei, K., & Sellin, R. H. (2000). Two-dimensional solution for straight and meandering overbank flows. *Journal of Hydraulic Engineering*, *126*(9), 653-669.

Fenton, J. D. (2005). On the energy and momentum principles in hydraulics. In *Proc. 31st Congress IAHR, Seoul* (pp. 625-636).

Filonovich, M. (2015). Numerical modelling of compound channel flow. PhD Thesis, University of Lisbon.

Filonovich, M. S., Leal, J. B., & Rojas-Solórzano, L. R. (2015). Prediction of compound channel secondary flows using anisotropic turbulence models. In *Informatics, Networking and Intelligent Computing: Proceedings of the 2014 International Conference on Informatics, Networking and Intelligent Computing (INIC 2014), 16-17 November 2014, Shenzhen, China* (p. 163). CRC Press.

Fischer-Antze, T., Stoesser, T., Bates, P., & Olsen, N. R. B. (2000). 3D numerical modelling of open-channel flow with submerged vegetation. *Journal of Hydraulic Research*, *39*(3), 303-310.

Gatski, T. B., & Speziale, C. G. (1993). On explicit algebraic stress models for complex turbulent flows. *Journal of fluid Mechanics*, *254*, 59-78.

Gessner, F. B. (1973). The origin of secondary flow in turbulent flow along a corner. *Journal of Fluid Mechanics*, *58*(1), 1-25.

Grass, A. J. (1971). Structural features of turbulent flow over smooth and rough boundaries. *Journal of fluid Mechanics, 50*(2), 233-255.

Guo, J., & Julien, P. Y. (2003). Modified log-wake law for turbulent flow in smooth pipes. *Journal of Hydraulic Research, 41*(5), 493-501.

Guo, J., & Julien, P. Y. (2008). Application of Modified Log-Wake Law in Open-Channels. *Journal of Applied Fluid Mechanics*, *1*(2), 17-23.

Hamidifar, H., Omid, M. H., & Keshavarzi, A. (2016). Kinetic energy and momentum correction coefficients in straight compound channels with vegetated floodplain. *Journal of hydrology*, *537*, 10-17.

Henderson, F. M. (1966). *Open Channel Flow*. New York: MacMillan.

Hinze, J. O. (1975). *Turbulence* (Second Edition ed.). New York: McGraw-Hill Book Company.

Ikeda, S., & McEwan, I. K. (Eds.). (2009). Flow and sediment transport in compound channels: the experience of Japanese and UK research. CRC Press.

Ikeda, S., Kawamura, K., & Kasuya, I. (2002). Quasi-three-dimensional computation and laboratory tests on flow in curved compound channels. In *Proc. River Flow* (pp. 233-245).

Ikeda, S., Kuga, K. and Toda, Y. (1995). Measurement of the instantaneous structures of periodical vortices in a compound open channel flow by Particle Image Velocimetry. *Proceedings of the Symposium on River Hydraulics and Environments*, JSCE, pp. 33.38.

Ikeda, S., Sano, T., Fukumoto, M., & Kawamura, K. (2000). Organized horizontal vortices and lateral sediment transport in compound open channel flows. *Doboku Gakkai Ronbunshu*, *2000*(656), 135-144.

Imamoto, H., & Ishigaki, T. (1988). Mean and turbulence structure near the inclined side-wall in an open channel flow. In *Proc. 3rd Int. Symp. on Refined flow modelling and turbulence measurements, IAHR, Tokyo, Japan* (pp. 545-552).

Jing, H., Guo, Y., Li, C., & Zhang, J. (2009). Three-dimensional numerical simulation of compound meandering open channel flow by the Reynolds stress model. *International journal for numerical methods in fluids*, 59(8), 927-943.

Jones, W. P., & Launder, B. (1972). The prediction of laminarization with a two-equation model of turbulence. *International journal of heat and mass transfer*, *15*(2), 301-314.

Kang, H., & Choi, S. U. (2004). 3D Numerical simulation of compound open channel flows with vegetated floodplains by reynolds stress model. In *Critical Transitions in Water and Environmental Resources Management* (pp. 1-10).

Kang, H., & Choi, S. U. (2006a). Reynolds stress modelling of rectangular open-channel flow. *International journal for numerical methods in fluids*, 51(11), 1319-1334.

Kang, H., & Choi, S. U. (2006b). Turbulence modeling of compound open-channel flows with and without vegetation on the floodplain using the Reynolds stress model. *Advances in Water Resources*, *29*(11), 1650-1664.

Kara, S., Stoesser, T., & Sturm, T. W. (2012). Turbulence statistics in compound channels with deep and shallow overbank flows. *Journal of Hydraulic Research*, *50*(5), 482-493.

Klebanoff, P. (1955). *Characteristics of turbulence in boundary layer with zero pressure gradient*. National Bureau of Standards; Washington, DC, United States.

Knight, D. (2013). Hydraulic problems in flooding: from data to theory and from theory to practice. In *Experimental and computational solutions of hydraulic problems* (pp. 19-52). Springer, Berlin, Heidelberg.

Knight, D. W. & Shiono, K. (1996) River Channel and Floodplain Hydraulics. *Floodplain Processes 5,* pp. 139-181. John Wiley & Sons Ltd.

Knight, D. W., & Demetriou, J. D. (1983). Flood plain and main channel flow interaction. *Journal of Hydraulic Engineering*, *109*(8), 1073-1092.

Knight, D. W., Caroline McGahey, Rob Lamb, Paul Samuels (2010). *Practical channel hydraulics: Roughness, conveyance and afflux*. CRC Press, Taylor & Francis Group, London, UK.

Knight, D. W., Demetriou, J. D., & Hamed, M. E. (1984). Boundary shear in smooth rectangular channels. *Journal of hydraulic engineering*, *110*(4), 405-422.

Knight, D. W., Omran, M., & Abril, J. B. (2004). Boundary conditions between panels in depth-averaged flow models revisited. In *River Flow 2004, Proc., 2nd Int. Conf. on Fluvial Hydraulics, 23–25 June, Napoli, Italy* (Vol. 1, pp. 371-380).

Knight, D. W., Omran, M., & Tang, X. (2007). Modeling depth-averaged velocity and boundary shear in trapezoidal channels with secondary flows. *Journal of Hydraulic Engineering*, *133*(1), 39-47.

Knight, D. W., Shiono, K., & Pirt, J. (1989). Prediction of depth mean velocity and discharge in natural rivers with overbank flow. In *Proceedings of the International Conference on Hydraulic and Environmental Modellling of Coastal, Estuarine and River Waters* (pp. 419-428). Gower Publishing.

Knight, D. W., Wright, N. G., & Morvan, H. P. (2005). Guidelines for applying commercial CFD software to open channel flow. *Report based on research work conducted under EPSRC Grants GR*, *43716*, 31.

Knight, D.W., Omran, M. and Tang, X. (2007). Modeling depth-averaged velocity and boundary shear in trapezoidal channels with secondary flows. *Journal of Hydraulic Engineering*, *133*(1), 39-47.

Knight, D.W., Yuen, K.W.H. and Al-Hamid, A.A.I. (1994). Boundary shear stress distributions in open channel flow, in *Physical Mechanisms of Mixing and Transport in the Environment,* (Eds K. Beven, P. Chatwin & J. Millbank), J. Wiley, Chapter 4, pp. 51–87.

Knight, D.W., Yuen, K.W.H. and Al-Hamid, A.A.I. (1994). Boundary shear stress distributions in open channel flow, in *Physical Mechanisms of Mixing and Transport in the Environment*, J. Wiley, Chapter 4, pp. 51–87.

Kolmogorov, A. N. (1942). Equations of motion of an incompressible turbulent fluid. *Izv Akad Nauk SSSR Ser Phys*, *6*(6), 56-58.

Krishnamurthy, M., & Christensen, B. A. (1972). Equivalent roughness for shallow channel. *Journal of the hydraulics division*, *98*(12), 2257-2263.

Krishnappan, B. G., & Lau, Y. L. (1986). Turbulence modeling of flood plain flows. *Journal of hydraulic engineering*, *112*(4), 251-266.

Ladson, A. R., Lang, S. M., Smart, G. M., Anderson, B. G., & Rutherfurd, I. D. (2013). Flow resistance in four rivers in Victoria, Australia. *Australasian Journal of Water Resources*, *16*(2), 173-180.

Lambert, M. F., & Sellin, R. H. J. (1996). Discharge prediction in straight compound channels using the mixing length concept. *Journal of Hydraulic Research*, *34*(3), 381-394.

Lassabatere, L., Pu, J. H., Bonakdari, H., Joannis, C., & Larrarte, F. (2012). Velocity distribution in open channel flows: Analytical approach for the outer region. *Journal of Hydraulic Engineering*, *139*(1), 37-43.

Launder, B. E., & Sharma, B. I. (1974). Application of the energy-dissipation model of turbulence to the calculation of flow near a spinning disc. *Letters in heat and mass transfer*, *1*(2), 131-137.

Launder, B. E., Reece, G. J., & Rodi, W. (1975). Progress in the development of a Reynolds-stress turbulence closure. *Journal of fluid mechanics*, *68*(3), 537-566.

Launder, B.E. & D.B. Spalding (1974). The numerical computation of turbulent flows. *Computer Methods in Applied Mechanics and Engineering, 3* (2): 269 289.

Li, D., & Hager, W. H. (1991). Correction coefficients for uniform channel flow. *Canadian Journal of Civil Engineering*, *18*(1), 156-158.

Liao, H., & Knight, D. W. (2007). Analytic stage-discharge formulas for flow in straight prismatic channels. *Journal of Hydraulic Engineering*, *133*(10), 1111-1122.

Liu, C., Wright, N., Liu, X., & Yang, K. (2014). An analytical model for lateral depth-averaged velocity distributions along a meander in curved compound channels. *Advances in water resources*, *74*, 26-43.

Lotter, G. K. (1933). Considerations on hydraulic design of channels with different roughness of walls. *Transactions, All-Union Scientific Research Institute of Hydraulic Engineering, Leningrad*, *9*, 238-241.

Luo, E. C. R. (2012). Energy and momentum coefficients in straight symmetric compound-channel flows. *International Journal of Hydraulic Engineering*, *1*(3), 15-20.

Menter, F. R. (1994). Two-equation eddy-viscosity turbulence models for engineering applications. *AIAA journal*, *32*(8), 1598-1605.

Menter, F. R. (2009). Review of the shear-stress transport turbulence model experience from an industrial perspective. *International Journal of Computational Fluid Dynamics*, *23*(4), 305-316.

Mohammadi, B., & Pironneau, O. (1994). Analysis of the k-epsilon turbulence model. *John Wiley&Sons*.

Morvan, H., Knight, D., Wright, N., Tang, X., & Crossley, A. (2008). The concept of roughness in fluvial hydraulics and its formulation in 1D, 2D and 3D numerical simulation models. *Journal of Hydraulic Research*, *46*(2), 191-208.

Morvan, H., Pender, G., Wright, N. G., & Ervine, D. A. (2002). Three-dimensional hydrodynamics of meandering compound channels. *Journal of Hydraulic Engineering*, *128*(7), 674-682.

Müller, A. and Studerus, X. (1979). Secondary flow in an open channel. *Proceedings of 18th IAHR Congress*, Cagliari, Italy. Vol.3, pp. 19-24.

Myers, W. R. C. (1978). Momentum transfer in a compound channel. *Journal of Hydraulic Research*, *16*(2), 139-150.

Myers, W. R. C., & Brennan, E. K. (1990). Flow resistance in compound channels. *Journal of Hydraulic Research*, *28*(2), 141-155.

Myers, W. R. C., Knight, D. W., Lyness, J. F., Cassells, J. B., & Brown, F. (1999). Resistance coefficients for inbank and overbank flows. *Proceedings of the Institution of Civil Engineers-Water Maritime and Energy*, *136*(2), 105-115.

Naot, D., & Rodi, W. (1982). Calculation of secondary currents in channel flow. *Journal of the Hydraulics Division*, *108*(8), 948-968.

Naot, D., Nezu, I., & Nakagawa, H. (1993). Hydrodynamic behavior of compound rectangular open channels. *Journal of Hydraulic Engineering*, *119*(3), 390-408.

Naot, D., Nezu, I., & Nakagawa, H. (1996). Hydrodynamic behavior of partly vegetated open channels. *Journal of Hydraulic Engineering*, *122*(11), 625-633.

Nezu, I. (1996). Experimental and numerical study on 3-D turbulent structures in compound open channel flows. In Chen, C. J. (ed.), *Flow Modelling and Turbulence Measurements*, Hemisphere Pub Co-op, pp. 65.74.

Nezu, I. and Rodi, W. (1985). Experimental study on secondary currents in open channel flow. *Proceedings of 21st IAHR Congress*, Melbourne, Australia. Vol. 2, pp. 115-19.

Nezu, I., & Nakagawa, H. (1984). Cellular secondary currents in straight conduit. *Journal of hydraulic engineering*, *110*(2), 173-193.

Nezu, I., & Nakagawa, H. (1993). *Turbulence in Open-Channel Flows.* Rotterdam: IAHR Monograph Series, A.A. Balkema.

Nezu, I., & Rodi, W. (1986). Open-channel flow measurements with a laser Doppler anemometer. *Journal of Hydraulic Engineering*, *112*(5), 335-355.

Nezu, I., Nakagawa, H., & Saeki, K. I. (1994). Coherent structures in compound open-channel flows by making use of particle-tracking visualization technique. In *Fundamentals and Advancements in Hydraulic Measurements and Experimentation* (pp. 406-415). ASCE.

Nezu, I.; Nakagawa, Hi.; Rodi, W (1989). Significant difference between secondary currents in closed channels and narrow open channels. *Proceedings of 23rd IAHR Congress*, Ottawa, Canada. Vol. A. S., pp. 125-132.

Patel, V. C. (1965). Calibration of the Preston tube and limitations on its use in pressure gradients. *Journal of Fluid Mechanics, 23*(1), 185-208.

Peric, M., Rüger, M., & Scheuerer, G. (1988). *Calculation of the two-dimensional turbulent flow over a sand dune model*. University of Erlangen, Germany.

Pezzinga, G. (1994). Velocity distribution in compound channel flows by numerical modeling. *Journal of Hydraulic Engineering*, *120*(10), 1176-1198.

Pope, S. B. (2001). *Turbulent flows*. Cornell University, New York.

Prandtl, L. (1925). Report on Investigation of Developed Turbulence. *Math. Mech.*, *5*, 136-139.

Prandtl, L. (1952). Essentials of fluid dynamics: with applications to hydraulics, aeronautics, meteorology and other subjets. Hafner Pub. Co., New York, U.S.

Preston, J. (1954). The determination of turbulent skin friction by means of Pitot tubes. *The Aeronautical Journal*, *58*(518), 109-121.

Pu, J. H. (2013). Universal velocity distribution for smooth and rough open channel flows. *Journal of Applied Fluid Mechanics*, *6*(3), 413-423.

Ramesh, R., Datta, B., Bhallamudi, S. M., & Narayana, A. (2000). Optimal estimation of roughness in open-channel flows. *Journal of Hydraulic Engineering*, *126*(4), 299-303.

Rameshwaran, P., & Naden, P. S. (2003). Three-dimensional numerical simulation of compound channel flows. *Journal of hydraulic engineering*, *129*(8), 645-652.

Reece, G. J. (1977). A generalized Reynolds stress model of turbulence. *Ph.D. Thesis,* Imperial College, University of London, London, England.

Rezaei, B., & Knight, D. W. (2009). Application of the Shiono and Knight Method in compound channels with non-prismatic floodplains. *Journal of Hydraulic Research*, *47*(6), 716-726.

Rodi, W. (1993), *Turbulence Models and Their Applications in Hydraulics*, 3rd ed., IAHR Monograph, Delft, The Netherlands.

Rodi, W. (2017). Turbulence modeling and simulation in hydraulics: a historical review. *Journal of Hydraulic Engineering*, *143*(5), 03117001.

Rodríguez, J. F., & García, M. H. (2008). Laboratory measurements of 3-D flow patterns and turbulence in straight open channel with rough bed. *Journal of Hydraulic Research*, *46*(4), 454-465.

Rouse, H. ed. (1959). *Advanced Mechanics of Fluids*, Wiley, New York.

Schilchting, H. (1979). *Boundary Layer Theory*, 7th ed., McGraw–Hill, New York.

Schlichting H, Gersten K (2000) Boundary layer theory. Springer, Berlin

Seckin, G., Ardiclioglu, M., Cagatay, H., Cobaner, M., & Yurtal, R. (2009). Experimental investigation of kinetic energy and momentum correction coefficients in open channels. *Scientific Research and Essays*, *4*(5), 473-478.

Sellin, R. (1964). A laboratory investigation into the interaction between the flow in the channel of a river and that over its floodplain. *La Houille Blanche, 19*(9), pp. 793–801.

Sharifipour, M., Bonakdari, H., Zaji, A. H., & Shamshirband, S. (2015). Numerical investigation of flow field and flowmeter accuracy in open-channel junctions. *Engineering Applications of Computational Fluid Mechanics*, *9*(1), 280-290.

Shi, J., Thomas, T. G., & Williams, J. J. R. (1999). Large-eddy simulation of flow in a rectangular open channel. *Journal of Hydraulic Research, 37*(3), 345-361.

Shih, T. H., Liou, W. W., Shabbir, A., Yang, Z., & Zhu, J. (1995). A new k-ϵ eddy viscosity model for high Reynolds number turbulent flows. *Computers & Fluids*, *24*(3), 227-238.

Shiono, K., & Knight, D. W. (1988). Two-dimensional analytical solution for a compound channel. In *Proc., 3rd Int. Symp. on refined flow modeling and turbulence measurements* (pp. 503-510).

Shiono, K., & Knight, D. W. (1989). Transverse and vertical Reynolds stress measurements in a shear layer region of a compound channel. In *Proc. 7th Symp. On Turbulent Shear Flows, Stanford, U. S. A.* (Vol. 28, pp. 1-6).

Shiono, K., & Knight, D. W. (1991). Turbulent open-channel flows with variable depth across the channel. *Journal of Fluid Mechanics*, *222,* 617-646.

Singh, S. (2012). *Experiments in Hydraulic Engineering.* New Delhi: PHI Learning Private Limited.

Sofialidis, D., & Prinos, P. (1998). Compound open-channel flow modeling with nonlinear low-Reynolds k-ϵ models. *Journal of Hydraulic Engineering*, *124*(3), 253-262.

Spalart, P. R. (2000). Strategies for turbulence modelling and simulations. *International Journal of Heat and Fluid Flow*, *21*(3), 252-263.

Speziale, C. G., Sarkar, S., & Gatski, T. B. (1991). Modelling the pressure–strain correlation of turbulence: an invariant dynamical systems approach. *Journal of fluid mechanics*, *227*, 245-272.

Strauss, V. (1967). The Kinetic Energy Correction Factor and the Momentum Correction Factor in Open Channels. *12th IAHR World Congress* (pp. 314-323). Colorado, USA: International Association for Hydro-Environment Engineering and Research (IAHR).

Sukhodolov, A., Thiele, M., & Bungartz, H. (1998). Turbulence structure in a river reach with sand bed. *Water Resources Research*, *34*(5), 1317-1334.

Tang, X., & Knight, D. W. (2008). Lateral depth-averaged velocity distributions and bed shear in rectangular compound channels. *Journal of Hydraulic Engineering*, *134*(9), 1337-1342.

Te Chow, V. (1959). *Open channel hydraulics*. McGraw-Hill Book Company, Inc; New York.

Thomas, T. G., & Williams, J. J. R. (1995). Large eddy simulation of turbulent flow in an asymmetric compound open channel. *Journal of Hydraulic Research*, *33*(1), 27-41.

Tominaga, A., & Nezu, I. (1991). Turbulent structure in compound open-channel flows. *Journal of Hydraulic Engineering*, *117*(1), 21-41.

Tominaga, A., Nezu, I., Ezaki, K., & Nakagawa, H. (1989). Three-dimensional turbulent structure in straight open channel flows. *Journal of hydraulic research*, *27*(1), 149-173.

Van Prooijen, B. C., Battjes, J. A., & Uijttewaal, W. S. (2005). Momentum exchange in straight uniform compound channel flow. *Journal of hydraulic engineering*, *131*(3), 175-183.

Wang, Z. Q., & Cheng, N. S. (2005). Secondary flows over artificial bed strips. *Advances in water resources*, *28*(5), 441-450.

Wang, Z. Q., & Cheng, N. S. (2006). Time-mean structure of secondary flows in open channel with longitudinal bedforms. *Advances in water resources*, *29*(11), 1634-1649.

Wasantha Lal, A. M. (1995). Calibration of riverbed roughness. *Journal of Hydraulic Engineering*, *121*(9), 664-671.

Wilcox, D. A. (1994). Simulation of transition with a two-equation turbulence model. *AIAA journal*, *32*(2), 247-255.

Wilcox, D. C. (1988). Reassessment of the scale-determining equation for advanced turbulence models. *AIAA journal*, *26*(11), 1299-1310.

Wormleaton, P. R., Allen, J., & Hadjipanos, P. (1982). Discharge assessment in compound channel flow. *Journal of the Hydraulics Division*, *108*(9), 975-994.

Wu, S., & Rajaratnam, N. (2000). A simple method for measuring shear stress on rough boundaries. *Journal of Hydraulic Research*, *38*(5), 399-401.

Wu, W., Rodi, W., & Wenka, T. (2000). 3D numerical modeling of flow and sediment transport in open channels. *Journal of Hydraulic Engineering*, *126*(1), 4-15.

Wu, Y., Liu, Z., Chen, Y., & Li, M. (2018). Investigation of velocity distribution and turbulence characteristics in subcritical circular open channel flows using a modified Reynolds stress model. *Journal of Hydro-environment Research*, *19*, 68-77.

Xia, R., & Yen, B. C. (1994). Significance of averaging coefficients in open-channel flow equations. *Journal of hydraulic engineering*, *120*(2), 169-190.

Xiao, Y., Wang, N., Liang, D., & Liu, J. (2017). Flow Structures in Trapezoidal Compound Channels with Different Side Slopes of Main Channel. *International Journal of Civil Engineering*, 1-13.

Xie, Z., Lin, B., & Falconer, R. A. (2013). Large-eddy simulation of the turbulent structure in compound open-channel flows. *Advances in water resources*, *53*, 66-75.

Yakhot, V., & Orszag, S. A. (1986). Renormalization-group analysis of turbulence. *Physical review letters*, *57*(14), 1722.

Yang, Q. Y., Liu, T. H., Lu, W. Z., & Wang, X. K. (2013). Numerical simulation of confluence flow in open channel with dynamic meshes techniques. *Advances in Mechanical Engineering*, *5*, 860431.

Yang, S. Q., Tan, S. K., & Lim, S. Y. (2004). Velocity distribution and dip-phenomenon in smooth uniform open channel flows. *Journal of hydraulic engineering*, *130*(12), 1179-1186.

Yang, S. Q., Xu, W. L., & Yu, G. L. (2006). Velocity distribution in a gradually accelerating free surface flow. *Advances in water resources*, *29*(12), 1969-1980.

Appendices

Appendix A: Examples of velocity measurements and calculations

This Appendix gives examples for collecting the data used to calculate flow velocity in rectangular and compound channel experiments.

Table A.1 Measurements and calculations of local velocities in rectangular channel cases of the smallest flow depth (*H* = 60 mm).

Test Case: S6		***H* = 60 mm**	
y [mm]	*z* [mm]	Δ*p* [mm]	*u* [m/s]
10	0	0.0	0.000
10	10	3.1	0.246
10	20	3.6	0.264
10	30	3.8	0.272
10	40	3.8	0.275
10	50	3.7	0.269
10	60	3.5	0.262
30	0	0.0	0.000
30	10	3.8	0.273
30	20	4.4	0.294
30	30	4.7	0.305
30	40	4.9	0.310
30	50	4.8	0.308
30	60	4.7	0.305
50	0	0.0	0.000
50	10	4.1	0.282
50	20	4.7	0.305
50	30	5.1	0.317
50	40	5.4	0.324
50	50	5.4	0.326
50	60	5.4	0.326
70	0	0.0	0.000
70	10	3.9	0.276
70	20	4.5	0.298
70	30	5.0	0.312
70	40	5.2	0.320
70	50	5.3	0.324
70	60	5.4	0.326
90	0	0.0	0.000
90	10	3.8	0.274
90	20	4.5	0.297
90	30	4.9	0.311
90	40	5.2	0.320
90	50	5.4	0.325
90	60	5.5	0.329
110	0	0.0	0.000
110	10	3.9	0.277
110	20	4.6	0.301
110	30	5.1	0.315
110	40	5.4	0.325
110	50	5.6	0.331
110	60	5.8	0.336
130	0	0.0	0.000
130	10	3.9	0.276
130	20	4.6	0.300
130	30	5.0	0.315
130	40	5.4	0.325
130	50	5.6	0.332
130	60	5.8	0.338
150	0	0.0	0.000
150	10	3.9	0.278
150	20	4.6	0.302
150	30	5.1	0.317
150	40	5.5	0.328
150	50	5.7	0.335
150	60	5.9	0.342

Test Case: T6		***H* = 60 mm**	
y [mm]	*z* [mm]	Δ*p* [mm]	*u* [m/s]
10	0	0.0	0.000
10	10	1.5	0.171
10	20	1.8	0.188
10	30	2.0	0.196
10	40	2.0	0.198
10	50	1.9	0.193
10	60	1.8	0.186
30	0	0.0	0.000
30	10	1.9	0.191
30	20	2.3	0.212
30	30	2.5	0.222
30	40	2.6	0.228
30	50	2.6	0.226
30	60	2.5	0.223
50	0	0.0	0.000
50	10	1.9	0.195
50	20	2.4	0.217
50	30	2.7	0.229
50	40	2.8	0.236
50	50	2.9	0.238
50	60	2.9	0.238
70	0	0.0	0.000
70	10	1.8	0.188
70	20	2.2	0.210
70	30	2.5	0.223
70	40	2.7	0.231
70	50	2.8	0.235
70	60	2.9	0.237
90	0	0.0	0.000
90	10	1.8	0.187
90	20	2.2	0.209
90	30	2.5	0.222
90	40	2.7	0.231
90	50	2.8	0.236
90	60	2.9	0.240
110	0	0.0	0.000
110	10	1.8	0.188
110	20	2.2	0.210
110	30	2.6	0.224
110	40	2.8	0.233
110	50	2.9	0.240
110	60	3.1	0.245
130	0	0.0	0.000
130	10	1.8	0.187
130	20	2.2	0.209
130	30	2.5	0.223
130	40	2.8	0.233
130	50	2.9	0.240
130	60	3.1	0.246
150	0	0.0	0.000
150	10	1.8	0.187
150	20	2.2	0.210
150	30	2.6	0.224
150	40	2.8	0.234
150	50	3.0	0.242
150	60	3.1	0.248

Test Case: R6		***H* = 60 mm**	
y [mm]	*z* [mm]	Δ*p* [mm]	*u* [m/s]
10	0	0.0	0.000
10	10	0.8	0.128
10	20	1.1	0.145
10	30	1.2	0.154
10	40	1.2	0.156
10	50	1.1	0.150
10	60	1.0	0.143
30	0	0.0	0.000
30	10	1.0	0.142
30	20	1.3	0.163
30	30	1.5	0.174
30	40	1.6	0.180
30	50	1.6	0.178
30	60	1.6	0.175
50	0	0.0	0.000
50	10	1.0	0.143
50	20	1.4	0.165
50	30	1.6	0.178
50	40	1.8	0.185
50	50	1.8	0.187
50	60	1.8	0.188
70	0	0.0	0.000
70	10	1.0	0.138
70	20	1.3	0.160
70	30	1.5	0.173
70	40	1.7	0.182
70	50	1.8	0.186
70	60	1.8	0.188
90	0	0.0	0.000
90	10	0.9	0.136
90	20	1.3	0.158
90	30	1.5	0.172
90	40	1.7	0.181
90	50	1.8	0.187
90	60	1.9	0.191
110	0	0.0	0.000
110	10	1.0	0.137
110	20	1.3	0.159
110	30	1.5	0.173
110	40	1.7	0.184
110	50	1.8	0.190
110	60	2.0	0.196
130	0	0.0	0.000
130	10	0.9	0.136
130	20	1.3	0.158
130	30	1.5	0.173
130	40	1.7	0.183
130	50	1.9	0.191
130	60	2.0	0.197
150	0	0.0	0.000
150	10	0.9	0.136
150	20	1.3	0.159
150	30	1.5	0.174
150	40	1.7	0.185
150	50	1.9	0.193
150	60	2.0	0.199

Table A.2 Measurements and calculations of local velocities in rectangular channel cases of the largest flow depth (H = 20 mm).

Test Case: S20		**H = 200 mm**	
y [mm]	**z [mm]**	**Δp [mm]**	**u [m/s]**
10	0	0.0	0.000
10	10	5.9	0.340
10	20	6.7	0.363
10	30	7.2	0.377
10	40	7.6	0.387
10	50	7.9	0.394
10	60	8.1	0.399
10	70	8.3	0.404
10	80	8.4	0.407
10	90	8.6	0.410
10	100	8.6	0.412
10	110	8.7	0.413
10	120	8.7	0.413
10	130	8.7	0.413
10	140	8.7	0.412
10	150	8.6	0.410
10	160	8.4	0.407
10	170	8.2	0.402
10	180	7.9	0.393
10	190	7.2	0.376
10	200	6.6	0.359
30	0	0.0	0.000
30	10	7.3	0.377
30	20	8.3	0.403
30	30	8.9	0.419
30	40	9.4	0.429
30	50	9.8	0.437
30	60	10.0	0.444
30	70	10.3	0.449
30	80	10.5	0.453
30	90	10.6	0.456
30	100	10.7	0.458
30	110	10.8	0.460
30	120	10.8	0.461
30	130	10.8	0.461
30	140	10.8	0.461
30	150	10.7	0.459
30	160	10.6	0.456
30	170	10.4	0.451
30	180	10.0	0.442
30	190	9.2	0.426
30	200	8.5	0.409
50	0	0.0	0.000
50	10	7.9	0.394
50	20	9.0	0.421
50	30	9.7	0.437
50	40	10.3	0.449
50	50	10.7	0.457
50	60	11.0	0.464
50	70	11.2	0.470
50	80	11.5	0.474
50	90	11.6	0.478
50	100	11.8	0.480
50	110	11.9	0.482
50	120	11.9	0.484
50	130	12.0	0.484
50	140	11.9	0.484
50	150	11.9	0.483
50	160	11.8	0.480
50	170	11.5	0.476
50	180	11.2	0.468
50	190	10.4	0.453
50	200	9.7	0.437

Test Case: T20		**H = 200 mm**	
y [mm]	**z [mm]**	**Δp [mm]**	**u [m/s]**
10	0	0.0	0.000
10	10	3.5	0.261
10	20	4.1	0.285
10	30	4.6	0.300
10	40	4.9	0.311
10	50	5.2	0.318
10	60	5.4	0.325
10	70	5.5	0.329
10	80	5.7	0.333
10	90	5.8	0.336
10	100	5.8	0.338
10	110	5.9	0.340
10	120	5.9	0.340
10	130	5.9	0.340
10	140	5.8	0.339
10	150	5.8	0.336
10	160	5.6	0.332
10	170	5.4	0.326
10	180	5.1	0.316
10	190	4.5	0.296
10	200	3.9	0.276
30	0	0.0	0.000
30	10	4.3	0.290
30	20	5.2	0.318
30	30	5.7	0.335
30	40	6.1	0.347
30	50	6.4	0.356
30	60	6.7	0.363
30	70	6.9	0.368
30	80	7.1	0.373
30	90	7.2	0.376
30	100	7.3	0.379
30	110	7.4	0.381
30	120	7.4	0.382
30	130	7.4	0.382
30	140	7.4	0.381
30	150	7.3	0.379
30	160	7.2	0.375
30	170	6.9	0.369
30	180	6.6	0.359
30	190	5.9	0.339
30	200	5.2	0.319
50	0	0.0	0.000
50	10	4.8	0.305
50	20	5.7	0.335
50	30	6.3	0.352
50	40	6.8	0.365
50	50	7.2	0.375
50	60	7.4	0.382
50	70	7.7	0.388
50	80	7.9	0.393
50	90	8.1	0.397
50	100	8.2	0.401
50	110	8.3	0.403
50	120	8.3	0.404
50	130	8.4	0.405
50	140	8.3	0.405
50	150	8.3	0.403
50	160	8.2	0.400
50	170	8.0	0.395
50	180	7.6	0.386
50	190	6.9	0.367
50	200	6.2	0.349

Test Case: R20		**H = 200 mm**	
y [mm]	**z [mm]**	**Δp [mm]**	**u [m/s]**
10	0	0.0	0.000
10	10	2.3	0.211
10	20	2.9	0.237
10	30	3.3	0.253
10	40	3.6	0.264
10	50	3.8	0.273
10	60	4.0	0.280
10	70	4.1	0.285
10	80	4.3	0.289
10	90	4.4	0.293
10	100	4.4	0.295
10	110	4.5	0.297
10	120	4.5	0.297
10	130	4.5	0.297
10	140	4.5	0.296
10	150	4.4	0.293
10	160	4.2	0.289
10	170	4.0	0.282
10	180	3.7	0.270
10	190	3.1	0.248
10	200	2.6	0.225
30	0	0.0	0.000
30	10	2.7	0.232
30	20	3.5	0.261
30	30	4.0	0.278
30	40	4.3	0.291
30	50	4.6	0.301
30	60	4.8	0.308
30	70	5.0	0.314
30	80	5.2	0.319
30	90	5.3	0.323
30	100	5.4	0.326
30	110	5.5	0.328
30	120	5.5	0.329
30	130	5.5	0.329
30	140	5.5	0.328
30	150	5.4	0.326
30	160	5.3	0.321
30	170	5.0	0.314
30	180	4.7	0.303
30	190	4.0	0.279
30	200	3.3	0.256
50	0	0.0	0.000
50	10	3.1	0.247
50	20	3.9	0.278
50	30	4.5	0.297
50	40	4.9	0.311
50	50	5.3	0.321
50	60	5.5	0.330
50	70	5.8	0.337
50	80	6.0	0.342
50	90	6.1	0.347
50	100	6.3	0.350
50	110	6.3	0.353
50	120	6.4	0.354
50	130	6.4	0.355
50	140	6.4	0.355
50	150	6.4	0.353
50	160	6.2	0.350
50	170	6.0	0.344
50	180	5.7	0.333
50	190	5.0	0.312
50	200	4.3	0.290

Table A.2 (continued)

Test Case: S20		**H = 200 mm**	
y [mm]	z [mm]	Δp [mm]	u [m/s]
70	0	0.0	0.000
70	10	8.4	0.405
70	20	9.6	0.434
70	30	10.3	0.450
70	40	10.9	0.462
70	50	11.3	0.471
70	60	11.7	0.479
70	70	12.0	0.484
70	80	12.2	0.489
70	90	12.4	0.493
70	100	12.5	0.496
70	110	12.7	0.499
70	120	12.8	0.500
70	130	12.8	0.501
70	140	12.8	0.501
70	150	12.8	0.500
70	160	12.7	0.498
70	170	12.5	0.495
70	180	12.1	0.488
70	190	11.4	0.473
70	200	10.7	0.459
90	0	0.0	0.000
90	10	8.6	0.411
90	20	9.9	0.440
90	30	10.6	0.457
90	40	11.2	0.469
90	50	11.7	0.479
90	60	12.0	0.486
90	70	12.4	0.492
90	80	12.6	0.497
90	90	12.8	0.501
90	100	13.0	0.505
90	110	13.1	0.507
90	120	13.2	0.509
90	130	13.3	0.511
90	140	13.3	0.511
90	150	13.3	0.511
90	160	13.2	0.510
90	170	13.1	0.506
90	180	12.8	0.500
90	190	12.1	0.488
90	200	11.5	0.475
110	0	0.0	0.000
110	10	8.9	0.417
110	20	10.2	0.447
110	30	11.0	0.464
110	40	11.6	0.477
110	50	12.1	0.487
110	60	12.5	0.494
110	70	12.8	0.501
110	80	13.0	0.506
110	90	13.3	0.510
110	100	13.5	0.514
110	110	13.6	0.517
110	120	13.7	0.519
110	130	13.8	0.521
110	140	13.9	0.522
110	150	13.9	0.522
110	160	13.8	0.521
110	170	13.7	0.518
110	180	13.4	0.513
110	190	12.9	0.502
110	200	12.3	0.491

Test Case: T20		**H = 200 mm**	
y [mm]	z [mm]	Δp [mm]	u [m/s]
70	0	0.0	0.000
70	10	5.1	0.315
70	20	6.1	0.345
70	30	6.7	0.364
70	40	7.2	0.377
70	50	7.6	0.387
70	60	8.0	0.395
70	70	8.2	0.402
70	80	8.5	0.407
70	90	8.6	0.412
70	100	8.8	0.415
70	110	8.9	0.418
70	120	9.0	0.420
70	130	9.0	0.421
70	140	9.1	0.421
70	150	9.0	0.421
70	160	8.9	0.418
70	170	8.7	0.414
70	180	8.4	0.406
70	190	7.7	0.389
70	200	7.1	0.373
90	0	0.0	0.000
90	10	5.2	0.321
90	20	6.3	0.352
90	30	7.0	0.371
90	40	7.5	0.385
90	50	8.0	0.395
90	60	8.3	0.404
90	70	8.6	0.411
90	80	8.8	0.417
90	90	9.0	0.421
90	100	9.2	0.425
90	110	9.4	0.428
90	120	9.5	0.431
90	130	9.5	0.432
90	140	9.6	0.433
90	150	9.5	0.433
90	160	9.5	0.431
90	170	9.3	0.428
90	180	9.0	0.421
90	190	8.4	0.406
90	200	7.8	0.392
110	0	0.0	0.000
110	10	5.4	0.325
110	20	6.5	0.356
110	30	7.2	0.376
110	40	7.7	0.390
110	50	8.2	0.401
110	60	8.5	0.409
110	70	8.8	0.417
110	80	9.1	0.423
110	90	9.3	0.428
110	100	9.5	0.432
110	110	9.7	0.436
110	120	9.8	0.438
110	130	9.9	0.440
110	140	9.9	0.441
110	150	9.9	0.442
110	160	9.9	0.441
110	170	9.8	0.438
110	180	9.5	0.432
110	190	9.0	0.419
110	200	8.4	0.407

Test Case: R20		**H = 200 mm**	
y [mm]	z [mm]	Δp [mm]	u [m/s]
70	0	0.0	0.000
70	10	3.3	0.255
70	20	4.2	0.287
70	30	4.8	0.307
70	40	5.3	0.322
70	50	5.6	0.333
70	60	6.0	0.342
70	70	6.2	0.349
70	80	6.4	0.355
70	90	6.6	0.360
70	100	6.8	0.364
70	110	6.9	0.367
70	120	7.0	0.370
70	130	7.0	0.371
70	140	7.0	0.371
70	150	7.0	0.370
70	160	6.9	0.367
70	170	6.7	0.362
70	180	6.4	0.353
70	190	5.7	0.334
70	200	5.1	0.315
90	0	0.0	0.000
90	10	3.5	0.262
90	20	4.4	0.295
90	30	5.1	0.315
90	40	5.6	0.330
90	50	6.0	0.342
90	60	6.3	0.352
90	70	6.6	0.359
90	80	6.8	0.366
90	90	7.0	0.371
90	100	7.2	0.376
90	110	7.3	0.380
90	120	7.4	0.382
90	130	7.5	0.384
90	140	7.6	0.385
90	150	7.5	0.385
90	160	7.5	0.383
90	170	7.3	0.379
90	180	7.0	0.371
90	190	6.4	0.354
90	200	5.8	0.337
110	0	0.0	0.000
110	10	3.5	0.263
110	20	4.5	0.296
110	30	5.1	0.317
110	40	5.6	0.333
110	50	6.1	0.345
110	60	6.4	0.354
110	70	6.7	0.362
110	80	7.0	0.369
110	90	7.2	0.375
110	100	7.4	0.380
110	110	7.5	0.384
110	120	7.6	0.387
110	130	7.7	0.389
110	140	7.8	0.391
110	150	7.8	0.391
110	160	7.7	0.390
110	170	7.6	0.387
110	180	7.4	0.380
110	190	6.8	0.366
110	200	6.3	0.351

Table A.2 (continued)

Test Case: S20 **H = 200 mm**

y [mm]	z [mm]	Δp [mm]	u [m/s]
130	0	0.0	0.000
130	10	8.9	0.417
130	20	10.2	0.446
130	30	11.0	0.464
130	40	11.6	0.477
130	50	12.1	0.487
130	60	12.5	0.495
130	70	12.8	0.501
130	80	13.1	0.507
130	90	13.3	0.511
130	100	13.5	0.515
130	110	13.7	0.518
130	120	13.8	0.521
130	130	13.9	0.523
130	140	14.0	0.524
130	150	14.0	0.524
130	160	14.0	0.524
130	170	13.9	0.522
130	180	13.7	0.518
130	190	13.2	0.508
130	200	12.7	0.498
150	0	0.0	0.000
150	10	8.8	0.415
150	20	10.1	0.444
150	30	10.9	0.462
150	40	11.5	0.475
150	50	12.0	0.484
150	60	12.4	0.492
150	70	12.7	0.499
150	80	13.0	0.505
150	90	13.2	0.509
150	100	13.4	0.513
150	110	13.6	0.517
150	120	13.7	0.519
150	130	13.9	0.522
150	140	13.9	0.523
150	150	14.0	0.524
150	160	14.0	0.524
150	170	13.9	0.522
150	180	13.7	0.519
150	190	13.3	0.511
150	200	12.9	0.502

Test Case: T20 **H = 200 mm**

y [mm]	z [mm]	Δp [mm]	u [m/s]
130	0	0.0	0.000
130	10	5.4	0.325
130	20	6.5	0.357
130	30	7.2	0.376
130	40	7.8	0.391
130	50	8.2	0.402
130	60	8.6	0.411
130	70	8.9	0.418
130	80	9.2	0.424
130	90	9.4	0.430
130	100	9.6	0.434
130	110	9.8	0.438
130	120	9.9	0.441
130	130	10.0	0.443
130	140	10.1	0.445
130	150	10.1	0.445
130	160	10.1	0.445
130	170	10.0	0.443
130	180	9.8	0.438
130	190	9.3	0.427
130	200	8.8	0.416
150	0	0.0	0.000
150	10	5.3	0.323
150	20	6.4	0.355
150	30	7.1	0.375
150	40	7.7	0.389
150	50	8.1	0.400
150	60	8.5	0.409
150	70	8.8	0.417
150	80	9.1	0.423
150	90	9.4	0.428
150	100	9.6	0.433
150	110	9.7	0.437
150	120	9.9	0.440
150	130	10.0	0.443
150	140	10.1	0.445
150	150	10.1	0.446
150	160	10.1	0.446
150	170	10.1	0.444
150	180	9.9	0.440
150	190	9.5	0.431
150	200	9.0	0.421

Test Case: R20 **H = 200 mm**

y [mm]	z [mm]	Δp [mm]	u [m/s]
130	0	0.0	0.000
130	10	3.6	0.264
130	20	4.5	0.298
130	30	5.2	0.319
130	40	5.7	0.334
130	50	6.1	0.346
130	60	6.5	0.356
130	70	6.8	0.365
130	80	7.0	0.372
130	90	7.3	0.378
130	100	7.5	0.383
130	110	7.6	0.387
130	120	7.8	0.391
130	130	7.9	0.393
130	140	8.0	0.395
130	150	8.0	0.396
130	160	8.0	0.396
130	170	7.9	0.393
130	180	7.7	0.388
130	190	7.2	0.375
130	200	6.7	0.362
150	0	0.0	0.000
150	10	3.5	0.263
150	20	4.5	0.296
150	30	5.1	0.318
150	40	5.7	0.333
150	50	6.1	0.345
150	60	6.4	0.355
150	70	6.8	0.364
150	80	7.0	0.371
150	90	7.3	0.377
150	100	7.5	0.383
150	110	7.6	0.387
150	120	7.8	0.391
150	130	7.9	0.394
150	140	8.0	0.396
150	150	8.0	0.397
150	160	8.0	0.397
150	170	8.0	0.396
150	180	7.8	0.391
150	190	7.4	0.380
150	200	7.0	0.369

Table A.3 Measurements and calculations of local velocities in the compound channel case CS0.40 that has a smooth floodplain.

Test Case: CS0.4 ***Dr*** **= 0.40**

Main channel (smooth)

y	*z*	Δ*p*	*u*	*y*	*z*	Δ*p*	*u*
[mm]	[mm]	[mm]	[m/s]	[mm]	[mm]	[mm]	[m/s]
10	10	4.6	0.301	110	10	6.1	0.345
10	20	5.2	0.318	110	20	7.2	0.376
10	30	5.7	0.335	110	30	7.3	0.378
10	40	6.2	0.349	110	40	7.8	0.390
10	50	6.5	0.358	110	50	7.8	0.392
10	60	6.6	0.359	110	60	8.0	0.396
10	70	6.7	0.362	110	70	8.5	0.409
10	80	6.3	0.353	110	80	8.5	0.408
10	90	5.5	0.329	110	90	9.0	0.420
10	95	5.7	0.333	110	95	8.9	0.419
30	10	5.3	0.324	130	10	5.8	0.338
30	20	6.5	0.358	130	20	6.9	0.368
30	30	7.0	0.371	130	30	7.0	0.370
30	40	6.9	0.368	130	40	7.4	0.382
30	50	7.5	0.384	130	50	7.5	0.384
30	60	8.0	0.396	130	60	7.6	0.387
30	70	7.8	0.392	130	70	8.2	0.400
30	80	8.0	0.397	130	80	8.1	0.399
30	90	7.8	0.391	130	90	8.6	0.412
30	95	7.5	0.384	130	95	8.6	0.410
50	10	5.8	0.337	150	10	5.7	0.333
50	20	7.1	0.372	150	20	6.7	0.362
50	30	7.6	0.387	150	30	7.2	0.377
50	40	7.5	0.383	150	40	7.4	0.380
50	50	8.2	0.400	150	50	7.7	0.388
50	60	8.7	0.412	150	60	7.7	0.389
50	70	8.5	0.408	150	70	7.6	0.385
50	80	8.8	0.414	150	80	7.8	0.392
50	90	8.5	0.407	150	90	8.2	0.402
50	95	8.2	0.400	150	95	8.4	0.405
70	10	5.9	0.340	170	10	5.7	0.335
70	20	6.9	0.368	170	20	6.4	0.354
70	30	7.3	0.379	170	30	6.7	0.363
70	40	8.1	0.398	170	40	6.7	0.363
70	50	8.2	0.402	170	50	6.8	0.365
70	60	8.3	0.404	170	60	6.6	0.361
70	70	8.4	0.407	170	70	6.9	0.368
70	80	8.7	0.412	170	80	7.3	0.378
70	90	8.7	0.412	170	90	8.2	0.402
70	95	8.9	0.417	170	95	8.4	0.405
90	10	5.8	0.337	190	10	5.2	0.318
90	20	6.8	0.365	190	20	5.5	0.328
90	30	7.2	0.376	190	30	6.0	0.343
90	40	7.9	0.395	190	40	6.0	0.343
90	50	8.1	0.398	190	50	5.5	0.329
90	60	8.2	0.400	190	60	5.4	0.325
90	70	8.3	0.403	190	70	6.2	0.348
90	80	8.5	0.408	190	80	7.0	0.371
90	90	8.5	0.408	190	90	8.3	0.404
90	95	8.7	0.413	190	95	8.1	0.399

Floodplain (smooth)

y	*z*	Δ*p*	*u*	*y*	*z*	Δ*p*	*u*
[mm]	[mm]	[mm]	[m/s]	[mm]	[mm]	[mm]	[m/s]
210	10	6.8	0.365	270	10	5.2	0.318
210	20	7.9	0.394	270	20	6.4	0.354
210	30	8.7	0.413	270	30	6.2	0.348
210	35	9.1	0.422	270	35	6.4	0.354
230	10	6.8	0.364	290	10	5.0	0.313
230	20	8.2	0.402	290	20	5.7	0.335
230	30	8.4	0.406	290	30	5.4	0.327
230	35	8.6	0.411	290	35	5.4	0.327
250	10	6.0	0.344	300	10	0.0	0.000
250	20	7.0	0.370	300	20	0.0	0.000
250	30	7.4	0.380	300	30	0.0	0.000
250	35	7.3	0.379	300	35	0.0	0.000

Table A.4 Measurements and calculations of local velocities in the compound channel case CR0.40 that has a rough floodplain.

Test Case: CR0.4 ***Dr*** **= 0.40**

Main channel (smooth)

y	***z***	**Δ*p***	***u***	***y***	***z***	**Δ*p***	***u***
[mm]	**[mm]**	**[mm]**	**[m/s]**	**[mm]**	**[mm]**	**[mm]**	**[m/s]**
10	10	3.8	0.271	110	10	4.9	0.312
10	20	4.2	0.287	110	20	5.7	0.336
10	30	4.4	0.295	110	30	6.3	0.350
10	40	4.9	0.310	110	40	6.5	0.358
10	50	5.6	0.331	110	50	6.8	0.364
10	60	5.5	0.327	110	60	6.8	0.367
10	70	5.7	0.333	110	70	7.1	0.373
10	80	5.9	0.341	110	80	7.0	0.371
10	90	5.6	0.332	110	90	7.0	0.370
10	100	5.7	0.335	110	100	7.1	0.372
10	110	5.3	0.323	110	110	7.1	0.372
10	120	5.3	0.323	110	120	7.1	0.372
30	10	4.4	0.293	130	10	4.8	0.307
30	20	4.9	0.310	130	20	5.5	0.328
30	30	5.2	0.318	130	30	6.2	0.348
30	40	5.7	0.336	130	40	6.4	0.355
30	50	6.2	0.349	130	50	6.5	0.358
30	60	6.2	0.350	130	60	6.8	0.364
30	70	6.4	0.354	130	70	6.7	0.363
30	80	6.4	0.355	130	80	6.8	0.364
30	90	6.4	0.355	130	90	6.5	0.357
30	100	6.4	0.353	130	100	6.8	0.366
30	110	6.2	0.348	130	110	6.8	0.365
30	120	6.2	0.348	130	120	6.8	0.365
50	10	5.0	0.313	150	10	4.7	0.303
50	20	5.6	0.331	150	20	5.3	0.322
50	30	5.9	0.340	150	30	5.7	0.334
50	40	6.6	0.360	150	40	5.8	0.337
50	50	6.8	0.366	150	50	5.8	0.339
50	60	7.0	0.371	150	60	5.8	0.337
50	70	7.1	0.374	150	70	6.0	0.343
50	80	6.9	0.368	150	80	6.1	0.347
50	90	7.2	0.377	150	90	6.4	0.355
50	100	7.0	0.370	150	100	6.6	0.360
50	110	7.0	0.371	150	110	6.9	0.368
50	120	7.0	0.371	150	120	6.9	0.368
70	10	5.0	0.315	170	10	4.4	0.293
70	20	5.8	0.337	170	20	4.8	0.306
70	30	6.1	0.346	170	30	5.2	0.319
70	40	6.6	0.361	170	40	5.1	0.315
70	50	6.9	0.369	170	50	4.9	0.311
70	60	7.0	0.370	170	60	4.6	0.301
70	70	7.3	0.378	170	70	4.3	0.291
70	80	7.1	0.373	170	80	5.3	0.323
70	90	7.3	0.379	170	90	6.3	0.351
70	100	7.1	0.374	170	100	6.4	0.354
70	110	7.2	0.375	170	110	6.4	0.356
70	120	7.2	0.375	170	120	6.4	0.356
90	10	5.1	0.316	190	10	3.7	0.269
90	20	6.0	0.343	190	20	3.9	0.276
90	30	6.3	0.353	190	30	4.2	0.287
90	40	6.7	0.362	190	40	4.1	0.282
90	50	7.0	0.371	190	50	3.7	0.270
90	60	6.9	0.369	190	60	3.2	0.252
90	70	7.5	0.383	190	70	2.9	0.238
90	80	7.2	0.377	190	80	3.9	0.277
90	90	7.4	0.382	190	90	4.9	0.311
90	100	7.3	0.378	190	100	5.8	0.339
90	110	7.3	0.379	190	110	6.4	0.354
90	120	7.3	0.379	190	120	6.4	0.354

Floodplain (rough)

y	***z***	**Δ*p***	***u***	***y***	***z***	**Δ*p***	***u***
[mm]	**[mm]**	**[mm]**	**[m/s]**	**[mm]**	**[mm]**	**[mm]**	**[m/s]**
210	10	2.8	0.235	270	10	2.3	0.212
210	20	5.0	0.313	270	20	3.1	0.245
210	30	5.2	0.319	270	30	3.5	0.262
210	40	5.7	0.334	270	40	3.6	0.266
210	50	5.7	0.334	270	48	3.6	0.266
230	10	2.5	0.223	290	10	2.3	0.213
230	20	4.1	0.282	290	20	3.0	0.242
230	30	4.6	0.300	290	30	3.0	0.244
230	40	4.9	0.312	290	40	3.0	0.242
230	48	4.9	0.312	290	50	3.0	0.242
250	10	2.3	0.211	300	10	0.0	0.000
250	20	3.1	0.247	300	20	0.0	0.000
250	30	4.0	0.280	300	30	0.0	0.000
250	40	4.2	0.287	300	40	0.0	0.000
250	50	4.2	0.287	300	50	0.0	0.000

Table A.5 The Absolute Relative Differences (ARD) between the measured and integrated flow rates for all test cases.

Case #	**Channel Geometry**	**Roughness Conditions**	***Q* (m3/s)**	***Q* (m3/s)**	**ARD (%)**
			EMFM	**Integrated (Eq. 3.5)**	**[(Q-Q_m) /Q]x100**
S6	Rectangular	Smooth	5.22	5.13	1.8
S10	Rectangular	Smooth	11.39	11.26	1.1
S15	Rectangular	Smooth	21.17	20.61	2.6
S20	Rectangular	Smooth	32.86	31.89	2.9
T6	Rectangular	Transitional	4.13	4.02	2.6
T10	Rectangular	Transitional	9.33	9.06	2.8
T15	Rectangular	Transitional	17.42	17.00	2.4
T20	Rectangular	Transitional	26.14	25.38	2.9
R6	Rectangular	Rough	3.12	3.04	2.8
R10	Rectangular	Rough	7.36	7.17	2.5
R15	Rectangular	Rough	14.92	14.52	2.7
R20	Rectangular	Rough	24.59	23.90	2.8
CS0.25	Compound	Smooth	6.09	6.16	1.1
CS0.33	Compound	Smooth	7.49	7.60	1.5
CS0.40	Compound	Smooth	9.01	9.18	1.9
CS0.50	Compound	Smooth	12.40	12.67	2.1
CT0.25	Compound	Transitional	5.28	5.37	1.7
CT0.33	Compound	Transitional	6.57	6.76	2.9
CT0.40	Compound	Transitional	7.99	8.13	1.7
CT0.50	Compound	Transitional	11.21	11.45	2.1
CR0.25	Compound	Rough	6.60	6.75	2.2
CR0.33	Compound	Rough	8.11	8.26	1.8
CR0.40	Compound	Rough	9.90	10.10	2.0
CR0.50	Compound	Rough	13.79	14.14	2.5

Appendix B: Examples of CFX input file

```
Name                                          Value
Root
  SIMULATION CONTROL :
  LIBRARY :
  FLOW : Flow Analysis 1
    SOLUTION UNITS :
      Angle Units                             [rad]
      Length Units                            [m]
      Mass Units                              [kg]
      Solid Angle Units                       [sr]
      Temperature Units                       [K]
      Time Units                              [s]
    ANALYSIS TYPE :
      Option                                  Steady State
      EXTERNAL SOLVER COUPLING :
        Option                                None
    DOMAIN : Default Domain
      Coord Frame                             Coord 0
      Domain Type                             Fluid
      Location                                B16
      BOUNDARY : Domain Interface 1 Side 1
        Boundary Type                         INTERFACE
        Location                              inlet
        BOUNDARY CONDITIONS :
          MASS AND MOMENTUM :
            Option                            Conservative Interface Flux
          TURBULENCE :
            Option                            Conservative Interface Flux
```

```
Name                                          Value
      BOUNDARY : Domain Interface 1 Side 2
        Boundary Type                         INTERFACE
        Location                              outlet
        BOUNDARY CONDITIONS :
          MASS AND MOMENTUM :
            Option                            Conservative Interface Flux
          TURBULENCE :
            Option                            Conservative Interface Flux
      BOUNDARY : FS
        Boundary Type                         WALL
        Location                              top
        BOUNDARY CONDITIONS :
          MASS AND MOMENTUM :
            Option                            Free Slip Wall
      BOUNDARY : bed
        Boundary Type                         WALL
        Location                              bed
        BOUNDARY CONDITIONS :
          MASS AND MOMENTUM :
            Option                            No Slip Wall
          WALL ROUGHNESS :
            Option                            Smooth Wall
      BOUNDARY : sidewall
        Boundary Type                         WALL
        Location                              left,right
        BOUNDARY CONDITIONS :
          MASS AND MOMENTUM :
            Option                            No Slip Wall
```

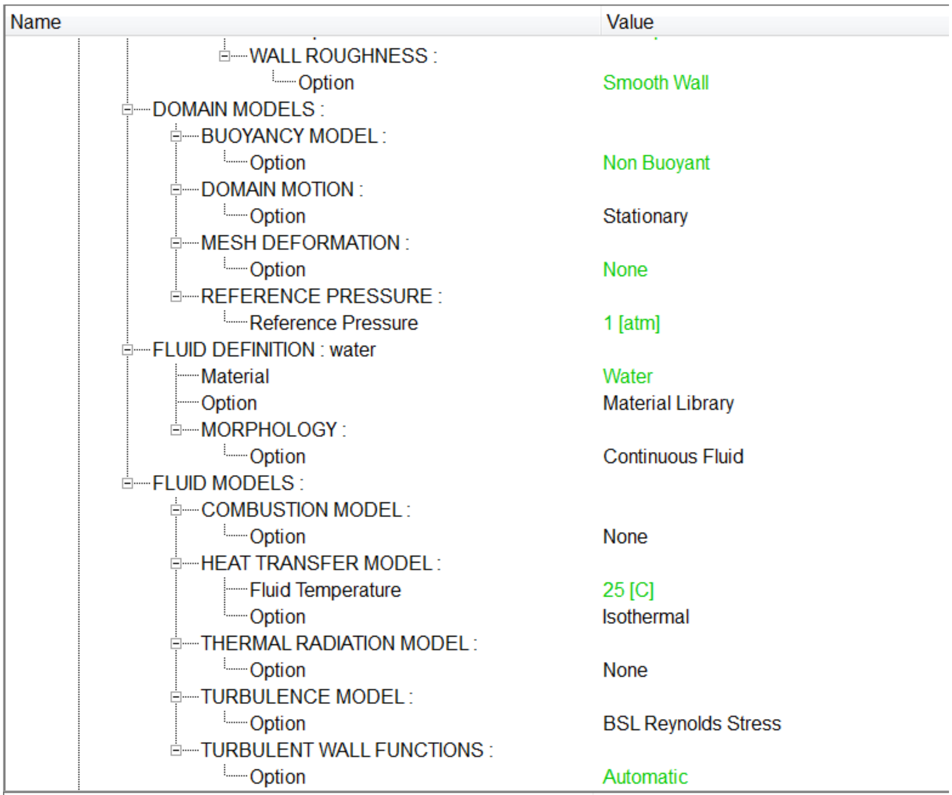

Name	Value
WALL ROUGHNESS :	
Option	Smooth Wall
DOMAIN MODELS :	
BUOYANCY MODEL :	
Option	Non Buoyant
DOMAIN MOTION :	
Option	Stationary
MESH DEFORMATION :	
Option	None
REFERENCE PRESSURE :	
Reference Pressure	1 [atm]
FLUID DEFINITION : water	
Material	Water
Option	Material Library
MORPHOLOGY :	
Option	Continuous Fluid
FLUID MODELS :	
COMBUSTION MODEL :	
Option	None
HEAT TRANSFER MODEL :	
Fluid Temperature	25 [C]
Option	Isothermal
THERMAL RADIATION MODEL :	
Option	None
TURBULENCE MODEL :	
Option	BSL Reynolds Stress
TURBULENT WALL FUNCTIONS :	
Option	Automatic

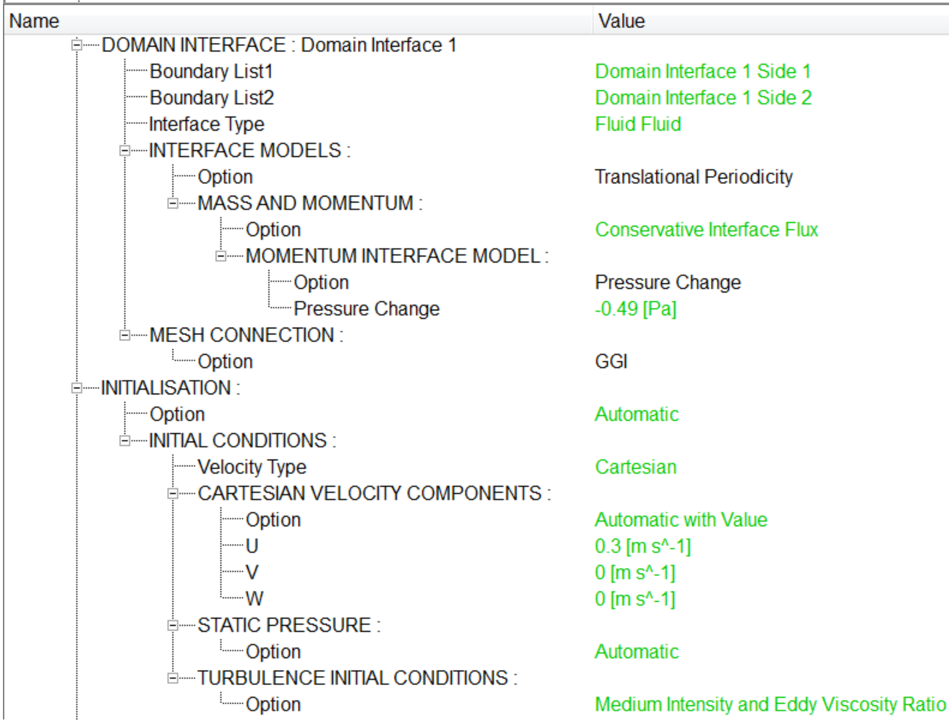

Name	Value
DOMAIN INTERFACE : Domain Interface 1	
Boundary List1	Domain Interface 1 Side 1
Boundary List2	Domain Interface 1 Side 2
Interface Type	Fluid Fluid
INTERFACE MODELS :	
Option	Translational Periodicity
MASS AND MOMENTUM :	
Option	Conservative Interface Flux
MOMENTUM INTERFACE MODEL :	
Option	Pressure Change
Pressure Change	-0.49 [Pa]
MESH CONNECTION :	
Option	GGI
INITIALISATION :	
Option	Automatic
INITIAL CONDITIONS :	
Velocity Type	Cartesian
CARTESIAN VELOCITY COMPONENTS :	
Option	Automatic with Value
U	0.3 [m s^-1]
V	0 [m s^-1]
W	0 [m s^-1]
STATIC PRESSURE :	
Option	Automatic
TURBULENCE INITIAL CONDITIONS :	
Option	Medium Intensity and Eddy Viscosity Ratio

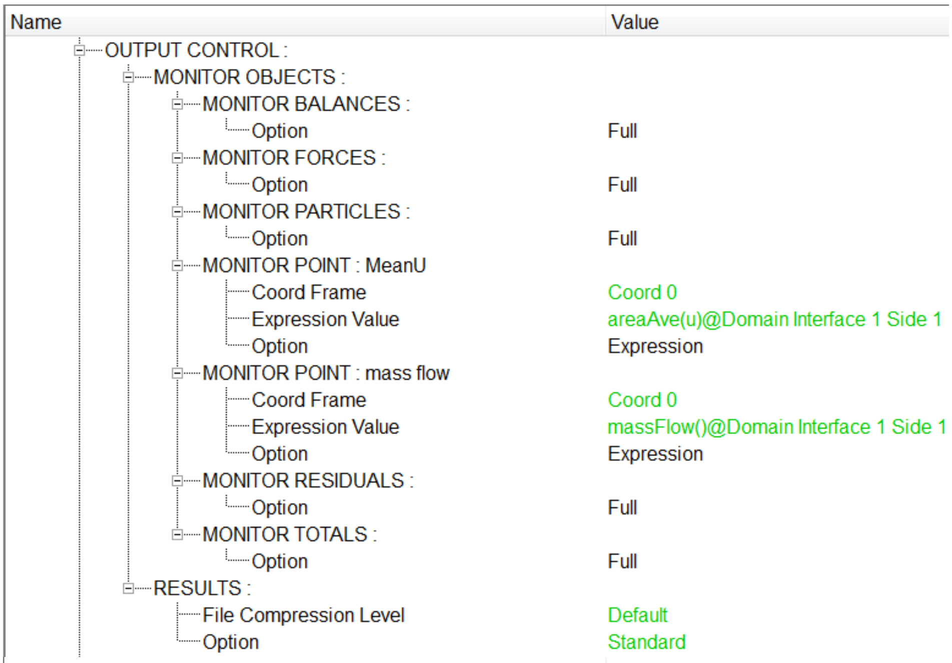

```
Name                                          Value
OUTPUT CONTROL :
  MONITOR OBJECTS :
    MONITOR BALANCES :
      Option                                  Full
    MONITOR FORCES :
      Option                                  Full
    MONITOR PARTICLES :
      Option                                  Full
    MONITOR POINT : MeanU
      Coord Frame                             Coord 0
      Expression Value                        areaAve(u)@Domain Interface 1 Side 1
      Option                                  Expression
    MONITOR POINT : mass flow
      Coord Frame                             Coord 0
      Expression Value                        massFlow()@Domain Interface 1 Side 1
      Option                                  Expression
    MONITOR RESIDUALS :
      Option                                  Full
    MONITOR TOTALS :
      Option                                  Full
  RESULTS :
    File Compression Level                    Default
    Option                                    Standard
```

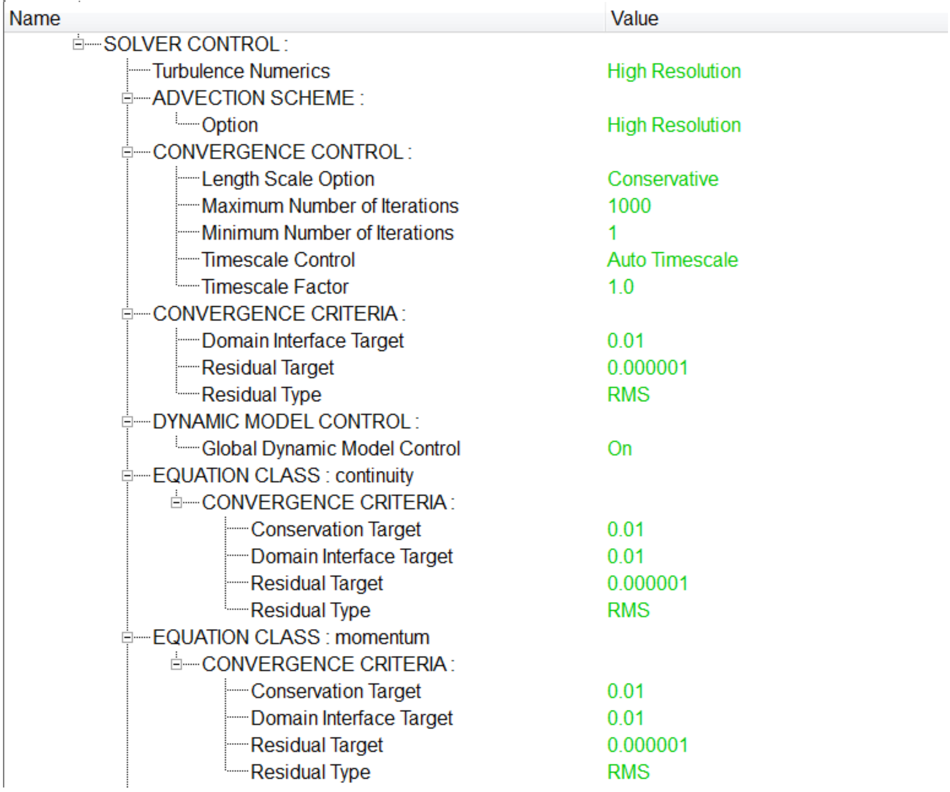

```
Name                                          Value
SOLVER CONTROL :
  Turbulence Numerics                         High Resolution
  ADVECTION SCHEME :
    Option                                    High Resolution
  CONVERGENCE CONTROL :
    Length Scale Option                       Conservative
    Maximum Number of Iterations              1000
    Minimum Number of Iterations              1
    Timescale Control                         Auto Timescale
    Timescale Factor                          1.0
  CONVERGENCE CRITERIA :
    Domain Interface Target                   0.01
    Residual Target                           0.000001
    Residual Type                             RMS
  DYNAMIC MODEL CONTROL :
    Global Dynamic Model Control              On
  EQUATION CLASS : continuity
    CONVERGENCE CRITERIA :
      Conservation Target                     0.01
      Domain Interface Target                 0.01
      Residual Target                         0.000001
      Residual Type                           RMS
  EQUATION CLASS : momentum
    CONVERGENCE CRITERIA :
      Conservation Target                     0.01
      Domain Interface Target                 0.01
      Residual Target                         0.000001
      Residual Type                           RMS
```

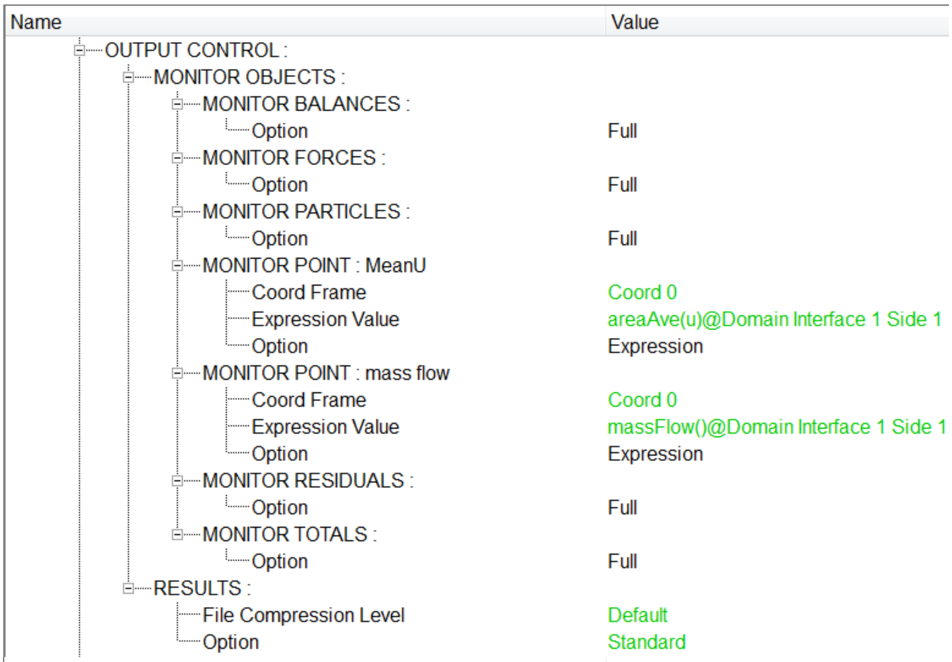

```
Name                                        Value
OUTPUT CONTROL :
  MONITOR OBJECTS :
    MONITOR BALANCES :
      Option                                Full
    MONITOR FORCES :
      Option                                Full
    MONITOR PARTICLES :
      Option                                Full
    MONITOR POINT : MeanU
      Coord Frame                           Coord 0
      Expression Value                      areaAve(u)@Domain Interface 1 Side 1
      Option                                Expression
    MONITOR POINT : mass flow
      Coord Frame                           Coord 0
      Expression Value                      massFlow()@Domain Interface 1 Side 1
      Option                                Expression
    MONITOR RESIDUALS :
      Option                                Full
    MONITOR TOTALS :
      Option                                Full
  RESULTS :
    File Compression Level                  Default
    Option                                  Standard
```

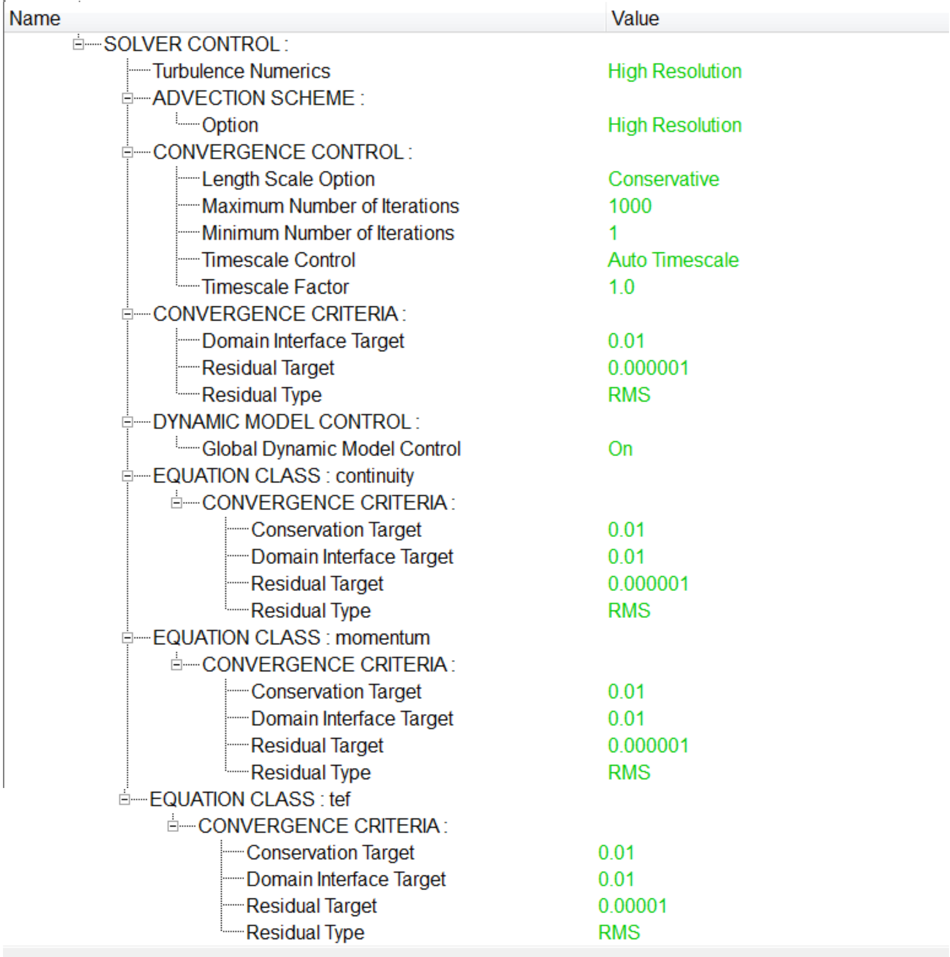

```
Name                                        Value
SOLVER CONTROL :
  Turbulence Numerics                       High Resolution
  ADVECTION SCHEME :
    Option                                  High Resolution
  CONVERGENCE CONTROL :
    Length Scale Option                     Conservative
    Maximum Number of Iterations            1000
    Minimum Number of Iterations            1
    Timescale Control                       Auto Timescale
    Timescale Factor                        1.0
  CONVERGENCE CRITERIA :
    Domain Interface Target                 0.01
    Residual Target                         0.000001
    Residual Type                           RMS
  DYNAMIC MODEL CONTROL :
    Global Dynamic Model Control            On
  EQUATION CLASS : continuity
    CONVERGENCE CRITERIA :
      Conservation Target                   0.01
      Domain Interface Target               0.01
      Residual Target                       0.000001
      Residual Type                         RMS
  EQUATION CLASS : momentum
    CONVERGENCE CRITERIA :
      Conservation Target                   0.01
      Domain Interface Target               0.01
      Residual Target                       0.000001
      Residual Type                         RMS
  EQUATION CLASS : tef
    CONVERGENCE CRITERIA :
      Conservation Target                   0.01
      Domain Interface Target               0.01
      Residual Target                       0.00001
      Residual Type                         RMS
```

Appendix C: MATLAB Code for the analytical solution of the SKM

```
function Ud = SKM(B,b,H,D,S,YU,f1,La1,Ga1,f2,La2,Ga2)
% Program to compute depth-averaged velocity profile from
%the SKM analytical solution for asymmetric compound channels
% B,b,H,D,S,YU are the data related to the experimental test 
case
% f is the friction factor
% La is the dimension less eddy viscosity
% Ga is the secondary flow term
%% Arranging SKM inputs
h(1:2)=H; % flow depth in each panel
S0(1:2)=S; % bed slope of each panel
f=[f1 f2];
La=[La1 La2];
Ga=[Ga1 Ga2];
%% Calculating SKM variables (Beta,k,Nu,Phi)
Beta=Ga./(9.81*1000.*h.*S0);
k=8*9.81.*S0.*h./f.*(1-Beta);
Nu=((2./La).^0.5).*((f/8).^0.25).*(1./h);
Phi=0.5*1000.*La.*h.^2.*(f./8).^0.5;
%% Calculating the variable matrix (X)
X=ones(4,4);
X(1,1:2)=1;
X(1,3:4)=0;
X(2,1:2)=0;
X(2,3)=exp(Nu(1,2)*B);
X(2,4)=exp(-1*Nu(1,2)*B);
X(3,1)=exp(Nu(1,1)*b);
X(3,2)=exp(-1*Nu(1,1)*b);
X(3,3)=-exp(Nu(1,2)*b);
X(3,4)=-exp(-1*Nu(1,2)*b);
X(4,1)=(Phi(1,1)*Nu(1,1)+1000*f1*D/8)*exp(Nu(1,1)*b);
X(4,2)=-1*(Phi(1,1)*Nu(1,1)-1000*f1*D/8)*exp(-1*Nu(1,1)*b);
X(4,3)=-1*Phi(1,2)*Nu(1,2)*exp(Nu(1,2)*b);
```

```
X(4,4)=Phi(1,2)*Nu(1,2)*exp(-1*Nu(1,2)*b);
%% Introducing the coefficient matrix (C)
C(1,1)=-k(1,1);
C(2,1)=-k(1,2);
C(3,1)=k(1,2)-k(1,1);
C(4,1)=-1000*f1*D*k(1,1)/8;
%% Calculating the A coefficient matrix
A=X\C;
%% Calculating depth-averaged velocity (Ud)
y=YU;
for i=1:length(YU);
    if y(1,i)< b
Ud(1,i)=real((A(1,1)*exp(Nu(1,1)*y(1,i))+A(2,1)*exp(-
1*Nu(1,1)*...
y(1,i))+k(1,1))^0.5);
    else
Ud(1,i)=real((A(3,1)*exp(Nu(1,2)*y(1,i))+A(4,1)*exp(-
1*Nu(1,2)*...
y(1,i))+k(1,2))^0.5);
    end
end
plot(y,Ud)
end
```